CRANFIELD UNIVERSITY

OBINNA HYACINTH EHIRIM

AERODYNAMICS AND PERFORMANCE ENHANCEMENT OF A GROUND-EFFECT DIFFUSER

CRANFIELD DEFENCE AND SECURITY
Centre for Defence Engineering
Aeromechanical Systems Group

PhD Thesis

Supervisors:
Professor Kevin Knowles
Dr. Alistair J. Saddington

October 2017

CRANFIELD UNIVERSITY

CRANFIELD DEFENCE AND SECURITY
Centre for Defence Engineering
Aeromechanical Systems Group

PhD Thesis

Academic Year 2017 - 2018

Obinna Hyacinth Ehirim

AERODYNAMICS AND PERFORMANCE ENHANCEMENT OF A GROUND-EFFECT DIFFUSER

Supervisors: Professor Kevin Knowles and Dr. Alistair J. Saddington

ABSTRACT

This study involved experimental and equivalent computational investigations into the automobile-type 3—D flow physics of a diffuser bluff body in ground-effect and novel passive flow-control methods applied to the diffuser flow to enhance the diffuser's aerodynamic performance. The bluff body used in this study is an Ahmed-like body employed in an inverted position with the slanted section together with the addition of side plates along both sides forming the ramped diffuser section.

The first part of the study confirmed reported observations from previous studies that the downforce generated by the diffuser in proximity to a ground plane is influenced by the peak suction at the diffuser inlet and subsequent static pressure-recovery towards the diffuser exit. Also, when the bluff body ride height is gradually reduced from high to low, the diffuser flow as indicated by its force curve and surface flow features undergoes four distinct flow regimes (types A to D). The types A and B regimes are reasonably symmetrical, made up of two low-pressure core longitudinal vortices travelling along both sides of the diffuser length and they increase downforce and drag with reducing ride height. However, below the ride heights of the type B regime, types C and D regimes are asymmetrical because of the breakdown of one vortex; consequently a significant loss in downforce and drag occurs.

The second part of the study involved the use — near the diffuser exit — of a convex bump on the diffuser ramp surface and an inverted wing between the diffuser side plates as passive flow control devices. The modification of the diffuser geometry with these devices employed individually or in combination, induced a second-stage pressure-drop and recovery near the diffuser exit. This behaviour was due to the radial pressure gradient induced on the diffuser flow by the suction surface

curvature of the passive devices. As a result of this aerodynamic phenomenon, the diffuser generated across the flow regimes additional downforce, and a marginal increase in drag due to the profile drag induced by the devices.

Keywords: ground-effect aerodynamics, diffuser, passive flow control, inverted wing, convex bump, downforce, drag

To my parents

for always supporting me

ACKNOWLEDGEMENTS

Firstly, I would like to thank my supervisors, Professor Kevin Knowles and Dr. Alistair Saddington for the guidance and support I received over the course of this research work. Due to their supervision, I have gained an in-depth insight of the subject matter.

I would also like to acknowledge the financial support to undertake this research project from the Niger Delta Development Commission (NDDC) of Nigeria and from Cranfield University. Without such monetary assistance, it would have been impossible for me to embark on this PhD research work.

Thanks also goes to Mike, Brian and Karl at the workshop who helped me build the test model for the wind tunnel experiments. Likewise, I appreciate the assistance of Dr. Mark Finnis and Professor Nicholas Lawson with the use of the wind tunnel and the laser Doppler velocimetry equipment respectively.

I acknowledge the cordiality all through my time working on this research from fellow PhD students' — Joao, Rahim, Luke and David. I would also like to thank Rachel, Iain, Lauren, and other staff members of the Cranfield Barrington Library for providing a friendly atmosphere during my part-time hours working at the library.

Finally, I am grateful for the support and encouragement I received from my family and friends here in the United Kingdom, the United States, and Nigeria; particularly from my parents in Nigeria, and my buddy — the late Chinweike Okegbe, PhD.

All thanks to God.

TABLE OF CONTENTS

Abstract i

Acknowledgements iv

List of Figures ix

List of Tables xxiv

Nomenclature xxv

Thesis Overview xxviii

1 Introduction 1

1.1 Research Background 1

1.1.1 Ground-effect aerodynamics 1

1.1.2 Internal flow diffusers 2

1.1.3 The ground-effect diffuser 4

1.2 The Ground-effect Diffuser and Downforce Production 7

1.3 Aerodynamic Performance Definition of the Ground-effect Diffuser 10

2 Literature Review 15

2.1 Experimental Studies 16

2.1.1 Longitudinal vortices 16

2.1.2 Diffuser length and area ratio 20

2.1.3 Diffuser ride height 23

2.1.4 Diffuser angle 26

2.2 Computational Studies 30

2.2.1 Steady-state numerical simulations 30

2.2.2 Transient numerical simulations 32

2.3 Ground-effect Diffuser Performance Enhancement 34

2.3.1 Active and passive flow control 36

2.3.2 Coandă effect 41

2.3.3 Flow-curvature effect 43

2.4 Aims and Objectives of the Current Work 44

3 Research Methods and Set-up 47

3.1 Experimental Set-up 47

3.1.1 Wind tunnel facility and test operating conditions 47
3.1.2 Wind tunnel test models 49
3.1.3 Test model installation and ride height positioning 54
3.2 Experimental Techniques 55
3.2.1 Force measurements 55
3.2.2 Surface pressure measurements 56
3.2.3 Surface flow visualisation 58
3.2.4 Laser Doppler velocimetry measurements 60
3.3 Computational Set-up and Techniques 65
3.3.1 Computational domain and grid 65
3.3.2 Boundary conditions 69
3.3.3 Numerical methods 69
3.3.4 Governing equations 71
3.3.5 Simulation procedure 77
4 Plane Diffuser (Baseline): Forces, Pressures and Flow Characteristics 84
4.1 Diffuser Flow Behaviour and Flow Regime Types 84
4.1.1 Force enhancement (flow regime A) 90
4.1.2 Maximum force (flow regime B) 92
4.1.3 Force reduction (flow regime C) 100
4.1.4 Low force (flow regime D) 101
4.2 Further Measurements in Freestream 102
4.2.1 Fixed and moving ground conditions 103
4.2.2 Flow hysteresis 105
4.2.3 Reynolds number sensitivity 106
4.2.4 Pitching moment and pitch angle sensitivity 109
4.2.5 Effects of transition fixing 113
4.2.6 Base surface pressures 115
4.3 Baseline Downforce and Drag (CFD vs. Experiments) 118
4.4 Surface Pressure (CFD vs. Experiment) 121
4.5 Surface Flow Features (CFD vs. Experiment) 129
4.6 Further Discussion 137

4.7 Summary 140

5 Plane Diffuser (Baseline): Edge Vortex Behaviour and Velocity Profiles 141

5.1 Diffuser Edge Vortex Development 141

5.1.1 Vortex behaviour in flow regime A 147

5.1.2 Vortex behaviour in flow regime B 155

5.1.3 Vortex behaviour in flow regime C 160

5.1.4 Vortex behaviour in flow regime D 164

5.2 Velocity Profile Development 168

5.2.1 Underbody boundary layer profiles 172

5.2.2 Velocity profiles of diffuser near-wake region 176

5.2.3 Flow structures of diffuser near-wake region 184

5.3 Further Discussion 188

5.4 Summary 190

6 Flow Physics of Diffuser with Passive Flow Control 192

6.1 Flow Control Methods: Introduction 192

6.1.1 Convex bump 193

6.1.2 Inverted wing in diffuser 198

6.1.3 Combination of convex bump and inverted wing 203

6.2 Flow Characteristics: Baseline and Passive Flow Control Methods 205

6.2.1 Diffuser body downforce and drag measurements 206

6.2.2 Reynolds number sensitivity 210

6.2.3 Aerodynamic efficiency (lift-to-drag ratio) 212

6.2.4 Underbody and diffuser surface pressure measurements 214

6.2.5 Diffuser ramp surface flow features 220

6.3 Flow Characteristics: CFD vs. Experiments 227

6.3.1 Force measurements (downforce and drag) 227

6.3.2 Surface pressure measurements 229

6.3.3 Surface flow features 237

6.3.4 Skin friction drag 244

6.4 Velocity Profile Measurements 250

6.4.1 Flow structures of diffuser near-wake region 250

6.4.2 Velocity profiles of diffuser near-wake region 251
6.4.3 Circulation in diffuser near-wake region 257
6.5 Further Discussion 259
6.6 Summary 261
7 Conclusions and Future Work Recommendations 263
7.1 Conclusions 263
7.2 Recommendations for Future Work 268
References 271
Appendices 281
Appendix A — Measurements Uncertainty and Repeatability Analysis 281
Appendix B — Wind Tunnel Model Geometry 286
Appendix C — Experimental and Numerical Test Conditions 289
Appendix D — Experimental Downforce and Drag Measurements 293
Appendix E — Publications Prepared from this Thesis 294

LIST OF FIGURES

Figure 1-1: Illustrations of **(a)** $2-\mathrm{D}$ conical **(b)** $3-\mathrm{D}$ plane-wall diffuser dimensional parameters....3

Figure 1-2: Illustrations of **(a)** an inverted aerofoil and **(b)** the Lotus 78 and 79 underbody....6

Figure 1-3: Downforce effect on cornering speeds around a corner radius of 40 m at maximum effective tyre cornering coefficient $\mathrm{k_c}$ (max), (Barnard, 2011)....6

Figure 1-4: Drag and downforce distribution of a 2009 F1 racing car (Toet, 2013)....9

Figure 1-5: An illustration of vortex upwash along the diffuser channels of a racing car....10

Figure 1-6: **(a)** Schematic of an Ahmed body dimensioned in mm as outlined by Ahmed et al., (1984) and **(b)** an inverted Ahmed-like bluff body as a diffuser bluff body....11

Figure 1-7: Schematic of the centreline pressure behaviour along the flat underbody and diffuser sections of a diffuser bluff body; adapted from Marklund (2013)....11

Figure 2-1: **(a)** Bubble and spiral types of vortex breakdown on a delta wing, (Lambourne & Bryer, 1962) **(b)** Double-helix vortex breakdown in a swirling flow through a tube, (Van Dyke, 1982) **(c)** Q-criterion velocity iso-surfaces of spiral type vortex breakdown within a diffuser bluff body (CFD studies by thesis author)....17

Figure 2-2: Schematic of bluff body geometries (with dimensions in mm) as studied by George (1981)....19

Figure 2-3: Schematics of the 'Venturi' bluff body model as studied by George and Donis (1983)....20

Figure 2-4: Illustrations of the bluff body diffuser geometries (with dimensions in mm) and pressure tap positions as used by Cooper et al. (1998, 2000)....21

Figure 2-5: Downforce comparison for bluff body diffusers of Breslouer & George (2008) and Cooper et al. (1998 & 2000) presented in Breslouer & George (2008) 23

Figure 2-6: Schematic of the diffuser-equipped bluff body geometry (with dimensions in mm) used by Senior & Zhang. (2000a, 2000b) 24

Figure 2-7: Flow regions within plots of lift coefficient against normalized ride height as presented by Senior (2002) 24

Figure 2-8: Downforce curve for flow regions (a-e) and flow hysteresis regions (b' and c') for the 15° diffuser angle as presented by Ruhrmann & Zhang (2003) 26

Figure 2-9: Flow regime maps for diffuser angles and corresponding area ratios Ruhrmann & Zhang (2003) 27

Figure 2-10: Flow visualisation on the ramp surfaces of **(a)** 5°, **(b)** 10° and **(c)** 15° diffusers at maximum-downforce ride height (flow direction from top to bottom) (Ruhrmann & Zhang, 2003) 28

Figure 2-11: Diagrams of the diffuser bluff body (with dimensions in mm) and splitter configurations as used by Jowsey & Passmore (2010) and Jowsey (2013) 29

Figure 2-12: Schematic of the 'boat tail' model (with dimensions in mm) as used by Marklund & Lofdahl (2009) and Marklund (2013) 31

Figure 2-13: Centreline underbody surface pressure comparison between CFD and experimental measurements at the normalised ride height of $\mathrm{h/H} = 0.2\ (\mathrm{h/d} = 0.286)$ for a boat-tailed diffuser bluff-body (Marklund, 2013) 32

Figure 2-14: Time-averaged CFD surface pressure coefficients $\mathrm{C_p}$ at $\mathrm{h/H} = 0.09$ or $\mathrm{h/d} = 0.140$ along the centre-line length of the underbody surface of a bluff body (Puglisevich, 2013) 33

Figure 2-15: $2-\mathrm{D}$ illustration of the pressure behaviour along the underbody with a 2-stage pressure recovery on the diffuser section of a diffuser bluff body (adapted from Marklund, 2013) 35

Figure 2-16: Illustration of **(a)** 'blowing' and **(b)** 'suction' flow control mechanisms as described by Gad-el-Hak, 2000 37

Figure 2-17: A schematic of a trapped-vortex cavity on a diffuser ramp surface 38

Figure 2-18: Schematic of the double-deck diffuser concept and its centreline cross-section 39

Figure 2-19: An illustration of a diffuser trailing edge flap on a Formula 1 racing car ... 40

Figure 2-20: A schematic of air-jet vortex generator configurations on a diffuser ramp surface 40

Figure 2-21: Coandă flow effect over a curved surface (adapted from Houghton & Carpenter, 2003) 42

Figure 2-22: The curved surface along the exhaust exit on a 2012 F1 racing car. The surface induces the Coandă effect by turning the flow downwards towards the diffuser at the rear of the car Available at: www.f1fanatic.co.uk/2012/10/12/lotus-coanda-exhaust-race (Accessed: September, 2016) 43

Figure 2-23: A schematic of flow curvature effect over a curved diffuser ramp surface 44

Figure 3-1: A schematic of the Cranfield University DS Houghton wind tunnel 48

Figure 3-2: Isometric CAD representations of the diffuser-equipped bluff body geometries used by Senior (2002) and in this present study 50

Figure 3-3: Schematic of the cross-sectional and rear views of the diffuser bluff body (Dimensions in mm) for the plane diffuser (baseline) 50

Figure 3-4: Schematic of the cross-sectional and rear views of the diffuser bluff body (Dimensions in mm) for the diffuser with convex bump 51

Figure 3-5: Schematic of the cross-sectional and rear views of the diffuser bluff body (Dimensions in mm) for the diffuser with wing 51

Figure 3-6: Schematic of the cross-sectional and rear views of the diffuser bluff body (Dimensions in mm) for the diffuser with both the convex bump and wing 52

Figure 3-7: Photographs of diffuser bluff model wind tunnel setup showing: **(a)** The nose section of the model fitted with a wire trip for fixing transition and **(b)** The model mounted on the strut of the DS Houghton wind tunnel open test section 53

Figure 3-8: AEROTECH 6-component force balance 55

Figure 3-9: Details of pressure measurements setup: **(a)** A schematic of the pressure tapping distribution on the 17° diffuser ramp bluff body (Dimensions in mm) **(b)** Photograph of Scanivalve pressure transducer 57

Figure 3-10: Experimental setup for flow visualisation image capture 59

Figure 3-11: Schematics of LDV measurement planes and locations showing: **(a)** Measurement planes behind diffuser near-wake in isometric view (dimensions in mm) and **(b)** Underbody boundary layer measurement location 63

Figure 3-12: Photograph of diffuser bluff body and LDV probe on traverse mount 63

Figure 3-13: Details of experimental laser velocimetry setup: **(a)** Top view schematic of wind tunnel working section with LDV probe, traverse and seeding generator **(b)** Schematic of LDV system components (adapted from TSI LDV system Manual) 64

Figure 3-14: The computational domain showing mesh resolution distribution and dimensions in m representing the wind tunnel test section 67

Figure 3-15: A cross section of the computational domain for the bluff body diffuser with a wing showing prismatic cells 67

Figure 3-16: Convergence of SRANS residuals over 10,000 iterations 79

Figure 4-1: Force measurements (wind tunnel) across ride heights $\mathrm{h/d} = 0.764 \text{ to } 0.064$ and flow regimes ('A' to 'D'): **(a)** lift coefficient **(b)** drag coefficient, **(c)** lift coefficient slope **(d)** drag coefficient slope 86

Figure 4-2: Force measurement (wind tunnel) comparison between present study and that of Senior (2002): coefficients of **(a)** lift **(b)** drag 87

Figure 4-3: Force measurement comparison between Senior (2002) wind tunnel measurements and CFD methods: coefficients of **(a)** lift **(b)** drag 88

Figure 4-4: Force measurement (wind tunnel) comparison between corrected values from Senior (2002) and present study: coefficients of **(a)** lift **(b)** drag 89

Figure 4-5: Flat underbody and diffuser centreline pressure distribution measurements (wind tunnel) for the ride heights representing the four flow regimes for the present study 89

Figure 4-6: Diffuser ramp surface spanwise pressure measurements (wind tunnel) for flow regime types: **(a & b)** Type A; **(c)** Type B; **(d)** Type C; **(e)** Type D 94

Figure 4-7: Diffuser surface flow features with visualization paint for flow regime Type A (Flow direction from top to bottom) 95

Figure 4-8: Diffuser surface flow features with flow visualization paint for flow regime Type A (Flow direction from top to bottom) 96

Figure 4-9: Diffuser surface flow features with flow visualization paint for flow regime Type B (Flow direction from top to bottom) 97

Figure 4-10: Diffuser surface flow features with flow visualization paint for flow regime Type C (Flow direction from top to bottom) 98

Figure 4-11: Diffuser surface flow features with visualization paint for flow regime Type D (Flow direction from top to bottom) 99

Figure 4-12: Force measurements (wind tunnel) across ride heights $(\mathrm{h/d} = 0.764$ to $0.064)$ under fixed and moving ground conditions: **(a)** downforce **(b)** drag 104

Figure 4-13: Hysteresis highlighted between $\mathrm{h/d} = 0.159$ to 0.204 with a magnified $\mathrm{h/d}$ plot scale: **(a)** Downforce **(b)** Drag and **(c)** Slopes of increasing and decreasing ride height between $\mathrm{h/d} = 0.159$ to 0.204 with a magnified $\mathrm{h/d}$ plot scale 106

Figure 4-14: Reynolds number sensitivity across ride heights $(\mathrm{h/d} = 0.764$ to $0.064)$: **(a)** downforce **(b)** drag 107

Figure 4-15: Reynolds number sensitivity across ride heights $(\mathrm{h/d} = 0.764$ to $0.064)$: **(a)** drag polar **(b)** lift-to-drag ratio 108

Figure 4-16: Pitching moments across ride heights $(\mathrm{h/d} = 0.764$ to $0.064)$ under fixed and moving wind tunnel ground conditions 110

Figure 4-17: Force measurements (wind tunnel) across ride heights $(\mathrm{h/d} = 0.764$ to $0.064)$ with bluff body positioned at pitch angle (nose down) of 0.08°: **(a)** downforce **(b)** drag 112

Figure 4-18: Force measurements (wind tunnel) across ride heights $(h/d = 0.764$ to $0.064)$ with bluff body positioned at pitch angle (nose down) of 0.17°: **(a)** Downforce **(b)** Drag 113

Figure 4-19: Force measurements (wind tunnel) across ride heights $(h/d = 0.764$ to $0.064)$ with bluff body positioned at pitch angle (nose down) of 0.27°: **(a)** Downforce **(b)** Drag 113

Figure 4-20: Force measurements (wind tunnel) comparison across ride heights $(h/d = 0.764$ to $0.064)$ between fixed and without fixed transition: **(a)** downforce (**b)** drag 114

Figure 4-21: Force measurements (wind tunnel) comparison across ride heights $(h/d = 0.764$ to $0.064)$ between fixed transition (with bluff body positioned at a nose down pitch angle of 0.08°) and without fixed transition (with zero bluff body pitch): **(a)** Downforce **(b)** Drag.....115

Figure 4-22: Surface pressure measurements (wind tunnel) along the vertical centre line of diffuser bluff body base plate at $h/d = 0.764,\ 0.382,\ 0.191,\ 0.153,\ and\ 0.064$ 116

Figure 4-23: Near-wake (wind tunnel experiments) and flow pathlines on diffuser bluff body base plate (predicted with CFD) of the counter-rotating upper and lower near-wake vortices.....118

Figure 4-24: Measured (wind tunnel) and CFD-predicted force coefficients across ride heights and flow regimes: **(a)** downforce **(b)** drag 119

Figure 4-25: **(a)** Time history and **(b)** Power Spectral Density of downforce coefficient of diffuser bluff body at $h/d = 0.191$ using URANS 120

Figure 4-26: **(a)** Time history and **(b)** Power Spectral Density of downforce coefficient of diffuser bluff body at $h/d = 0.153$ using IDDES 121

Figure 4-27: Measured (wind tunnel) and CFD-predicted surface pressure distributions for $h/d = 0.764$ along **(a)** underbody centreline **(b)** $x/d = 3.63$ **(c)** $x/d = 5.02$ **(d)** $x/d = 6.29$ **(e)** bluff-body base centreline $(z/d = 0)$.....124

Figure 4-28: Measured (wind tunnel) and CFD-predicted surface pressure distributions for $h/d = 0.382$ along **(a)** underbody centreline **(b)** $x/d = 3.63$ **(c)** $x/d = 5.02$ **(d)** $x/d = 6.29$ **(e)** bluff-body base centreline $(z/d = 0)$.....125

Figure 4-29: Measured (wind tunnel) and CFD-predicted surface pressure distributions for $h/d = 0.191$ along **(a)** underbody centreline **(b)** $x/d = 3.63$ **(c)** $x/d = 5.02$ **(d)** $x/d = 6.29$ **(e)** bluff-body base centreline $(z/d = 0)$ 126

Figure 4-30: Measured (wind tunnel) and CFD-predicted surface pressure distributions for $h/d = 0.153$ along **(a)** underbody centreline **(b)** $x/d = 3.63$ **(c)** $x/d = 5.02$ **(d)** $x/d = 6.29$ **(e)** bluff-body base centreline $(z/d = 0)$ 127

Figure 4-31: Measured (wind tunnel) and CFD-predicted surface pressure distributions for $h/d = 0.064$ along **(a)** underbody centreline **(b)** $x/d = 3.63$ **(c)** $x/d = 5.02$ **(d)** $x/d = 6.29$ **(e)** bluff-body base centreline $(z/d = 0)$ 128

Figure 4-32: Experimental and CFD-predicted diffuser surface flow features for flow regime Type A (Flow direction from top to bottom) 129

Figure 4-33: Experimental and CFD-predicted diffuser surface flow features for flow regime Type A (Flow direction from top to bottom) 131

Figure 4-34: Experimental and CFD-predicted diffuser surface flow features for flow regime Type B (Flow direction from top to bottom) 134

Figure 4-35: Experimental and CFD-predicted diffuser surface flow features for flow regime Type C (Flow direction from top to bottom) 135

Figure 4-36: Experimental and CFD-predicted diffuser surface flow features for flow regime Type D (Flow direction from top to bottom) 136

Figure 4-37: Experimental and CFD-predicted flow pathlines on underbody and side surfaces of the diffuser bluff body (Flow direction from left to right) 139

Figure 5-1: Total velocity vectors U predicted with CFD on spanwise plane at $x/d = 5.02$ showing the counter-rotating directions of the diffuser vortices at: **(a)** $h/d = 0.764$ (flow regime A) **(b)** $h/d = 0.382$ (flow regime A) **(c)** $h/d = 0.191$ (flow regime B) **(d)** $h/d = 0.153$ (flow regime C) **(e)** $h/d = 0.064$ (flow regime D) 143

Figure 5-2: Crossflow velocity w contours predicted with CFD on spanwise plane near the diffuser inlet $(x/d = 3.63)$ highlighting the inflow induced by the counter-rotating vortices at: **(a)** $h/d = 0.764$ **(b)** $h/d = 0.382$ **(c)** $h/d = 0.191$ **(d)** $h/d = 0.153$ **(e)** $h/d = 0.064$ 144

Figure 5-3: CFD iso-surface of the Q–$\mathrm{Criterion}$ $(\mathrm{Q} = 150{,}000)$ highlighting the longitudinal vortex pair formed within the diffuser at the normalised ride heights of the force-enhancement flow regimes: **(a)** $\mathrm{h/d} = 0.764$ and **(b)** $\mathrm{h/d} = 0.382$. The iso-surface is coloured by time-averaged total velocity $\mathrm{U} = \sqrt{\mathrm{u}^2 + \mathrm{v}^2 + \mathrm{w}^2}$ 146

Figure 5-4: CFD iso-surface of the Q–$\mathrm{Criterion}$ $(\mathrm{Q} = 150{,}000)$ highlighting the solitary surviving longitudinal vortex within the diffuser at the normalised force-reduction flow regime ride height of $\mathrm{h/d} = 0.153$. The iso-surface is coloured by time-averaged total velocity $\mathrm{U} = \sqrt{\mathrm{u}^2 + \mathrm{v}^2 + \mathrm{w}^2}$ 147

Figure 5-5: Streamwise velocity u contours predicted with CFD at $\mathrm{h/d} = 0.764$ for spanwise planes on: **(a)** $\mathrm{x/d} = 3.63$ **(b)** $\mathrm{x/d} = 5.02$ **(c)** $\mathrm{x/d} = 6.29$ 149

Figure 5-6: Streamwise vorticity ω_x contours predicted with CFD at $\mathrm{h/d} = 0.764$ for spanwise planes on: **(a)** $\mathrm{x/d} = 3.63$ **(b)** $\mathrm{x/d} = 5.02$ **(c)** $\mathrm{x/d} = 6.29$ 150

Figure 5-7: Turbulent kinetic energy (TKE) contours predicted with CFD at $\mathrm{h/d} = 0.764$ for spanwise planes on: **(a)** $\mathrm{x/d} = 3.63$ **(b)** $\mathrm{x/d} = 5.02$ **(c)** $\mathrm{x/d} = 6.29$ 151

Figure 5-8: Streamwise velocity u contours predicted with CFD at $\mathrm{h/d} = 0.382$ for spanwise planes on: **(a)** $\mathrm{x/d} = 3.63$ **(b)** $\mathrm{x/d} = 5.02$ **(c)** $\mathrm{x/d} = 6.29$ 152

Figure 5-9: Streamwise vorticity ω_x contours predicted with CFD at $\mathrm{h/d} = 0.382$ for spanwise planes on: **(a)** $\mathrm{x/d} = 3.63$ **(b)** $\mathrm{x/d} = 5.02$ **(c)** $\mathrm{x/d} = 6.29$ 153

Figure 5-10: Turbulent kinetic energy (TKE) contours predicted with CFD at $\mathrm{h/d} = 0.382$ for spanwise planes on: **(a)** $\mathrm{x/d} = 3.63$ **(b)** $\mathrm{x/d} = 5.02$ **(c)** $\mathrm{x/d} = 6.29$ 154

Figure 5-11: Streamwise velocity u contours predicted with CFD at $\mathrm{hd} = 0.191$ for spanwise planes on: **(a)** $\mathrm{x/d} = 3.63$ **(b)** $\mathrm{x/d} = 5.02$ **(c)** $\mathrm{x/d} = 6.29$ 156

Figure 5-12: Streamwise pressure coefficient $(\mathrm{C_p})$ contours predicted with CFD at $\mathrm{h/d} = 0.191$ for spanwise planes on: **(a)** $\mathrm{x/d} = 3.63$ **(b)** $\mathrm{x/d} = 5.02$ **(c)** $\mathrm{x/d} = 6.29$ 157

Figure 5-13: Streamwise vorticity ω_x contours predicted with CFD at $\mathrm{h/d} = 0.191$ for spanwise planes on: **(a)** $\mathrm{x/d} = 3.63$ **(b)** $\mathrm{x/d} = 5.02$ **(c)** $\mathrm{x/d} = 6.29$ 158

Figure 5-14: Turbulent kinetic energy (TKE) contours predicted with CFD at $h/d = 0.191$ for spanwise planes on: **(a)** $x/d = 3.63$ **(b)** $x/d = 5.02$ **(c)** $x/d = 6.29$ 159

Figure 5-15: Streamwise velocity u contours predicted with CFD at $h/d = 0.153$ for spanwise planes on: **(a)** $x/d = 3.63$ **(b)** $x/d = 5.02$ **(c)** $x/d = 6.29$ 161

Figure 5-16: Streamwise vorticity ω_x contours predicted with CFD at $hd = 0.153$ for spanwise planes on: **(a)** $x/d = 3.63$ **(b)** $x/d = 5.02$ **(c)** $x/d = 6.29$ 162

Figure 5-17: Turbulent kinetic energy (TKE) contours predicted with CFD at $h/d = 0.153$ for spanwise planes on: **(a)** $x/d = 3.63$ **(b)** $x/d = 5.02$ **(c)** $x/d = 6.29$ 163

Figure 5-18: Streamwise velocity u contours predicted with CFD at $h/d = 0.064$ for spanwise planes on: **(a)** $x/d = 3.63$ **(b)** $x/d = 5.02$ **(c)** $x/d = 6.29$ 165

Figure 5-19: Streamwise vorticity ω_x contours predicted with CFD at $h/d = 0.064$ for spanwise planes on: **(a)** $x/d = 3.63$ **(b)** $x/d = 5.02$ **(c)** $x/d = 6.29$ 166

Figure 5-20: Turbulent kinetic energy (TKE) contours predicted with CFD at $h/d = 0.064$ for spanwise planes on: **(a)** $x/d = 3.63$ **(b)** $x/d = 5.02$ **(c)** $x/d = 6.29$ 167

Figure 5-21: Streamwise velocity u contours predicted with CFD at: **(a)** $h/d = 0.191$ for streamwise centreline plane on $z/d = 0$ **(b)** $h/d = 0.191$ for streamwise plane on $z/d = 0.490$ **(c)** $h/d = 0.153$ for streamwise plane on $z/d = 0.490$.....170

Figure 5-22: Total pressure coefficient contours predicted with CFD at: **(a)** $h/d = 0.191$ for streamwise centreline plane on $z/d = 0$ **(b)** $h/d = 0.191$ for streamwise plane on $z/d = 0.490$ **(c)** $h/d = 0.153$ for streamwise plane on $z/d = 0.490$ 171

Figure 5-23: LDV-measured and CFD-predicted boundary layer profiles at diffuser inlet $x/d = 3.14$ centre point $z/d = 0$ for: **(a)** $h/d = 0.382$ **(b)** $h/d = 0.191$ **(c)** $h/d = 0.153$ **(d)** $h/d = 0.064$ 174

Figure 5-24: LDV-measured and CFD-predicted boundary layer profiles at either side $z/d = 0.363$ and -0.363 of diffuser inlet centre point $x/d = 3.14$ at $z/d = 0$ for:**(a)** $h/d = 0.382$ at $z/d = 0.363$ **(b)** $h/d = 0.382$ at z/d = -0.363 **(c)** $h/d = 0.191$ at $z/d = 0.363$ **(d)** $h/d = 0.191$ at z/d = -0.363 **(e)** $h/d = 0.153$ at $z/d = 0.363$ **(f)** $h/d = 0.153$ at z/d = -0.363 175

Figure 5-25: Near-wake non-dimensionalised U contours for the diffuser body measured with LDV at $h/d = 0.191$ on: **(a)** plane at $z/d = 0.490$ and **(b)** plane at z/d = -0.490 177

Figure 5-26: Near-wake non-dimensionalised turbulence intensity u'/U_∞ contours for the diffuser body measured with LDV at $h/d = 0.191$ on: **(a)** plane at $z/d = 0.490$ and **(b)** plane at z/d = -0.490 177

Figure 5-27: Near-wake non-dimensionalised U contours for the diffuser body measured with LDV at $h/d = 0.153$ on: **(a)** plane at $z/d = 0.490$ and **(b)** plane at z/d = -0.490 179

Figure 5-28: Near-wake non-dimensionalised turbulence intensity u'/U_∞ contours for the diffuser body measured with LDV at $h/d = 0.153$ on: **(a)** plane at $z/d = 0.490$ and **(b)** plane at z/d = -0.490 179

Figure 5-29: Near-wake non-dimensionalised U contours for the diffuser body measured with LDV at centreline plane $z/d = 0$ for: **(a)** $h/d = 0.191$ and **(b)** $h/d = 0.153$.....180

Figure 5-30: Near-wake non-dimensionalised turbulence intensity u'/U_∞ contours for the diffuser body measured with LDV at centreline plane $z/d = 0$ for: **(a)** $h/d = 0.191$ and **(b)** $h/d = 0.153$.....180

Figure 5-31: Velocity power spectral densities for u and v measured by LDV at the near wake location $y/d = 1.6$ and $x/d = 7.84$ for: **(a)** $h/d = 0.382$ **(b)** $h/d = 0.191$ and **(c)** $h/d = 0.153$ 182

Figure 5-32: Near-wake non-dimensionalised U contours for the diffuser body at $h/d = 0.191$ and on the centreline plane at $z/d = 0$ for: **(a)** Wind tunnel LDV measurements **(b)** time-averaged URANS predictions 183

Figure 5-33: Near-wake non-dimensionalised U contours for the diffuser body at $h/d = 0.191$ and on the plane at $z/d = 0.490$ for: **(a)** Wind tunnel LDV measurements **(b)** time-averaged URANS predictions 183

Figure 5-34: Near-wake non-dimensionalised U contours for the diffuser body at $h/d = 0.153$ and on the plane at $z/d = 0.490$ for: **(a)** Wind tunnel LDV measurements **(b)** time-averaged IDDES predictions 184

Figure 5-35: Near-wake U flow structures for the diffuser body measured with LDV at $h/d = 0.191$ on **(a)** plane at $z/d = 0.490$ and **(b)** plane at z/d = -0.490 187

Figure 5-36: Near-wake U flow structures for the diffuser body measured with LDV at $\mathrm{h/d} = 0.153$ on: **(a)** plane at $\mathrm{z/d} = 0.490$ and **(b)** plane at $\mathrm{z/d} = -0.490$ 188

Figure 5-37: Near-wake U flow structures for the diffuser body on centreline plane $\mathrm{z/d} = 0$ measured with LDV at: **(a)** $\mathrm{h/d} = 0.191$ and **(b)** $\mathrm{h/d} = 0.153$ 188

Figure 6-1: CFD total velocity contours on centreline plane $\mathrm{z/d} = 0$ of the diffuser bluff body at $\mathrm{h/d} = 0.764$ for: **(a)** plane diffuser **(b)** a convex bump 50 mm long and 10 mm thick **(c)** a convex bump 92 mm long and 5.6 mm thick **(d)** a convex bump 150 mm long and 5.6 mm thick **(e)** a convex bump 170 mm long and 5.6 mm thick **(f)** a convex bump 280 mm long and 5.6 mm thick 196

Figure 6-2: CFD total velocity contours on centreline plane $\mathrm{z/d} = 0$ of the diffuser bluff body at $\mathrm{h/d} = 0.764$ with a moving convex bump wall 92 mm long and 5.6 mm thick, travelling in the streamwise direction at $20\ \mathrm{m/s}$ 197

Figure 6-3: CFD total velocity contours on centreline plane $\mathrm{z/d} = 0$ of the diffuser bluff body at $\mathrm{h/d} = 0.764$ for: **(a)** plane diffuser **(b)** diffuser with an inverted wing at $\alpha = 0°$ (diverging gap g_p), and $\mathrm{c} = 83.7\ \mathrm{mm}$ **(c)** diffuser with an inverted wing at $\alpha = 17°$, $g_p = 14.35\ \mathrm{mm}$ and $\mathrm{c} = 83.7\ \mathrm{mm}$ **(d)** diffuser with an inverted wing $\alpha = 17°$, $g_p = \sim 82\ \mathrm{mm}$ and $c = 83.7\ \mathrm{mm}$ 201

Figure 6-4: CFD total velocity contours on centreline plane $\mathrm{z/d} = 0$ of the diffuser bluff body with an inverted wing at $\alpha = 17°$, $g_p = 14.35\ \mathrm{mm}$ and different chord lengths c at $\mathrm{h/d} = 0.764$ for: **(a)** $\mathrm{c} = 140\ \mathrm{mm}$ **(b)** $\mathrm{c} = 225\ \mathrm{mm}$ **(c)** $\mathrm{c} = 365\ \mathrm{mm}$ 202

Figure 6-5: CFD total velocity contours on centreline plane $\mathrm{z/d} = 0$ of the diffuser bluff body at $\mathrm{h/d} = 0.764$ for diffuser with a convex bump 92 mm long, 5.6 mm thick; and an inverted wing with $\alpha = 17°$, $g_p = 8.75\ \mathrm{mm}$**,** and $\mathrm{c} = 83.7\ \mathrm{mm}$ 204

Figure 6-6: An expanded view of CFD total velocity contour profiles from inlet to exit of the diffuser on centreline plane $\mathrm{z/d} = 0$ of the diffuser bluff body at $\mathrm{h/d} = 0.764$ with: **(a)** a convex bump 92 mm long and 5.6 mm thick **(b)** a convex bump 150 mm long and 5.6 mm thick **(c)** a convex bump 92 mm long and 5.6 mm thick; and an inverted wing with $\alpha = 17°$, $g_p = 8.75\ \mathrm{mm}$**,** and $\mathrm{c} = 83.7\ \mathrm{mm}$ 205

Figure 6-7: Force measurement (wind tunnel) comparison between plane diffuser (baseline) and diffuser with passive flow control methods: **(a)** downforce coefficients **(b)** drag coefficients 206

Figure 6-8: Percentage difference in force coefficients across the range of ride heights $(\mathrm{h/d} = 0.764 \text{ to } 0.064)$ between the plane diffuser and the diffuser with the wing for: **(a)** $\mathrm{C_L}$; **(b)** $\mathrm{C_D}$ 209

Figure 6-9: Reynolds number sensitivity across ride heights $\mathrm{h/d} = 0.764$ to 0.064: **(a)** Downforce coefficients for diffuser with bump **(b)** Drag coefficients for diffuser with bump **(c)** Downforce coefficients for diffuser with wing **(d)** Drag coefficients for diffuser with wing 211

Figure 6-10: **(a)** Lift-to-drag ratio magnitude measured (wind tunnel) across ride heights $\mathrm{h/d} = 0.764 \text{ to } 0.064$ for plane diffuser (baseline) and diffuser with passive flow control methods; **(b)** Percentage difference in lift-to-drag ratio magnitude between the plane diffuser (baseline) and diffuser with passive flow control methods 213

Figure 6-11: Underbody centreline pressure distribution measurements (wind tunnel) for the plane diffuser and diffuser with passive flow control methods at: **(a)** $\mathrm{h/d} = 0.764$ **(b)** $\mathrm{h/d} = 0.382$ **(c)** $\mathrm{h/d} = 0.191$ **(d)** $\mathrm{h/d} = 0.153$ **(e)** $\mathrm{h/d} = 0.064$ 217

Figure 6-12: Spanwise surface pressure distribution measurements (wind tunnel) on $\mathrm{x/d} = 6.29$ for the plane diffuser and diffuser with passive flow control methods at: **(a)** $\mathrm{h/d} = 0.764$ **(b)** $\mathrm{h/d} = 0.382$ **(c)** $\mathrm{h/d} = 0.191$ **(d)** $\mathrm{h/d} = 0.153$ **(e)** $\mathrm{h/d} = 0.064$ 218

Figure 6-13: Surface pressure distribution measured (wind tunnel) along $\mathrm{z/d} = 0$ of the base plate of the diffuser body with and without the passive flow control methods at: **(a)** $\mathrm{h/d} = 0.764$ **(b)** $\mathrm{h/d} = 0.382$ **(c)** $\mathrm{h/d} = 0.191$ **(d)** $\mathrm{h/d} = 0.153$ **(e)** $\mathrm{h/d} = 0.064$ 219

Figure 6-14: Diffuser surface flow features with flow visualisation paint for the Type A flow regime (force-enhancement) at $\mathrm{h/d} = 0.764$ (Flow direction from top to bottom) 222

Figure 6-15: Diffuser surface flow features with flow visualisation paint for the Type A flow regime (force-enhancement) at $\mathrm{h/d} = 0.382$ (Flow direction from top to bottom) 223

Figure 6-16: Diffuser surface flow features with flow visualisation paint for the Type B flow regime (maximum-force) at $\mathrm{h/d} = 0.191$ (Flow direction from top to bottom) 224

Figure 6-17: Diffuser surface flow features with flow visualisation paint for the Type C flow regime (force-reduction) at $h/d = 0.153$ (Flow direction from top to bottom) 225

Figure 6-18: Diffuser surface flow features with flow visualisation paint for the Type D flow regime (low-force) at $h/d = 0.064$ (Flow direction from top to bottom) 226

Figure 6-19: Measured (wind tunnel) and CFD-predicted force coefficients across ride heights and flow regimes for the diffuser with the bump: **(a)** downforce **(b)** drag 228

Figure 6-20: Measured (wind tunnel) and CFD-predicted force coefficients across ride heights and flow regimes for the diffuser with the wing, and with both bump and wing: **(a)** downforce **(b)** drag 229

Figure 6-21: Measured (wind tunnel) and CFD-predicted underbody surface pressure distributions on centreline $z/d = 0$ for plane diffuser and diffuser with bump at: **(a)** $h/d = 0.764$ **(b)** $h/d = 0.382$ **(c)** $h/d = 0.191$ **(d)** $h/d = 0.153$ **(e)** $h/d = 0.064$ 233

Figure 6-22: Measured (wind tunnel) and CFD-predicted diffuser spanwise surface pressure distributions on $x/d = 6.29$ for plane diffuser and diffuser with bump at: **(a)** $h/d = 0.764$ **(b)** $h/d = 0.382$ **(c)** $h/d = 0.191$ **(d)** $h/d = 0.153$ **(e)** $h/d = 0.064$ 234

Figure 6-23: Measured (wind tunnel) and CFD-predicted underbody surface pressure distributions on centreline $z/d = 0$ for plane diffuser and diffuser with the wing at: **(a)** $h/d = 0.764$ **(b)** $h/d = 0.382$ **(c)** $h/d = 0.191$ **(d)** $h/d = 0.191$ (with both the wing and bump) **(e)** $h/d = 0.153$ **(f)** $h/d = 0.064$ 235

Figure 6-24: Measured and CFD-predicted diffuser spanwise surface pressure distributions on $x/d = 6.29$ for plane diffuser and diffuser with the wing (and both the wing and bump) at: **(a)** $h/d = 0.764$ **(b)** $h/d = 0.382$ **(c)** $h/d = 0.191$ **(d)** $h/d = 0.191$ (with both the wing and bump) **(e)** $h/d = 0.153$ **(f)** $h/d = 0.064$ 236

Figure 6-25: Predicted surface flow features (using CFD) for plane diffuser and diffuser with flow control methods for flow regime A at $h/d = 0.764$ (Flow direction from top to bottom) 239

Figure 6-26: Predicted surface flow features (using CFD) for plane diffuser and diffuser with flow control methods for flow regime A at $h/d = 0.382$ (Flow direction from top to bottom) 240

Figure 6-27: Predicted surface flow features (using CFD) for plane diffuser and diffuser with flow control methods for flow regime B at $h/d = 0.191$ (Flow direction from top to bottom) 241

Figure 6-28: Predicted surface flow features (using CFD) for plane diffuser and diffuser with flow control methods for flow regime C at $h/d = 0.153$ (Flow direction from top to bottom) 242

Figure 6-29: Predicted surface flow features (using CFD) for plane diffuser and diffuser with flow control methods for flow regime D at $h/d = 0.064$ (Flow direction from top to bottom) 243

Figure 6-30: CFD predictions of skin friction coefficient C_f for the plane diffuser (baseline) at maximum downforce ride height $h/d = 0.191$ and force reduction ride height $h/d = 0.153$ on: **(a)** $z/d = 0.490$, **(b)** $z/d = 0$, and **(c)** $z/d = -0.490$ 245

Figure 6-31: CFD-predicted boundary layer profiles normal to the diffuser ramp surface for maximum downforce ride height $h/d = 0.191$ (with $y'/d = 0$ at the diffuser surface and positive downwards; U'/U_∞ is relative to the diffuser surface) taken at: **(a)** $x/d = 3.49$ **(b)** $x/d = 4.10$ **(c)** $x/d = 4.71$ **(d)** $x/d = 5.63$ **(e)** $x/d = 6.29$.....246

Figure 6-32: CFD predictions of skin friction coefficient C_f at maximum downforce ride height $h/d = 0.191$ for the plane diffuser (baseline) and diffuser with the passive flow control methods on: **(a)** $z/d = 0.490$ **(b)** $z/d = 0$, and **(c)** $z/d = -0.490$ 248

Figure 6-33: Centreline plane near-wake U flow structures measured with LDV at $h/d = 0.191$ for **(a)** plane diffuser **(b)** diffuser with bump **(c)** diffuser with wing **(d)** diffuser with both bump and wing 251

Figure 6-34: Centreline $z/d = 0$ plane near-wake non-dimensionalised u-component contours measured with LDV at $h/d = 0.191$ for **(a)** plane diffuser (baseline), **(b)** diffuser with bump, **(c)** diffuser with wing, and **(d)** diffuser with both bump and wing 254

Figure 6-35: Near-wake non-dimensionalised ΔU contours measured with LDV at $h/d = 0.191$ between plane diffuser and **(a)** diffuser with bump: plane at $z/d = 0.490$, **(b)** diffuser with wing: plane at $z/d = 0.490$, **(c)** diffuser with bump: plane at $z/d = 0$, **(d)** diffuser with wing: plane at $z/d = 0$, and **(e)** diffuser with both bump and wing: plane at $z/d = 0$ ..255

Figure 6-36: Near-wake non-dimensionalised $\Delta u'$ contours measured with LDV at $h/d = 0.191$ between plane diffuser and **(a)** diffuser with bump: plane at $z/d = 0.490$, **(b)** diffuser with wing: plane at $z/d = 0.490$, **(c)** diffuser with bump: plane at $z/d = 0$, **(d)** diffuser with wing: plane at $z/d = 0$, and **(e)** diffuser with both bump and wing: plane at $z/d = 0$..256

Figure 6-37: A vector field schematic across the near-wake streamwise centreline plane $z/d = 0$.....258

LIST OF TABLES

Table 2-1: Details of diffuser research reviewed in Chapter 2 46

Table 3-1: Force measurements test cases (B = baseline; C = with convex bump; W = with wing; C&W = with convex bump and wing) 79

Table 3-2: Surface pressure, surface flow visualisation and CFD test cases 82

Table 3-3: LDV boundary layer profile measurements at diffuser inlet $\mathrm{x/d} = 3.14$ for baseline diffuser test cases 83

Table 3-4: Diffuser near-wake streamwise plane LDV measurement test cases 83

Table 6-1: CFD predictions of downforce, drag, and lift-to-drag ratio at $\mathrm{h/d} = 0.764$ (type A regime) for the baseline plane diffuser, and the diffuser with a bump of varied dimensions 197

Table 6-2: CFD predictions of downforce, drag, and lift-to-drag ratio at $\mathrm{h/d} = 0.764$ (type A regime) for the baseline plane diffuser; and the diffuser with a wing ($\alpha = 17°$, $g_p = 14.35\ mm$) with varied chord lengths c 202

Table 6-3: CFD predictions of downforce and drag coefficients at $\mathrm{h/d} = 0.764$ (type A regime) and at $\mathrm{h/d} = 0.191$ (type B regime) for the baseline diffuser, and the diffuser with passive flow control methods of varied dimensions 204

Table 6-4: Streamwise-length-averaged skin friction coefficient along $\mathrm{z/d} = 0.490$, 0, and -0.490 for the plane diffuser and the diffusers with passive flow control at $\mathrm{h/d} = 0.191$ and 0.153 250

Table 6-5: Comparisons of relative changes in the near-wake streamwise centreline plane $(\mathrm{z/d} = 0)$ circulation to changes in measured body lift and drag 259

NOMENCLATURE

Notation

A	= bluff body frontal area (m^2)
A_1	= diffuser inlet area (m^2)
A_2	= diffuser exit area (m^2)
b	= inverted wing span (m)
c	= chord length of inverted wing (m)
C_D	= coefficient of drag $\frac{D}{q_\infty A}$
C_{DES}, C_{DES1}, C_{DES2}	= empirical model constants
C_f	= skin friction coefficient $\frac{\tau_w}{q_\infty}$
$\bar{\bar{C}}_f$	= streamwise-length-averaged skin friction coefficient
C_{f_x}	= local skin friction coefficient at any given x −wise position
C_L	= coefficient of lift $\frac{L}{q_\infty A}$
C_p	= coefficient of pressure $\frac{p - p_\infty}{q_\infty}$
$\bar{C}_p$	= overall pressure-recovery coefficient of diffuser with a single-stage pressure recovery
$\bar{C}_{p_s}$	= overall pressure-recovery coefficient of diffuser with a two-stage pressure recovery
C_μ, C_ω	= model constant
$C_{\omega 1}$, $C_{\omega 2}$, $C_{\omega 3}$,	= model constants
d	= bluff-body half-width of diffuser (m)
d_ω	= distance to the nearest wall
D	= aerodynamic drag (N)
D_L	= near-wall laminar dissipation term
D_T	= near-wall turbulent dissipation term
$\check{f}_d$	= empirical blending function
f_e	= elevating function
f_W	= damping function
$F_{\theta t}$	= switching function
F_1	= blending function
g_p	= gap between inverted wing and diffuser ramp or bump (m)
h	= bluff body ride height (m)
h_d	= distance between the rolling-road and diffuser bluff body side plate vertex at a pitch angle η
h_{max}	= maximum cell edge length

H = bluff body height (m)

l_r = distance between leading edge of diffuser bluff body flat underbody section and side plate vertex

L = aerodynamic downforce (N)

L_B = bluff body length (m)

L_D = diffuser length (m)

L_f = flat underbody section length (m)

l_d = diffuser ramp surface length (m)

l_{IDDES}, l_{LES}, l_{RANS} = length scale for IDDES, LES and RANS

N = weight of vehicle or bluff body (N)

p = static pressure (Pa)

p_∞ = atmospheric pressure (Pa)

P_k = production term

P_{k_L} = production term for laminar kinetic energy

P_{k_T} = production term for turbulent kinetic energy

q_∞ = freestream dynamic pressure $\frac{\rho U_\infty^2}{2}$

Re = Reynolds number $\frac{U_\infty L_B}{\nu}$

R_{BP} = model term for bypass transition

R_{NAT} = model term for natural transition

S = diffuser ramp surface area (m^2)

Δ_t = time-step

Δ_{tmin} = minimum time-step

ΔU = baseline diffuser U *minus* modified diffuser U, $(m\,s^{-1})$

$\Delta u'$ = baseline diffuser u' *minus* modified diffuser u', $(m\,s^{-1})$

Δ_x = grid size in the x direction

u_i , u_j = ensemble-averaged velocity tensors

μ_t = dynamic turbulent viscosity

u, v, w = velocity components in x, y, z directions

u' = root mean square of turbulent velocity fluctuations $(m\,s^{-1})$

U = total velocity $\sqrt{u^2 + \mathrm{v}^2 + w^2}$, $(m\,s^{-1})$

U_1 = diffuser inlet velocity $(m\,s^{-1})$

U_2 = diffuser outlet velocity $(m\,s^{-1})$

U_∞ = freestream velocity $(m\,s^{-1})$

ν_t = kinematic eddy-viscosity

W = width of diffuser (m)

x_i , x_j = directional tensors

x, y, z = Cartesian coordinates from origin: x is positive downstream, y is positive upwards, z is positive to port side

y^+ = dimensionless distance from wall in y direction

Greek Symbols

α	= angle of attack of inverted wing ($degrees$)
α_T	= effective diffusivity
$\beta^*,\ \beta$	= model constants
γ	= intermittency
γ_s	= specific heat ratio
Γ	= circulation ($m^2 s^{-1}$)
η	= diffuser bluff body pitch angle
θ	= diffuser ramp angle/divergence angle ($degrees$)
k	= turbulent kinetic energy
μ	= dynamic viscosity ($kg\ m^{-1}\ s^{-1}$)
σ	= closure coefficient
υ	= kinematic viscosity $\frac{\mu}{\rho},\ (m^2 s^{-1})$
ρ	= air density ($kg\ m^{-3}$)
τ_{ij}	= viscous stress tensor
τ_w	= wall shear stress (Pa)
ω_s	= specific dissipation rate
ω_x	= streamwise vorticity (s^{-1})

Abbreviations

1-D	= one-dimensional
2-D	= two-dimensional
3-D	= three-dimensional
CAD	= computer aided design
CFD	= computational fluid dynamics
DES	= detached eddy simulation
DDES	= delayed detached eddy simulation
F1	= Formula One
FIA	= Fédération Internationale de l'Automobile
IDDES	= improved delayed detached eddy simulation
LDA/ LDV	= laser Doppler anemometry (velocimetry)
LES	= large eddy simulation
PIV	= particle image velocimetry
RANS	= Reynolds-averaged Navier-Stokes
SRANS	= steady Reynolds-averaged Navier-Stokes
TKE	= turbulent kinetic energy
URANS	= unsteady Reynolds-averaged Navier-Stokes

THESIS OVERVIEW

The ground-effect diffuser has become a mainstay on the aft section of the underbody of automobiles — more so on racing cars. Its application on racing cars of the modern era leads to an aerodynamic performance benefit due to the additional downforce it generates. At this point in time, numerous documented studies have been done to understand its complex flow behaviour. However, the flow physics behind advanced diffuser concepts applied in the auto racing industry over the years has not been extensively explained. More so, research that could generate a further performance improvement of the diffuser has not been defined and presented. The thesis presented here intends to validate the flow physics established by background research work done on this subject and also present an understanding of the aerodynamics of a diffuser in ground effect. In addition, it investigates novel diffuser geometrical alterations aimed at enhancing its downforce production and its aerodynamic performance.

The focus of the thesis is on the flow through the diffuser of a bluff body in freestream. Chapter 1 presents a background of the diffuser from its use in aeronautical and industrial applications to its inception as a ground effect-diffuser on racing cars. The chapter also presents an exposition of the aerodynamic principles behind the application of the ground-effect diffuser. Chapter 2 presents and discusses previous research done to understand the characteristics of the diffuser flow. Flow control principles that could potentially enhance the aerodynamic performance of the diffuser are also discussed in the chapter. The chapter concludes by describing the incentives for this research and sets out its objectives. Chapter 3 elucidates the experimental and computational methods employed in this research work. Chapters 4 to 6 presents the result data extracted from the research methods used in the study and also provides an analysis of the results. Chapter 4 and 5 focuses on experimental and computational results

analysis for the plane diffuser as the baseline while Chapters 6 presents experimental and computational data, and analysis for two novel passive flow control techniques applied to enhance the baseline diffuser's aerodynamic performance. Finally, Chapter 7 presents an overall summary drawn from the study and proffers future research ideas to further enhance the understanding of the subject presented in this thesis.

Chapter 1

Introduction

The chapter begins by explaining the aerodynamic principles behind the ground-effect phenomenon. Then the fundamental fluid dynamics principles of internal flow diffusers are introduced. This is followed by a description of a diffuser in ground effect together with the flow physics that governs its downforce production. The functionality of the ground-effect diffuser on racing cars is also outlined and the aerodynamic performance of the ground-effect diffuser is defined.

1.1 Research Background

1.1.1 Ground-effect aerodynamics

Ground-effect aerodynamics is a term associated with aircraft and racing cars. When an aircraft flies in close proximity to the ground (typically at a height of one to two times its wingspan), the 3—D flow around its (up-lifting) wings is influenced by the ground. This is as a result of the downwash produced by the wing-tip vortices being obstructed by the surface of the ground. Consequently, this obstruction diminishes the downwash from the wings and results in a reduced rearward tilt of the local lift vector. The induced drag decreases and an increase of the useful component of the lift vector takes place (Asselin, 1997).

A flow interaction also occurs between the front wing of a racing car and the road surface but because the lift is acting downwards, the effect of the ground proximity is different. As the racing car travels with its inverted front wing near to the road surface, the airflow between the wing and road surface is

constrained. The constrained airflow accelerates due to the curvature of the wing suction surface. Therefore the airflow accelerates between the suction surface of the inverted wing and the road surface causing a drop — below free air pressure — of the static pressure on the suction surface of the wing and road surface (Knowles et al., 1994; Ranzenbach & Barlow, 1994, 1995, 1996, 1997; Jasinski & Selig, 1999). This results in an increase of the negative lift vector (downforce) on the wing. Comparably, an airflow interaction occurs in the displacement between the smooth underbody floor/diffuser of a racing car and the road surface when the underbody is in near proximity to the road surface. As in the case of the front wing, when the car travels along the road, the velocity of the airflow between the underbody and road surface increases. This then lowers the static pressure of the underbody surface and road surface consequently generating downforce on the car (Hucho, 1998; Sovran, 1994). The ground-effect phenomenon associated with the front wing and underbody of the racing car is governed by the Bernoulli principle which states that an increase in velocity of an inviscid flow simultaneously occurs with a decrease in static pressure.

1.1.2 Internal flow diffusers

The distinct feature of a diffuser is its increasing cross sectional area which extends from the diffuser inlet to its exit. As deduced from the continuity principle for an incompressible flow, the mean velocity at the inlet is higher than the mean velocity at the exit. This implies that if a minimal loss in the kinetic energy of the flow occurs, then the pressure at the exit is higher than the pressure at the inlet (Massey & Ward-Smith, 2012). Before the inception of ground-effect diffusers as applied in the automobile industry, internal flow diffusers have been employed in aeronautical and industrial applications. Internal flow diffusers (Figures 1—1a and 1—1b) such as conical, annular and plane-walled type diffusers (ESDU, 2007) exist in symmetric or asymmetric shapes. The use of internal flow diffusers includes: in reducing the velocity and increasing the pressure of the airflow supplied to the combustion

chamber of jet engines; in heating, ventilating and air condition (HVAC) systems; and in industrial turbomachinery. The performance of an internal flow diffuser with inlet pressure coefficient C_{p1} and outlet pressure coefficient C_{p2} is reflected by its pressure recovery[1] coefficient $[\bar{C_p} = (C_{p2} - C_{p1})/(1 - C_{p1})]$ which in turn is generally influenced by the diffuser ramp angle, inlet and outlet conditions (Kline et al., 1959; Sovran & Klomp, 1967). The area ratio and aspect ratio of the plane-walled diffuser illustrated in Figure 1–1b is h_2/h_1 and W/h_1 respectively.

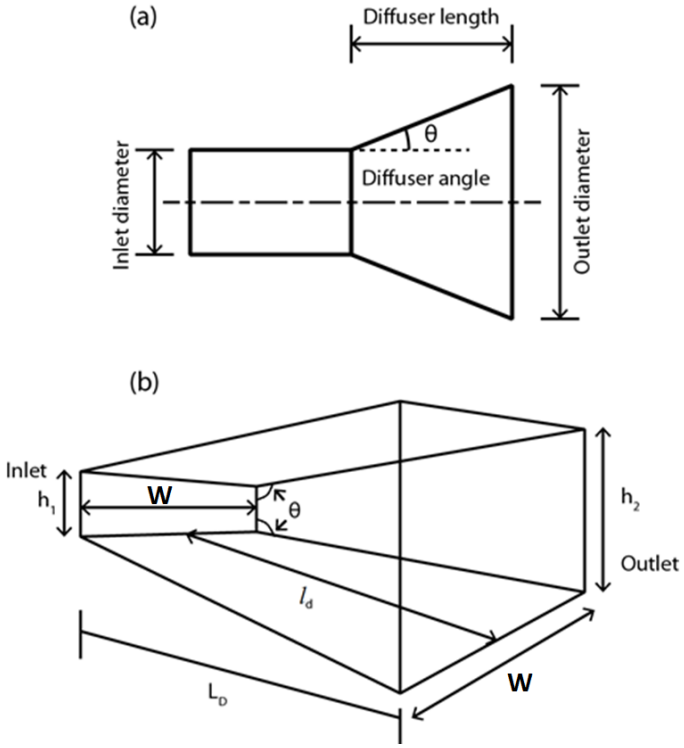

Figure 1-1: Illustrations of **(a)** 2-D conical **(b)** 3-D plane-wall diffuser dimensional parameters

As deduced from the incompressible 1-D continuity equation (Dixon, 1998; White, 2011), which is represented as $U_1A_1 = U_2A_2$, the diffuser flow can be represented mathematically (Equation 1.1) as:

[1] The term "pressure recovery" here refers to the rise in pressure through the diffuser.

$$U_1/U_2 = A_2/A_1 \tag{1.1}$$

This implies (as in Equation 1.2) that the ideal pressure rise coefficient (which is a frictionless and reversible pressure recovery) is then represented as:

$$C_{pr} = 1 - \left(U_2/U_1\right)^2 = 1 - \left(A_1/A_2\right)^2 \tag{1.2}$$

However, the pressure recovery will be adversely reduced if there is boundary layer separation from the diffuser walls. Duncan et al. (1970) observed that for a particular diffuser area ratio, the diffuser will have to be long if it is to maintain a small diffuser angle (Θ) to avoid separation, but this then leads to a large flow resistance for a real viscous flow. Likewise, the total pressure loss will also be large if Θ is large; in this case due to flow separation from the diffuser wall giving rise to an enhanced mechanical energy dissipation and formation of eddies. Furthermore, there is a negative slope linear relationship between the dimensionless parameter $\theta\delta_t/d_1$ and the diffuser pressure recovery coefficient. Thus, if $\theta\delta_t/d_1$ increases then the diffuser pressure recovery coefficient will reduce (Winternitz & Ramsey, 1957) with δ_t representing the boundary layer momentum thickness of the diffuser inlet and d_1 is the inlet diameter for a conical diffuser (h_1 for a plane wall diffuser) as shown in Figure 1–1.

1.1.3 The ground-effect diffuser

The **ground-effect diffuser** is generally located at the aft section of a racing car's underbody. It is asymmetric in shape — unlike the plane-walled diffuser; it consists of a solitary diverging ramp surface. When in near proximity to the road surface, the diffuser becomes an increasing area duct which provides a region in which the high-velocity/low-pressure underbody airflow entering the diffuser exits the diffuser as low velocity/high pressure airflow. This velocity-pressure relationship of a diffuser flow in ground effect was first employed effectively in 1977 on the Lotus 78 and 79 Formula 1 cars to generate

downforce (Katz, 2006a). The underbody of the Lotus racing cars were designed in the shape of cambered aerofoils with the inclusion of vertical side skirts to seal the underbody to the road surface (Tipler, 2009). This design as shown in Figure 1–2, exploited the 2—D effects (thickness, camber, and angle of attack) of an infinite inverted wing and the skirts prevented the interruption of underbody low pressure by the higher pressure outside the underbody.

Extensive experimental investigations by Zerihan & Zhang (2000); Zhang & Zerihan (2002, 2003a, 2003b) of an inverted wing over a range of ride heights close to the ground and a range of incidence angles generally indicated that the suction surface of an inverted wing produces low pressure. For a flat plate in proximity to a ground plane, the constrained flow acceleration underneath the plate generates equal low static pressure on the surfaces of the plate and the ground plane. However for an inverted wing in ground effect, the low pressure suction underneath the wing is further enhanced as a result of the flow-curvature induced on the constrained flow between the curved suction surface of the wing and the ground surface. This in turn increases flow velocity and generates a radial pressure gradient between both surfaces and as a consequence downforce is produced. Likewise, when the Lotus racing cars travel along the racing track, the airflow traveling between their aerofoil-shaped underbody and the road surface accelerates and creates a low-pressure region between both surfaces (Wright, 1982; Dominy, 1992; Agathangelou & Gascoyne, 1998). As a consequence, downforce is produced and it pushes the tyres of the cars onto the road surface. In turn, lap times around the race track reduces as the enhanced tyre grip enables the cars to become much quicker through the corners due to the application of ground effect (Zhang et al., 2006). The plot in Figure 1–3 demonstrates the influence of downforce on the cornering speeds of a racing car when slick and grooved tyres are used in dry and wet conditions respectively (Barnard, 2011). In modern road cars, where having less drag is paramount to their performance, a smooth underbody-diffuser combination can reduce the disturbance of the airflow traveling

underneath the vehicle thereby leading to a decrease in aerodynamic drag (Tortosa et al. 2011; Palin et al. 2012).

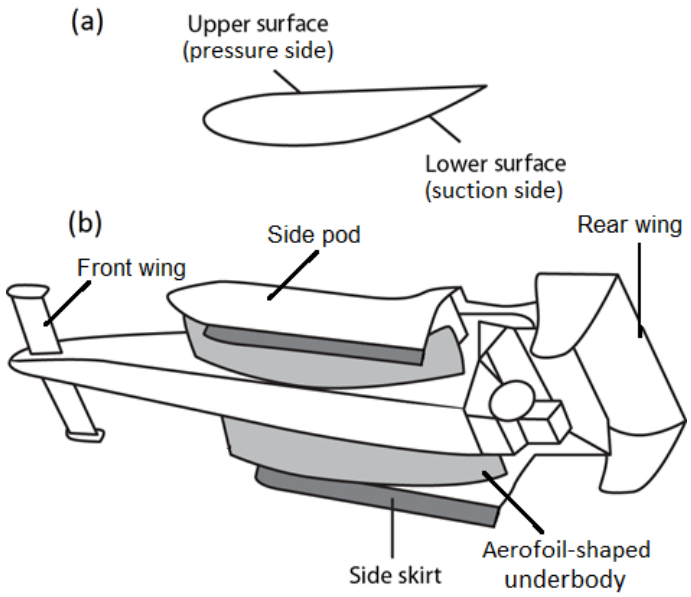

Figure 1-2: Illustrations of **(a)** an inverted aerofoil and **(b)** the Lotus 78 and 79 underbody

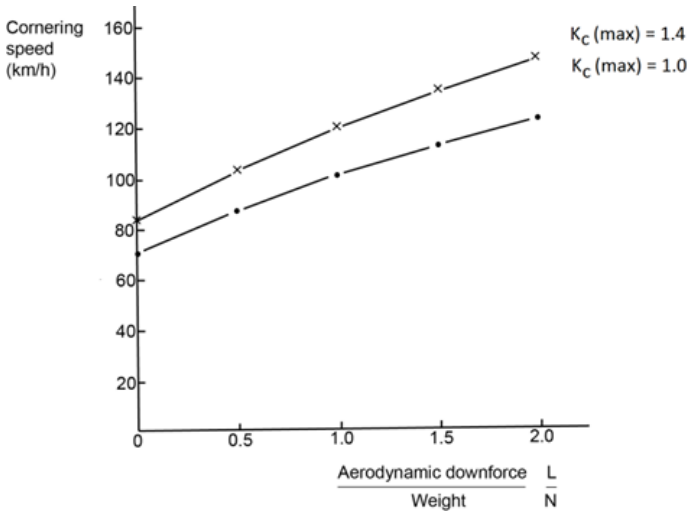

Figure 1-3: Downforce effect on cornering speeds around a corner radius of 40 m at maximum effective tyre cornering coefficient $\boldsymbol{k_c}$ (max), (Barnard, 2011)

1.2 The Ground-effect Diffuser and Downforce Production

The major aerodynamic components of a Formula 1 racing car include its front wing, rear wing, the underbody floor and diffuser. At the maximum speed of the racing car its aerodynamic devices generate a significant downforce far in excess of its weight (Rendle, 2011). The downforce-producing aerodynamic devices also generate aerodynamic drag and, as a result, there is an interdependent relationship between downforce and drag (Jeffrey & Alperin, 2000). A downforce increase that will increase tyre grip and speed on the corners of the race track implies that there is an analogous increase in drag that will slow the racing car on the straights of the race track. Figure 1–4 outlines the distribution of downforce and drag across the entire F1 racing car. As shown in Figure 1–4, the underbody floor and diffuser together produce the most downforce and the least drag among other major aerodynamic components of the racing car (Toet, 2013).

Downforce is generated by the ground-effect diffuser due to the suction effect created underneath the racing car. As the airflow with a high velocity travels underneath the smooth underbody-floor of the car, the diffuser — which starts downstream of the floor — serves as an area where the airflow gradually transitions into low velocity airflow at the exit of the diffuser. Likewise, the diverging area of the diffuser eases the low pressure airflow at its inlet into higher pressure airflow at its exit. This creates a pressure recovery which begins from the suction peak (due to peak velocity) at the diffuser inlet to the higher pressure downstream of the inlet (due to reduced velocity). It is this ground effect phenomenon that generates downforce. The downforce mechanisms that further explain the downforce-producing effect of the diffuser are namely: 'diffuser pumping', 'diffuser upsweep' and 'diffuser ground interaction' (Cooper et al., 1998).

Diffuser pumping denotes the interaction of the diffuser exit on the inlet due to pressure recovery between both points thus indicating the underlying purpose of a diffuser as a pressure recovery device. Because the area ratio

increases along the diffuser length, the static pressure rises along the length but must reach the constant base pressure (atmospheric pressure) at the diffuser exit. As a result, the pressure at the diffuser inlet becomes lower than the diffuser exit pressure. Consequently, the diffuser acts as a 'pump down' mechanism which decreases the underbody static pressure as the airflow travels through the diffuser. Thus, the underbody flow velocity increases and downforce is generated.

Diffuser upsweep describes the change in flow momentum between the diffuser inlet and outlet. Similar to the suction surface (or lower surface) of an inverted airfoil, it is cambered in shape (Figure 1–2). When airflow travels through the diffuser, the change in airflow to an upward direction to follow the ramp requires a resultant pressure force causing the pressure on the diffuser surface at inlet to be lower than that on the ground. The upsweep of the diffuser also orientates upwardly the counter-rotating streamwise vortex pair generated by the pressure difference within the diffuser and outside its longitudinal sides as shown in Figure 1–5.

Diffuser ground interaction represents the existing relationship between the ride height of the underbody-diffuser and the level of downforce it produces. A body with a flat underbody and in proximity to the ground generates low pressure close to the underbody leading edge assuming that there is no flow separation at that location. However, pressure recovery quickly occurs downstream of the underbody leading edge. The inclusion of a diffuser at the end of the flat underbody delays the pressure recovery upstream of the diffuser inlet and gradually recovers pressure towards the diffuser exit due to the diffuser pump down effect.

Therefore, a smooth symmetrical body in freestream high above the ground plane generates negligible downforce. However, if the body is within proximity to the ground plane, the flow velocity above and underneath the body becomes asymmetrical due to the ground constraint causing the underbody flow to

accelerate. Therefore, when a body with a smooth underbody surface and a diffuser is brought closer to the ground, the combined effect of the constrained underbody flow acceleration and the pressure difference created between the diffuser inlet and exit lowers underbody static pressure and generates downforce. If the ride height is further reduced, the flow interaction consequently leads to a gradual downforce increase up to a point where the ride height becomes too small and the effects of fluid viscosity dominate the underbody flow. Consequently, the downforce reduces with further height reductions.

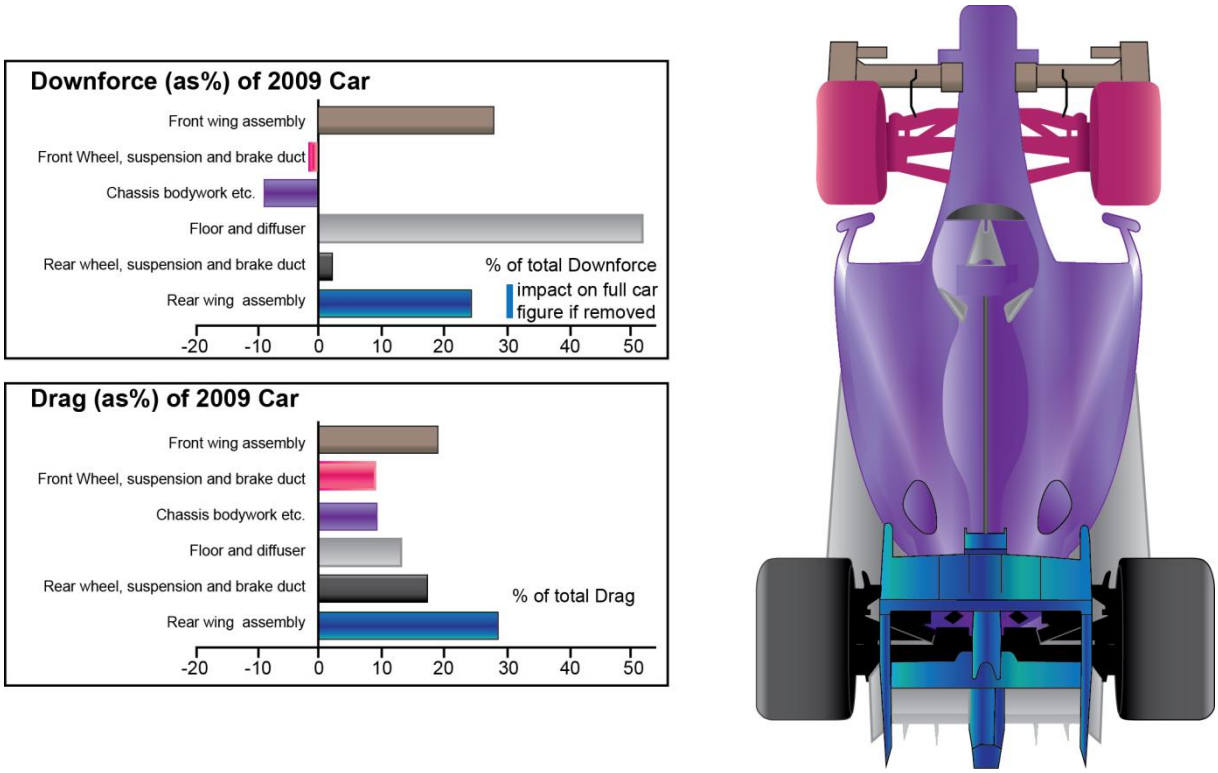

Figure 1-4: Drag and downforce distribution of a 2009 F1 racing car (Toet, 2013)

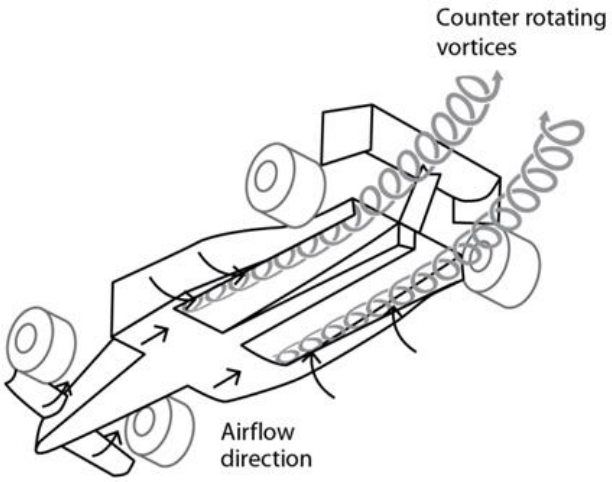

Figure 1-5: An illustration of vortex upwash along the diffuser channels of a racing car

1.3 Aerodynamic Performance Definition of the Ground-effect Diffuser

A typical geometry used to study automotive-type bluff body flows is the Ahmed bluff body (Ahmed et al., 1984) as illustrated in Figure 1–6a. However in relevant studies (such as Cooper et al., 1998 & 2000; Senior, 2002), Ahmed-like bluff bodies with alternative dimensions have been employed as discussed below. In using an Ahmed body-like bluff body for ground-effect diffuser research, the body is inverted with the slanted section (with angle φ) forming the diffuser ramp surface (with a diffuser angle θ) as shown in Figure 1–6b. The ground-effect diffuser performance can be evaluated by the static pressure on its ramp surface. As represented in Equation 1.3, this can be expressed mathematically by the pressure coefficient.

$$C_p = \frac{p - p_\infty}{0.5\,\rho U_\infty^2} \tag{1.3}$$

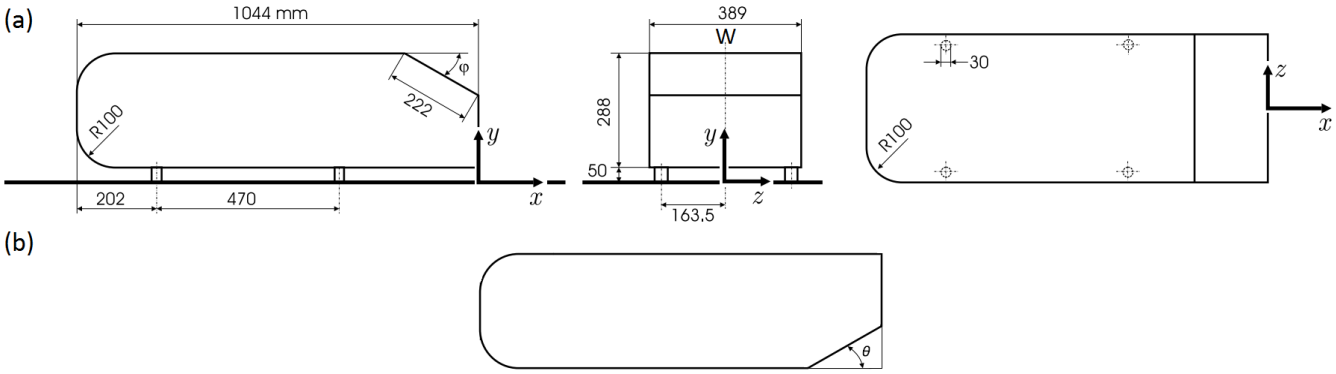

Figure 1-6: (a) Schematic of an Ahmed body dimensioned in mm as outlined by Ahmed et al., (1984) and **(b)** an inverted Ahmed-like bluff body as a diffuser bluff body

A net downforce and net drag (as represented in Equations 1.4 and 1.5) is created due to the static pressure distribution on the whole surface of the diffuser bluff body. A representative pressure distribution along the centreline of the nose and underbody of the diffuser bluff body is presented in Figure 1–7.

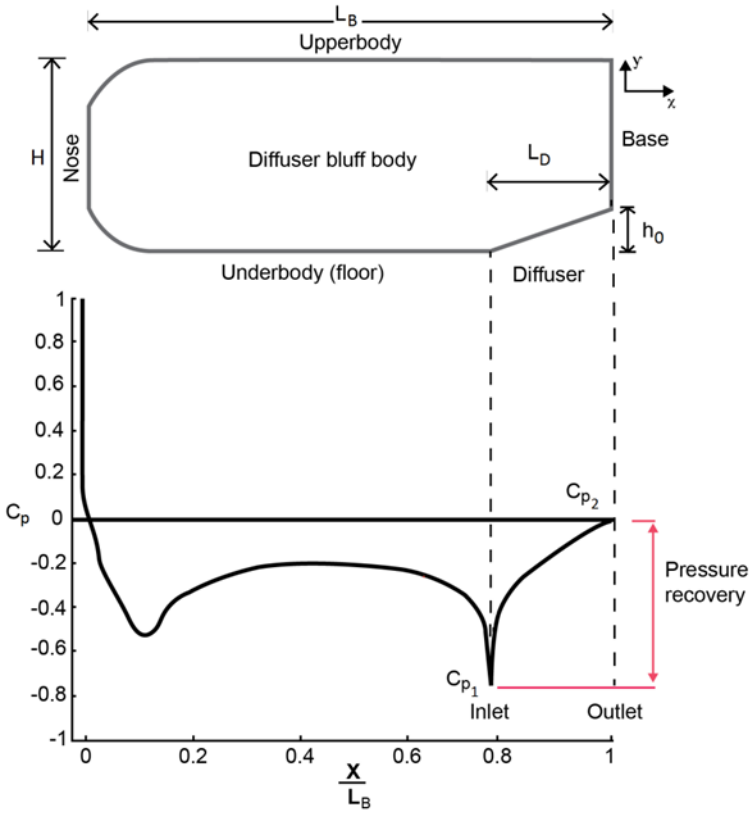

Figure 1-7: Schematic of the centreline pressure behaviour along the flat underbody and diffuser sections of a diffuser bluff body; adapted from Marklund (2013)

The stagnation point is at the centre of the nose section with negative pressures along the underbody floor. A suction peak occurs at the diffuser inlet with a pressure recovery at the diffuser exit. Assuming that the centreline pressures appropriately represent the average pressures at all cross sections and across the span of the diffuser body with width represented as W, then the aerodynamic downforce L (due to pressure differences) and the net drag D (pressure drag) of the body can be expressed in Equations 1.4 and 1.5 as:

$$L = W\left[\left[\underbrace{\int_0^{L_B-L_D} p_f(x)\,dx}_{Flat\ Underbody\ (floor)} + \underbrace{\int_{L_B-L_D}^{L_B} p_d(x)\,dx}_{Diffuser}\right] - \underbrace{\int_0^{L_B} p_u(x)\,dx}_{Upperbody}\right] \quad (1.4)$$

$$D = W\left[\underbrace{\int_0^{H} p_n(y)\,dy}_{Nose} - \left[\underbrace{\int_0^{h_0} p_d(y)\,dy}_{Diffuser} + \underbrace{\int_{h_0}^{H} p_b(y)\,dy}_{Base}\right]\right] \quad (1.5)$$

As illustrated in Figure 1–7, the distance between the floor plane of the diffuser and the top of the diffuser exit is represented as h_0. Also, the complete length of the bluff body and diffuser length are represented by L_B and L_D respectively. In addition, the static pressures for the flat underbody floor, diffuser, upper body, nose and the base of the diffuser bluff body are represented by the subscripts: $f, d, u, n, b,$ respectively.

An extensive mathematical formulation of the performance of a ground-effect diffuser subjected to an incompressible and inviscid flow was presented (in Equations 1.6 to 1.10) by Cooper et al. (1998, 2000). In extrapolating the diffuser performance, it was noted that the downforce on the entire body is determined by the static pressure difference between the upper and underbody surfaces. Hence, to investigate the influence on underbody pressures by the underbody airflow, a simple bluff body with varying diffuser lengths and ride heights was studied. Fundamentally, as expressed in Equation 1.6, the

streamwise-distanced-averaged pressure coefficient $\bar{\bar{C}}_{pi}$ across a streamwise length x_i was defined as:

$$\bar{\bar{C}}_{pi} \equiv \frac{1}{x_i}\int_0^{x_i} C_p\,(x)dx \tag{1.6}$$

Thus, to evaluate the specific value of the mean-effective pressure coefficient across the streamwise length of the whole underbody $\bar{\bar{C}}_{pl}$, it was defined (in Equation 1.7) as a whole component which is comprised of the mean-effective pressure coefficients of the flat underbody section $\bar{\bar{C}}_{pf}$ and the diffuser section $\bar{\bar{C}}_{pd}$.

$$\bar{\bar{C}}_{pl} = \left(1 - \frac{L_D}{L_B}\right)\bar{\bar{C}}_{pf} + \left(\frac{L_D}{L_B}\right)\bar{\bar{C}}_{pd} \tag{1.7}$$

The overall pressure recovery coefficient of the diffuser $\bar{C}_p$ was then established (Equation 1.8) with C_{p1} and C_{p2} (illustrated in Figure 1.7) as the pressure coefficients at the diffuser inlet and exit respectively.

$$\bar{C}_p = \frac{\left(C_{p2} - C_{p1}\right)}{\left(1 - C_{p1}\right)} \tag{1.8}$$

This means that if p_2 is the static pressure at the diffuser exit with p_∞ and q_∞ representing the static and dynamic pressures of the freestream flow respectively, then the diffuser exit pressure coefficient C_{p2} is expressed in Equation 1.9 as:

$$C_{p2} \equiv \left(\frac{p_2 - p_\infty}{q_\infty}\right) \tag{1.9}$$

Cooper et al. (2000) then formulated (Equation 1.10) the mean-effective pressure coefficient of the diffuser $\bar{\bar{C}}_{pd}$ as:

$$\bar{\bar{C}}_{pd} = 1 - \frac{\left(1 - C_{p_2}\right)}{\sqrt{1 - \bar{C}_p}} \tag{1.10}$$

In conclusion, it is noted that the distribution of centreline pressures of the diffuser is non-linear in shape. Also, the downforce generated by the entire underbody is influenced by the pressure recovery performance of the diffuser. Hence, as presented in Equation 1.7, if $\bar{\bar{C}}_{pd}$ is more negative then $\bar{\bar{C}}_{pl}$ is also correspondingly more negative which implies that the downforce produced will be larger.

Chapter 2

Literature Review

As stated in the previous chapter, the production of downforce by the diffuser is dependent on the velocity-pressure relationship that exists in the diffuser flow. Despite that, the flow behaviour within the diffuser also depends on particular design variables which consequently dictate the downforce and aerodynamic drag produced by the diffuser. The characteristic influences of these design parameters are highlighted with the diffuser area ratio which regulates the diffuser pressure recovery, and for a fixed diffuser length, it determines the angle of the diffuser. As a result, the diffuser angle can affect the flow entering the diffuser because a high diffuser angle (and also a low ride height) can lead to flow separation at the diffuser inlet. In addition, another major property of the diffuser flow is the counter-rotating longitudinal vortex pair. The vortices originate from the sides of the diffuser inlet and travel downstream along the diffuser endplates. As an integral component of the diffuser flow physics, the vortices enhance the streamwise flow velocity of the diffuser which in turn increases the suction created by the diffuser. In spite of this, the vorticity, swirl and streamwise pressure gradient of the diffuser flow governs the formation and breakdown of the counter-rotating vortices.

In this chapter, a review of research studies on the diffuser in ground effect is presented. The studies include experimental and numerical research work done to understand the flow physics and characteristics of the diffuser flow. Furthermore, as a means of enhancing the aerodynamic performance of the diffuser, studies on flow control methods that influence the boundary layer of wall-bounded flows are reviewed. Also, flow control measures applied over the years on F1 racing cars are also discussed.

2.1 Experimental Studies

2.1.1 Longitudinal vortices

Likewise to the trailing vortices generated by the pressure difference around airplane wing-tips or by front wing endplates of a Formula 1 racing car (Pegrum, 2006), the vortices of the ground effect diffuser travel in the streamwise direction. The vortices in a diffuser flow are critical to its aerodynamic performance because they enhance the underbody suction generated by the diffuser through the increase of near-wall flow velocity and flow separation suppression. Several definitions of a vortex have been used widely. Green (1995) described a vortex flow as 'a region of concentrated vorticity'. However, succinct definitions as that are not adequate because there is no general margin over which vorticity can be considered as high. Also, some of the definitions seem to inadequately only identify re-circulatory streamlines at a particular point in time or different structures as vortices in frames that rotate relative to each other (Lugt, 1979; Haller, 2005).

However, the streamwise vortex of the ground-effect diffuser can be described as a region of rotating flow characterised by a region of vorticity at its core. The low pressure linked to the vortex core is as a result of its rotational velocity. Furthermore, the occurrence of an abrupt change of the vortex structure with flow retardation along its axis, which causes the stream surfaces near the axis to diverge can be described as a vortex breakdown (Hall, 1972). Leibovich (1978) explains further that a vortex breakdown is the formation of an internal stagnation point on the vortex axis followed by a region of axial flow reversal. In the case of the longitudinal vortices of the diffuser, it is a region of streamwise flow reversal. Even so, the emergence and breakdown of streamwise vortices can have a favourable or adverse effect. In a ground-effect diffuser the breakdown of its longitudinal vortices reduces the downforce generated. The images in Figure 2–1 illustrate the types of a vortex breakdown including spiral, bubble and the double-helix.

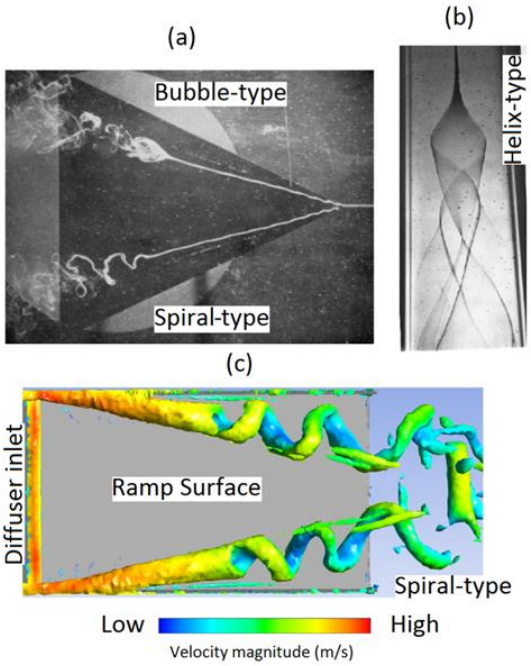

Figure 2-1: (a) Bubble and spiral types of vortex breakdown on a delta wing, (Lambourne & Bryer, 1962) **(b)** Double-helix vortex breakdown in a swirling flow through a tube, (Van Dyke, 1982) **(c)** Q-criterion velocity iso-surfaces of spiral type vortex breakdown within a diffuser bluff body (CFD studies by thesis author)

In fixed- and moving-ground wind tunnel conditions George (1981) investigated the aerodynamic effects of the diffuser flow using a diffuser-equipped bluff body. Two diffuser angles (10° and 20°) and the pitch angle η sensitivity of the bluff body were investigated. The pitch angles of the bluff body studied were in 5° increments within the range of −10° (nose up) to +35° (nose down) and were defined at the transverse centre point of the sides of the bluff body. Additionally, the inclusion of 10° and 20° upswept upper body surface, underbody roughness and wheels were also studied (Figure 2–2).

It was observed that when η was gradually increased from zero by 5° increments for the 20° diffuser, a longitudinal vortex pair close to the side edges of the underbody was formed. At low pitch angles the vortices travel towards the rear of the underbody and as η was further increased, the vortices extended further forward in the streamwise direction and are strengthened. This vortex behaviour was linked to the induced inflow into the diffuser which averted a separation bubble from appearing on the ramp surface of the

diffuser. Moreover, when the pitch was at the maximum angle of +35° where the separation bubble appeared upstream of the underbody, the strong vortices enabled the flow reattach downstream of the underbody. At a pitch angle of −10° with a 10° diffuser and 10° upswept upper body, an upstream separating shear layer established the longitudinal vortex flow.

However, when wheels were added to the bluff body with a 20° diffuser angle and 20° upswept upper body surface, the flow remained attached as a result of the vortices created by the wheels. Also, the flow remained attached with the further inclusion of roughness strips on the flat underbody section. In spite of that, the strength of the vortices reduced at a 5° pitch angle and this caused the flow to separate downstream of the strips. Moreover, the flow separation diminished when a test model configuration comprising of zero pitch, flat upper body, 20° diffuser and the addition of wheels was tested. This was as a result of an enhanced vortex strength which in turn led to an increase in downforce. Despite that, the strength of the vortices diminished when roughness strips where added to the test configuration. This was attributed to the flow separation created on the diffuser ramp by the strips and this culminated to a considerable increase in drag and decrease in downforce.

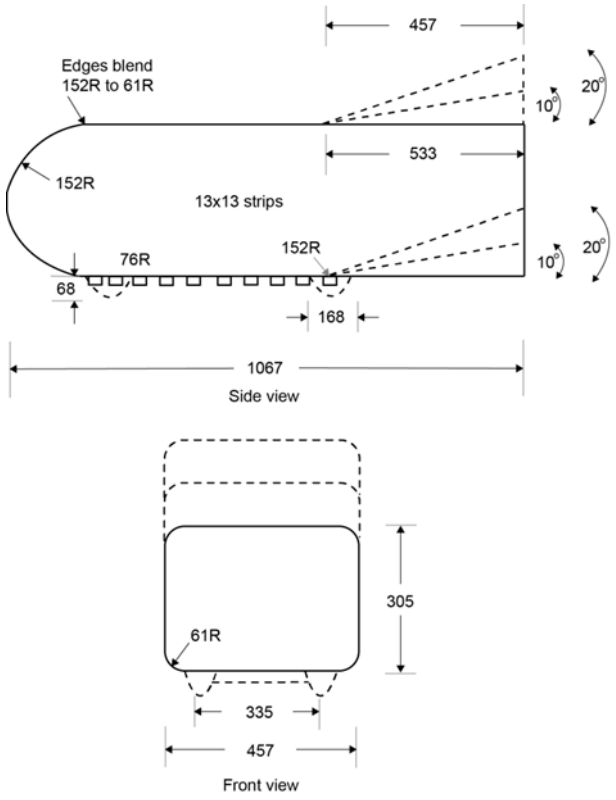

Figure 2-2: Schematic of bluff body geometries (with dimensions in mm) as studied by George (1981)

Dissimilar longitudinal vortex behaviour was observed in the study done by George and Donnis (1983). In the wind tunnel study, the characteristic influences of side skirts were investigated. The "Venturi" bluff body employed in the study was equipped with a Venturi-like diffuser channel as shown in Figure 2—3. When the diffuser of 5° was tested with side skirts that sealed the underbody and diffuser to the ground, the downforce generated was larger than the downforce produced when there was a ground displacement between the skirts and the ground. This was due to the discharge of the low pressure flow underneath when underbody/diffuser was unsealed despite the existence of weak vortices that kept the flow attached to the diffuser ramp surface. In contrast, when 10° and 15° diffusers with skirts that sealed the underbodies to the ground were tested, the diffuser flow stalled. This was attributed to the restriction of inflow into the diffuser from the longitudinal edge vortices formed in the diffuser. As a result, the downforce generated was less than that

generated when there was a clearance between the side skirts and the ground surface. Therefore, the delta wing-like roll-up vortices from the open skirt 10° and 15° diffusers were critical to their aerodynamic performance. Moreover, when a centre body ("Tub") was added to the underbody-diffuser surface of the test model (Figure 2–3), it decreased the effective area of the diffuser — inhibiting the diffuser flow and consequently reducing downforce.

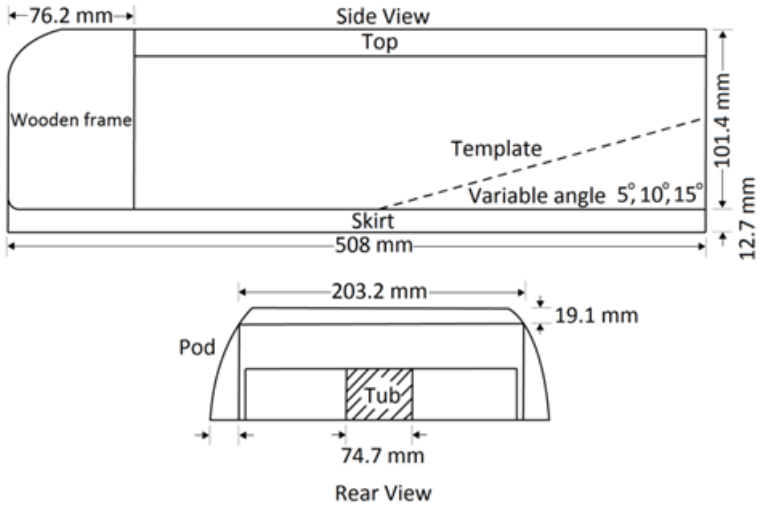

Figure 2-3: Schematics of the 'Venturi' bluff body model as studied by George and Donis (1983)

2.1.2 Diffuser length and area ratio

The existence of the aerodynamic performance relationship between the diffuser area ratio and its length was studied by Cooper et al. (1998 & 2000). In the investigation, two diffusers of 25% and 75% bluff body lengths as shown in Figure 2–4 were tested in both fixed and moving wind tunnel ground conditions. Also, the diffusers were studied within a diffuser angle range of 0° to 16°. It was observed from the pressure recovery and contour maps extracted from the experiments that the optimum performance geometry of the diffuser relies on the use of a fixed or a moving ground condition. This was attributed to a less significant boundary layer flow development with a moving ground plane when compared with a fixed ground plane. Consequently, if the boundary layer flow blockage is considered, then the effective area ratio for a

given geometric area ratio is larger with a moving ground plane than with a fixed ground. Hence, a particular pressure recovery for a given diffuser length can be achieved with a lesser geometric area ratio when a moving ground is employed relatively to a fixed ground.

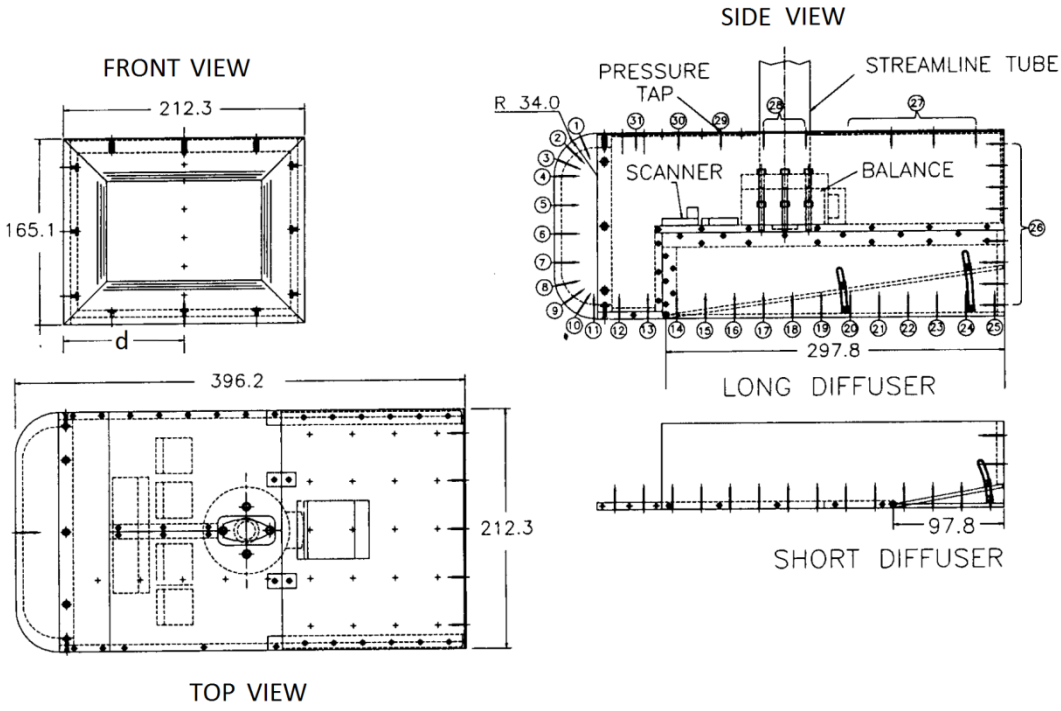

Figure 2-4: Illustrations of the bluff body diffuser geometries (with dimensions in mm) and pressure tap positions as used by Cooper et al. (1998, 2000)

The relationship between the area ratio of the asymmetric ground-effect diffuser and the diffuser length was then formulated and represented in Equation 2.1 as:

$$AR = 1 + \left(\frac{L_D}{h}\right)\tan\theta \qquad (2.1)$$

Where,

θ = diffuser angle

h = ride height

Thus, it also implies that a large ride height will have a lesser area ratio for a given diffuser angle relative to a diffuser with a lower ride height.

Alternatively, Bresolouer & George (2008) noted that severe flow separation and downforce loss can occur for a small diffuser area ratio due to the restriction of sufficient air expansion and pressure recovery within the diffuser. A comparable downforce investigation by George and Bresolouer (2008) using an approximate 25% bluff body diffuser length as used by Cooper et al. (1998 & 2000) reflected a similar downforce production as the ride height was reduced. Despite that, there was a deviation at the ride heights (Figure 2–5) where the maximum downforce[2] exists. It can be inferred that the deviation, which is more profound in the 9° diffuser, may have been due to the use of a diffuser angle of 9° rather than 9.64° as employed by Cooper et al. (1998 & 2000).

Even so, the disparities — at the ride heights where the maximum downforce was measured — occurred within and near the estimated boundary layer region for both the 0° and 9° diffusers. This is if a flat plate boundary layer approximation is considered because the experiments of George and Breslouer (2008) were done under a fixed ground condition unlike the moving ground investigations done by Cooper et al., (1998 & 2000). Also, the experiments of George and Bresolouer (2008) were done under a body-length-based Re = $\sim 6.91\, x\, 10^5$ unlike the Re of $\sim 8.3\, x\, 10^5$ employed by Cooper et al. (1998 & 2000). These experiments further highlight the possibility of Reynolds number sensitivity on diffuser downforce production and at maximum downforce ride heights the effects of Reynolds number variation can become profound due to induced flow instabilities. Finally, the downforce disparities can also be attributed to the different freestream velocity and slight difference in bluff body geometry employed between the two investigations. Cooper et al. (1998 & 2000) used a freestream velocity of $30\, m/s$ while George & Bresolouer (2008) stated a freestream of $90\, km/hr$ $(\sim 25\, m/s)$. Also, the bluff body (with a

[2] In this thesis, C_L is +ve upwards so $-C_L$ represents downforce and $-C_p$ represents suction (sub-atmospheric pressures).

.

diffuser length of 25% bluff body length) employed for both investigations had a 7.3 *mm* and 9.2 *mm* difference in width and length respectively.

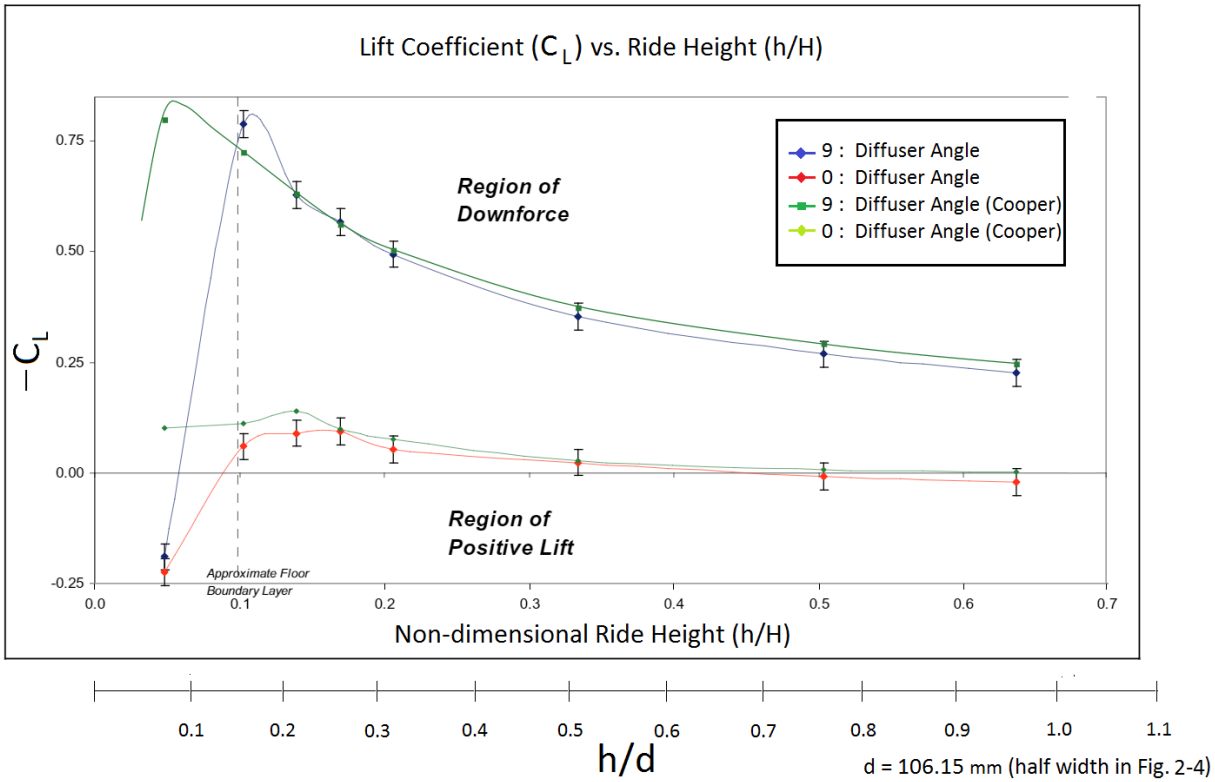

Figure 2-5: Downforce comparison for bluff body diffusers of Breslouer & George (2008) and Cooper et al. (1998 & 2000) presented in Breslouer & George (2008)

2.1.3 Diffuser ride height

The amount of downforce produced by the diffuser is dependent on its ride height. This is because the diffuser flow is sensitive to the diffuser ground displacement. Therefore, when the ride height is reduced gradually, the flow through the diffuser channel changes from an attached flow to a separated flow and as a result the aerodynamic performance of the diffuser is affected. This ground-effect interaction was highlighted in the studies of Senior and Zhang (2000a, 2000b), Senior (2002), and Zhang et al. (2004) where the downforce levels of a bluff body with a 17° diffuser (Figure 2–6) were tested over a range of ride heights.

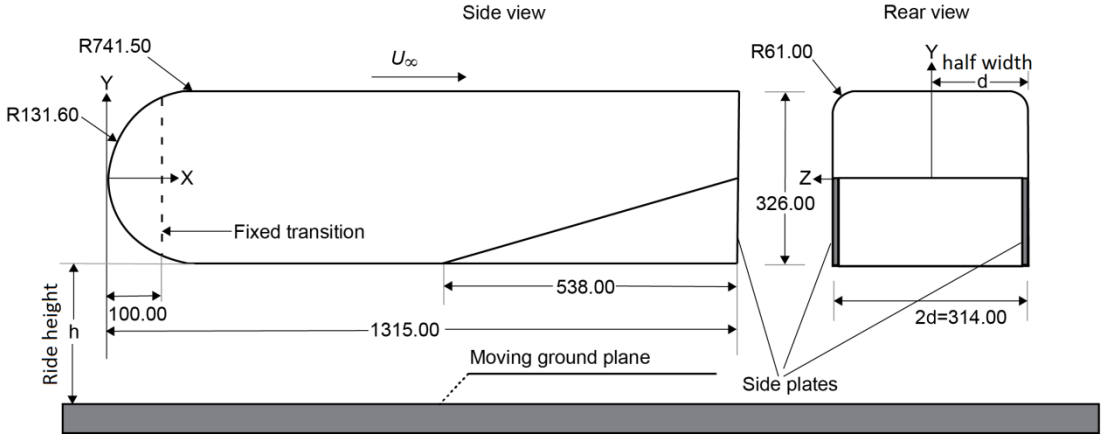

Figure 2-6: Schematic of the diffuser-equipped bluff body geometry (with dimensions in mm) used by Senior & Zhang. (2000a, 2000b)

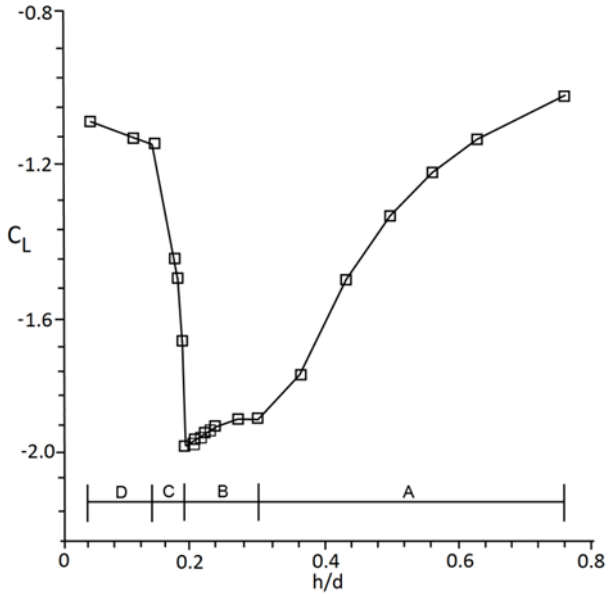

Figure 2-7: Flow regions within plots of lift coefficient against normalized ride height as presented by Senior (2002)

Force measurements extracted from the investigations mentioned above and presented in Figure 2–7 show that over the range of normalized ride heights (h / d) studied, four distinct flow regions (A-D) were identified. As the ride height was reduced from the highest point in region A, the downforce and drag increased and this region was designated as the force enhancement region. Subsequently, a further reduction of ride height in region B (or maximum force region) led to a further increase in downforce and drag until a peak for both quantities was reached. However, in region C, an additional reduction of ride height from that of maximum downforce and drag in region B led to a decrease in downforce and drag and this region was described as the force reduction region. In region D, a further reduction in ride height from that of region C resulted in low force measurements due to the flow entering the diffuser being largely dominated by slow-moving boundary layer flow. Velocity profile measurements using LDA and PIV indicated the presence of a strengthening longitudinal vortex pair along the length-wise sides of the diffuser (as reported by George, 1981 and George & Donnis, 1983) as the ride height was lowered towards that of maximum downforce. Thereafter, the velocity measurements indicated an asymmetric weakening of the vortices initially beginning with the breakdown of one of the vortices when a subsequent ride height reduction past that of maximum downforce was implemented.

However, the wind tunnel investigations by Ruhrmann & Zhang (2003) done over a diffuser angle range (5° to 20°) with the same diffuser bluff body as employed in the studies of Senior and Zhang (2000a & 2000b), Senior (2002), and Zhang et al. (2004) indicated the occurrence of flow hysteresis. As shown in Figure 2–8, the flow hysteresis (Regions b' and c') occurred between regions b (maximum force region) and c (force reduction) as the ride height was decreased and increased across the range of ride heights studied. Flow instability and the increasing dominance of boundary layer flow entering the diffuser at low ride heights were attributed as the cause of the distinct flow

hysteresis. Furthermore, a further downforce reduction region (region e) after the low force region (Region d) was identified by Ruhrmann & Zhang (2003), which is in contrast to the studies of Senior and Zhang (2000a & 2000b), Senior (2002), and Zhang et al. (2004). This is because the lowest ride height tested by Ruhrmann & Zhang (2003) is lower than those of Senior and Zhang (2000a & 2000b), Senior (2002), and Zhang et al. (2004).

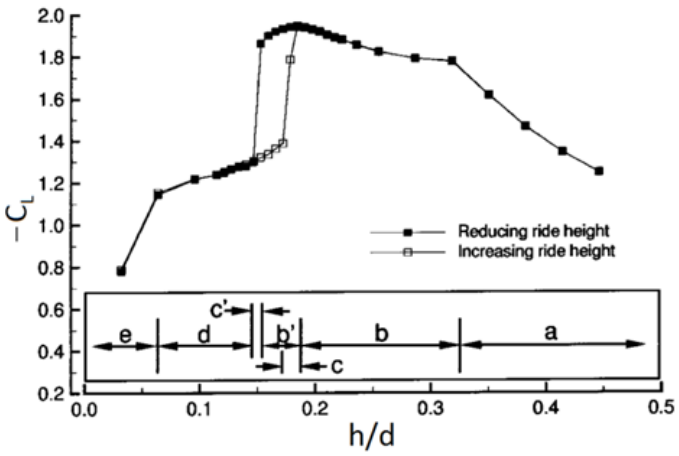

Figure 2-8: Downforce curve for flow regions (a-e) and flow hysteresis regions (b' and c') for the 15° diffuser angle as presented by Ruhrmann & Zhang (2003)

2.1.4 Diffuser angle

Further to the diffuser ride height studies by Ruhrmann & Zhang (2003), the effects of diffuser angles on the diffuser flow and its influence on the diffuser's aerodynamic performance was also investigated. The relationship between the diffuser area ratio and diffuser angle has a characteristic influence on flow stability as represented in Figure 2–9. In the investigation of the 5° diffuser angle, there was no flow separation bubble (Figure 2–10) on the diffuser ramp surface when the diffuser ride height was reduced towards that of maximum downforce. Also, the longitudinal vortices within the diffuser flow were observed to be weak and this is similar to the observations made by George and Donnis (1983). In contrast, a flow separation bubble appeared on the diffuser ramp of the 10° diffuser at a position downstream of the diffuser

inlet. In addition, an onset of a breakdown of the longitudinal vortices occurred downstream of the diffuser inlet. However, for the 10°, 15° and 17° diffusers, the separation bubble appeared near the diffuser inlet with a much earlier breakdown of the vortices due to the entrainment of the separation bubble. Due to vortex breakdown being the only cause of the loss of downforce in the case of the 5° diffuser it was designated as a low-angle diffuser. However, the 10° diffuser was categorized as a transitional angle because its diffuser flow consists of a separated flow and a breakdown of the longitudinal vortices. Also, the 15°, 17° and 20° diffuser angles were classified as high-angled diffusers due to the existence of a separated flow close to the diffuser inlet and an increased breakdown of the vortices within the diffuser flow of these angles. Above all, the 20° diffuser produced the largest downforce at its maximum downforce ride height and this is because the strength of the vortices remained strong enough to create additional low pressure along the sides of the diffuser.

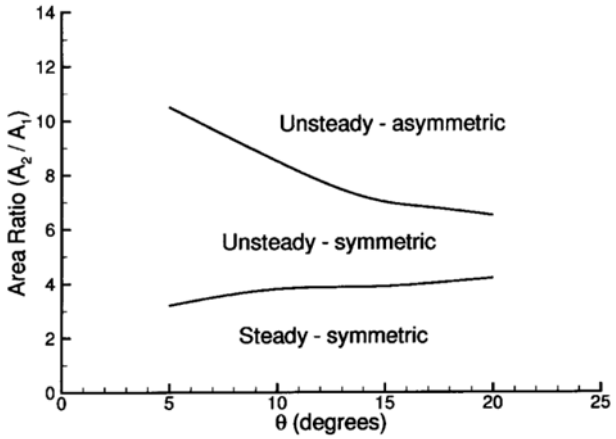

Figure 2-9: Flow regime maps for diffuser angles and corresponding area ratios Ruhrmann & Zhang (2003)

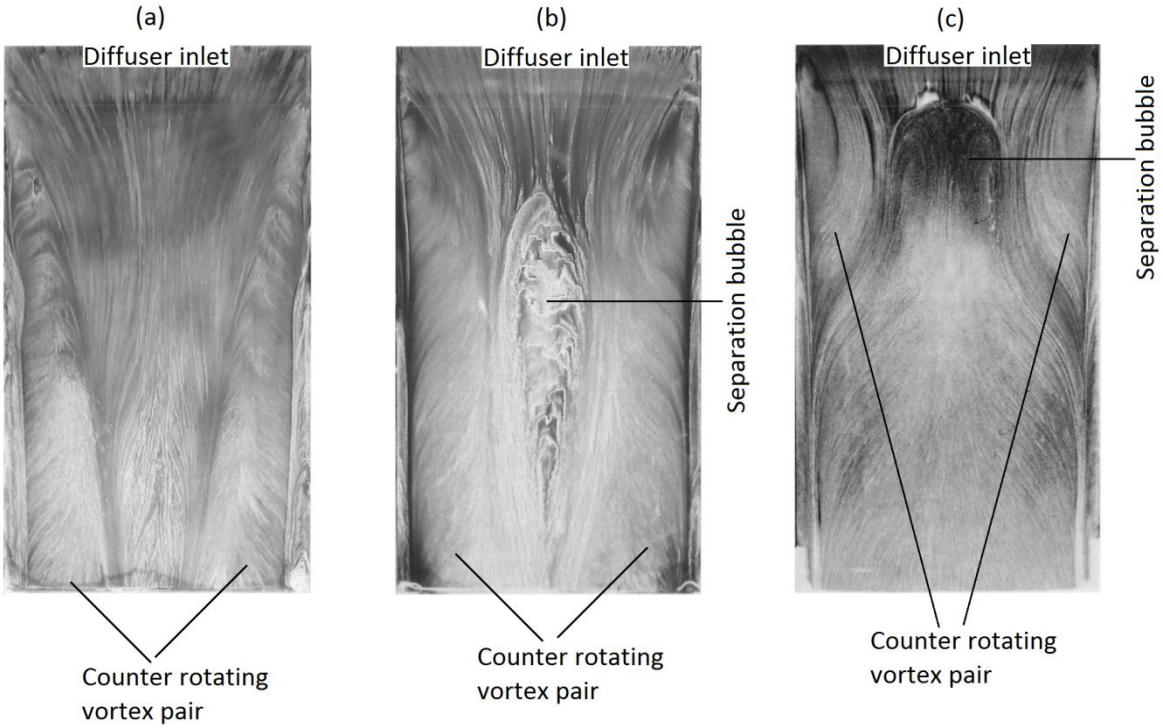

Figure 2-10: Flow visualisation on the ramp surfaces of **(a)** 5°, **(b)** 10° and **(c)** 15° diffusers at maximum-downforce ride height (flow direction from top to bottom) (Ruhrmann & Zhang, 2003)

In the studies of Jowsey & Passmore (2010) and Jowsey (2013), a range of diffuser angles (0° to 30°) were studied in plane and multiple flow channel configurations as illustrated in Figure 2–11. However, a contrasting observation to Ruhrmann & Zhang (2003) was made by a similar diffuser angle investigation by Jowsey & Passmore (2010) and Jowsey (2013). It was observed that the 13° plane diffuser produced the most downforce. Also, surface pressure measurements indicated that the separation bubble appeared near the diffuser inlet for diffuser angles above 13°. Unlike in the studies of Ruhrmann & Zhang (2003), the separation bubble appeared initially on the 10° diffuser and the 20° diffuser generated the most downforce. Despite that, the disparities between the studies of Ruhrmann & Zhang (2003) and those of Jowsey & Passmore (2010) and Jowsey (2013) was because the latter was conducted in a wind tunnel under a fixed ground condition. This implies that the enhanced boundary layer development along the fixed ground (as also

observed by Breslouer & George, 2008) may have contributed to the disparities between the studies of Ruhrmann & Zhang (2003) and those of Jowsey & Passmore (2010) and Jowsey (2013).

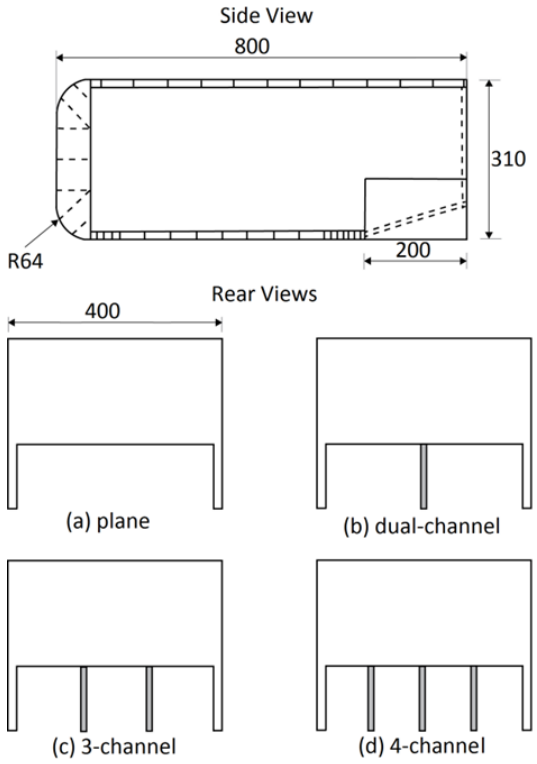

Figure 2-11: Diagrams of the diffuser bluff body (with dimensions in mm) and splitter configurations as used by Jowsey & Passmore (2010) and Jowsey (2013)

Also, the PIV measurements extracted from the experiments of Jowsey & Passmore (2010) and Jowsey (2013) indicated that the multiple-channel diffuser had an improved aerodynamic performance than that of the plane-diffuser because the former generated an enhanced diffuser pump down effect. The three- and four-channel diffusers were also discovered to produce more downforce at high diffuser angles because the channels appeared to inhibit flow separation by constraining the vortices. The largest downforce created among the diffuser configurations was from the four-channel diffuser. This was because longitudinal secondary vortices were generated along the sides of the inner splitters close to the outer end plates of the diffuser. These secondary

vortices were generated from the cross flow of the primary longitudinal vortices along the outer end plates of the diffuser.

2.2 Computational Studies

A numerical study on the ground-effect diffuser provides additional information on the flow physics of the diffuser flow and can be validated by wind tunnel experiments. Comprehensive numerical modelling using computational fluid dynamics (CFD) have been conducted on the ground-effect diffuser. These studies include the use of steady-state Reynolds-Averaged Navier-Stokes (RANS) modelling and advanced models such as Detached Eddy Simulation (DES) and Large Eddy Simulations (LES).

2.2.1 Steady-state numerical simulations

The Realizable $\kappa-\varepsilon$ turbulence RANS model was employed by Marklund & Lofdahl (2009) and Marklund (2013) to model bluff body flow and was validated by wind tunnel experiments. In the numerical study, five bluff-body shapes ('square back', 'boat tail', 'fastback 21°', 'fastback 30°' and sedan/wagon shaped models) with a range of diffuser angles from 0° to 14°. As shown in Figure 2–12, the 'boat tail' model is made up of a 21° backlight section that converges by 15° on both sides and a 9.4° diffuser ramp with no endplates.

It was observed from the experiments of the boat-tail model under a moving ground condition and at a ride height ($h = 40\ mm$) that the underbody mid-plane surface pressure coefficients reflected the characteristic underbody pressure recovery behaviour. As plotted in Figure 2–13, there is a pressure downstream of the nose section followed by a suction peak at the diffuser inlet and a subsequent pressure recovery towards the diffuser exit. Notably, the pressure at the diffuser exit is above that of freestream. This occurrence may be attributed to the additional pressure recovery from other sides of the converging backlight section. Among the various bluff body models tested, the pressure distribution on the base plate of the 'boat tail' model was the highest (with C_p within 0.15 to 0.2).

In addition, the pressure coefficients extracted from CFD to a large extent correlates with the wind tunnel measurements as shown in Figure 2–13. However, at the diffuser inlet the CFD measurements appeared to over-predict the peak suction of the inlet. Marklund (2013) credited this occurrence to the use of a 'very dense' mesh which enhanced numerical resolution, but more so due to the lack of a pressure tap at the start of the diffuser to measure the suction peak. However, it is imperative to note that the Realizable $\kappa-\varepsilon$ turbulence RANS model is capable of predicting swirling flows and boundary layers in a separated or adverse pressure gradient flow. Despite that, the addition of mean rotation effects in the computation of turbulent viscosity generates non-physical turbulent viscosities (Shih et al. 1994). Hence, the possible effects of turbulent viscosities on the peak suction at the diffuser inlet could have been investigated with the $\kappa-\omega$ SST turbulence model. It is worth noting (as explained by Menter, 1994) that the $\kappa-\omega$ SST turbulence model also performs efficiently in modelling adverse pressure gradient and separated flows without producing non-physical turbulent viscosities.

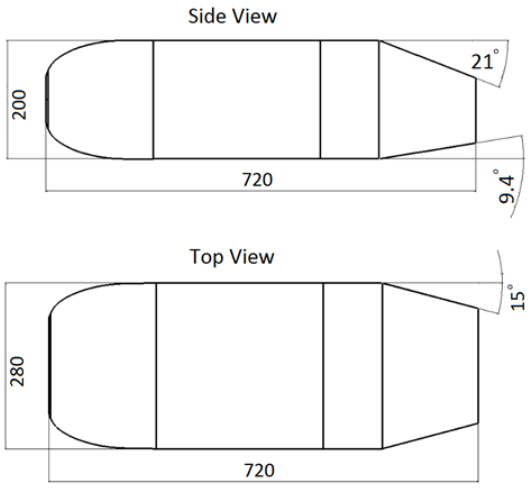

Figure 2-12: Schematic of the 'boat tail' model (with dimensions in mm) as used by Marklund & Lofdahl (2009) and Marklund (2013)

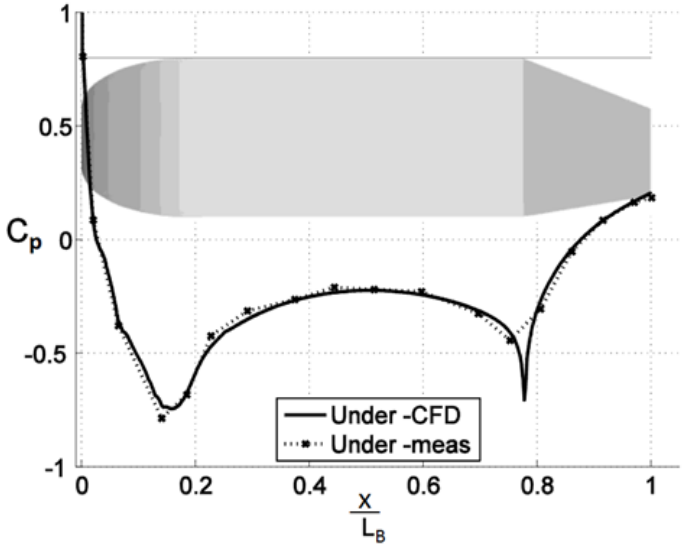

Figure 2-13: Centreline underbody surface pressure comparison between CFD and experimental measurements at the normalised ride height of $h/H = 0.2$ $(h/d = 0.286)$ for a boat-tailed diffuser bluff-body (Marklund, 2013)

2.2.2 Transient numerical simulations

Time-averaged transient CFD computations using LES were done by Puglisevich & Page (2011) and Puglisevich (2013) to correlate wind tunnel measurements from the studies done by Jowsey (2013). In the numerical investigation of the 13° plane-diffuser it was observed that the mesh refinement from 10 million cells to 20 million cells enhanced the correlation between CFD and wind tunnel underbody pressure measurements (Figure 2–14). However, the 20 million cell computational grid did not predict accurately the surface pressures in the diffuser section even though it improved its prediction along the nose and flat section of the underbody of the bluff body. This mesh inadequacy may have resulted in the insufficient computational modelling of the underbody laminar-to-turbulent transition flow. In addition, mesh inadequacy can prevent the LES standard Smagorinsky subgrid-scale (SGS) model (Smagorinsky, 1963) from excessively dissipating energy for resolved small scale motions in near-wall turbulence because of the severe eddy-viscosity in boundary layers of turbulent flows (Piomelli, 1999; Lévêque et al., 2007; Layton, 2016).

It is also worth noting that the numerical solution in the investigations of Puglisevich & Page (2011) and Puglisevich (2013) captured the flow interactions between the upper and lower recirculation in the near-wake of the 'square back' bluff body similar to the studies of Krajnovic & Davidson (2001). Howell (1998) and Soso & Wilson (2008) observed that the flow interaction between the near-wake vortex structures dominates the near-wake region of the bluff body. Consequently, this near-wake flow interaction regulates the extraction levels of the underbody flow through the diffuser exit (which determines downforce) and the base pressures of the bluff body (which determines drag). This implies that the exit of the flow from the diffuser can be restricted and the base pressure reduced if the upper near-wake flow recirculation generated by the downwash from the backlight is dominant over the lower near-wake flow recirculation generated by the upwash from the diffuser. All things considered, a further mesh refinement of the computational domain or only within the diffuser may have improved the correlation between pressure measurements of LES and wind tunnel experiments. This is because LES turbulence modelling is sensitive to the x–y–z grid size of any given computational domain.

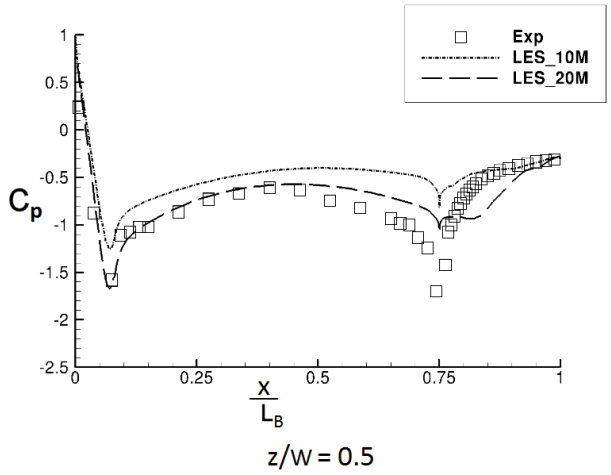

Figure 2-14: Time-averaged CFD surface pressure coefficients C_p (at $h/H = 0.09$ or $h/d = 0.140$) along the centre-line length of the underbody surface of a bluff body (Puglisevich, 2013)

2.3 Ground-effect Diffuser Performance Enhancement

The experimental and numerical studies presented and discussed in this chapter have provided an understanding of the flow physics of the ground-effect diffuser. Also, the impact of the diffuser flow on the aerodynamic performance of the diffuser has been analytically discussed. In summary, the maximum downforce produced by the diffuser is dependent on its ride height. In addition, the diffuser angle (and ride height) can determine if the diffuser flow will separate from the diffuser ramp or if flow separation will occur at the diffuser inlet or at a positon downstream of the diffuser inlet. Also, the longitudinal vortices along the length-wise sides of the diffuser enhance the aerodynamic performance of the diffuser by creating additional suction within the diffuser.

However, there is a gap in ground effect diffuser research. While previous studies have provided an understanding of the characteristics of the diffuser flow, a means to enhancing its aerodynamic performance has not been defined. It is well documented that the pressure recovery within the diffuser is critical for downforce production. Therefore, an alteration of the diffuser pressure recovery behaviour — which has not been explored — can lead to gains in downforce. A possible performance enhancement exploration involves the use of a flow control device to induce a second pressure recovery at a location downstream of the diffuser inlet. The flow control device when positioned close to the diffuser exit acts to delay flow separation and enhance the exit flow velocity. This thereby induces a pressure drop close to the diffuser exit and a subsequent pressure recovery occurs as the airflow exits from the diffuser.

As presented in Equation 1.8, Cooper et al. (2000) mathematically expressed the overall pressure-recovery coefficient $\bar{C_p}$ of a diffuser with a solitary pressure-recovery curve as: $\bar{C_p} = (C_{p2} - C_{p1})/(1 - C_{p1})$.

This implies that downforce can be enhanced if a second pressure-recovery region which begins at a location downstream of the diffuser inlet and

congruent with the initial pressure-recovery which begins at the diffuser inlet is induced. As a result, we can theoretically express the overall pressure recovery coefficient for a two-stage pressure-recovery diffuser $\bar{C}_{p_s}$ in Equation 2.2 as:

$$\bar{C}_{p_s} = \underbrace{\frac{(C_{p3} - C_{p1})}{(1 - C_{p1})}}_{\bar{C}_{p1}} + \underbrace{\left[\frac{(C_{p2} - C_{p3})}{(1 - C_{p3})}\right]}_{\bar{C}_{p2}} \frac{(1 - C_{p3})}{(1 - C_{p1})} \tag{2.2}$$

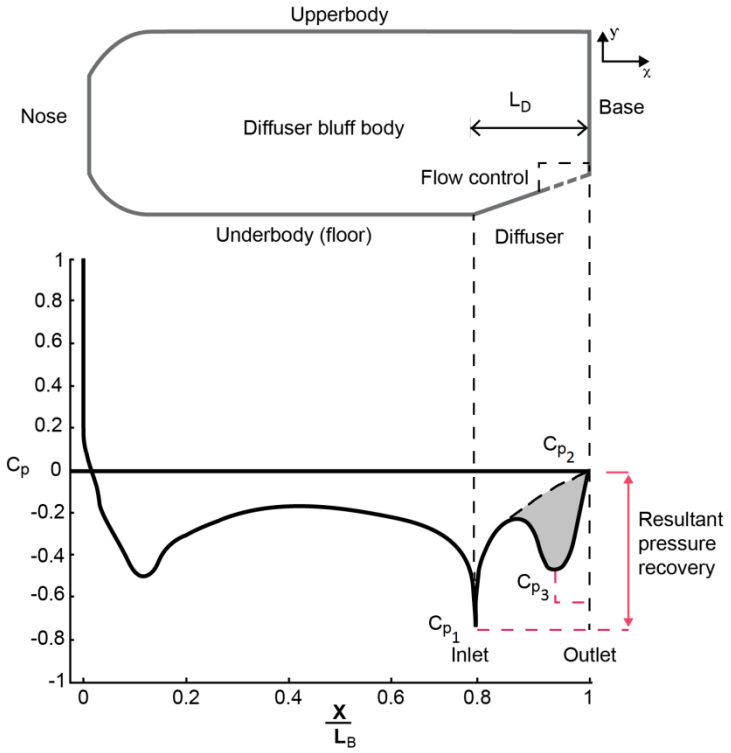

Figure 2-15: 2-D illustration of the pressure behaviour along the underbody with a 2-stage pressure recovery on the diffuser section of a diffuser bluff body (adapted from Marklund, 2013)

As illustrated in Figure 2–15, the second pressure recovery region that develops from the initial pressure-recovery is induced by flow control and C_{p3} is the pressure coefficient at the start of the second pressure-recovery region. As represented in Equation 2.2, $\bar{C}_{p1}$ and $\bar{C}_{p2}$ are the constituent pressure recovery coefficients of the first and second pressure recovery stages respectively. This implies that comparatively, the two-stage pressure-recovery diffuser produces

a greater downforce than the diffuser with a single-stage pressure-recovery. The two-stage pressure recovery diffuser accomplishes this because its average pressure is lower than that of the single-stage diffuser. As a result, an alteration of the pressure-recovery of the diffuser by employing a flow control device close to the diffuser exit to keep the flow attached and enhance the exit airflow velocity can enhance the performance of the diffuser.

2.3.1 Active and passive flow control

Active flow control technologies have been developed over the years to manage aerodynamic flows. Active flow control was first used in 1945 and defined as a system that employs the injection of energy into a flow to delay flow separation on high-lift surfaces (Crowther et al., 2010). Likewise active flow control devices have used on aerofoils to control the shedding of vortices or on road cars to reduced aerodynamic drag. Active flow control systems either employ 'suction' or 'blowing' actions to manage continuous flows (Gad-el-Hak & Bushnell, 1991a; Gad-el-Hak & Bushnell, 1991b; Gad-el-Hak et al. 1998; Gad-el-Hak, 2000). As illustrated in Figure 2–16, the suction action implies the extraction of slow-moving boundary layer flow while the blowing action involves the injection of higher energy flow to energize a continuous flow. Moreover, another effectual active flow control system involves the use of moving surfaces to control boundary layer separation thereby increasing lift and reducing drag (Modi et al., 1988; Modi et al., 1990). All in all, the total power consumed — including propulsive power — by a controlled system must be less than an uncontrolled system for the system to be of practical use.

In racing cars, active flow control devices have been used over the years in underbody designs. In the Chaparral 2J and Brabham BT46B racing cars of 1969 and 1978 engine-driven fan(s) positioned at the rear of the cars were employed to extract streamwise airflow underneath the cars (Katz, 2006b). This action enhanced the suction underneath the car and thus enabled the cars to maintain a high downforce even at low speeds. The discharge of airflow at the rear of the cars was employed to reduce base drag of the Chaparral 2J

racing car and in the case of the Brabham BT46B it was used to cool the engine. On other aerodynamic devices of F1 racing cars, such as the rear wing, active flow control systems (like the drag reduction system or DRS) have been employed to reduce the aerodynamic drag of the rear wing. However, due to restrictive racing technical regulations, active flow control technologies are banned to a large extent. One of such is the exhaust-blown diffuser which involved the use of engine exhaust gases to energise the diffuser flow and to prevent the intrusion of high pressure turbulent inflow into the diffuser. Despite that, it is worth noting that the unfavourable cost of energy to power active flow control technologies coupled with the legalities of their use on F1 racing cars has led to less focus on exploring active flow control technologies for ground-effect diffusers. However, active flow control techniques employed on aerofoils such as the use of a trapped vortex to delay flow separation (Ringleb, 1961; Rossow, 1992; 1994) can be explored in managing flow separation from the diffuser ramp surface (Figure 2–17) even though it may require suction in the cavity to maintain vortex stability (Donelli et al., 2010).

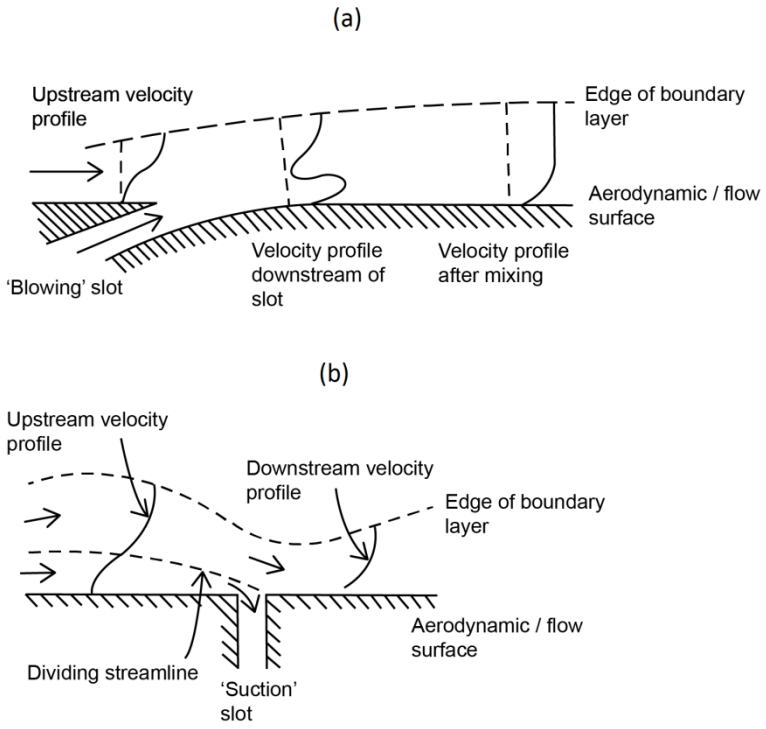

Figure 2-16: Illustration of **(a)** 'blowing' and **(b)** 'suction' flow control mechanisms as described by Gad-el-Hak, 2000

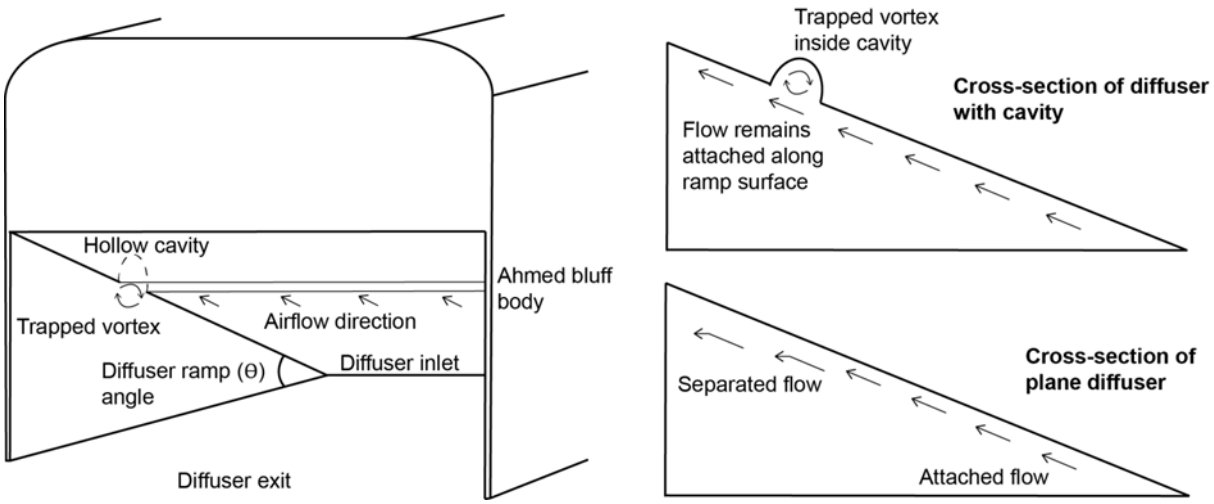

Figure 2-17: A schematic of a trapped-vortex cavity on a diffuser ramp surface

Passive flow control techniques largely involve the alteration of the surface of a high-lift aerodynamic surface. Passive flow control first appeared 20 years after the onset of active flow control, and passive flow control methods mainly act on a continuous flow by redistributing the energy in the flow (Crowther et al., 2010). Geometric or aerodynamic surface alterations employed as passive flow control techniques includes vortex generators and rough surfaces that re-energise slow-moving boundary flow and as a result delay flow separation (Gad-el-Hak & Bushnell, 1991a; Gad-el-Hak & Bushnell, 1991b; Gad-el-Hak et al. 1998; Gad-el-Hak, 2000). A major advantage of passive techniques is that they require no energy input or feedback control to function. However, this implies that they continuously act on the flow even in instances where their actions may be of less aerodynamic benefit.

In racing car applications, such as the ground-effect diffuser of Formula 1 racing cars, passive flow control methods have been employed over the years to enhance aerodynamic performance. The double-deck diffuser design of 2009, as illustrated in Figure 2–18, involved the inclusion of an additional diverging ramp surface above the central section of the main diffuser. This increases the diffuser area ratio (due to the increase of the diffuser exit area). As a result, airflow expansion is enhanced and suction at the diffuser inlet is increased thus leading to an increase in downforce (Rendle, 2011). Vortex generators

employed in ground effect (Garcia & Katz, 2003; Katz & Morey, 2008; Kuya et al., 2009) can be used to redistribute energy to locations on a diffuser ramp where the flow stalls. Garcia & Katz (2003) discovered that large rectangular vortex generators (with height above boundary layer thickness) generated the most downforce on a flat plate in ground effect while the large triangular vortex generators were efficient in terms of incremental lift-to-drag ratio. However, Kuya et al. (2009) observed that on an inverted wing in ground effect, both counter rotating small vortex generators (with height below boundary layer thickness) and large vortex generators control flow separation effectively and enhance downforce with a low drag penalty. On the other hand, co-rotating small vortex generators were found to diminish the aerodynamic performance of the wing in ground-effect. Moreover, as shown in Figure 2–19, small aerofoil-shaped flaps have been employed on diffusers of F1 racing cars to enhance the extraction of airflow through the diffuser exit. The flap is mounted above the trailing edge of the diffuser exit across the span of the diffuser. At an attack angle (α), the suction surface of the aerofoil-shaped flap generates low pressure and this accelerates the extraction of airflow from the diffuser and thus downforce is increased.

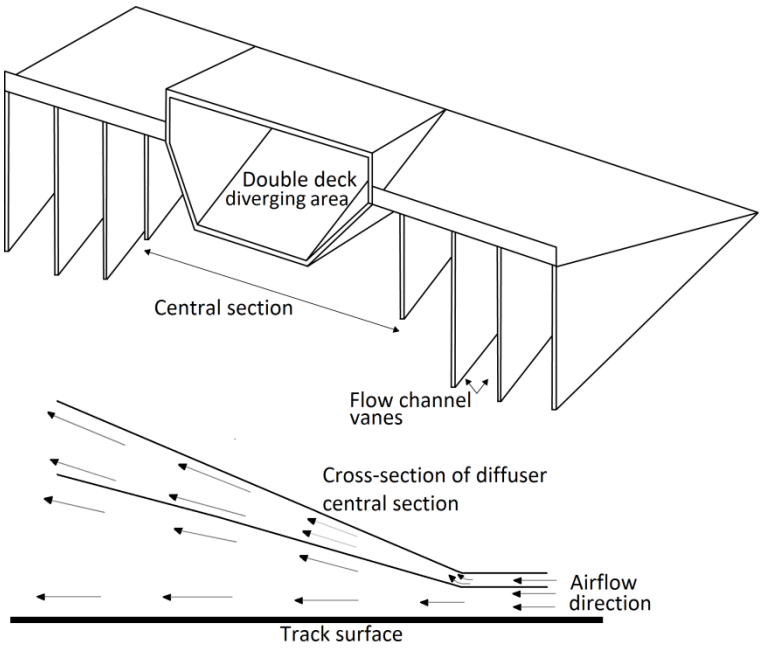

Figure 2-18: Schematic of the double-deck diffuser concept and its centreline cross-section

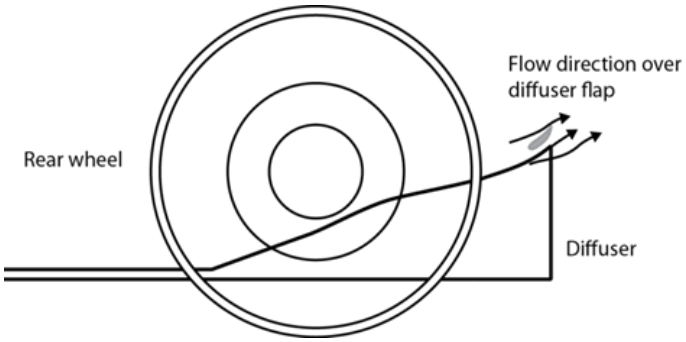

Figure 2-19: An illustration of a diffuser trailing edge flap on a Formula 1 racing car

It is worth noting that passive flow control techniques on aerofoils can be transferable to the diffuser ramp surface. This implies that the ramped surface of the diffuser can be considered as the suction surface of an inverted wing in ground effect. Low pressure suction underneath the wing is produced by the high velocity airflow traveling through the constrained area between the suction surface of the wing and ground surface. This flow behaviour is similar to the flow travelling through a diffuser in ground effect. Hence, passive air-jet vortex generators (Prince et al., 2009) that enhance the velocity of the boundary layer of a flow over a wing can be applied to the diffuser ramp.

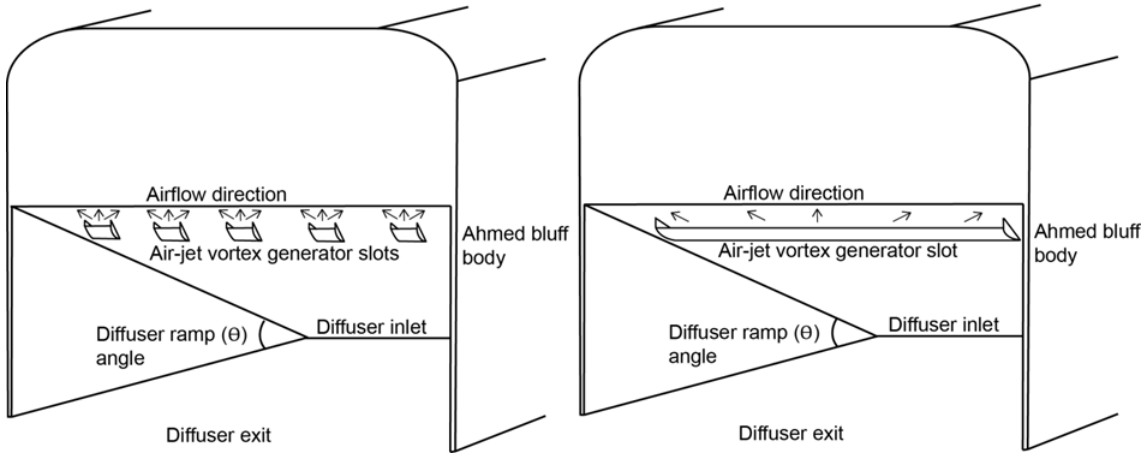

Figure 2-20: A schematic of air-jet vortex generator configurations on a diffuser ramp surface

As illustrated in Figure 2–20, passive air-jet generators located near the exit of the diffuser ramp can delay flow separation and create a second pressure drop/pressure recovery region downstream of the diffuser inlet. Such a passive system can be provided with a high pressure flow through ducts from a stagnation point on the aerodynamic body. However, due to potential losses in flow pressure through the duct as a result of skin friction, a more efficient pulsed pneumatic system can be employed. The vortex air-jet pulsed pneumatic system generator as investigated by Johnston & Nishi (1989); Johari & Rixon (2003) and Scholz et al. (2008) actively works to delay flow separation by energizing the slow-moving boundary through the generation of longitudinal vortices and turbulent mixing. Additionally, spanwise grooves can be employed on the diffuser ramp surface also to manage flow separation passively. Howard & Goodman (1985) discovered that radiusing and grooving (both longitudinal and circumferential) were effective in reducing the aerodynamic drag of a bluff body by reducing the separation of airflow from the high-angled slanted section of a cylindrical bluff body.

2.3.2 Coandă effect

Since its discovery by Henri Coandă in 1910, the Coandă effect has been applied either as a part of an active flow control system or passive flow control technique. The phenomenon is established on the premise that a jet flow travelling over a convex surface tends to remain attached to the surface (Bradshaw, 1973; Newman, 1981; Trancossi, 2011). Houghton & Carpenter (2003) indicated that the phenomenon is readily explained by the radial pressure gradient that forms for a curved flow and keeps the flow attached to the curved surface (as outlined in Figure 2–21). Why the jet follows the surface in the first place is hypothesized to be due to viscous drag and/or enhanced entrainment between the jet flow and the curved wall. However, as the jet decays downstream it slows and eventually separates. Relative to a jet stream over a plane wall, a jet stream over a convex surface tends to generate lower pressure and increase its velocity due to the flow curvature while entraining

surrounding fluid as it moves over the curved surface. This then implies that the pressure p of the inviscid tangential jet flow over the curved surface is less than ambient freestream pressure p_∞.

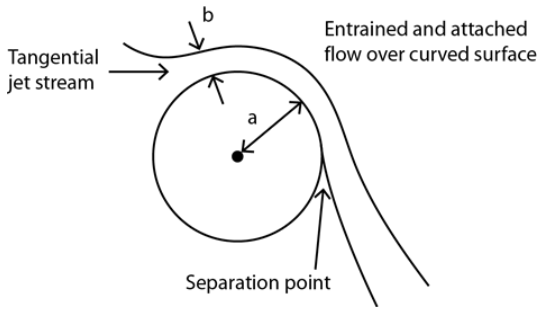

Figure 2-21: Coandă flow effect over a curved surface (adapted from Houghton & Carpenter, 2003)

Freund & Mungal (1994) discovered that the application of a Coandă jet blowing flow control system produced a drag reduction on a cylindrical bluff body by increasing base pressure. This was achieved by the elimination of the recirculating wake of the bluff body and its replacement with entrained freestream. The Coandă effect has also been applied in racing cars to enhance diffuser performance. Before its ban in 2012, the Coandă effect was employed in F1 racing cars to direct the jet stream of engine exhaust gases over a convex surface into the diffuser channels and along the outer sides of the diffuser endplates (Figure 2–22). The diffuser flow is energized and the turbulent high pressure wake from the tyres is prevented from disturbing the diffuser flow by the blowing action of the exhaust gases (Rendle, 2011). It is worth noting that due to the operational dependence of the jet stream from the engine exhaust when the throttle is engaged by the driver the 'exhaust-blown diffuser' can be classified partly as an active flow control system. Thus, the additional downforce generated by the Coandă effect is dependent on throttle position.

Figure 2-22: The curved surface along the exhaust exit on a 2012 F1 racing car. The surface induces the Coandă effect by turning the flow downwards towards the diffuser at the rear of the car Available at: www.f1fanatic.co.uk/2012/10/12/lotus-coanda-exhaust-race (Accessed: September, 2016)

2.3.3 Flow-curvature effect

Ground-effect diffuser performance can be enhanced by employing the effect of flow-curvature. The Coandă effect as described in Section 2.3.2 involves a jet stream, however, a potential flow travelling over a convex surface due to flow turning causes the flow to increase its velocity and induces a turbulent boundary layer thickness smaller than that of a flat surface. This in turn leads to a pressure drop and a reduction in wall friction, turbulent intensities and shear stress of the wall-bounded flow (So & Mellor, 1973; Gibson et al., 1984; Muck et al., 1985). As a means of augmenting the downforce produced by a diffuser, flow-curvature effect can be employed near the diffuser exit to induce a similar suction peak and subsequent pressure recovery that occurs at the diffuser inlet and downstream respectively.

As illustrated in Figure 2–23, the second-stage pressure recovery near the exit of the diffuser can be created by the addition of a convex surface on the diffuser ramp surface close to the diffuser exit. The convex surface acts as a suction surface as the flow accelerates over the surface due to the induce flow-curvature. Subsequently, the flow recovers its pressure and exits the diffuser at a higher pressure. As a result, downforce is enhanced because the two-stage pressure-recovery enables the diffuser maintain a low average pressure longer

than a single-stage pressure-recovery diffuser before the flow exits the diffuser into freestream at a much higher pressure.

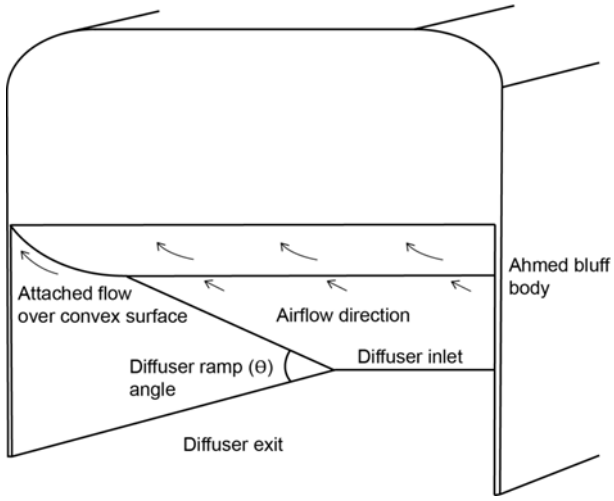

Figure 2-23: A schematic of flow curvature effect over a curved diffuser ramp surface

2.4 Aims and Objectives of the Current Work

As established in the literature review, previous research work on the ground-effect diffuser has focused on understanding its flow physics and aerodynamic effects. However, the alteration of the diffuser pressure recovery behaviour as a means of enhancing the diffuser aerodynamic performance has not been adequately explored. This presents a major gap that this thesis intends to fill by firstly corroborating with extensive baseline investigations the diffuser flow physics as established by the studies presented in the literature review. Secondly, novel flow-control methods governed by aerodynamic principles are developed and studied to examine their potential in enhancing the aerodynamic performance of the diffuser.

The diffuser flow studied in this thesis is applicable to the ground effect aerodynamics of diffusers of racing and road cars. Further knowledge presented by this thesis will not only extend the database of diffuser flow research but can be applied on racing cars to increase downforce or on road cars to reduced underbody flow drag.

The aim of this study is to improve understanding and performance of the ground-effect diffuser. The objectives to be achieved over the course of this research project are as follows:

1. To investigate the 3—D flow field within a fixed-angle diffuser in ground effect.
2. To validate pre-existing diffuser flow physics understanding and further extend the experimental and computational database of the diffuser flow field.
3. To correlate experimental data with CFD using RANS and URANS turbulence models in addition to the more advanced IDDES approach.
4. To develop and provide analysis of novel passive flow control methods that enhance the aerodynamic performance of the diffuser in ground effect.

As a means of accomplishing the set objectives, wind tunnel model testing under moving ground conditions and equivalent numerical investigations using CFD were determined as the effective means of conducting the research. The subsequent chapter delineates in detail the experimental and computational methods employed in the research. Also, details of the test model (including the baseline and the three novel passive flow control geometries) as well as the experimental and computational conditions are presented in Chapter 3. Details of ground-effect diffuser research reviewed in this chapter are listed in Table 2–1.

Table 2-1: Details of diffuser research reviewed in Chapter 2

Study Author(s)	Exp/CFD	Model Geometry	Diffuser Angle (deg.)	Freestream velocity (m/s	Time step (s)	Number of cells	Re	Ground Condition	Result Types
George [1981]	Exp	Bluff body diffuser	0 - 20	—	—	—	$1.4 - 3.4\ x\ 10^6$	stationary, moving	force, oil flow, smoke, tuft
George & Donis [1983]	Exp	Bluff body diffuser	5 - 15	30	—	—	$9.0\ x\ 10^6$	stationary, moving	force, oil flow
Howell [1994]	Exp	Road car type body	0-20	25	—	—	—	stationary, moving	force, pressure
Cooper et al. [1998, 2000]	Exp/CFD	Bluff body diffuser	0 - 15.6	30	—	—	$8.3\ x\ 10^5$	stationary, moving	force, pressure
Breslouer & George [2008]	Exp	Bluff body diffuser with wheels	0, 9	25	—	—	—	stationary	force, flow visualization (tuft, helium bubbles)
Senior [2002]	Exp	Bluff body diffuser	17	8 - 30	—	—	$0.7 - 2.7\ x\ 10^6$	stationary, moving	force, pressure, oil flow, LDA, PIV
Ruhrmann & Zhang [2003]	Exp	Bluff body diffuser	5 - 20	30	—	—	—	moving	force, pressure, oil flow, LDA
Soso & Wilson [2008]	Exp	Bluff body diffuser with wing	5 – 16.7	20	—	—	$3.0 - 3.09\ x\ 10^5$	moving	force, pressure, oil flow, LDA
Jowsey [2013]	Exp	Bluff body diffuser	0 – 30	5 - 45	—	—	$3.16\ x\ 10^6$ – $2.5\ x\ 10^6$	stationary	force, pressure, PIV
Marklund [2013]	Exp/CFD (RANS)	Bluff body diffuser and Road car type body	0 - 14	30 - 45	—	55 – 70 million	—	stationary	force, pressure, velocity, flow streamlines
Puglisevich [2013]	CFD (LES)	Bluff body diffuser	13	80	$3.6 - 5.9\ x\ 10^{-8}$	10 – 20 million	$1.01\ x\ 10^6$	stationary	force, pressure, velocity, flow streamlines

Chapter 3

Research Methods and Set-up

This chapter provides a description of the wind tunnel facility employed for the experiments. Also, details of the wind tunnel test models investigated in this research are outlined and presented. This is followed by descriptions of the experimental procedures and measurement techniques used in extracting data from the experiments. Thereafter, details of the numerical methods employed to correlate with the experimental data are also presented. Measurement repeatability and uncertainties are presented in Appendix A of this thesis.

3.1 Experimental Set-up

3.1.1 Wind tunnel facility and test operating conditions

The wind tunnel experiments for this research project were conducted in the DS Houghton wind tunnel of Cranfield University. The wind tunnel is a $2.74\ m\ x\ 1.66\ m$ closed-return, three-quarter open jet tunnel. The wind tunnel facility also includes a continuous-belt rolling-road system to simulate a moving ground condition. This makes the wind tunnel appropriate for testing automobile-related ground-effect aerodynamics. The belt is moved by a set of tension rollers, and boundary layer across the belt surface is removed by a boundary layer suction system. The boundary layer control system comprises of a perforated plate near the nozzle exit of the wind tunnel and suction is also applied below the splitter plate to remove any residual boundary layer built up on the returning belt. The distribution and *a priori* optimisation of suction

keeps boundary layer growth on the belt at a minimum. In addition, the lifting of the belt as a result of aerodynamic loading is prevented by an equal distribution of suction underneath the rolling belt. Also, chiller units and heat exchangers are employed to regulate the temperature of the belt platen and freestream tunnel air. A Pitot-static tube located above the test model was used to measure total pressure in the working section. Freestream turbulence was recorded to be about 0.3% with 98.4% of total pressure recorded at $2\,mm$ above the belt. A schematic of the wind tunnel is outlined in Figure 3–1.

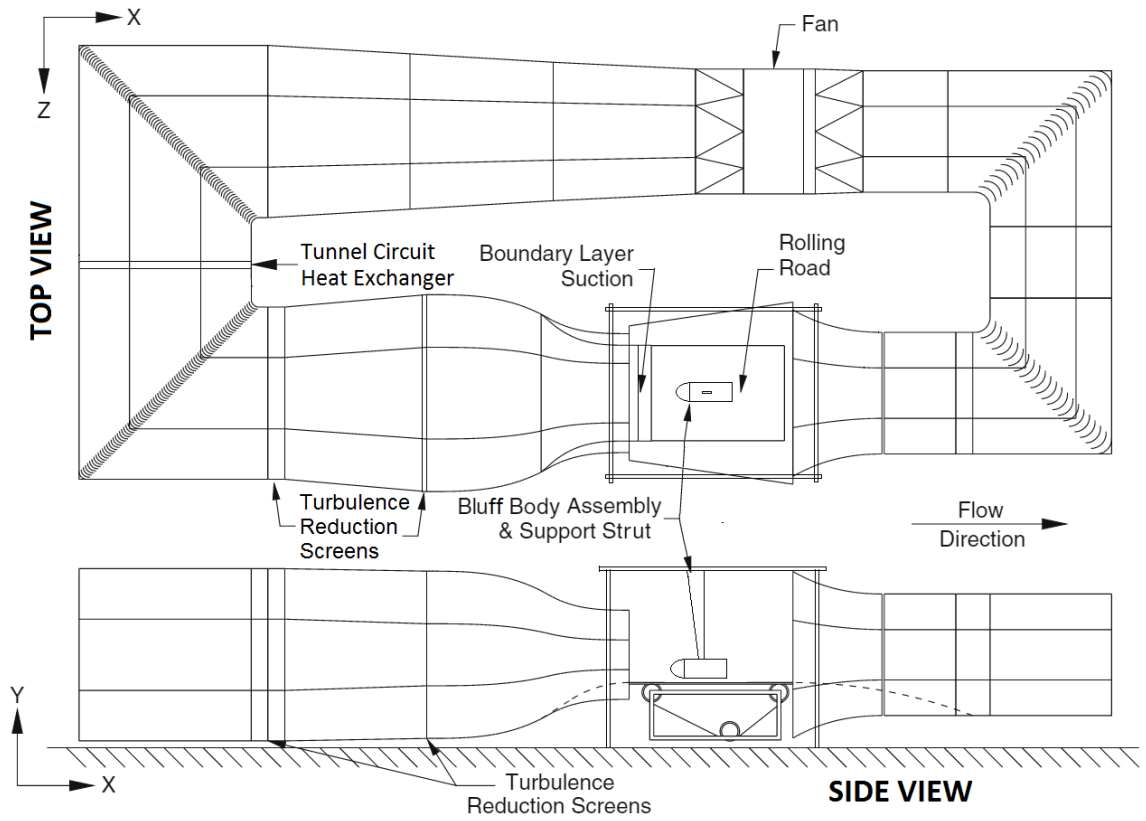

Figure 3-1: A schematic of the Cranfield University DS Houghton wind tunnel

The overhead strut of the wind tunnel was employed to hold the test model in position and a force balance used to measure aerodynamic forces on the test model was mounted on the strut. Due to the possible interference of the LDA equipment, it was positioned outside the working section. Most of the experiments were done at a Reynolds number of $1.8\,x\,10^6$ based on bluff body length, which correlates to a freestream velocity U_∞ of $20\,m/s$. Likewise, the

rolling road was also run at a velocity of $20\,m/s$. However, additional force measurements were conducted at Reynolds numbers of $1.35\,x\,10^6$ and $2.25\,x\,10^6$ which equates to $15\,m/s$ and $25\,m/s$ respectively. The blockage created by the streamwise cross section of the model was 2.25%. No corrections were made to results extracted from the experiments because the open test section of the tunnel minimises the need for blockage corrections. Also, the wind tunnel was equipped with the Pi Aero computer-controlled system to automate the hydraulic motor on the strut (for ride height adjustment), to regulate the rolling road and freestream at the same velocity, and to control other wind tunnel operating conditions. The computer-controlled system was also employed for logging of data before transfer to Microsoft Excel for post-processing. Further details of the facility are provided by Knowles and Finnis (1998).

3.1.2 Wind tunnel test models

To understand the complex flow physics of an underbody diffuser flow, it was imperative to study the diffuser in isolation before the addition of further aerodynamic devices. A generic bluff body, as described in Section 1.3, is a suitable geometry to study representative complex flows around bluff bodies such as automobiles. This also makes it the appropriate representative geometry to study the diffuser flow. The nose section curvature of the bluff body enables freestream to travel around all sides of the body without flow interruption. The flat section underneath the bluff body represents the underbody floor of a racing car and a slanted section serves as a diffuser. The inclusion of side plates along the lengthwise sides of the diffuser section consummates the diffusing section as a complete representation of a racing car diffuser.

For this study, the 3—D bluff body employed has a diffuser length of about 41% of the bluff body length. This ensured that the underbody ground effect phenomenon is largely dictated by the diffuser. The overall dimensions of the baseline bluff body and its diffuser are the same as that used in the studies of

Senior (2002). However, geometrical differences exist between the bluff body employed by Senior (2002) and in this present study. In the case of Senior (2002), the nose section was comprised of two merging radii and also the lengthwise top and bottom edges were radiused (Figure 3–2). The bluff body model for this present study was made from aluminium with the nose section made from SikaBlock Polyurethane and the bluff body model is 0.326 m high, 0.314 m wide, and 1.315 m long (Figure 3–3). Its diffuser ramp angle is 17° with 5 mm-thick endplates extending along the edges of the diffuser length. The start of the diffuser (or inlet) is faired with its ramp surface at a radius of 0.04 m and the diffuser length is 0.538 m with a height of 161.5 m.

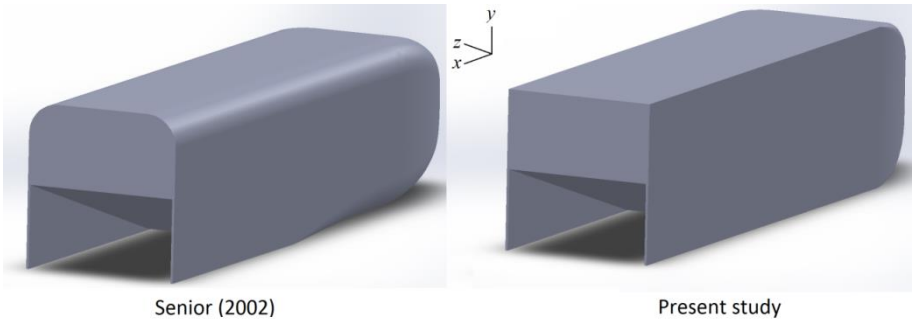

Figure 3-2: Isometric CAD representations of the diffuser-equipped bluff body geometries used by Senior (2002) and in this present study

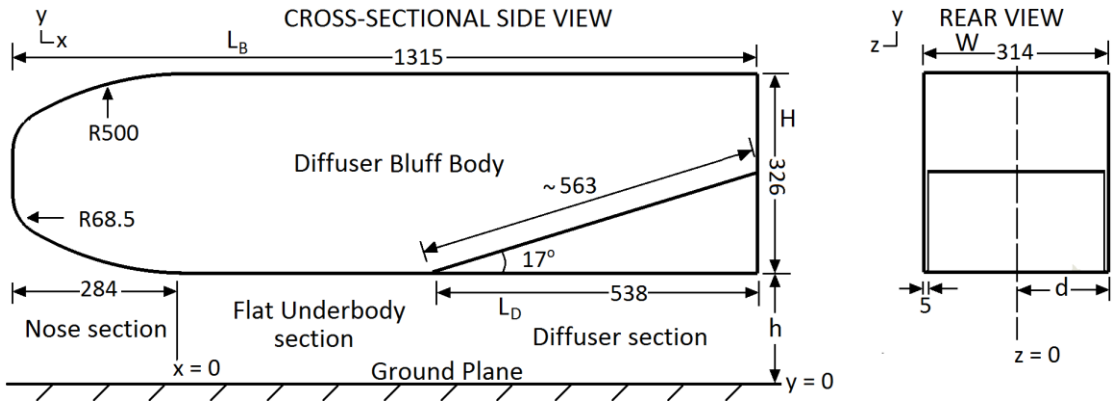

Figure 3-3: Schematic of the cross-sectional and rear views of the diffuser bluff body (Dimensions in mm) for the plane diffuser (baseline)

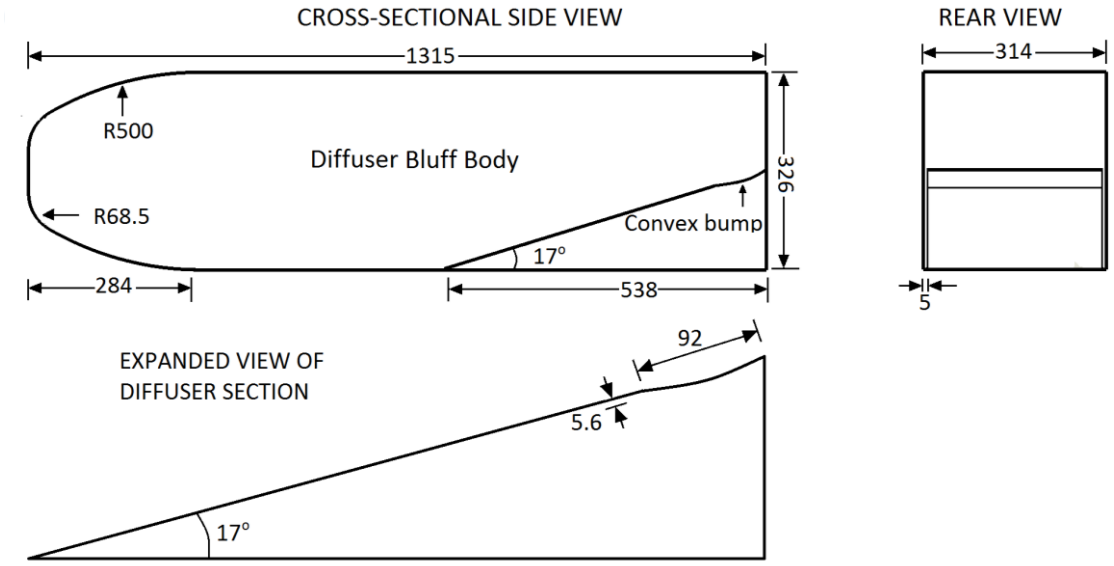

Figure 3-4: Schematic of the cross-sectional and rear views of the diffuser bluff body (Dimensions in mm) for the diffuser with convex bump

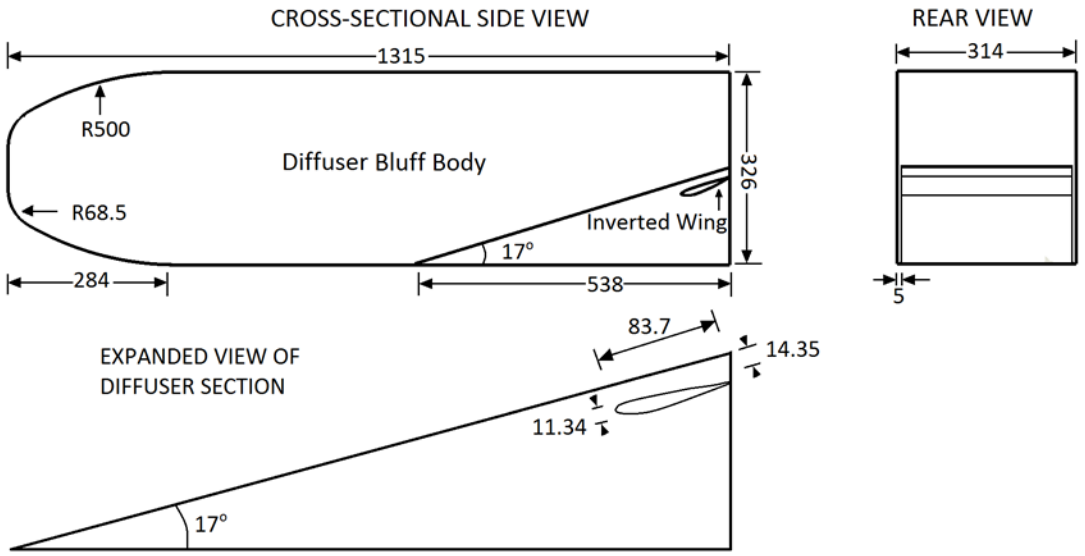

Figure 3-5: Schematic of the cross-sectional and rear views of the diffuser bluff body (Dimensions in mm) for the diffuser with wing

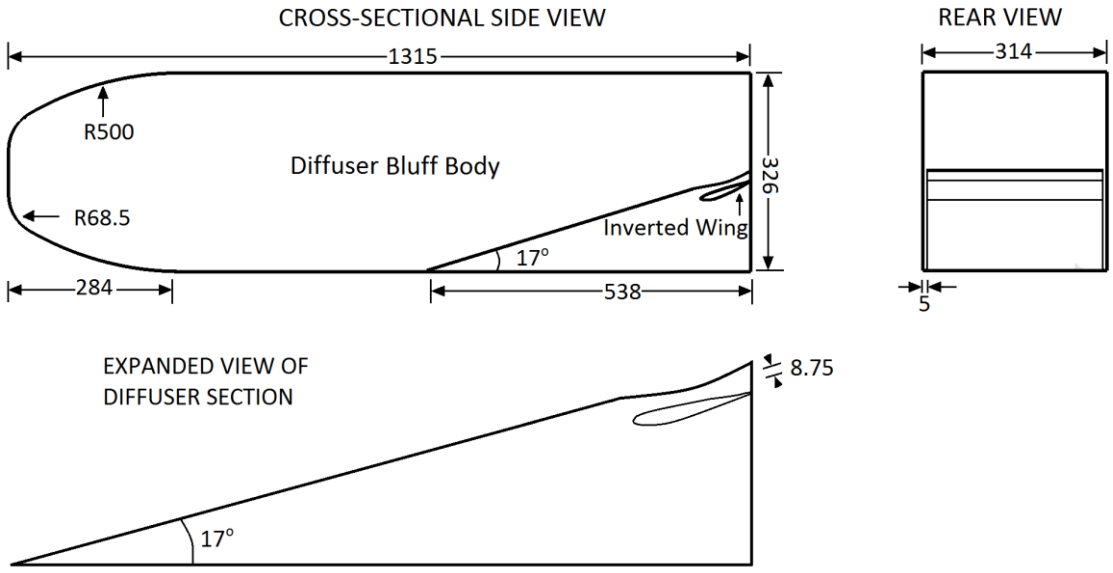

Figure 3-6: Schematic of the cross-sectional and rear views of the diffuser bluff body (Dimensions in mm) for the diffuser with both the convex bump and wing

Additional passive flow control devices were tested within the diffuser flow channel to examine their potential to control flow separation and enhance the aerodynamic performance of the diffuser. The passive flow control components of the diffuser model included a $0.092\,m$ long, $0.0056\,m$ high, and $0.304\,m$ wide convex-shaped bump on the diffuser ramp positioned near the diffuser exit (Figure 3–4). The other passive flow control device (as illustrated in Figure 3–5) is a modified NASA GA (W) type LS (1) -0413 inverted wing (Zerihan & Zhang, 2000) with a chord length c of $0.0837\,m$ and a span b between both diffuser end plates of $0.304\,m$ (aerofoil profile coordinates in Appendix B). The inverted wing is mounted close to the exit of the diffuser flow channel at a distance or gap g_p of $0.01435\,m$ from the diffuser ramp surface (which is about 50% more than the estimated boundary layer thickness before the diffuser inlet). Here turbulent boundary layer thickness δ (to 99% of local freestream velocity) of the underbody flat section of the diffuser bluff body was estimated using the boundary layer theory for a flat plate in Equation 3.1. In addition, the use of both the bump and wing together (with a gap g_p of $0.00875\,m$) as shown in Figure 3–6 was also investigated.

$$\delta \approx \frac{0.382 L_f}{Re^{0.2}} = 10.6\, mm \tag{3.1}$$

Most of the wind tunnel experiments were done without a fixed transition on the body. This was done to investigate the correlative efficacy of the advanced computational turbulence models in predicting the location of laminar-to-turbulent transition and in capturing the laminar separation bubble formed on all sides of the bluff body's nose section. However, force measurements across the range of ride heights tested were also done with a fixed transition at a location $0.1\, m$ from the leading edge of the nose section using a $1.2\, mm$-diameter wire trip (Figure 3–7a). This was done to study the effects of a flow with fixed transition on the aerodynamic forces acting on the bluff body. Also, to measure surface pressures, a second flat underbody and diffuser ramp surface was made and fitted with pressure tappings along the centreline of the underbody and across the diffuser ramp in the spanwise direction respectively. In addition, pressure taps were also fitted along the vertical centreline of the base surface at the rear of the bluff body. Technical drawings of the bluff body model and passive flow control devices (convex bump and wing) are presented in Appendix B.

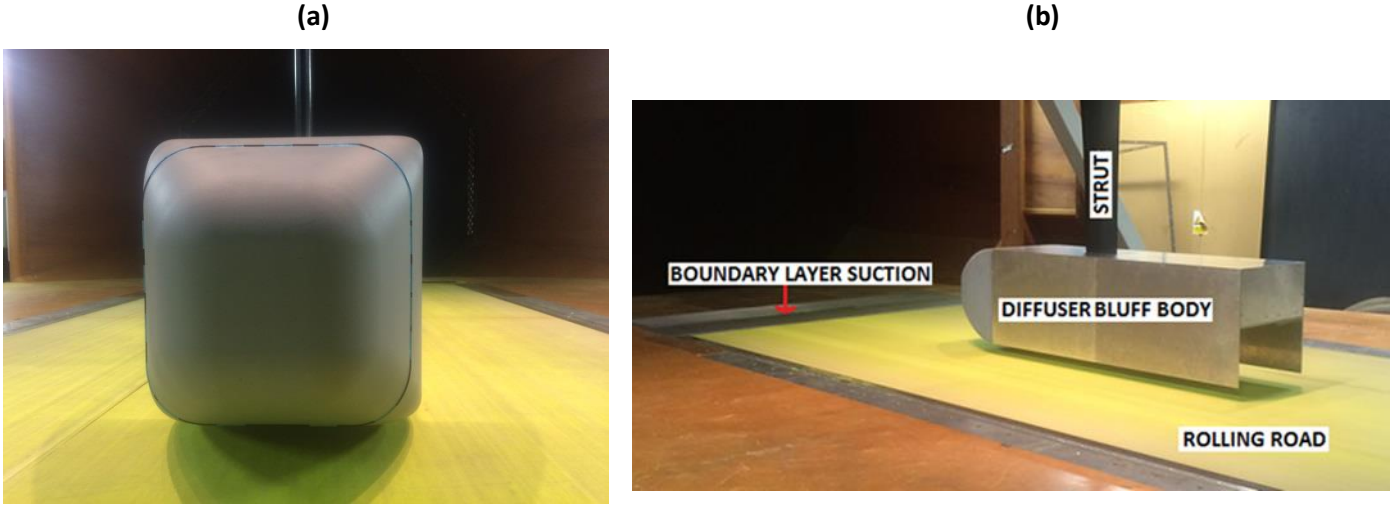

Figure 3-7: Photographs of diffuser bluff model wind tunnel setup showing: **(a)** The nose section of the model fitted with a wire trip for fixing transition and **(b)** The model mounted on the strut of the DS Houghton wind tunnel open test section

3.1.3 Test model installation and ride height positioning

The bluff body test model was held above the rolling road surface by an aerofoil-shaped overhead strut (Figure 3–7b). The strut was attached to the bluff body via the force balance inside the body which was fastened to an aluminium mount frame positioned $0.113\,m$ above the floor of the body. This provided enough enclosure inside the bluff body model to house the force balance and the section of the strut which was attached to the force balance. The strut was positioned at the centre of the bluff body's top surface and a lateral pin attached to the mount of the strut that held the force balance was used to adjust the position of the bluff body model to the centre of the rolling road. The distance between the trailing edge of the strut and the rear of the bluff body is about $0.595\,m$ while the distance between the leading edge of the strut and the leading edge of the nose section of the bluff body is $0.575\,m$.

As a means of ensuring that the bluff body ride height was even along its length and span, and also parallel to the rolling road, a Vernier drop height gauge was employed to measure the heights in four locations to within $\pm 0.02\,mm$. These locations were at both sides of the body — the leading corner of the bluff body's flat section and the trailing corner of the end plates. The ride height of the bluff body was pre-determined and calibrated by using a $24\,mm$ aluminium block and the computer-controlled motion system of the overhead strut was employed to set the ride height to within $\pm 0.01\,mm$. Also, to ensure that the yaw of the model was kept to within $\pm 0.05°$ from zero, the distances between the bluff body sides to the lengthwise edges of the rolling belt platen were measured to within $\pm 0.05\,mm$ at two locations, the leading corner of the bluff body's flat section and the trailing corner of the end plate, on either side of the bluff body. The positional measurements of the bluff body were examined before and after each run of the wind tunnel to maintain a high level of accuracy.

3.2 Experimental Techniques

3.2.1 Force measurements

As described in Section 3.1.3, a force balance mounted on the overhead strut and attached to the bluff body test model was employed to measure aerodynamic forces acting on the model during the wind tunnel runtime. This AEROTECH 6-component force balance (Figure 3–8) measured drag, side force and downforce, and rolling, pitching and yawing moments. Force and moment measurements were taken for thirty five ride heights within the range 120 mm to 10 mm (normalised to $h/d = 0.764$ to 0.064).

Figure 3-8: AEROTECH 6-component force balance

The test run was a computer-automated process which started by taking the zero of the force balance with the wind tunnel turned off. Then, the wind tunnel was run up to the required freestream dynamic pressure and corresponding rolling road velocity. After a settling time of 3 s between each ride height, force and moment measurements for each ride height were taken for a sampling time of 8 s at a logging frequency of 1 kHz while the tunnel was running. A total of four thousand and ninety six samples were averaged for each ride height force measurement after which the wind tunnel was turned off and another zero measurement was taken. The data extraction settings were implemented because they sufficiently enabled measurement repeatability as presented in Appendix A. Also, the measurement procedure

implies that the force measurements extracted were only dictated by the freestream traveling around the bluff body test model. The force measurements were reduced to coefficients of lift C_L and drag C_D with the datum offset between the zero force measurements taken with the tunnel off at the start and end of each test run, and also with the density and dynamic viscosity of freestream recorded for each measurement.

A detailed description of experimental uncertainties is presented in Appendix A, however, the uncertainties of C_L and C_D are ± 0.0025 and ± 0.0032 respectively. Also, as noted earlier, C_L values are positive upwards so negative values correspond to downforce. Force measurement test cases are detailed in Table 3–1.

3.2.2 Surface pressure measurements

Surface pressure measurements were taken along the centreline of the flat underbody and diffuser sections of the bluff body, across the diffuser and on the base surface of the body. As shown in Figure 3–9a, there were 11 tappings along the flat underbody, 12 tappings along the diffuser centreline and forty tappings distributed equally across the ramp surface in four transverse rows ($x/d = 3.63,\ 4.10,\ 5.02,\ 5.95$) with an additional fifth row ($x/d = 6.29$) of eight tappings. In the case of the diffuser with convex bump, the additional row of tappings was along the transverse centreline of the bump. Finally, five pressure tappings were also positioned along the vertical centreline of the base surface of the bluff body to capture surface pressure in the wake region. Each surface pressure tapping consists of an outer hole, $2\ mm$ deep and $0.5\ mm$ in diameter and an inner hole of $1.67\ mm$ in diameter and $3\ mm$ deep to tightly fit the hypodermic tubes of $20\ mm$ in length. Plastic tubes were attached to the hypodermic tubes and connected to the ports of Scanivalve pressure transducers (Figure 3–9b). A total of seventy six pressure tappings were created, therefore two Scanivalve pressure transducers with each having forty eight ports were attached inside the bluff body model and employed for the experiments. Pressure tappings were not provided on the wing when it was

fitted in the diffuser because its thickness of about 11.34 mm was not sufficient to accommodate the holes and hypodermic tubes. Also, if the wing were pressure tapped, the plastic tubes would have intruded in the flow through the diffuser channel.

(a)

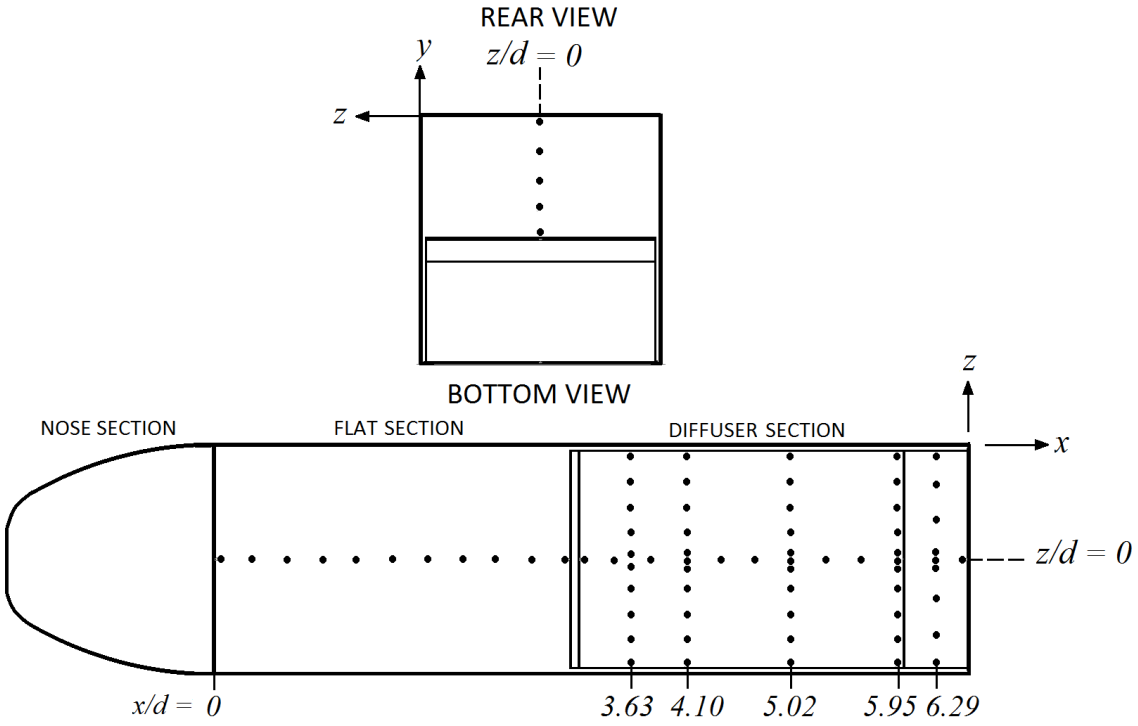

(b)

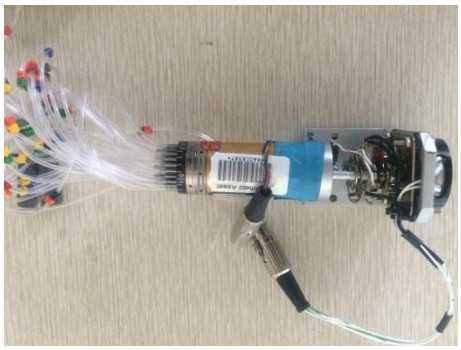

Figure 3-9: Details of pressure measurements setup: **(a)** A schematic of the pressure tapping distribution on the 17° diffuser ramp bluff body (Dimensions in mm) **(b)** Photograph of Scanivalve pressure transducer

Calibration checks of the Scanivalve transducers were done and it confirmed that for the same pressure measurement taken by both transducers, the variation was within $0.1\,Pa$ of each other's measurements. Also, the transducer ports were set to zero before each run and checks were done to ensure that the ports returned to zero after each run. Pressure readings were measured at five ride heights representing the four flow regimes ($h/d = 0.764$, 0.382, 0.191, 0.153, and 0.064). For each reading from the ports connected to a pressure tapping on the diffuser body, a total pressure p_t reading was likewise measured by the tunnel's overhead Pitot-static tube. In addition, the surface pressure measurement data extracted for each pressure tapping was averaged at a logging frequency of $20\,kHz$ from four thousand and ninety six samples. The samples were collected over $12\,s$ of sampling time and $3\,s$ of settling time as it gave a satisfactory repeatability at these data extraction conditions. Each tapping's reading was taken one after the other during the tunnel runtime. As a result, a $1.5\,s$ delay response time was set for the Scanivalve transducers to provide ample time for it to switch from one measurement port to another before readings were taken. Coefficient of pressure C_p for each static pressure p reading from the tappings was calculated by subtracting freestream dynamic pressure q_∞ from the corresponding Pitot-static total pressure reading p_t to obtain freestream static pressure p_∞. Using $C_p = \frac{p - p_\infty}{0.5\,\rho U_\infty^2}$ as delineated in Equation 1.3, C_p is then calculated. As a means of ascertaining repeatability, repeat runs were conducted and the uncertainty of surface pressure measurements was calculated to be ± 0.057. Further details of surface pressure uncertainties and details of test repeatability are presented in Appendix A. Surface pressure test cases are detailed in Table 3–2.

3.2.3 Surface flow visualisation

Visualisation of the flow pathlines across surfaces of the bluff body test model was done with a mixture of fluorescent pigments, paraffin and oleic acid. The quantity distribution of each component of the mixture was: $250\,ml$ of paraffin, $85\,g$ of fluorescent pigments, and $10\,ml$ of oleic acid. After the test

model was set to the required ride height, the mixture was applied to the surface(s) of interest by a paint brush roller. Then the wind tunnel was run for about 35 to 40 *minutes* at the required freestream and rolling road velocity — providing sufficient time for the mixture dry. The flow features are highlighted by the residue of dry pigments and ultra-violet fluorescent lights were employed to illuminate the flow features. This provided a high contrast for images of the flow features to be taken by a high resolution camera. The digital camera used was a FUJIFILM FinePix *S*5700 and images were taken in shutter-priority exposure mode with the shutter speed adjusted between 1/25 to 1/4 *s* corresponding to an aperture focal ratio (or f-stop) setting of F3.5 at a light sensitivity ISO number of 100. Figure 3–10 shows the experimental setup of bluff body test model, ultra-violet lights, and a mirror to reflect the underbody image to the camera mounted on a tripod stand. The camera was inclined at 107° in order to align parallel the reflected image captured on the mirror to the 17° diffuser ramp. Surface flow visualisation test cases are shown in Table 3–2.

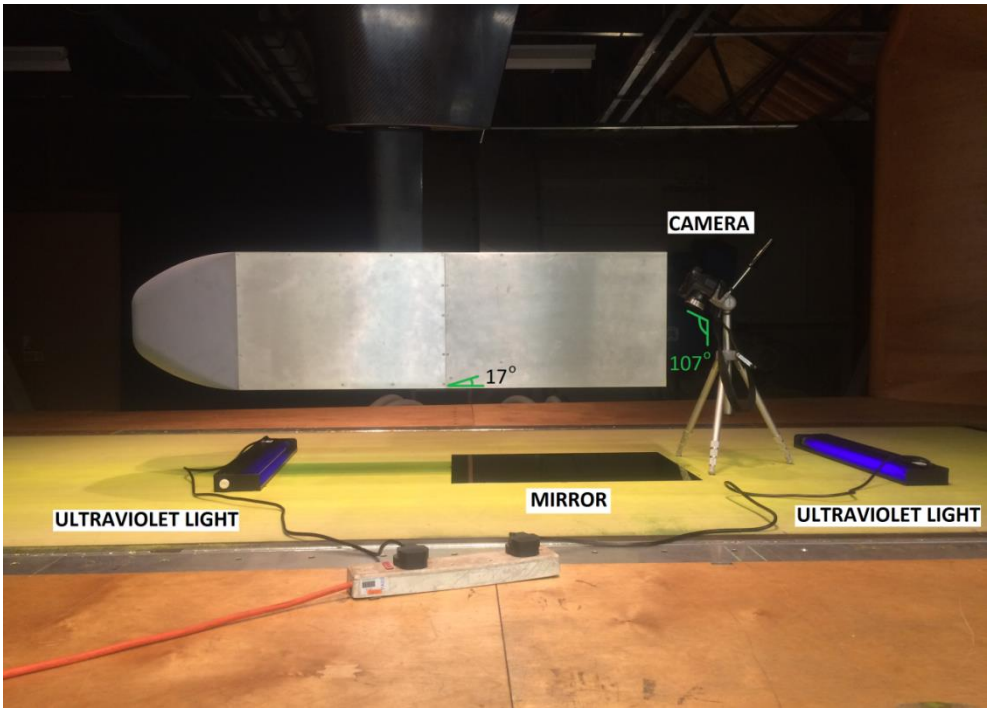

Figure 3-10: Experimental setup for flow visualisation image capture

3.2.4 Laser Doppler velocimetry measurements

Off-surface velocities of the boundary layer flow upstream of the diffuser and the near-wake downstream of the diffuser exit were measured using laser Doppler velocimetry (LDV). LDV is a laser-based system used for the non-intrusive, pointwise measurement of mean and instantaneous velocity in a fluid flow (McKeon et al., 2007). Velocities of flow particles are measured when the intersection of two laser beams forms interference fringes of low and high intensities (Durrani & Greated, 1977). When a seed particle travels through the intersection of the beams it scatters light that contains light components from the beams. However, the intensity of the components fluctuates with a Doppler shift – which is the frequency that is proportional to the velocity of the particle perpendicular to the bisector of the beams (Beauvais, 1994; Eder et al., 2001). The flow velocity of a particle is measured by an optical sensor on the LDV equipment as the seed particle travels through the intersection of the beams. It is also noteworthy that negative velocities, which are profound in recirculating and separated flows, are determined by the motion of interference fringes as the frequency of one beam is shifted by a fixed amount relative to the other (Senior, 2002).

The LDV equipment employed in this research was an LA6000 TSI Argon-ion LDV flow field measurement system. The LDV system includes a two-component TR160 series 83 mm long fibre optic probe (with an XPD60 series beam expander); two 1 W Multicolour Beam Generators (Separator) with two Bragg cells producing beams of wavelengths 514 nm and 488 nm; four fibre couplers (two for each beam generator); a photodetector module and a signal processor. The function of the fibre optic probe is to transmit the laser beams to form the measurement volume and also collect the scattered light from the travelling particles in the measurement volume. During operation, the Bragg cell of each beam generator splits the laser light into two beams with a shift frequency of 40 MHz between them. The collimated beams exit the probe and the beam expander which is attached to the probe increases the beam diameter

and fringe spacing. At the beam expander exit, the beams collimate once more and the lens ahead of the beam expander focuses and crosses the parallel beams to form the measurement volume. The probe is connected to the beam generator with a secondary connection to the photodetector module. The beam generator separates light from the argon-ion laser into different wavelengths of blue and green beams (representing the u, v velocity components). The optic fibres that connect the probe to the fibre couplers on the beam generators are linked to the green and blue beams (violet beams representing the w velocity component can be obtained by connecting additional fibre couplers to the beam generator). Scattered light from the particles are separated into colours and transformed into electrical signals by the photodetector module. The signals are extracted from the frequency data by the signal processor and interpreted by the FlowSizer Data Acquisition and Analysis 64 version 4.2.0 software installed on a Windows desktop computer.

Three grids are defined for three streamwise-oriented planes (Figure 3–11a) within the near-wake of the diffuser – one grid on the mid-plane and the two other grids were on planes positioned 77 mm from the mid-plane on each side ($z/d = 0.490,\ 0,\ 0.490$). The streamwise planes have dimensions of 340 mm by 290 mm with each plane having a total of 380 grid points and spatial resolution of 17 mm between each grid point. The positions of the grid planes were selected in order to capture the near-wake features of the vortex pair on either side of the diffuser mid-plane and the spatial resolution of the grid was chosen to prevent the overlapping of grid points. Two flow velocity components (u, v) are obtained at each grid point and the movement of the beam focus from one grid point to another is achieved by a two-directional automated probe traverse system. The computer-controlled probe mount was positioned outside the wind tunnel open test-section, requiring the use of a probe lens with a focal length (f) of 2.29 m. Boundary layer profiles were measured at the diffuser inlet ($x/d = 3.14$ see Figure 3–11b) on vertically-assembled grid points with 1 mm spacing at three spanwise locations ($z/d =$

0.363, 0, −0.363) – one at the centreline and two others 57 mm apart from either side of the centreline position. A matrix transformation is employed in the TSI Flow Sizer 64 v 4.2.0 software to resolve the flow velocities from the beams' axis system into the x–y–z coordinates of the wind tunnel.

Flow seeding particles with a mean particle size 0.9 μm where dispersed within the wind tunnel using a PIVTECH Part45 aerosol seeding generator. The generator was in operation throughout the duration of each test and produced seeding at ambient temperature for the seed particles in a solution of di (2-ethylhexyl) sebacate (DEHS) (see particle size distribution in Appendix C). Also, the generator was located outside the tunnel and the fog containing the seeding particles was supplied into the diffusing section of the subsonic tunnel downstream of the bluff body. This enabled the homogenous mixing of the fog and freestream before the circulating freestream reaches the nozzle of the test-section. Mean velocity at each data point was measured from an ensemble average of two thousand samples taken at each data point over a sampling time of 20 s because a reasonable test repeatability was achieved at this sampling time and number of samples. In addition, a settling time of 5 s was included after each probe movement to the next grid measurement point to allow the decay of probe-induced vibration. The sample size was determined by a comparison of mean velocities from the pitot-static tube of the tunnel and the LDV system. The tests were conducted at a freestream velocity of 20 m/s for the maximum force and force reduction ride heights ($h/d =$ 0.191 and 0.153). The uncertainties at a 95% confidence level indicate that 50% of the velocity measurements points had an error smaller than 1% and the remainder had an error below 8%. Details of the experimental errors and uncertainties are presented in Appendix A and were calculated as described by Knowles (2005), Saddington et al. (2007) and Correia (2015) who all carried out similar LDV experiments in the same wind tunnel as used in this present study. Figures 3–12, 3–13a, and 3–13b show the experimental setup of the LDV tests while Table 3–3 and 3–4 presents tabular details of the LDV test

cases. The system settings used in the LDV experiments are shown in the computer screenshots in Appendix C.

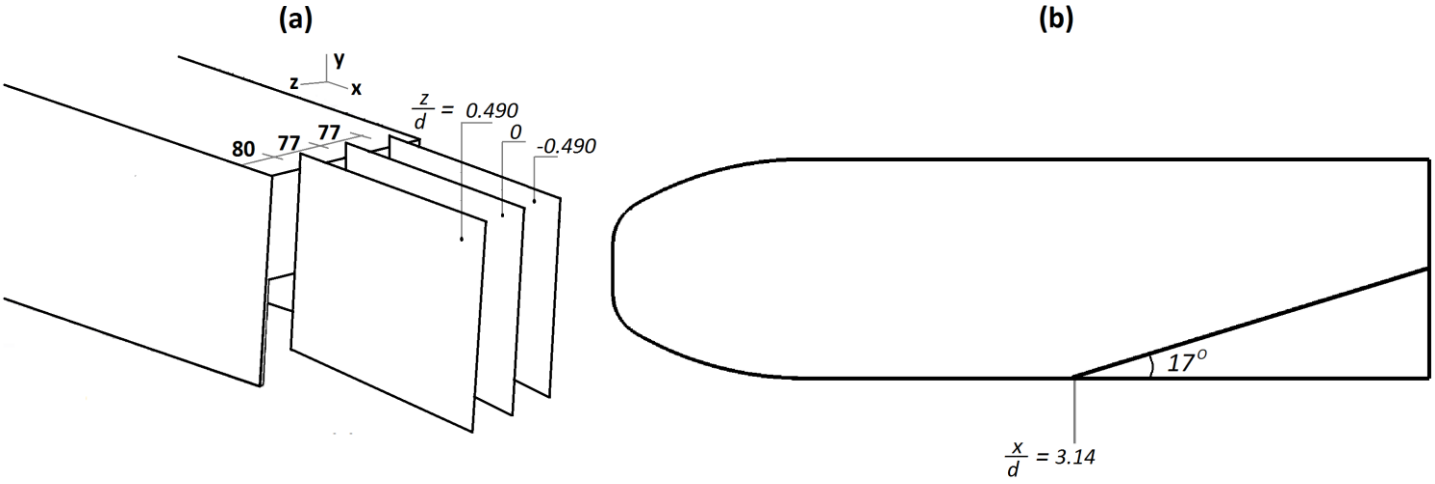

Figure 3-11: Schematics of LDV measurement planes and locations showing: **(a)** Measurement planes behind diffuser near-wake in isometric view (dimensions in mm) and **(b)** Underbody boundary layer measurement location

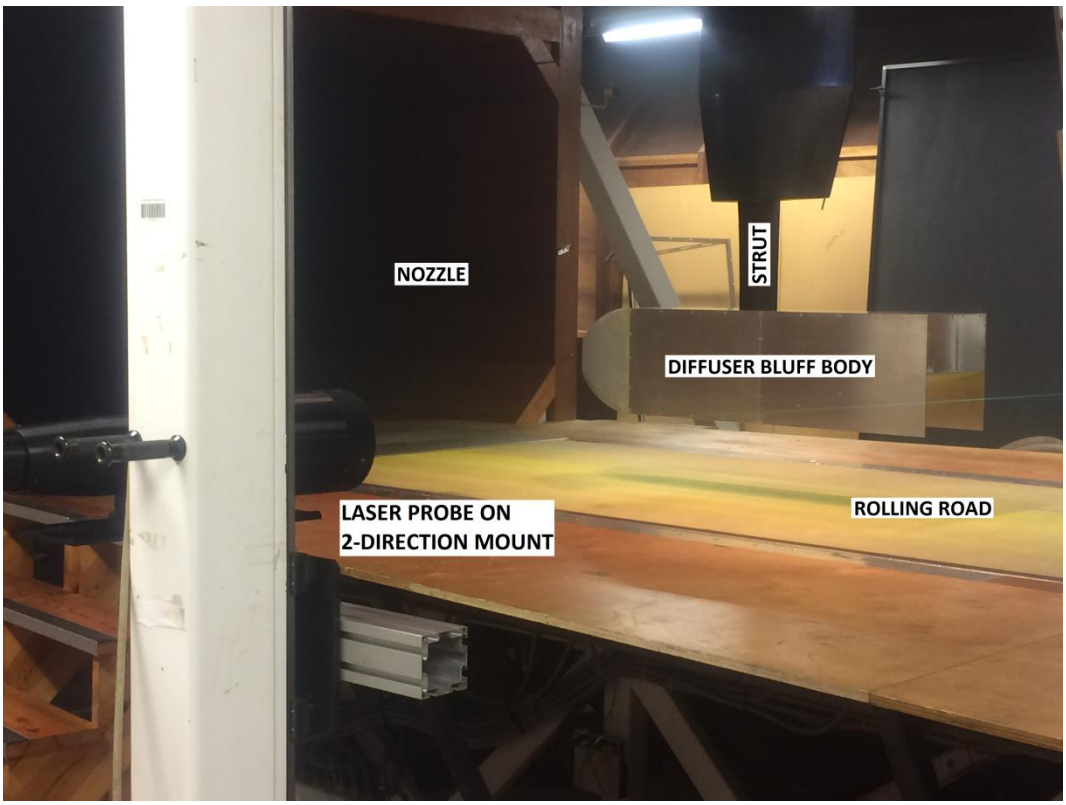

Figure 3-12: Photograph of diffuser bluff body and LDV probe on traverse mount

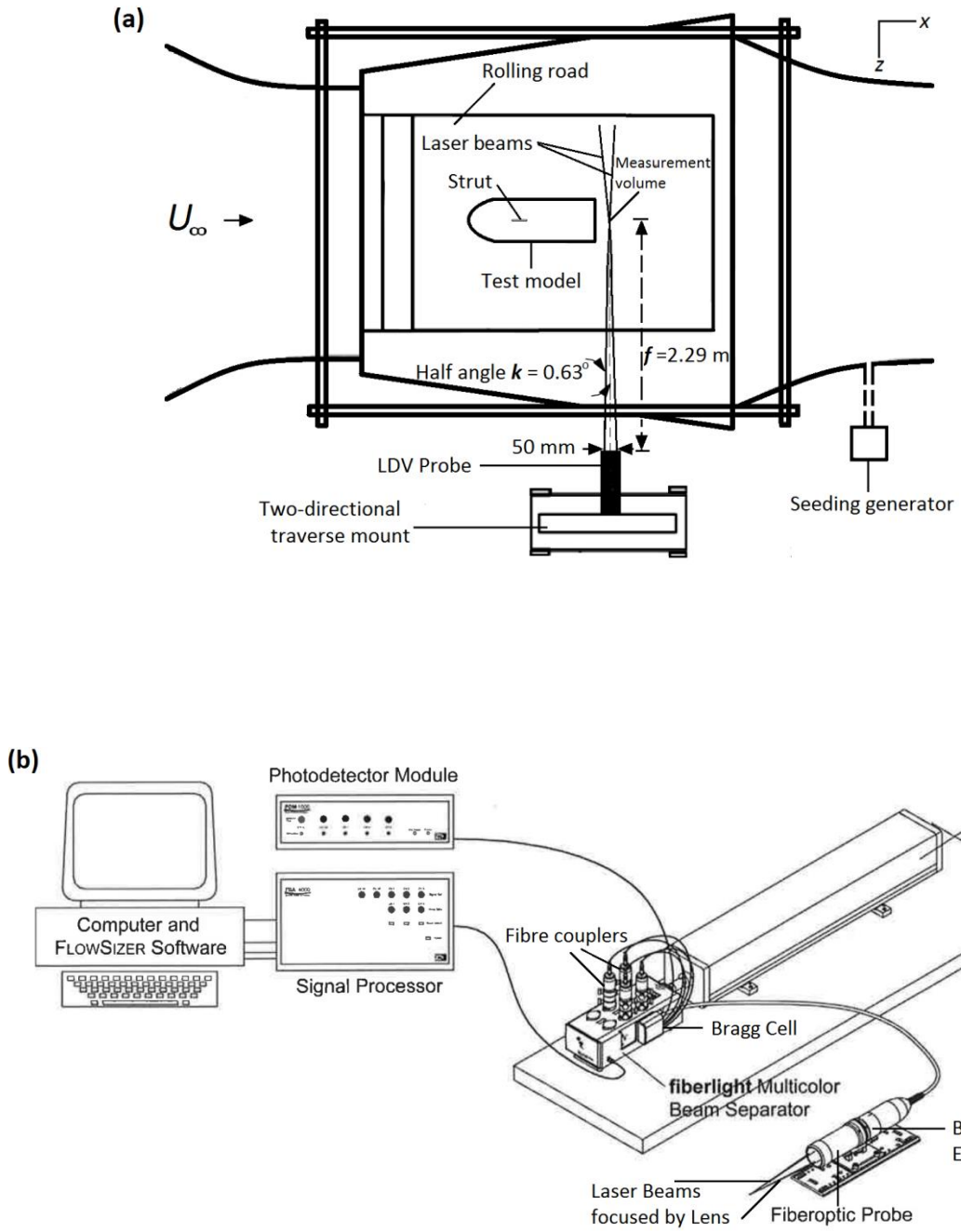

Figure 3-13: Details of experimental laser velocimetry setup: **(a)** Top view schematic of wind tunnel working section with LDV probe, traverse and seeding generator **(b)** Schematic of LDV system components (adapted from TSI LDV system manual)

3.3 Computational Set-up and Techniques

As a means of providing further understanding of the complex diffuser flow physics, equivalent investigations were done using computational fluid dynamics (CFD). Computational fluid dynamics provides a more detailed solution than experimental investigations. This means that a relatively simple computational solution provides more details of the flow physics to analyse than a similar experiment in the wind tunnel.

Thus, CFD investigations using a combination of Reynolds-Averaged Navier Stokes (RANS) modelling and the more advanced Detached Eddy Simulation (DES) modelling were employed to compare with wind tunnel results. The CFD studies were implemented for five ride heights from the range of thirty five ride heights investigated in the wind tunnel. It is worth noting that though CFD solutions produce a detailed flow solution, the computational cost and time can be expensive. The selection of ride heights investigated with CFD (in Table 3–2) includes two ride heights from the force enhancement flow regime ($h/d = 0.764$ and 0.382), the maximum downforce ride height ($h/d = 0.191$), and a single ride height each from the force reduction and low downforce flow regimes ($h/d = 0.151$ and 0.064). The computational work for this research project was done on the DELTA High Performance Computing (HPC) facility at Cranfield University and subsequent sections in this chapter provide details of the CFD methodology employed in this research work.

3.3.1 Computational domain and grid

In replicating the test section of the Cranfield University DS Houghton wind tunnel used for the experimental studies, the computational domain for the equivalent CFD studies was setup with use of the tunnel open test section dimensions. The computational domain dimensions as illustrated in Figure 3–14 includes, $2.74\,m$ wide, $1.66\,m$ high and $6\,m$ long. In addition, the CAD geometry of the bluff body model (with length L_B) was positioned in the domain

as shown in Figure 3–14 with a distance of ~$1.50L_B$ in front, ~$2.06L_B$ behind and ~$0.92L_B$ on each side. Surface and volume grids of the computational domain were created with the commercial ANSYS ICEM CFD meshing software (ANSYS 17.2). The grid generated for the domain is hybrid combination of unstructured tetrahedral and prism layers (Figure 3–15). The hybrid grid moderates the expense of CPU time and memory storage. However, hexahedral grids are more aligned (grid uniformity) with the flow than tetrahedral grids. This can lead to computational errors with tetrahedral grids due to numerical diffusion which is dependent on the rate-of-change of grid point spacing. Therefore, large changes in spacing or local mesh resolution in high gradient regions (like boundary layers) can lead to large truncation errors (Thompson et al.,1999).

Despite this, the combination of tetrahedral and prismatic boundary layer cells provides flexibility which enhances the alignment of the mesh with the boundary layer flow. The surface mesh of the bluff body was created by a tessellation of the CAD surface of the body. The *x*-wise surface mesh size on the bluff body was $0.006\,m$ and a maximum *x*-wise volume mesh size of $0.010\,m$ for a 'virtual box' which was created around the model and extends from the inlet to the outlet of the domain. The box, which has a height of $0.689\,m$ (~$0.52L_B$) and width of $0.64\,m$ (~$0.12L_B$ from each side of the bluff body), was created to enhance the resolution of the flow solution by maintaining a dense mesh around the bluff body and along the upstream freestream flow paths and downstream wake. This enabled the reduction of computational cost and time because the cells away from the bluff body model and 'virtual box' had a maximum *x*-wise mesh size of $0.070\,m$ (with a maximum *x*-wise mesh size of $0.050\,m$ for the rest of the moving ground).

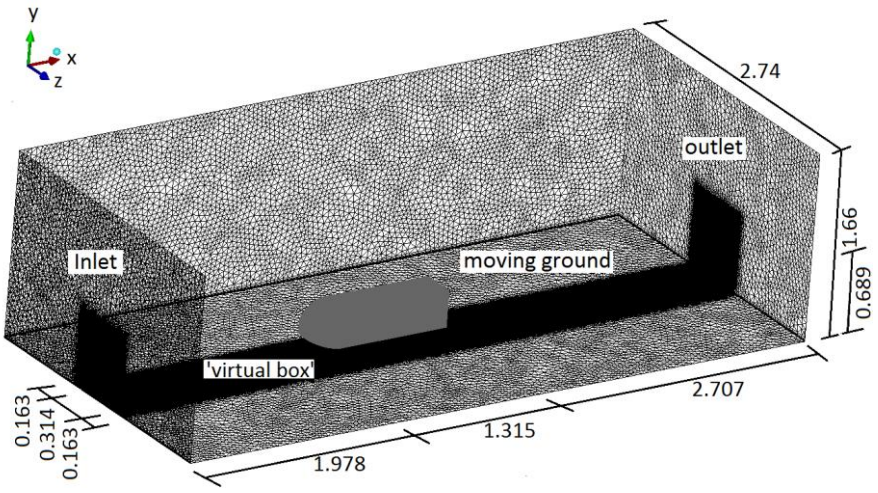

Figure 3-14: The computational domain showing mesh resolution distribution and dimensions in m representing the wind tunnel test section

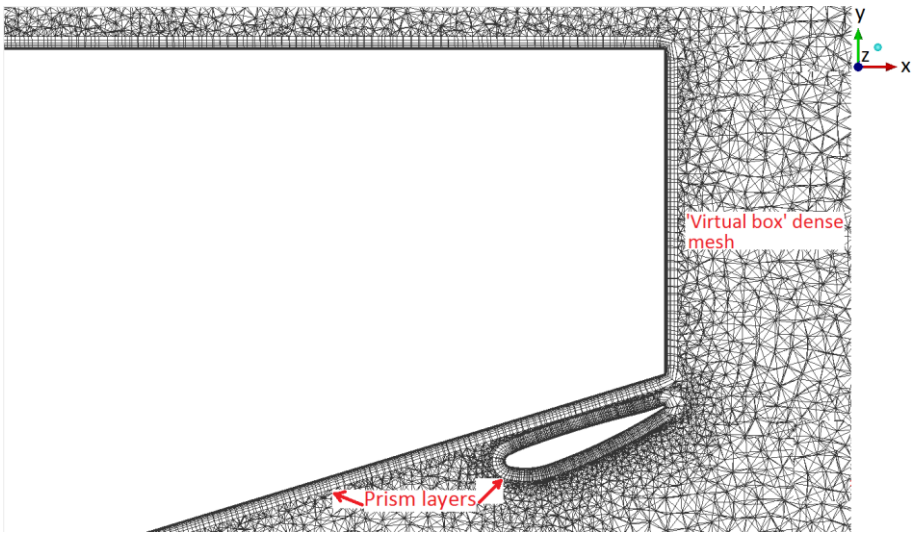

Figure 3-15: A cross section of the computational domain for the bluff body diffuser with a wing showing prismatic cells

The volume mesh of the domain was created from the surface mesh using the Delaunay triangulation, which ensures that the circumcircle associated with each triangle contains no other point in its interior. In addition, it enables a smoother volume transition between two different mesh densities within the domain. After each of the surface and volume generation steps, the mesh was smoothed using a patch-based technique that relies on the cell surface normal to adjust sizes of grid elements beyond a pre-set quality criterion. Boundary

layer flow resolution was enhanced by prism layers generated around the boundary of the model using an iso-parametric method in the wall-normal direction to attain a suitable resolution while also avoiding self-intersection of the elements (Figure 3—15). The computational domain y^+ was within the range $y^+ \leq 1$ and this met the meshing software user requirements. The sensitivity of the grid to C_L values was noticeable between a coarse mesh of ~14 million cells and a fine mesh of ~27 million cells. When the fine mesh was further refined to about ~50 million cells, an imperceptible difference between the C_L values for the fine and refined grid was observed. As a result, the need to conserve computational cost was prioritized and a minimum grid of ~27 million cells across the ride height test cases was used for this study.

Depending on the ride height of the bluff body, the number of prism layers and cell count were from 15 to 33 and 27 million to 40 million respectively with an exponential growth ratio ranging from 1.2 to 1.6. The first prism layer height h_i was estimated using Equations 3.2 to 3.5 as defined in the boundary layer theory (Schlichting, 1999; White, 2011).

$$C_f = 0.0576Re^{1/5} \tag{3.2}$$

$$\tau_w = 0.5C_f \rho U_\infty^2 \tag{3.3}$$

$$U_f = \sqrt{\frac{\tau_w}{\rho}} \tag{3.4}$$

$$h_i = \frac{y^+\mu}{\rho U_f} = 1.2\ x\ 10^{-5}\ m \tag{3.5}$$

Where, C_f is the skin friction coefficient; U_f is the friction velocity and τ_w is the wall shear stress.

The prism height h_n for a given layer number n and height ratio r is defined with the exponential growth law in Equation 3.6 as:

$$h_n = h_i r^{n-1} \tag{3.6}$$

Prism layers were grown exponentially with total prism layer height h_t mathematically defined in the ANSYS ICEM CFD commercial software (ANSYS ICEM 17.2 User Guide) and represented in Equation 3.7 as:

$$h_t = \frac{(r^n - 1)h_i}{(r - 1)} \tag{3.7}$$

3.3.2 Boundary conditions

In addition to replicating the wind tunnel test section dimensions in the computational domain, the test conditions were also reproduced within the domain. The upstream boundary was defined as the velocity inlet with a $20\ m/s$ ($Re \approx 1.8 \times 10^6$) freestream velocity. The downstream boundary was specified as a pressure outlet with a $0\ Pa$ gauge pressure. In addition, a $0.01\ m$ turbulence length scale, which corresponded to ~0.3% turbulence intensity of the wind tunnel, was specified for both the velocity inlet and pressure outlet. As a means of simulating the moving ground of the wind tunnel, a no-slip moving wall condition with a translational velocity of $20\ m/s$ was specified for the ground boundary of the domain. The surface of the bluff body within the domain was defined as a stationary wall with a no-slip condition. The surrounding boundaries (top and side walls of the domain) were defined as symmetry boundary condition slip walls (to represent the open test section of the wind tunnel). This boundary condition incorporates a zero normal velocity and zero normal gradients of all variables on the boundary. As a result, boundary layer development is mitigated and a steady static pressure is maintained on the boundary.

3.3.3 Numerical methods

The implicit pressure-based solver using the 3–D finite volume method was employed to solve the incompressible flow within the computational

domain. Initial SRANS simulations were done for the ride heights (h/d = 0.764, 0.382, 0.191, 0.153, 0.064) presented in this research. The standard κ—ω SST turbulence model (Menter,1994) was employed for the force enhancement flow regimes of $h/d = 0.784$ and 0.382; the γ–Re_θ (Gamma – Re Theta) transition SST turbulence model (Menter et al., 2006; Langtry & Menter, 2009) was used for the force reduction flow regime ($h/d = 0.153$). However, the k–kl–ω transition model (Walters & Cokljat, 2008) was employed for the maximum force flow regime ($h/d = 0.191$) and the low force flow regime ($h/d = 0.064$). The transition turbulence models were used to capture the separation bubble at the region of laminar-turbulent transition located about 0.3 m from the leading edge of the bluff body's nose section. This separation bubble becomes dominant in defining the surface/off-surface flow structure and pressure distribution of the diffuser ramp located downstream. As a result, the standard $\kappa - \omega$ SST becomes ineffective in correlating comparative wind tunnel experiments for ride heights from the maximum force flow regime ride height and below. Convective and viscous terms of the SRANS turbulence models were discretized using the second-order upwind scheme. In addition, the pressure term spatial discretization was implemented with the standard interpolation scheme. The Green-Gauss node-based scheme was applied in computing cell gradients with the SIMPLE algorithm employed in coupling the pressure-velocity fields.

Time-averaged solutions using URANS and IDDES methodologies were computed from the converged SRANS solutions. The IDDES approach was employed with SRANS solutions for ride heights h/d = 0.784, 0.382 and 0.153, while URANS was employed with the transition turbulence models for ride heights $h/d = 0.191$ and 0.064. The URANS and IDDES computations were implemented using the bounded central differencing scheme for the momentum terms. However, the second-order scheme was employed for temporal discretization and the pressure term made use of the standard interpolation scheme. Cell gradients were computed using the Green-Gauss

node-based scheme with the bounded second-order implicit method used for the transient formulation. Pressure-velocity fields were coupled using the PISO scheme with a factor of 1 for both the neighbour and skewness mesh correction factors. This was implemented to satisfy the corrected velocities of the momentum and continuity equations and to mitigate convergence difficulties.

3.3.4 Governing equations

The computational simulations were done using the ANSYS Fluent solver (ANSYS Fluent 17.2). The κ–ω SST turbulence model used in modelling the diffuser force-enhancement flow regime ($h/d = 0.784$ and 0.382), performs adequately in adverse pressure gradients and in separated flows. This is because it was developed by Menter (1994) to employ the fundamental κ–ω formulation (Wilcox, 1988) in the inner boundary layer region (viscous sub-layer) and interchanges to the standard κ—ε model (Launder & Spalding, 1972) in the outer boundary layer and in free shear flow. Also, a modification to its eddy-viscosity definition allows it to account for the turbulent shear stress. The two-equation eddy-viscosity transport governing formulations are given in Equations 3.8 and 3.9 as:

$$\frac{\partial(\rho k)}{\partial t} + \frac{\partial(\rho u_j k)}{\partial x_j} = \tau_{ij}\frac{\partial u_i}{\partial x_j} - \beta^* \rho\omega k + \frac{\partial}{\partial x_j}\left[(\mu + \sigma_k \mu_t)\frac{\partial k}{\partial x_j}\right] \tag{3.8}$$

$$\frac{\partial(\rho\omega)}{\partial t} + \frac{\partial(\rho u_j \omega)}{\partial x_j} = \frac{\gamma_s}{\nu_t}\tau_{ij}\frac{\partial u_i}{\partial x_j} - \beta\rho\omega^2 + \frac{\partial}{\partial x_j}\left[(\mu + \sigma_\omega \mu_t)\frac{\partial \omega}{\partial x_j}\right]$$

$$+2(1 - F_1)\frac{\rho\sigma_{\omega_2}}{\omega}\frac{\partial k}{\partial x_j}\frac{\partial \omega}{\partial x_j} \tag{3.9}$$

With x_i and x_j defined as directional tensors, u_i and u_j are the ensemble-averaged velocity tensors, μ_t is the dynamic turbulent viscosity ν_t is the kinematic eddy-viscosity, σ is a closure coefficient, k is the turbulent kinetic

energy, γ_s is the specific heat ratio, ω is the specific dissipation rate, τ_{ij} is the viscous stress tensor, F_1 is a blending function, β^* and β are constants.

In modelling the force-reduction diffuser flow regime ($h/d = 0.153$), the dominance of the laminar-turbulent transition upstream of the diffuser inlet in dictating the flow behaviour within the diffuser was taken into account. As a result, the natural transition of the flow, at $h/d = 0.153$, was modelled using the γ–Re_θ (Gamma-Re Theta) transition SST turbulence model. The transition model, developed by Menter et al. (2006), determines the onset of transition with a combination of experimental correlations and locally formulated transport equations. As a means of modelling the natural transition, two transport equations for intermittency γ and the transitional momentum thickness Reynolds number Re_θ are coupled with the transport formulations of the κ—ω SST model.

The intermittency function is employed to trigger the turbulent kinetic energy production term downstream of the boundary layer transition point. The intermittency factor also determines the percentage of time the flow is turbulent with a factor of 1 signifying a fully turbulent flow and 0 for a fully laminar flow. For the simulations at $h/d = 0.153$, an intermittency factor of 0.46 was employed because it was observed that the lateral location of the asymmetric diffuser flow features at that ride height was dependent on the intermittency factor. In addition, the Re_θ transport formulation captures the non-local influence of the turbulence intensity as the decay of turbulent kinetic energy and change in the free stream velocity outside the boundary layer alters the turbulence intensity. The Re_θ also connects the empirical correlation to the onset criteria of the intermittency formulation – enabling the use of the model on general geometries such as aerofoils. The governing equations for intermittency γ and the transitional momentum thickness Reynolds number Re_θ are presented in Equations 3.10 to 3.14.

Intermittency equation:

$$\frac{\partial(\rho\gamma)}{\partial t} + \frac{\partial(\rho U_j\gamma)}{\partial x_j} = P_\gamma - E_\gamma + \frac{\partial}{\partial x_j}\left[\mu + \left(\mu + \frac{\mu_i}{\sigma_f}\right)\frac{\partial\gamma}{\partial x_j}\right] \tag{3.10}$$

With transition source terms P_γ and the destruction/re-laminarization term E_γ defined as:

$$P_\gamma = F_{length}c_{a2}\rho S_r[\gamma F_{onset}]^{0.5}(1 - c_{e1}\gamma) \tag{3.11}$$

$$E_\gamma = c_{a2}\rho\Omega\gamma F_{turb}(c_{e1}\gamma - 1) \tag{3.12}$$

Where, S_r is the strain rate magnitude; F_{length} is an empirical correlation for the transition region length; F_{onset} defines the onset location of transition and Ω is the magnitude of vorticity.

The transition momentum thickness Reynolds number ($\overline{Re_{\theta t}}$) transport equation is expressed in Equation 3.13 as follows:

$$\frac{\partial(\rho\overline{Re_{\theta t}})}{\partial t} + \frac{\partial\left(\rho U_J\overline{Re_{\theta t}}\right)}{\partial x_j} = P_{\theta t} + \frac{\partial}{\partial x_J}\left[\sigma_{\theta t}(\mu + \mu_t)\frac{\partial\overline{Re_{\theta t}}}{\partial x_j}\right] \tag{3.13}$$

The $P_{\theta t}$ serves as a source term for forcing scalar $\overline{Re_{\theta t}}$ transported to match the local value of $Re_{\theta t}$ calculated from an empirical correlation and is expressed in Equation 3.14 as:

$$P_{\theta t} = c_{\theta t}\frac{\rho}{t}(Re_{\theta t} - \overline{Re_{\theta t}})(1 - F_{\theta t}) \tag{3.14}$$

Where, t is a time scale that is scaled to the transport equation's convective and diffusive terms; $F_{\theta t}$ is the switching function to turn off the source term in the boundary layer, with $F_{\theta t} = 0$ in the freestream and $F_{\theta t} = 1$ in the boundary layer.

The diffuser flows for the maximum-force ride height, $h/d = 0.191$ and the low-downforce ride height, $h/d = 0.064$ were modelled using the k–kl–ω transition model. This turbulence model required a $y^+ \leq 0.1$ (with first prism layer height $h_i = 1.7\,x\,10^{-6}\,m$ see Equation 3.5) to fully resolve the boundary

layer, transition location and adequately capture the lateral location of the symmetric and asymmetric diffuser flow features at $h/d = 0.191$ and $h/d = 0.064$ respectively. The transition process of the k–kl–ω turbulence model as defined by Walters and Cokljat (2008) is based on the transfer of laminar kinetic energy to turbulent kinetic energy. The laminar kinetic energy k_L is the energy from streamwise fluctuations (or Klebanoff modes as described by Klebanoff, 1971) in the pre-transitional boundary layer of the flow. The turbulent kinetic energy k_T represents the energy of fluctuations that exhibit behaviours of a fully turbulent flow such as considerable viscous dissipation, multiple length and timescales. When a shift in mean velocity boundary layer profile is followed by the growth of high amplitude fluctuations with an increase in skin friction and heat transfer, a transition through the breakdown of the fluctuations indicates the occurrence of bypass transition.

In the k–kl–ω transition model, the pressure-strain terms during the transition process represent the growth in strength of the turbulence fluctuations with a reduction in magnitude of the pre-transitional streamwise fluctuations. Hence, the action of the pressure terms denotes the energy transfer from laminar kinetic energy to turbulent kinetic energy. The onset of bypass transition is determined when the time-scale ratio (of turbulence production time-scale/molecular diffusion time-scale) is at a critical value. However, the criterion for the onset of natural transition is determined as a function of the ratio of Tollmien-Schlicting time-scale to the time-scale of molecular diffusion. The governing transport equations representing the turbulent kinetic energy k_T, laminar kinetic energy k_L and the scaling variable $\omega = \varepsilon/K_T$ (with ε denoting isotropic dissipation) are expressed in Equations 3.15 to 3.17.

Turbulent kinetic energy k_T:

$$\frac{Dk_T}{Dt} = P_{k_T} + R_{BP} + R_{NAT} - \omega_{k_T} - D_T + \frac{\partial}{\partial x_j}\left[\left(\nu + \frac{\alpha_T}{\sigma_k}\right)\frac{\partial k_T}{\partial x_j}\right] \qquad (3.15)$$

Laminar kinetic energy k_L:

$$\frac{Dk_L}{Dt} = P_{k_L} + R_{BP} + R_{NAT} - D_L + \frac{\partial}{\partial x_j}\left[\nu \frac{\partial k_L}{\partial x_j}\right] \tag{3.16}$$

Scaling variable ω:

$$\frac{D_\omega}{Dt} = C_{\omega 1}\frac{\omega}{k_T}P_{k_T} + \left(\frac{C_{\omega R}}{f_W} - 1\right)\frac{\omega}{k_T}(R_{NAT} + R_{NAT}) - C_{\omega 2}\omega^2 + C_{\omega 3}f_\omega \alpha_T f_W^2 \frac{\sqrt{k_T}}{d^3}$$

$$+ \frac{\partial}{\partial x_j}\left[\left(\nu \frac{\alpha_T}{\sigma_k}\right)\frac{\partial_\omega}{\partial x_j}\right] \tag{3.17}$$

Where P_{k_L} and P_{k_T} are production terms for laminar and turbulent kinetic energies respectively. R_{BP} and R_{NAT} are model terms for bypass and natural transition respectively. D_L and D_T are near-wall dissipation terms respectively. f_W represents the damping function, α_T is the effective diffusivity while $C_{\omega 1}, C_{\omega 2}, C_{\omega 3}$ are model constants.

For the ride height cases ($h/d = 0.191$ and $h/d = 0.064$) modelled using the k–kl–ω turbulence model, time-averaged simulations were done by initializing the URANS transient mode of the ANSYS Fluent solver. However time-averaged simulations for the force-enhancement ride heights $h/d = 0.784$, 0.382 and the force-reduction ride height $h/d = 0.153$ were implemented using the Improved Delayed Detached Eddy Simulation (IDDES) approach. The standard DES methodology involves the use of a hybrid RANS/LES approach to compute near-wall regions of the flow with RANS and the far-wall flow regions with LES (Spalart, 1997; 2000). However, the standard DES has a tendency to quickly trigger transition to LES mode in regions that require RANS. The Delayed-DES (DDES) methodology was designed as a modification of the standard DES and it includes blending functions in the governing formulations of the κ—ω SST turbulence model to curtail the quick transition to LES mode in the boundary layer region (Spalart, 2006). However, the DDES methodology produces log-layer mismatch anomalies along boundaries between the RANS and LES regions. As a result, the Improved Delayed

Detached Eddy Simulation (IDDES), which combines the strengths of DDES and the wall-modelled LES, was developed with the inclusion of empirical and elevating functions to curb log-layer mismatch and grid-induced separation (Shur et al., 2008; Spalart, 2009). The governing equations for the IDDES as developed from the $\kappa-\omega$ SST turbulence model are defined in Equations 3.18 and 3.19 as:

$$\frac{\partial(\rho k)}{\partial t}+\frac{\partial\left(\rho u_j k\right)}{\partial x_j}=\frac{\partial}{\partial x_j}\left[\left(\mu+\sigma_k\mu_t\right)\frac{\partial k}{\partial x_j}\right]+P_k-\frac{\rho\sqrt{k^3}}{l_{IDDES}} \tag{3.18}$$

$$\frac{\partial(\rho\omega)}{\partial t}+\frac{\partial\left(\rho u_j\omega\right)}{\partial x_j}=\frac{\partial}{\partial x_j}\left[\left(\mu+\sigma_\omega\mu_t\right)\frac{\partial\omega}{\partial x_j}\right]+2(1-F_1)\frac{\rho\sigma_{\omega_2}}{\omega}\frac{\partial k}{\partial x_j}\frac{\partial\omega}{\partial x_j}$$
$$+\alpha_3\frac{\rho}{\mu_t}P_k-\beta\rho\omega^2 \tag{3.19}$$

The grid scale Δ is defined in Equation 3.20 as:

$$\Delta=min\{C_\omega\ \max[d_\omega,h_{max}],h_{max}\} \tag{3.20}$$

Where α_3 in Equation 3.19 is defined as in Equation 3.21:

$$\alpha_3\ =0.25-\frac{d_\omega}{h_{max}} \tag{3.21}$$

With the empirical constant C_{DES} expressed in Equation 3.22 as:

$$C_{DES}=C_{DES1}\cdot F_1+C_{DES2}\cdot(1-F_1) \tag{3.22}$$

Then IDDES length scale l_{IDDES} in Equation (3.18) includes the empirical blending function $\check{f}_d$ and elevating function f_e to mitigate log-layer mismatch and is defined in Equations 3.23 to 3.25 as follows:

$$l_{LES}=C_{DES}\Delta \tag{3.23}$$

$$l_{RANS} = \frac{\sqrt{k}}{C_\mu \omega} \tag{3.24}$$

$$l_{IDDES} = \tilde{f}_d \cdot (1 + f_e) \cdot l_{RANS} + \left(1 - \tilde{f}_d\right) \cdot l_{LES} \tag{3.25}$$

With d_ω designated as the distance to the nearest wall and h_{max} is the maximum edge length of the cell; P_k is a production term, and C_μ, C_ω, C_{DES1}, C_{DES2} are model constants. In addition, when $f_e = 0$, IDDES reverts to DDES and the IDDES length scale is simplified as $l_{IDDES} = \tilde{f}_d \cdot l_{RANS} + \left(1 - \tilde{f}_d\right) \cdot l_{LES}$. A detailed formulation of IDDES is presented in Shur et al. (2008).

3.3.5 Simulation procedure

The SRANS simulations were initialized from the inlet and computed over 10,000 iterations with solution convergence achieved as the residuals reach a magnitude $\leq 10^{-5}$ (Figure 3–16). Subsequent transient simulations using the URANS and IDDES methodologies were initiated with corresponding SRANS solutions. The time-step Δ_t used in the time-averaged computations was estimated using the guidelines established by Spalart (2001) in which the minimum time-step Δ_{tmin} was employed as the time-step and is calculated for a given freestream velocity U_∞ and smallest *x*-wise grid size Δ_x as defined in Equation 3.26 as:

$$\Delta_{tmin} \approx \frac{\Delta_x}{1.5 U_\infty} \tag{3.26}$$

Hence, with $\Delta_x = 0.006\, m$ for the baseline bluff body diffuser and bluff body diffuser with a convex bump and $\Delta_x = 0.001\, m$ for the bluff body diffuser with a wing and diffuser with both the bump and wing, the time step at $U_\infty = 20\, m/s$ was calculated to be $2.0\, x\, 10^{-4}\, s$ and $3.33\, x\, 10^{-5}\, s$ respectively. Furthermore, convergence of the numerical approximations of the finite volume partial differential equations was achieved by meeting the ANSYS

Fluent solver's Courant–Friedrichs–Lewy (CFL) number criterion of $CFL \leq 1$. Where CFL is expressed in Equations 3.27 and 3.28 as:

For baseline diffuser and diffuser with convex bump using $\Delta_x = 0.006\, m$:

$$CFL \approx \frac{U_\infty \Delta_t}{\Delta_x} = 0.67 \tag{3.27}$$

For diffuser with wing and diffuser with both bump and wing using $\Delta_x = 0.001\, m$:

$$CFL \approx \frac{U_\infty \Delta_t}{\Delta_x} = 0.4 \tag{3.28}$$

For the transient URANS and IDDES simulations, the number of iterations determines the total simulation time (i.e. total simulation time = number of iterations **x** time step Δ_t). Hence estimating the total time for time-averaging was guided by the methodology described by Bruun (1995) and Romano et al. (2007) where the autocorrelation coefficient was calculated to ascertain the integral time scale with a 95% confidence level. However, constraints in computational cost (computational capacity and time) on a computing cluster was also considered. Therefore the total simulation time for the various diffuser body test geometries was implemented based on the time it takes the transient simulations to reach a pseudo-steady state. Time histories for lift, drag and pressure coefficients were individually collated during the simulations and averaged across the pseudo-steady part (i.e. when the flow has become fully developed) of their respective time histories. However, other physical quantities of the flow were averaged across the total simulation time.

The incompressible flow required a total simulation time of 6 s to fully develop and this equates to 30,000 time-step iterations for the bluff body diffuser baseline and the bluff body diffuser with a convex surface. For the case of the bluff body diffuser with a wing, the total simulation time was 3 s requiring 90,091 time-step iterations. However, for all cases, coefficients of lift and drag convergence was achieved within three decimal places and within 20 sub-iterations. Over the course of the total flow simulation time, a flow particle

travelling the length of the bluff body at freestream velocity completes 300 passes for the baseline diffuser and convex surface diffuser, and 900 passes for the diffuser with a wing. A single pass is completed after 100 iterations and after a pseudo-steady state is reached by the end of the transient flow simulations, statistical data (mean) were then collated for lift, drag and surface pressure coefficients with averaging done after 10 passes. The average time taken to complete each transient simulation was about 140 hours using 256 Giga Bytes of memory on the DELTA high performance computing (HPC) cluster at Cranfield University.

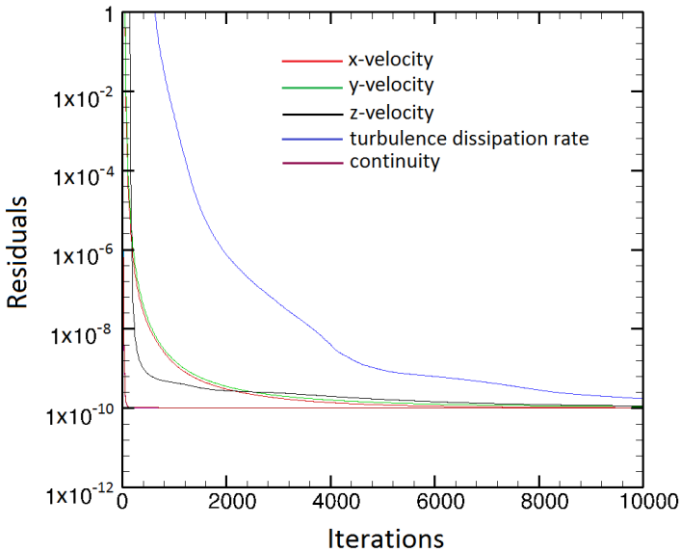

Figure 3-16: Convergence of SRANS residuals over 10,000 iterations

Table 3-1: Force measurements test cases (B = baseline; C = with convex bump; W = with wing; C&W = with convex bump and wing)

h/d	Diffuser bluff body diffuser type	Reynolds number (Re)	Ground Condition	Transition
0.064	B, C, W	$1.35\ x\ 10^6$	Moving	Free
0.064	B, C, W, C&W	$1.80\ x\ 10^6$	Stationary/Moving	Free/Fixed
0.064	B, C W	$2.25\ x\ 10^6$	Moving	Free
0.076	B, C, W	$1.35\ x\ 10^6$	Moving	Free
0.076	B, C, W, C&W	$1.80\ x\ 10^6$	Stationary/Moving	Free/Fixed
0.076	B, C W	$2.25\ x\ 10^6$	Moving	Free
0.089	B, C, W	$1.35\ x\ 10^6$	Moving	Free
0.089	B, C, W, C&W	$1.80\ x\ 10^6$	Stationary/Moving	Free/Fixed
0.089	B, C W	$2.25\ x\ 10^6$	Moving	Free

0.102	B, C, W	$1.35\ x\ 10^6$	Moving	Free
0.102	B, C, W, C&W	$1.80\ x\ 10^6$	Stationary/Moving	Free/Fixed
0.102	B, C W	$2.25\ x\ 10^6$	Moving	Free
0.115	B, C, W	$1.35\ x\ 10^6$	Moving	Free
0.115	B, C, W, C&W	$1.8\ 0x\ 10^6$	Stationary/Moving	Free/Fixed
0.115	B, C W	$2.25\ x\ 10^6$	Moving	Free
0.127	B, C, W	$1.35\ x\ 10^6$	Moving	Free
0.127	B, C, W, C&W	$1.80\ x\ 10^6$	Stationary/Moving	Free/Fixed
0.127	B, C W	$2.25\ x\ 10^6$	Moving	Free
0.140	B, C, W	$1.35\ x\ 10^6$	Moving	Free
0.140	B, C, W, C&W	$1.80\ x\ 10^6$	Stationary/Moving	Free/Fixed
0.140	B, C W	$2.25\ x\ 10^6$	Moving	Free
0.153	B, C, W	$1.35\ x\ 10^6$	Moving	Free
0.153	B, C, W, C&W	$1.80\ x\ 10^6$	Stationary/Moving	Free/Fixed
0.153	B, C W	$2.25\ x\ 10^6$	Moving	Free
0.166	B, C, W	$1.35\ x\ 10^6$	Moving	Free
0.166	B, C, W, C&W	$1.80\ x\ 10^6$	Stationary/Moving	Free/Fixed
0.166	B, C W	$2.25\ x\ 10^6$	Moving	Free
0.172	B, C, W	$1.35\ x\ 10^6$	Moving	Free
0.172	B, C, W, C&W	$1.80\ x\ 10^6$	Stationary/Moving	Free/Fixed
0.172	B, C W	$2.25\ x\ 10^6$	Moving	Free
0.178	B, C, W	$1.35\ x\ 10^6$	Moving	Free
0.172	B, C, W, C&W	$1.80\ x\ 10^6$	Stationary/Moving	Free/Fixed
0.172	B, C W	$2.25\ x\ 10^6$	Moving	Free
0.185	B, C, W	$1.35\ x\ 10^6$	Moving	Free
0.185	B, C, W, C&W	$1.80\ x\ 10^6$	Stationary/Moving	Free/Fixed
0.185	B, C W	$2.25\ x\ 10^6$	Moving	Free
0.191	B, C, W	$1.35\ x\ 10^6$	Moving	Free
0.191	B, C, W, C&W	$1.80\ x\ 10^6$	Stationary/Moving	Free/Fixed
0.191	B, C W	$2.25\ x\ 10^6$	Moving	Free
0.197	B, C, W	$1.35\ x\ 10^6$	Moving	Free
0.197	B, C, W, C&W	$1.80\ x\ 10^6$	Stationary/Moving	Free/Fixed
0.197	B, C W	$2.25\ x\ 10^6$	Moving	Free
0.204	B, C, W	$1.35\ x\ 10^6$	Moving	Free
0.204	B, C, W, C&W	$1.80\ x\ 10^6$	Stationary/Moving	Free/Fixed
0.204	B, C W	$2.25\ x\ 10^6$	Moving	Free
0.210	B, C, W	$1.35\ x\ 10^6$	Moving	Free
0.210	B, C, W, C&W	$1.80\ x\ 10^6$	Stationary/Moving	Free/Fixed

0.210	B, C W	$2.25\ x\ 10^6$	Moving	Free
0.217	B, C, W	$1.35\ x\ 10^6$	Moving	Free
0.217	B, C, W, C&W	$1.80\ x\ 10^6$	Stationary/Moving	Free/Fixed
0.217	B, C W	$2.25\ x\ 10^6$	Moving	Free
0.229	B, C, W	$1.35\ x\ 10^6$	Moving	Free
0.229	B, C, W, C&W	$1.80\ x\ 10^6$	Stationary/Moving	Free/Fixed
0.229	B, C W	$2.25\ x\ 10^6$	Moving	Free
0.242	B, C, W	$1.35\ x\ 10^6$	Moving	Free
0.242	B, C, W, C&W	$1.80\ x\ 10^6$	Stationary/Moving	Free/Fixed
0.242	B, C W	$2.25\ x\ 10^6$	Moving	Free
0.255	B, C, W	$1.35\ x\ 10^6$	Moving	Free
0.255	B, C, W, C&W	$1.80\ x\ 10^6$	Stationary/Moving	Free/Fixed
0.255	B, C W	$2.25\ x\ 10^6$	Moving	Free
0.271	B, C, W	$1.35\ x\ 10^6$	Moving	Free
0.271	B, C, W, C&W	$1.80\ x\ 10^6$	Stationary/Moving	Free/Fixed
0.271	B, C W	$2.25\ x\ 10^6$	Moving	Free
0.287	B, C, W	$1.35\ x\ 10^6$	Moving	Free
0.287	B, C, W, C&W	$1.80\ x\ 10^6$	Stationary/Moving	Free/Fixed
0.287	B, C W	$2.25\ x\ 10^6$	Moving	Free
0.303	B, C, W	$1.35\ x\ 10^6$	Moving	Free
0.303	B, C, W, C&W	$1.80\ x\ 10^6$	Stationary/Moving	Free/Fixed
0.303	B, C W	$2.25\ x\ 10^6$	Moving	Free
0.318	B, C, W	$1.35\ x\ 10^6$	Moving	Free
0.318	B, C, W, C&W	$1.80\ x\ 10^6$	Stationary/Moving	Free/Fixed
0.318	B, C W	$2.25\ x\ 10^6$	Moving	Free
0.334	B, C, W	$1.35\ x\ 10^6$	Moving	Free
0.334	B, C, W, C&W	$1.80\ x\ 10^6$	Stationary/Moving	Free/Fixed
0.334	B, C W	$2.25\ x\ 10^6$	Moving	Free
0.350	B, C, W	$1.35\ x\ 10^6$	Moving	Free
0.350	B, C, W, C&W	$1.80\ x\ 10^6$	Stationary/Moving	Free/Fixed
0.350	B, C W	$2.25\ x\ 10^6$	Moving	Free
0.366	B, C, W	$1.35\ x\ 10^6$	Moving	Free
0.366	B, C, W, C&W	$1.80\ x\ 10^6$	Stationary/Moving	Free/Fixed
0.366	B, C W	$2.25\ x\ 10^6$	Moving	Free
0.382	B, C, W	$1.35\ x\ 10^6$	Moving	Free
0.382	B, C, W, C&W	$1.80\ x\ 10^6$	Stationary/Moving	Free/Fixed
0.382	B, C W	$2.25\ x\ 10^6$	Moving	Free

0.414 0.414 0.414	B, C, W B, C, W, C&W B, C W	$1.35\ x\ 10^6$ $1.80\ x\ 10^6$ $2.25\ x\ 10^6$	Moving Stationary/Moving Moving	Free Free/Fixed Free
0.446 0.446 0.446	B, C, W B, C, W, C&W B, C W	$1.35\ x\ 10^6$ $1.80\ x\ 10^6$ $2.25\ x\ 10^6$	Moving Stationary/Moving Moving	Free Free/Fixed Free
0.510 0.510 0.510	B, C, W B, C, W, C&W B, C W	$1.35\ x\ 10^6$ $1.80\ x\ 10^6$ $2.25\ x\ 10^6$	Moving Stationary/Moving Moving	Free Free/Fixed Free
0.573 0.573 0.573	B, C, W B, C, W, C&W B, C W	$1.35\ x\ 10^6$ $1.80\ x\ 10^6$ $2.25\ x\ 10^6$	Moving Stationary/Moving Moving	Free Free/Fixed Free
0.637 0.637 0.637	B, C, W B, C, W, C&W B, C W	$1.35\ x\ 10^6$ $1.80\ x\ 10^6$ $2.25\ x\ 10^6$	Moving Stationary/Moving Moving	Free Free/Fixed Free
0.701 0.701 0.701	B, C, W B, C, W, C&W B, C W	$1.35\ x\ 10^6$ $1.80\ x\ 10^6$ $2.25\ x\ 10^6$	Moving Stationary/Moving Moving	Free Free/Fixed Free
0.764 0.764 0.764	B, C, W B, C, W, C&W B, C W	$1.35\ x\ 10^6$ $1.80\ x\ 10^6$ $2.25\ x\ 10^6$	Moving Stationary/Moving Moving	Free Free/Fixed Free

Table 3-2: Surface pressure, surface flow visualisation and CFD test cases

h/d	Diffuser bluff body type	Reynolds number (Re)	Ground Condition	Transition
0.064	Baseline, with convex bump, with wing, with convex bump & wing	$1.80\ x\ 10^6$	Moving	Free
0.153	Baseline, with convex bump, with wing, with convex bump & wing	$1.80\ x\ 10^6$	Moving	Free
0.191	Baseline, with convex bump, with wing, with convex bump & wing	$1.80\ x\ 10^6$	Moving	Free
0.382	Baseline, with convex bump, with wing, with convex bump & wing	$1.80\ x\ 10^6$	Moving	Free
0.764	Baseline, with convex bump, with wing, with convex bump & wing	$1.80\ x\ 10^6$	Moving	Free

Table 3-3: LDV boundary layer profile measurements at diffuser inlet $(x/d = 3.14)$ for baseline diffuser test cases

h/d	Measurement Locations z/d		
0.382	0.363	0	-0.363
0.191	0.363	0	-0.363
0.153	0.363	0	-0.363
0.064	—	0	—

Table 3-4: Diffuser near-wake streamwise plane LDV measurement test cases

h/d	Diffuser bluff body type	Measurement	Planes	z/d
0.153	Baseline	0.490	0	-0.490
0.191	Baseline	0.490	0	-0.490
0.191	With Convex bump	0.490	0	—
0.191	With Wing	0.490	0	—
0.191	With Convex bump & Wing	—	0	—

Chapter 4

Plane Diffuser (Baseline): Forces, Pressures and Flow Characteristics

Characteristic force measurements of the diffuser bluff body model and surface static pressure measurements on the flat underbody, diffuser ramp and base plate sections of the model are presented and discussed in this chapter. In addition, comparative CFD data are also presented as a means of correlating and validating computational modelling of the diffuser flow with experimental wind tunnel results. The analysis of the aerodynamic measurements and behaviour are presented with respect to the four distinct flow regimes as established by previous research on this subject. On-surface flow features captured by surface oil-flow visualisation on the diffuser ramp are also presented to highlight the distinctions among the diffuser flow regimes.

4.1 Diffuser Flow Behaviour and Flow Regime Types

When in proximity to the ground plane, the downforce generated by the diffuser is sensitive to ride height. However, Senior (2002) found that the flow through the diffuser exhibits four different flow regimes ('A', 'B', 'C' and 'D') as ride height is gradually reduced from a high to a low ride height. Senior (2002) classified the flow regimes across the ride height interval as: force enhancement (flow regime A), maximum force (flow regime B), force reduction (flow regime C) and low force (flow regime D).

The four different flow regimes were also discovered in this present study, as the bluff body ride height was gradually reduced from $h/d = 0.764$ to 0.064

(see Figure 4–1). The boundaries between the flow regimes are determined by comparing the rate of change of the downforce and drag curves with on-surface flow visualisation from preliminary investigations using CFD for a more extensive range of ride heights than the five ride heights presented for the experiments. Flow visualisation on either side of the boundaries between regimes A & B and C & D indicates a distinct change in flow behaviour, which corresponds to the points of inflection on the force curves, while the boundary between regimes B and C is at the point of maximum force. Regime A as the force enhancement region is distinguished by a reasonably symmetrical diffuser flow due to the presence of a pair of longitudinal vortices. Regime B is the maximum force region characterised by increased inlet suction and vortex pair size. Regime C is denoted as the force reduction region where the diffuser flow becomes asymmetric, and regime D is classified here as the low downforce region where the asymmetric flow is increasingly dominated by flow recirculation.

These flow characteristics that define the flow regimes are further explained in subsequent sections of this chapter using force curves, static pressure distributions, and flow features on the diffuser ramp surface. The flow regimes of the baseline diffuser with a plane ramp surface of this present study are distinguished from the curves of C_L & C_D and the rate of change of these curves with ride height; these are presented in Figures 4–1a to 4–1d. Also a C_L and C_D comparison with the investigations of Senior (2002) is presented in Figures 4–2a and 4–2b. In this chapter, the four distinct flow regimes are represented by data taken at $h/d = 0.764,\ 0.382,\ 0.191,\ 0.153$ and 0.064 as shown in Figure 4–1.

In this present study, the flow physics of the regimes (in Figures 4–1a and 4–1b) are explained with the coefficient of forces (C_L and C_D); surface pressures (C_p) along the underbody centreline and across the diffuser ramp; and on-surface flow visualisation. Downforce and drag increased as ride height was reduced from $h/d = 0.764$ to 0.318 within flow regime A. However, a

gradient change around $h/d = 0.318$ indicated a transition into flow regime B despite a steady increase in downforce and drag. Moreover, peak downforce and drag are reached at $h/d = 0.191$ after which a distinct sharp drop in both downforce and drag occurred when the ride height was further reduced. This steep drop is as a result of a flow change from regime B to C, and this flow regime terminates around $h/d = 0.127$. Below $h/d = 0.127$, a further drop in both downforce and drag as indicated by the change in slope from $h/d = 0.127$ to the last ride height, $h/d = 0.064$ is defined as the low downforce region (flow regime D).

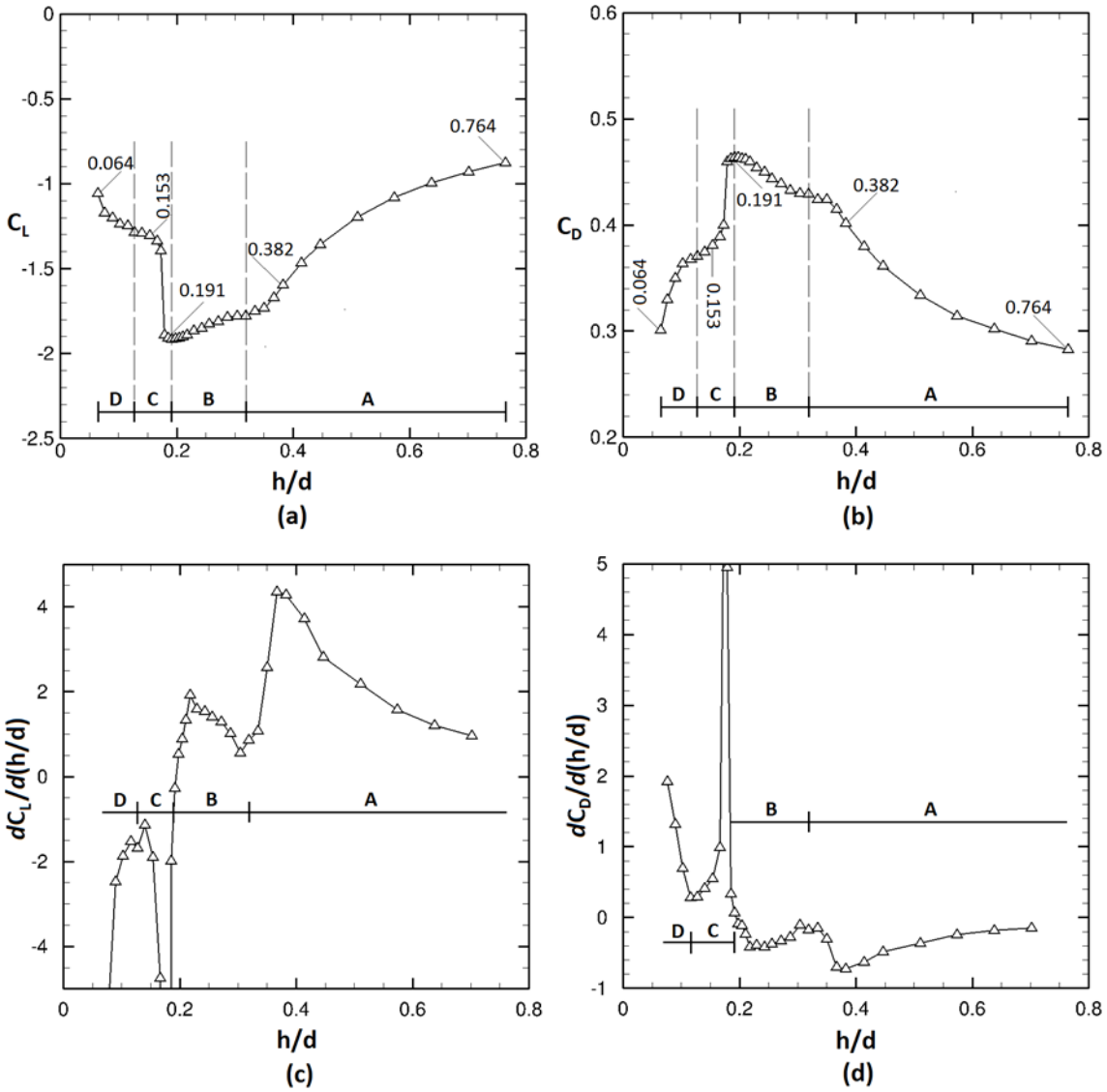

Figure 4-1: Force measurements (wind tunnel) across ride heights ($h/d = 0.764$ to 0.064) and flow regimes ('A' to 'D'): **(a)** lift coefficient **(b)** drag coefficient, **(c)** lift coefficient slope **(d)** drag coefficient slope

As shown in Figures 4–2a and 4–2b, downforce and drag comparison plots of wind tunnel investigations between this present study and that of Senior (2002) indicated a disparity. The diffuser bluff body of Senior (2002) appeared to have generated more downforce and drag respectively across most of the ride heights investigated than the diffuser bluff body used in this present study ($\sim 11.5\%$ more C_L and $\sim 11\%$ more C_D at the highest ride height tested, $h/d = 0.764$). In addition, the maximum downforce and drag occurred at $h/d = 0.21$ and $h/d = 0.191$ for Senior (2002) and the present study respectively. Figures 4–3a and 4–3b indicate that across ride heights, there were deviations between forces measured in the wind tunnel and forces predicted with CFD. The disparities in predicted forces were less profound with time-averaged transient CFD (DES) than with SRANS (κ—ω SST turbulence model) employed by Genua (2009). Senior (2002) reported that maximum downforce and drag varied between $h/d = 0.217$ and 0.210 however, as shown in Figures 4–3a and 4–3b, DES and SRANS predicted the maximum forces at $h/d = 0.217$ and 0.159 respectively. This suggests that the hybrid RANS/LES modes of the DES turbulence modelling method captured the near-wall flow physics and the separated flow region of the diffuser bluff body better than the SRANS κ—ω SST turbulence model.

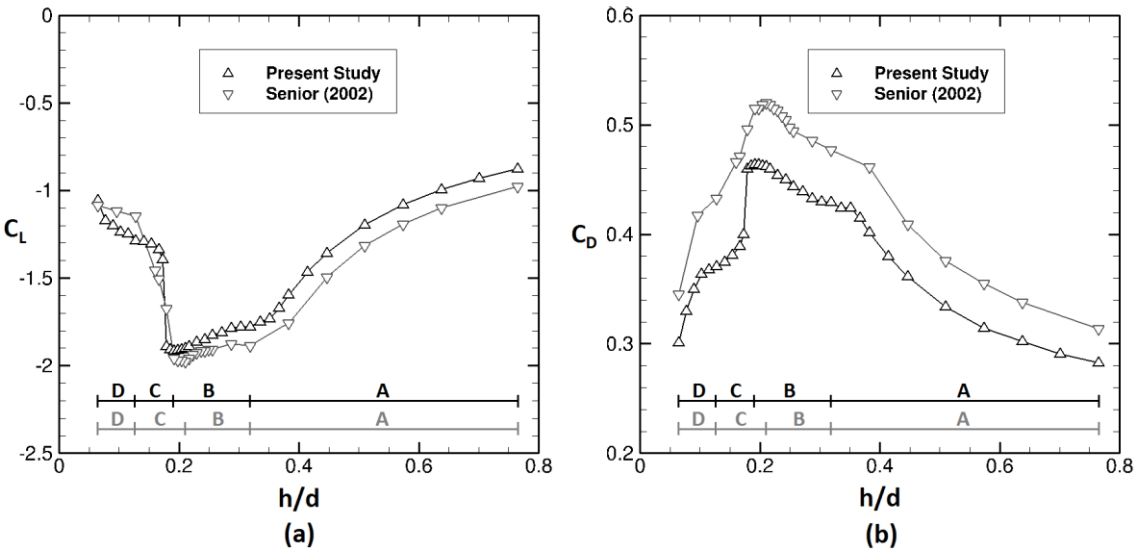

Figure 4-2: Force measurement (wind tunnel) comparison between present study and that of Senior (2002): coefficients of **(a)** lift **(b)** drag

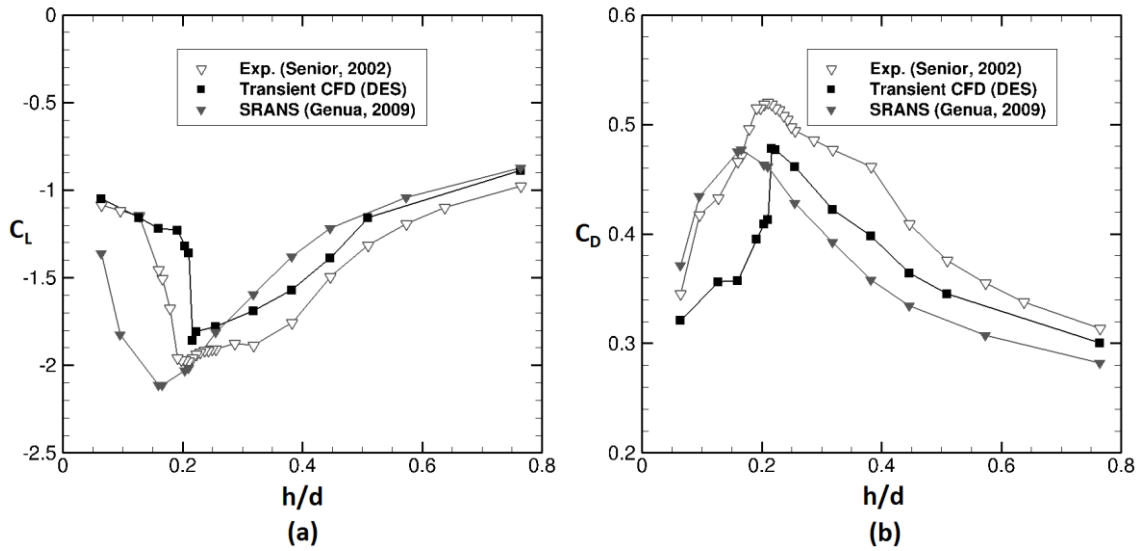

Figure 4-3: Force measurement comparison between Senior (2002) wind tunnel measurements and CFD methods: coefficients of **(a)** lift **(b)** drag

The disparities in experimental C_L and C_D between Senior (2002) and the present study might be attributed to the geometrical differences between the test models of the two studies and the fixed transition implemented by Senior (2002). The fixed transition eliminates the laminar separation bubble on the nose section and the radiused lengthwise corners (see Figure 3–2a) accelerate the underbody flow around the bottom corners of the bluff body thus further lowering underbody pressures. A further difference between the two studies, however, was the use of a closed section wind tunnel (Senior) versus the open test section of the present study. Using the wind tunnel blockage correction method (Maskell, 1963) in Equation 4.1 to estimate the corrected values for the coefficients of downforce and drag $(C_{L_c}$ and $C_{D_c})$ of Senior (2002) reduced the deviation from C_L and C_D values of the present study (Figures 4–4a and 4–4b). As indicated by Senior (2002), wind tunnel corrections were not implemented in the diffuser bluff body study done in a closed test section wind tunnel.

$$\frac{C_D}{C_{D_c}} = \frac{q_c}{q} \tag{4.1}$$

Where, subscript c refers to the corrected values of C_D and the dynamic pressure q.

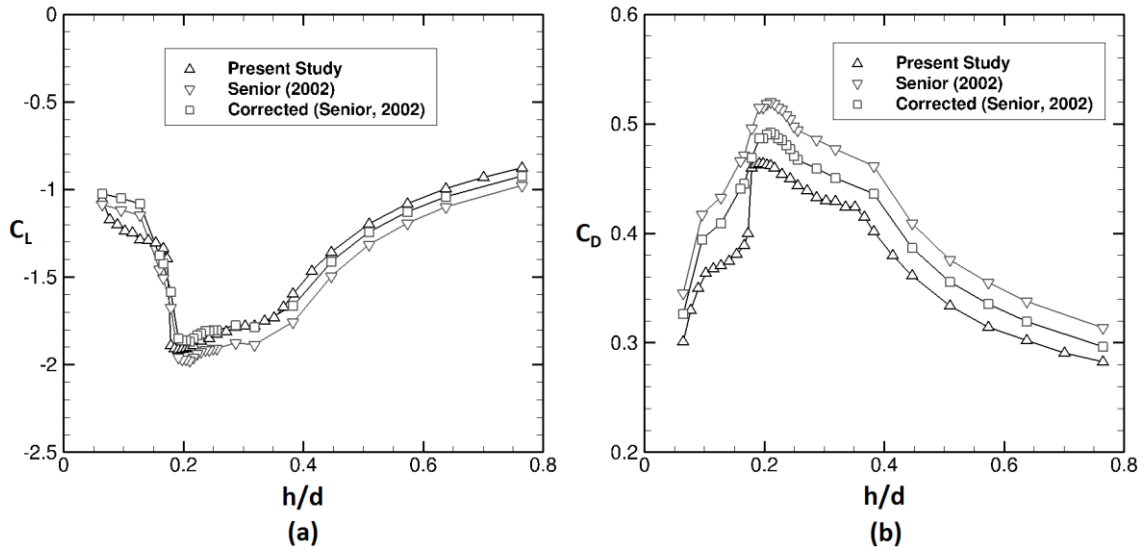

Figure 4-4: Force measurement (wind tunnel) comparison between corrected values from Senior (2002) and present study: coefficients of **(a)** lift **(b)** drag

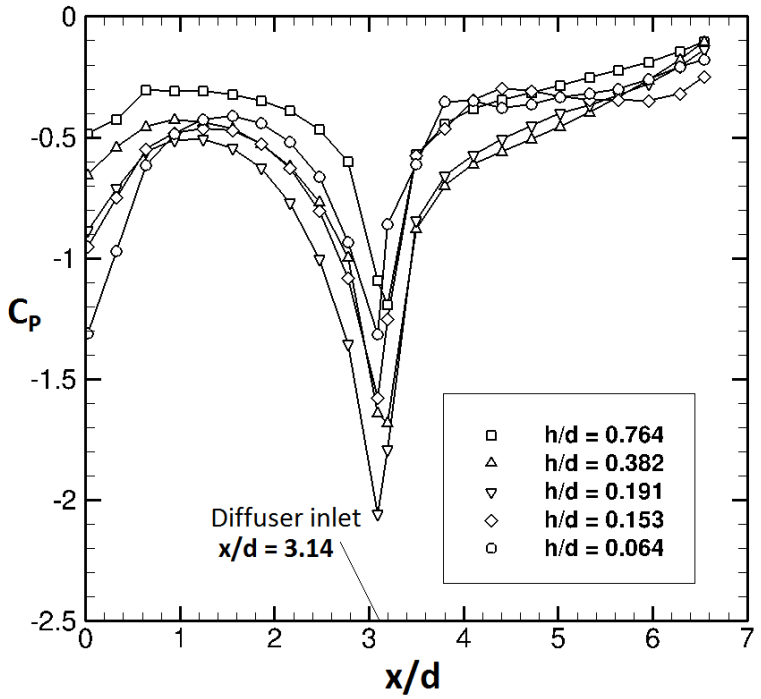

Figure 4-5: Flat underbody and diffuser centreline pressure distribution measurements (wind tunnel) for the ride heights representing the four flow regimes for the present study

The pressure distribution (Figure 4–5) along the underbody centreline for the ride heights from each of the four distinct flow regimes ($h/d = 0.764,\ 0.382,$

0.191, 0.153, and 0.064) indicates the variation of velocity of the flow underneath the diffuser bluff body. The curvature at the start of the underbody causes an increase in flow velocity and, hence an increased suction. Downstream of that location, pressure recovery occurred briefly due to a reduction in the flow velocity effect from the start of the flat section. However, beyond the brief pressure recovery, static pressure reduced gradually due to the 'pump down effect' of the diffuser located further downstream. This trend continues with the peak velocity at the diffuser inlet, caused by the local flow curvature, producing a corresponding peak suction at the same location. The subsequent pressure recovery downstream of the diffuser inlet indicated the presence of an adverse pressure gradient towards the diffuser exit. Peak suction at the diffuser inlet increased from that of the force enhancement ride height ($h/d = 0.764$) to the maximum force ride height ($h/d = 0.191$). Subsequently, a reduction in the diffuser inlet peak suction occurred below the maximum force ride height as represented by the force reduction ride height of $h/d = 0.153$ with a further force reduction at the low force ride height $h/d = 0.064$. Also for both ride heights ($h/d = 0.153$ and 0.064), the pressure distribution upward curvature close to the diffuser exit indicates the severe adverse pressure gradient induced by flow reversal and recirculation (as discussed subsequently in Section 4.1.3 and 4.1.4)

4.1.1 Force enhancement (flow regime A)

As shown in the C_L and C_D plots of Figure 4–1, regime A starts from the highest normalised ride height, $h/d = 0.764$ and ends at $h/d = 0.318$. Within this sub-range of twelve ride heights, downforce and drag increased gradually. This increase in downforce and drag also indicates the existence of an interdependent relationship between the downforce/drag and the ride height of the ground effect diffuser. Between the normalised ride heights, $h/d = 0.764$ and 0.318, C_L increased from -0.876 to -1.779 due to increased suction and likewise, C_D increased from 0.282 to 0.429 due to increased vortex drag.

Centreline and spanwise surface pressures of the flat underbody and diffuser ramp sections at $h/d = 0.764$ and 0.382 (within flow regime A) are presented in Figures 4–5, 4–6a and 4–6b. At $h/d = 0.764$, the peak suction at the diffuser inlet is $C_p = -1.192$ and increased to $C_p = -1.682$ at $h/d = 0.382$ indicating a corresponding increase in peak velocity at the diffuser inlet with reducing ride height. The increase in diffuser inlet peak suction likewise induced an increase in diffuser ramp suction from measurements at $h/d = 0.764$ to those at $h/d = 0.382$. The curvature on both sides of the spanwise pressure measurements at both $h/d = 0.764$ (Figure 4—6a) and 0.382 (Figure 4—6b) indicated that the diffuser flow is symmetric in flow regime A. However, the increase in the diffuser centreline and spanwise pressures at $x/d = 3.63$ to $x/d = 6.29$ signified that the static pressure recovery of the diffuser flow occurred under an adverse pressure gradient. As a result, the pressure distribution curvature gradually becomes more flat downstream of $x/d = 3.63$. Factually, the pressure recovery from the early to the later part of the diffuser ramp can be highlighted with the lowest C_p of the spanwise pressure distributions. At $h/d = 0.764$, the lowest C_p at $x/d = 3.63$ and $x/d = 6.29$ is -0.794 and -0.157 respectively, while at $h/d = 0.382$, the lowest C_p at $x/d = 3.63$ and $x/d = 6.29$ is -1.558 and -0.195 respectively.

Flow visualization on the surface of the diffuser ramp provided further information on the diffuser flow features. The on-surface flow features in the flow regime A ($h/d = 0.764$ and 0.382) as shown in Figure 4–7 and 4–8 indicated the presence of longitudinal vortices (curved pathlines) along both lengthwise edges of the diffuser ramp. The existence of the vortex pair corroborated the observations by Senior (2002). In this study, the longitudinal vortices originating from both sides of the diffuser inlet are propelled in the streamwise direction by the pressure difference outside and inside the diffuser. The diffuser flow shows symmetry about the centreline ($z/d = 0$). This occurrence provides an explanation to the symmetric curvature of the spanwise surface pressure distribution. A thin separation region appears along

the span of the diffuser inlet except for the sides where the longitudinal vortex pair originates. However, the vortex pair appears to travel downstream towards the centre of the diffuser ramp indicating a separation from the diffuser end plates. Also, the diffusion of the curved pathlines at the lower half of the diffuser surface — towards the diffuser exit — indicates the weakening in strength of the vortex pair and a detachment from the diffuser surface. When ride height was reduced from $h/d = 0.764$ to 0.382, it can be observed that there is a stronger cross flow angle of the curved pathlines and they extend further downstream of the diffuser inlet. This indicates enhanced vortex strength (as detailed in Chapter 5) which translates to increased downforce.

4.1.2 Maximum force (flow regime B)

Flow regime B as indicated in Figure 4–1, falls within the normalised ride height interval $h/d = 0.318$ to 0.191, and within this interval, a further increase in C_L and C_D occurred. Between $h/d = 0.318$ and 0.191, C_L and C_D increased from -1.779 to -1.915 and 0.429 to 0.463 respectively. The 7.64% and 7.92% increase in downforce and drag respectively between both ride heights is an indication that flow regime B is an enhancement of the previous type A flow. As explained in the case of the ride height interval in the type A flow (in Section 4.1.1), the increase in downforce and drag implied an increase in the velocity of the diffuser flow. Therefore, the subsequent increase in downforce and drag within the ride height interval of the type B flow with an increased gradient of the C_L and C_D curves implies a further increase in strength of the vortices in the type B flow. Moreover, the maximum downforce and drag of all ride heights investigated in this study occurred at $h/d = 0.191$.

At the maximum force ride height of the type B flow regime ($h/d = 0.191$), the centreline diffuser peak suction increased from the C_p of -1.682 at $h/d = 0.382$ (type A regime) to a C_p of -2.057 at $h/d = 0.191$ (Figure 4–5). The increase in suction as indicated by underbody surface pressures also indicates an increase in downforce. The curvature on each end of the spanwise pressure distribution at $h/d = 0.191$ also indicated that the type B flow regime is

symmetric (Figure 4–6c). In addition, the pressure recovery and adverse pressure gradient encountered by the diffuser flow are reflected in the diminishing curvature and increase in static pressure of the surface pressure distribution from $x/d = 3.63$ to $x/d = 6.29$. At $h/d = 0.191$, the lowest C_p at $x/d = 3.63$ and $x/d = 6.29$ is -1.850 and -0.246 respectively. Furthermore, the increased suction on either sides of the pressure distribution at $x/d = 3.63$ of $h/d = 0.191$ relatively to that of $h/d = 0.382$ indicated a relative enhancement of the flow physics along the lengthwise sides of the diffuser.

In Figure 4–9, the increased size of the curved pathlines in the force enhancement flow regime as represented in $h/d = 0.191$ further confirms that the strength of the vortex pair has further increased. Also, the diffuser flow remains reasonably symmetric on either side of the diffuser ramp centreline ($z = 0$) and the enhanced vortex strength is responsible for the lower surface pressures close to the endplates relative to those of $h/d = 0.382$. The separation line along both lengthwise sides of the diffuser appeared to have extended downstream. Also, the central separation region along the diffuser inlet (between $z/d = 0.25$ and -0.25) has thickened with the separation bubble extending downstream and along the centre of the diffuser ramp. These flow features implied that there was an increase in both the streamwise flow velocity into the diffuser and the adverse pressure gradient encountered by the diffuser flow. In addition, the reduced presence of the curved pathlines towards the exit of the diffuser implied that the vortex pair had detached from the ramp. In contrast, the diminished presence of the separation bubble towards the exit of the diffuser inferred that the diffuser flow between the vortex pair had reattached to the diffuser ramp.

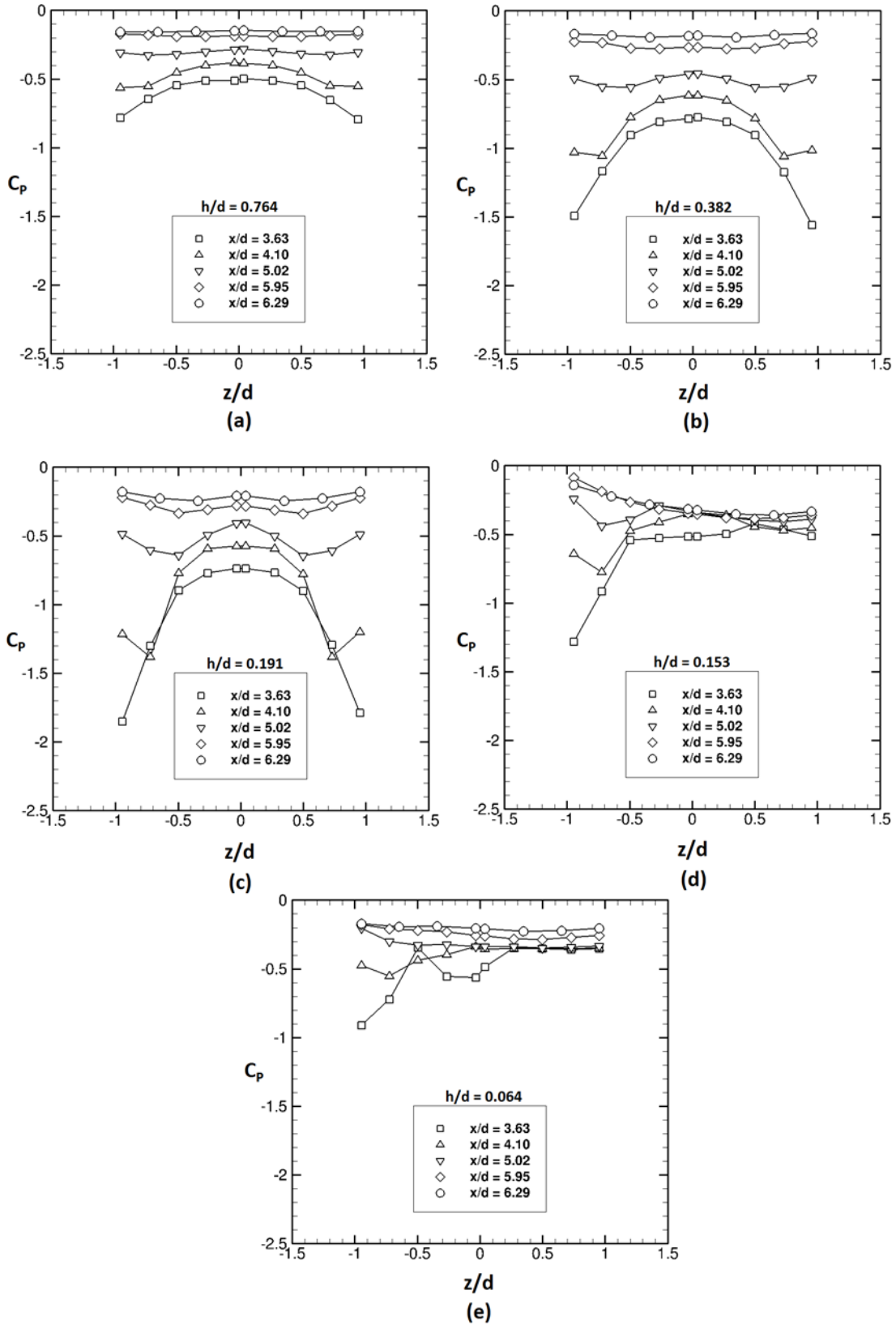

Figure 4-6: Diffuser ramp surface spanwise pressure measurements (wind tunnel) for flow regime types: **(a & b)** Type A; **(c)** Type B; **(d)** Type C; **(e)** Type D

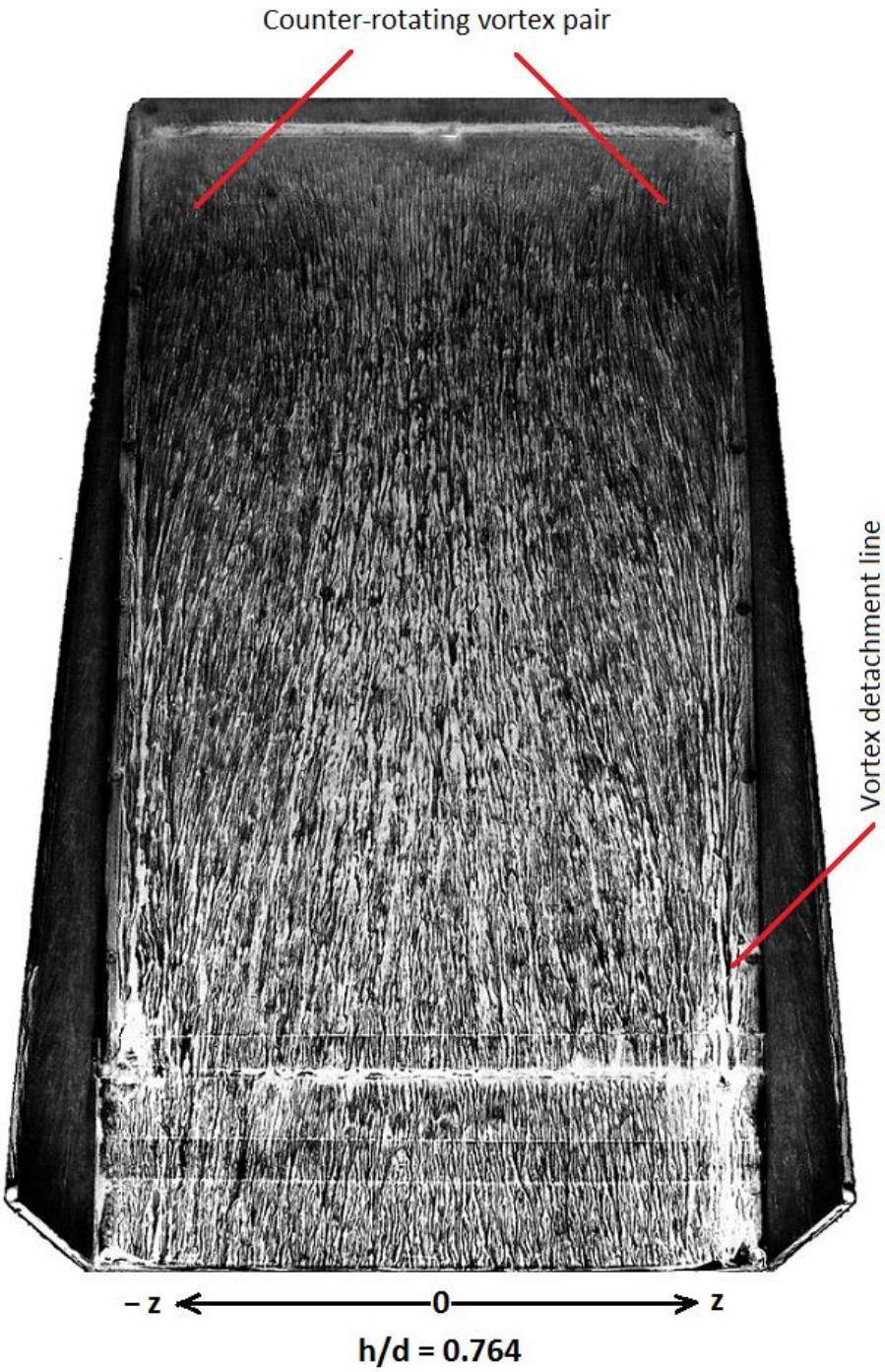

Figure 4-7: Diffuser surface flow features with visualization paint for flow regime Type A (Flow direction from top to bottom)

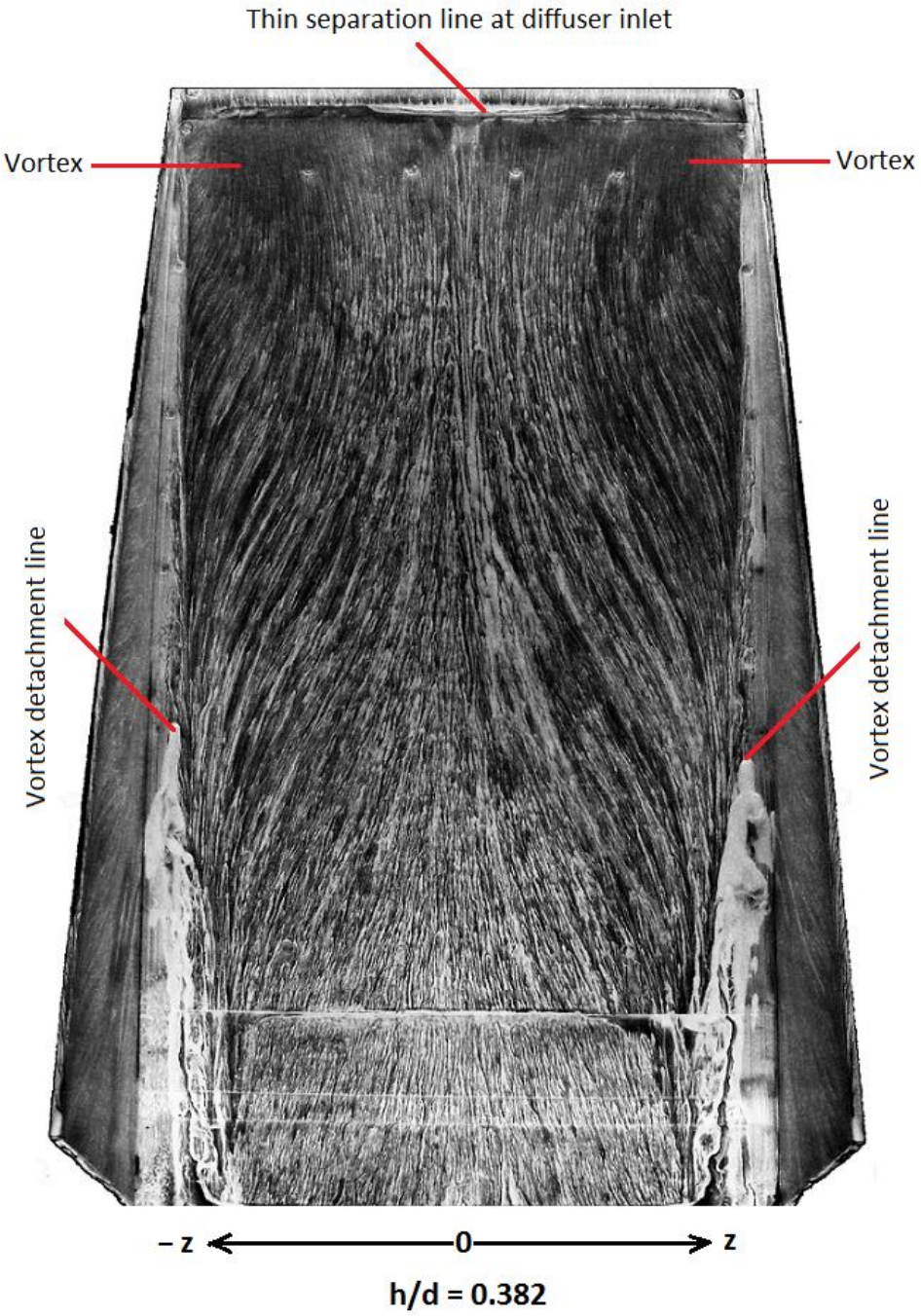

Figure 4-8: Diffuser surface flow features with flow visualization paint for flow regime Type A (Flow direction from top to bottom)

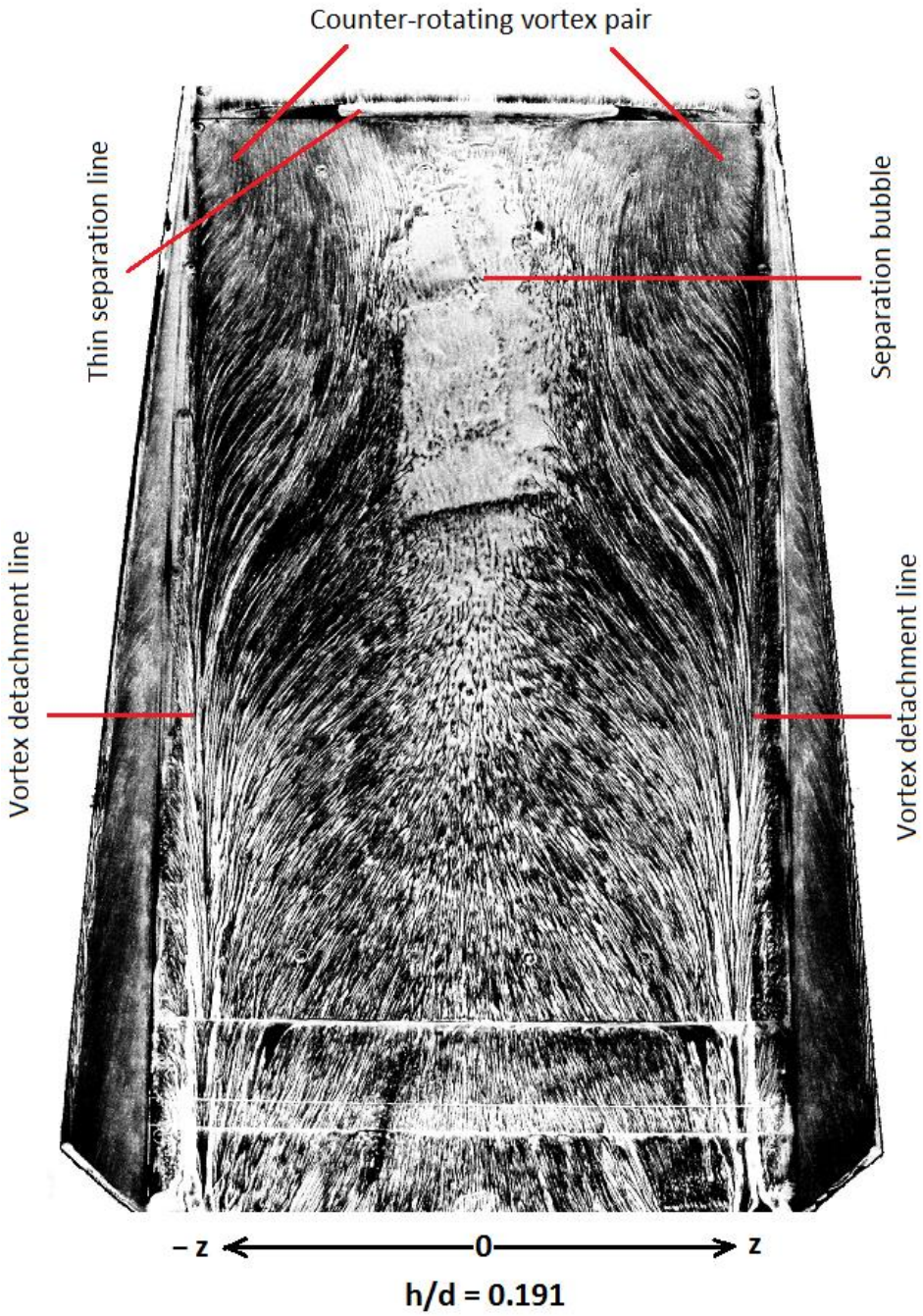

Figure 4-9: Diffuser surface flow features with flow visualization paint for flow regime Type B (Flow direction from top to bottom)

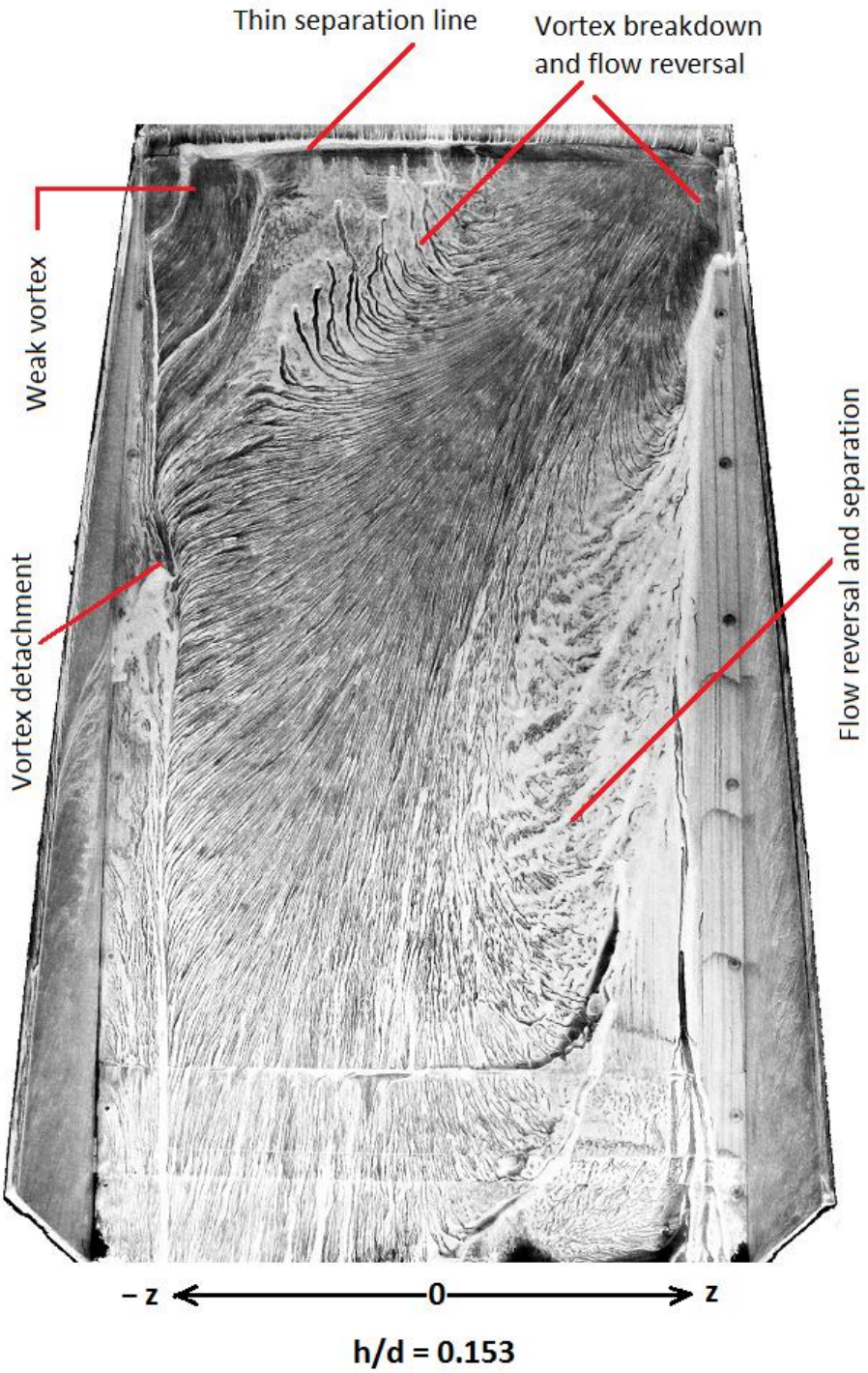

Figure 4-10: Diffuser surface flow features with flow visualization paint for flow regime Type C (Flow direction from top to bottom)

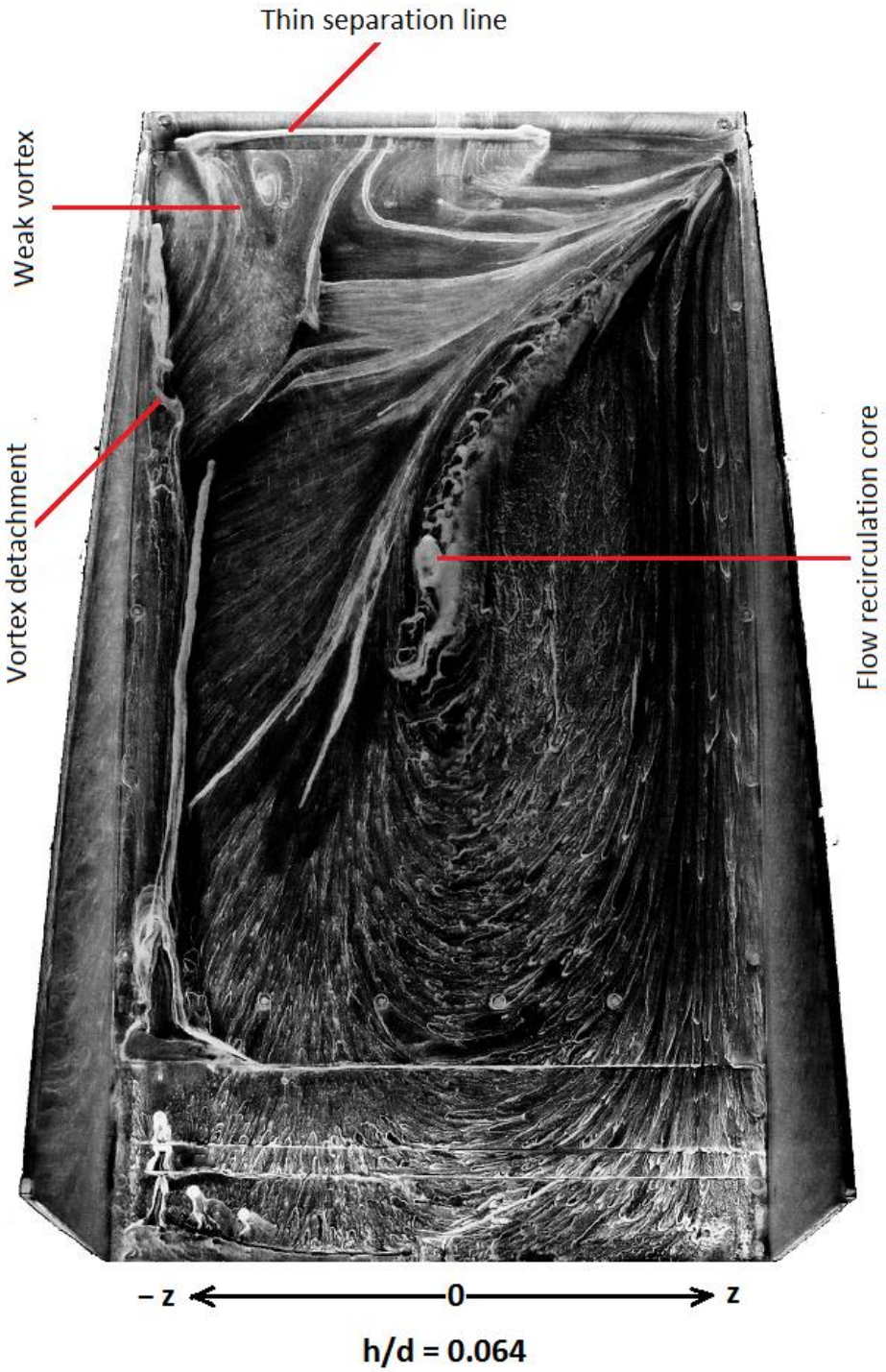

Figure 4-11: Diffuser surface flow features with visualization paint for flow regime Type D (Flow direction from top to bottom)

4.1.3 Force reduction (flow regime C)

Flow regime C occurs within the normalised ride height interval, $h/d =$ 0.191 to 0.127 (Figure 4–1) and the steep drop in the slope preceded by the inflection of the C_L and C_D curves around $h/d = 0.191$, indicated the occurrence of another change in the diffuser flow. The flow regime within this ride height interval is denoted as the force reduction region due to the severe reduction of C_L and C_D associated with the flow asymmetry of the type C diffuser flow. From $h/d = 0.191$ to 0.127, C_L and C_D reduced from -1.915 to -1.276 and 0.463 to 0.370 respectively. The 33.36% and 20.08% drops in C_L and C_D respectively confirm a significant transformation in the diffuser flow physics.

The suction peak at the diffuser inlet also reduced from a C_p of -2.068 at $h/d = 0.191$ to a C_p of -1.579 at $h/d = 0.153$ (Figure 4–5). In addition, there are lower surface pressures on one end of spanwise pressure distribution than at the other end as shown in Figure 4–6d, indicating that the diffuser flow of flow regime C is asymmetric. Furthermore, the static pressure recovery and adverse pressure gradient of the diffuser flow is exhibited by the gradually increasing pressure coefficients downstream of the diffuser inlet ($\sim x/d =$ 3.08). At $h/d = 0.153$, the lowest C_p on $x/d = 3.63$ is -1.280 and this increased to a low of -0.359 at $x/d = 6.29$. However, the higher static pressures on one end of the spanwise pressure distribution relative to the other end indicate that the suction-enhancing flow physics on side of the higher pressures is diminished.

The on-surface flow features on the diffuser ramp at $h/d = 0.153$ corroborate the asymmetric surface pressure distribution and provide further insights into the asymmetric flow of the type C diffuser flow. As seen in Figure 4–10, only one of the longitudinal edge vortices exists from the pair. In addition the vortex burst (breakdown) at one spanwise end of the diffuser is develops into a diagonal flow that appears to travel towards the location of the existing vortex. Part of the diagonal flow appears to have reversed towards the

diffuser inlet and the other portion of the diagonal flow appears to have reversed around a significant area of one side of the diffuser. However, along the longitudinal edge of the surviving vortex, the flow appears to have largely detached from the diffuser end plates. In addition, along the span of the diffuser inlet, the thin separation line appears to have moved to the side where the surviving vortex exists. This also implies that the surviving vortex has been weakened relative to the same vortex in the maximum force ride height ($h/d = 0.191$). Senior (2002) stated that the flow asymmetry of the diffuser flow in the force reduction ride height appeared to have occurred at random and that the vortex bursting occurrence switched from one vortex to the other during the experiments. Furthermore, she stated that the asymmetry may have been induced by error in aligning the model to a zero yaw angle or imperfections in the test model underbody surface as observed in missile and slender body aerodynamics (Dexter, 1982).

However, it is also noteworthy to state that as the ride height is lowered into the force reduction flow regime, the approximate turbulent boundary layer thickness of the flow (estimated before the diffuser inlet as $\sim 10.6\,mm$ using a flat plate approximation) increasingly dominates the constrained underbody 3–D flow. The flow retardation of the slow-moving boundary layer flow entering the diffuser is therefore responsible for the dominant separation and reversal of the diffuser flow. This also resulted in the characteristic vortex breakdown and thus, downforce reduction of the type C flow regime.

4.1.4 Low force (flow regime D)

Downforce and drag continue to reduce in flow regime D even though the diffuser generates a low downforce within this regime. Nonetheless, this flow behaviour also indicates another change in the diffuser flow physics from that of flow regime C. The type D flow regime extends beyond $h/d = 0.127$ to the lowest ride height ($h/d = 0.064$) investigated in this study. Between $h/d = 0.127$ and 0.064, C_L and C_D reduced from -1.288 to -1.058 and 0.370 to 0.300 respectively.

The diffuser ramp surface pressure distribution of the type D flow is represented by measurements taken at $h/d = 0.064$. The centreline pressure distribution shown in Figure 4–5, indicates that the diffuser inlet suction peak has reduced from the relatively higher suction peak of the type C flow $\left(C_p = -1.579 \text{ at } h/d = 0.153\right)$ to a C_p of -1.317 at $h/d = 0.064$. The presence of lower pressures on one side of the diffuser relative to the other side of the surface pressure distribution at $x/d = 3.63$ and 4.10 (Figure 4–6e) indicate that the type D flow regime remains asymmetric. In addition, the adverse pressure gradient faced by the diffuser flow is highlighted by the increasing static pressure distribution downstream of the diffuser inlet (Figures 4–5 and 4–6e).

In Figure 4–11, the surface flow features presented indicate that the diffuser flow regime of the low-force ride height of $h/d = 0.064$ is an enhancement of the flow characteristics of the force reduction flow regime ($h/d = 0.153$). This is because the low-force flow regime appears to be largely made up of flow separation and recirculation. The flow remains asymmetric with the core of the flow recirculation extending diagonally from the region of vortex breakdown to the centre of the diffuser ramp. Also, the separation along the diffuser inlet appeared to have extended across three-quarters of the diffuser inlet span. In addition, the flow detachment line along the side where the surviving vortex exists originates from the diffuser inlet. These flow features show that the flow entering the diffuser is completely dominated by slow-moving boundary layer flow encountering an adverse pressure gradient as indicated by the surface pressure distributions.

4.2 Further Measurements in Freestream

As a means of providing a further understanding of the flow physics and aerodynamics of the baseline diffuser bluff body geometry in freestream, additional wind tunnel investigations were conducted. This includes aerodynamic force measurements with a fixed ground condition and by increasing and reducing ride height within the force region where a sharp drop

in force occurred. Additional force measurements were done at varying freestream velocities to ascertain the impact of Reynolds number on the diffuser flow. Furthermore, base plate flow visualization was captured and surface pressures along the base plate longitudinal centreline ($z = 0$) were measured to provide an insight into the interaction between the off-surface separated flow above the body and the off-surface upsweeping diffuser flow. Pitching moments were also measured across all thirty five ride heights that make up the four flow regimes.

4.2.1 Fixed and moving ground conditions

A majority of the wind tunnel experiments and all CFD simulations of the diffuser body in freestream were done with a moving ground condition. However, to further understand the influence of the ground boundary layer on the downforce-producing flow traveling underneath and through the diffuser, a fixed ground plane was implemented. In addition, the boundary layer suction control before the rolling road was turned off for the fixed ground condition. The plots in Figure 4–12 represent a comparison of force measurements for the fixed and moving ground conditions. In general, the downforce and drag coefficient plots indicate that the diffuser above the fixed ground plane largely generated less downforce than with the moving ground plane. This implies that with the fixed ground, the retardation of boundary layer flow was increasingly dominant and thus induced a reduction in the underbody flow velocity. However with a moving ground, the dominance of boundary layer flow was reduced and the underbody flow velocity was enhanced. This enabled the enhancement of the diffuser pumping effect and diffuser inlet suction peak. As a result, downforce with the moving ground plane was greater than that generated with the fixed ground plane.

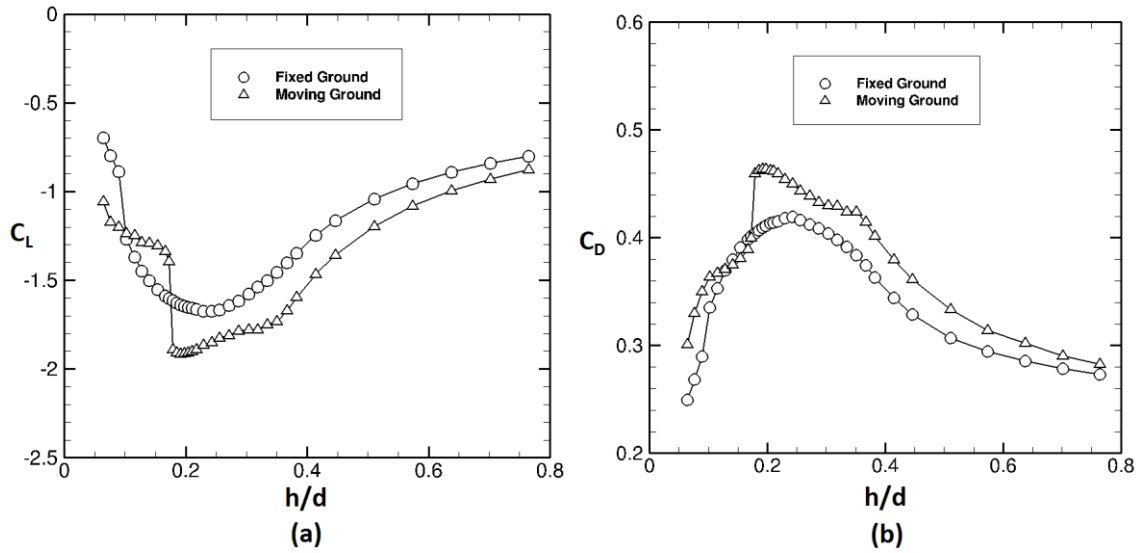

Figure 4-12: Force measurements (wind tunnel) across ride heights ($h/d = 0.764$ to 0.064) under fixed and moving ground conditions: **(a)** downforce **(b)** drag

Despite that, the downforce coefficient plot with a fixed ground indicates a distinct deviation from that with the moving ground from the maximum downforce flow region (type B flow) and beyond. As shown in Figure 4–12, the fixed-ground downforce curve gradually reduces from $h/d = 0.178$ to 0.172, whereas the downforce curve with the moving ground dropped abruptly within that ride height interval. Senior (2002), explained that this was as a result of the fixed ground flow remaining attached at the diffuser inlet at ride heights where the diffuser had stalled with the moving ground. In addition, the onset of force reduction occurred earlier with the fixed ground plane. Unlike the downforce curve with the moving ground, downforce gradually reduced between $h/d = 0.242$ to 0.102 before a significant drop occurred below the ride height interval. Hence, it can be stated that boundary layer flow is significantly responsible for the downforce sensitivities between the fixed and moving ground plane within the maximum-force and force-reduction flow regions.

4.2.2 Flow hysteresis

The dependence of a flow state on its past and present history can be described as flow hysteresis. Furthermore, it occurs when a flow's physical property trails behind a change in the effect causing it. As an instance, the reattachment of the flow over a wing occurs at a lower angle of attack, when incidence is reduced, than that at which flow detachment occurs as the angle of attack is increased (Yang et al., 2008; Mittal and Saxena, 2002). Likewise, as observed by Ruhrmann and Zhang (2003), the ride height of the 15° diffuser bluff body at which downforce increased when ride height was reduced is lower than the ride height at which downforce decreased when the ride height was increased (see Figure 2–8 in Chapter 2). The flow hysteresis phenomenon was attributed to dominance of flow instabilities within the particular ride height interval.

As a means of investigating the possible occurrence of flow hysteresis in this present study, force measurements were taken within the ride height interval ($h/d = 0.159$ to 0.204) that encompasses the sharp drop of downforce and drag in the force-reduction region. As shown in Figures 4–13a and 4–13b, the force measurements for this present study were taken as the ride height was increased and decreased within the ride height interval. The downforce and drag coefficient plots indicate that the ride height at which downforce decreased when ride height was reduced is lower than the ride height at which downforce increased when the ride height was increased. As indicated from the C_L and C_D plots, with reducing ride height, downforce and drag decreased to -1.488 and 0.410 respectively at $h/d = 0.172$ and with increasing ride height, downforce and drag increased to -1.892 and 0.459 respectively at $h/d = 0.178$. Although the ride height difference is highlighted in the force measurements between the ascending and descending order of the ride height interval, the slopes of the curves (Figure 4–13c) do not indicate a significant deviation as observed by Ruhrmann and Zhang(2003) (Figure 2–8). In actuality, the difference between the ride heights where flow hysteresis occurred in this

present study is $1\,mm$ while in the case of Ruhrmann and Zhang (2003) the difference is about $\sim 7\,mm$.

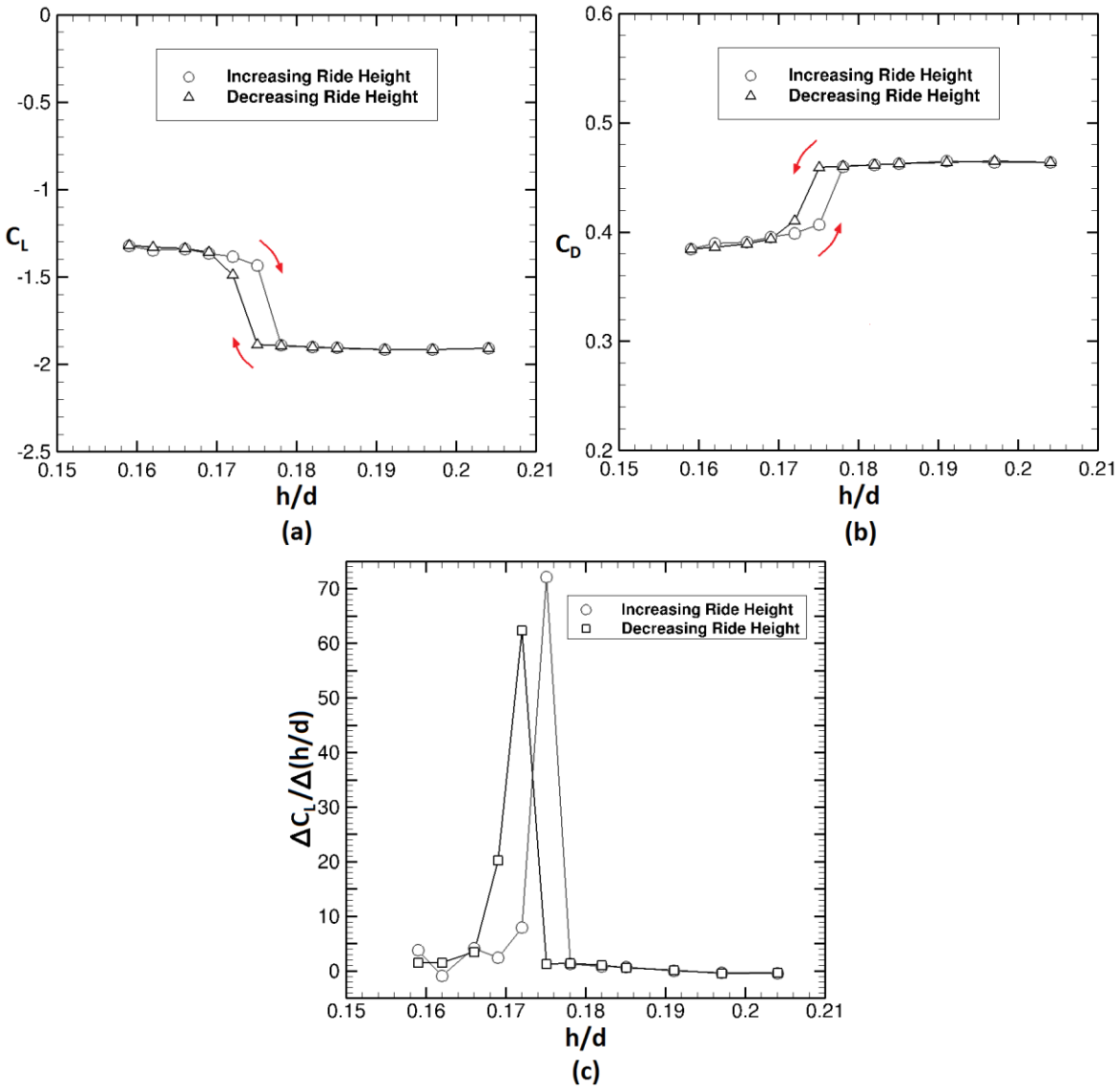

Figure 4-13: Hysteresis highlighted between $h/d = 0.159$ to 0.204 with a magnified h/d plot scale: **(a)** Downforce **(b)** Drag and **(c)** Slopes of increasing and decreasing ride height between $h/d = 0.159$ to 0.204 with a magnified h/d plot scale.

4.2.3 Reynolds number sensitivity

Senior (2002) investigated the influence of varying Reynolds number (Re) on downforce characteristics of a diffuser bluff body model in ground effect. The three Reynolds numbers investigated, $1.3\,x\,10^6$, $1.8\,x\,10^6$, and $2.7\,x\,10^6$ representing freestream velocities of $15\,m/s$, $20\,m/s$ and $30\,m/s$, indicated a

similar downforce coefficient curve. However, the maximum downforce coefficient for Re = $1.3\,x\,10^6$ occurred at a lower ride height ($1\,mm$ less) than the maximum downforce ride height for the other Reynolds numbers. Senior (2002) stated that the maximum downforce ride height disparity indicated that the downforce reduction phenomenon which occurs subsequently after the maximum downforce is reached is not induced by the merging of boundary layer flow at the diffuser inlet. This as explained was because the lowest Re should generate the highest boundary layer thickness among the three Reynolds numbers investigated. Thus, if merging of boundary layers (underbody and moving ground) induced the blockage at the diffuser inlet which in turn dictates maximum downforce and proceeding diffuser stall, then stall at the lower Re should occur at a larger ride height.

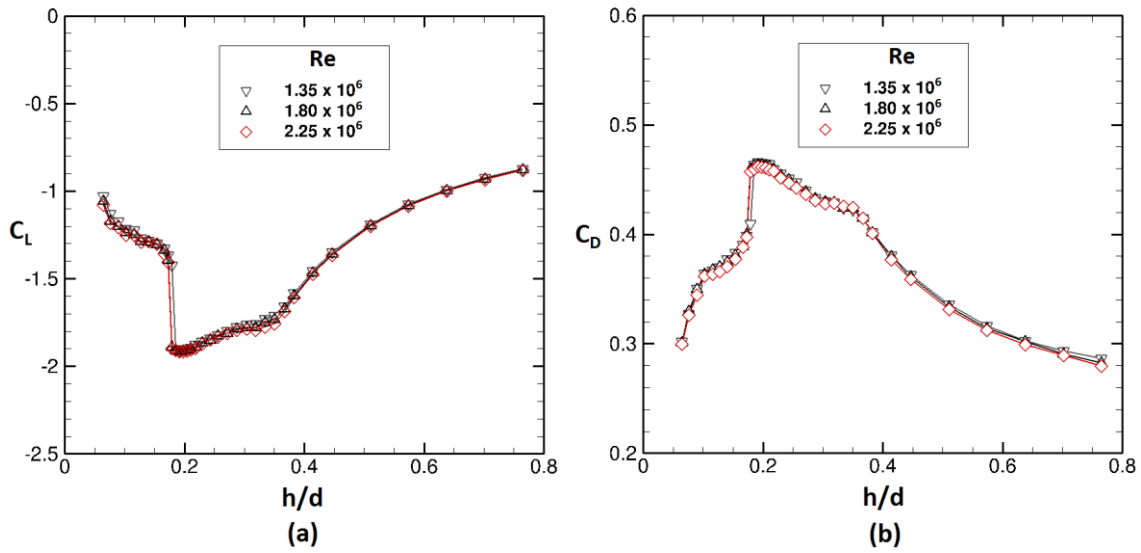

Figure 4-14: Reynolds number sensitivity across ride heights (h/d = 0.764 to 0.064): **(a)** downforce **(b)** drag

A similar Reynolds number sensitivity analysis was carried out in this present study at Re = $1.35\,x\,10^6$, $1.8\,x\,10^6$ and $2.25\,x\,10^6$. As shown in Figures 4–14a and 4–14b, the downforce and drag curves of all three Reynolds numbers share very similar characteristics. However, in contrast to the observations of Senior (2002), the maximum downforce and drag for the three Reynolds numbers occurred at the same ride height (h/d = 0.191). The distinct

disparity occurred in the force-reduction region, where the sharp drop in downforce and drag occurred at $h/d = 0.172$ for both $\mathrm{Re} = 1.8\,x\,10^6$ and $2.25\,x\,10^6$ whereas at $\mathrm{Re} = 1.35\,x\,10^6$, this reduction occurred at $h/d = 0.178$. This implies that although a variation in Re does not significantly alter the downforce characteristics of the flow, the force-reduction flow regime is sensitive to low Reynolds numbers due to increased boundary layer blockage.

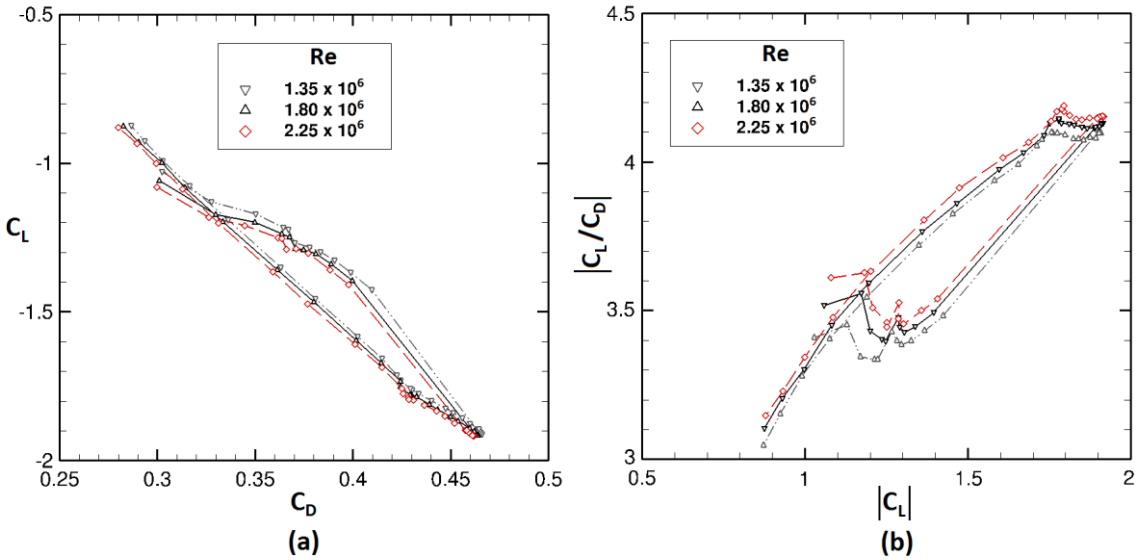

Figure 4-15: Reynolds number sensitivity across ride heights ($h/d = 0.764$ to 0.064): **(a)** drag polar **(b)** lift-to-drag ratio

Further Reynolds number sensitivity analysis was done for the drag polar and lift-to-drag ratio (C_L/C_D) of the diffuser bluff body employed in this study. As shown in Figures 4–15a and 4–15b, the drag polar and lift-to-drag ratio curves were done at $\mathrm{Re} = 1.35\,x\,10^6$, $1.8\,x\,10^6$ and $2.25\,x\,10^6$. The curves of the drag polar and lift-to-drag ratio indicate that minimum drag coefficient and maximum lift-to-drag ratio are functions of Reynolds number (Anderson, 2000). The drag polar curves indicate that as Reynolds number increased, the minimum drag coefficient decreased. Also, lift-to-drag curves show that the maximum magnitude of C_L/C_D increases with an increase in Reynolds number.

4.2.4 Pitching moment and pitch angle sensitivity

As a means of further understanding the underbody flow effects on the diffuser bluff body in ground effect, pitching moments were measured across the range of ride heights that covers the four distinct flow regimes. The point of reference of the force balance mounted inside the diffuser bluff body was located at about 57% of body length from the leading edge of the body's nose section. Also, a deflection of $0.5\,mm$ at the trailing edge of the diffuser body was measured without freestream. The comparison in pitching moment coefficients as shown in Figure 4–16 revealed a difference in pitching moment on the diffuser body in fixed and moving ground conditions. In the case of the fixed ground condition, the positive values of C_m (which indicate nose-up pitching moments), increased gradually from 0.028 to a peak of 0.062 between $h/d = 0.764$ to 0.334. Below $h/d = 0.334$, C_m gradually reduced to a negative value (which indicates a nose-down moment) of -0.007 at $h/d = 0.102$. Furthermore, an increase to a C_m of -0.003 occurred at $h/d = 0.089$ after which a further drop to a more negative C_m occurred at the lowest ride height investigated in this present study ($h/d = 0.064$). However in the case of the moving ground condition, C_m increased on a similar slope as with the fixed ground from a positive value of 0.026 at $h/d = 0.764$ to 0.058 at $h/d = 0.350$. Below the peak value at $h/d = 0.350$, C_m reduced to 0.034 at $h/d = 0.350$ but increased to 0.036 at $h/d = 0.204$. Furthermore, it dropped to a negative value of -0.008 at $h/d = 0.127$, before increasing to a positive C_m at $h/d = 0.102$ and subsequently drops to a negative value at $h/d = 0.064$.

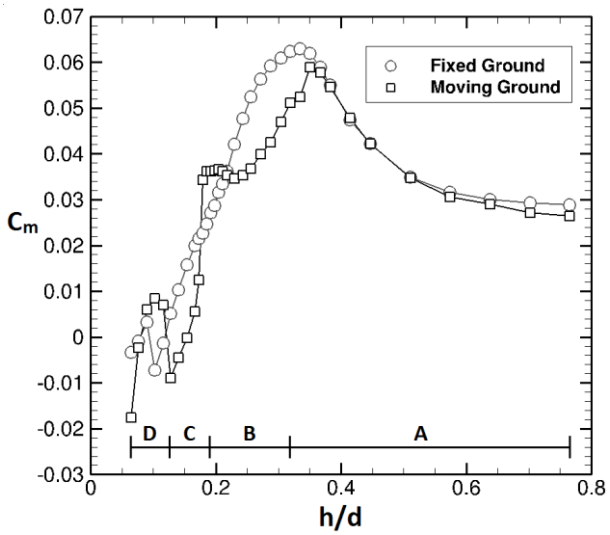

Figure 4-16: Pitching moments across ride heights ($h/d = 0.764$ to 0.064) under fixed and moving wind tunnel ground conditions

The pitching moment behaviour across the ride heights of the four flow regimes for both the fixed and moving conditions appear to have a sinusoidal-like behaviour to their respective force coefficient curves in Figure 4–12a (i.e. there is a rise and drop of pitching moment with each change in gradient of the force curves). Similar to the C_m curve with the fixed ground condition, the downforce curve with the fixed ground increased gradually from its value at the first ride height ($h/d = 0.764$) to a peak value towards the end of the type A flow regime. In addition, the reduction phase of the pitching moment which occurred from the type B flow regime ended with an increasing phase close to the end of the type C flow after which a second reduction phase occurred in the type D flow regime. Similarly, the trajectory (increase and reducing phases) of the C_m curve with the use of the moving ground appeared to interchange close to the transition between flow regimes as defined by its corresponding downforce curve. This implies that the differences in boundary layer flow blockage between the fixed and moving ground also influences the pitching moment acting on the body similarly to the downforce generated. It also implies that near the point of transition between flow regimes there is a resultant increase and a subsequent decrease in the pitching moment. This behaviour is increasingly distinct with the moving ground condition due to the

decrease in blockage effect of the boundary layer relative to the case of the fixed ground.

The downforce effect of increasing pitch angle of the diffuser bluff body in the nose down direction was also investigated because it effectively increases the diffuser area ratio. The centre of rotation for this investigation was located at about $0.554\,m$ from the trailing edge of the diffuser bluff body (see illustration in Equation 4.2). As shown in Figures 4–17, 4–18 and 4–19, the increase in pitch angle from 0° to 0.08°, 0.17° and 0.27° (as defined in Equation 4.2) marginally increased downforce and drag from the baseline levels at 0°.

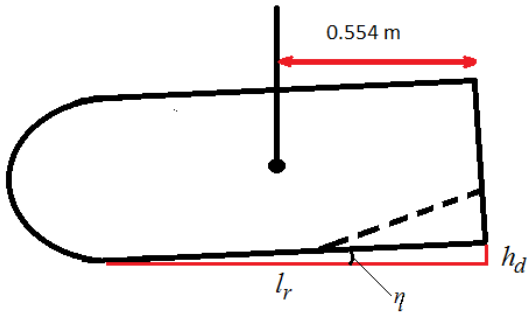

$$\eta = \tan^{-1}\left({}^{h_d}/_{l_r}\right) \tag{4.2}$$

Where,

η is the diffuser bluff body pitch angle

h_d is the rise or height of the diffuser side plate trailing vertex from the rolling – road

l_r is the run or horizontal distance from leading edge of the flat underbody section to the trailing vertex of the side plate of the diffuser bluff body = 1.031 m

The marginal increase in forces is assumed to be the effective increase in diffuser angle by an increment in pitch angle of the body. As a result, the suction generated by the diffuser increased marginally. This behaviour is similar to the investigations of George (1981) where an increase in pitch angle strengthened the longitudinal vortices along the lengthwise edges of the diffuser, thereby increasing downforce by inhibiting the separation bubble on

the diffuser ramp. In addition, the increase of pitch angle in this study also caused the sharp drop in downforce and drag coefficients to occur at a higher ride height than the baseline measurements at a zero pitch angle. As shown in Figures 4–17, 4–18 and 4–19, the distinct drop in downforce occurred at $h/d = 0.185$ for both pitch angle increments to 0.08° and 0.17° while for a pitch increase to 0.27°, the severe drop occurred at $h/d = 0.178$. This equates to an increase in ride height (at the diffuser inlet) of $2\,mm$ and $1\,mm$ respectively from the baseline ride height at zero pitch angle where the distinct drop in downforce and drag coefficients occurred at $h/d = 0.172$.

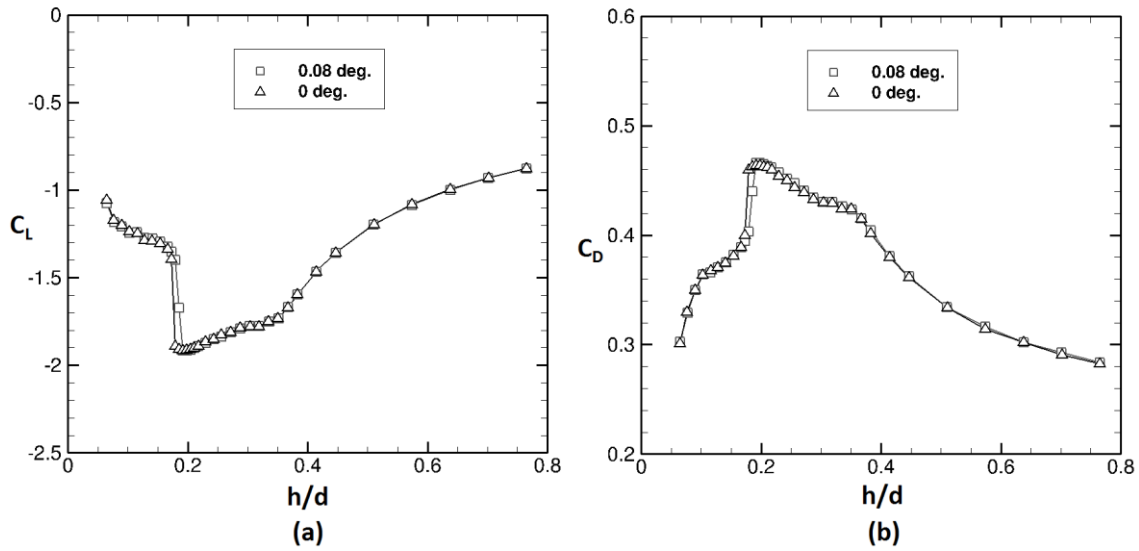

Figure 4-17: Force measurements (wind tunnel) across ride heights ($h/d = 0.764$ to 0.064) with bluff body positioned at pitch angle (nose down) of 0.08°: **(a)** downforce **(b)** drag

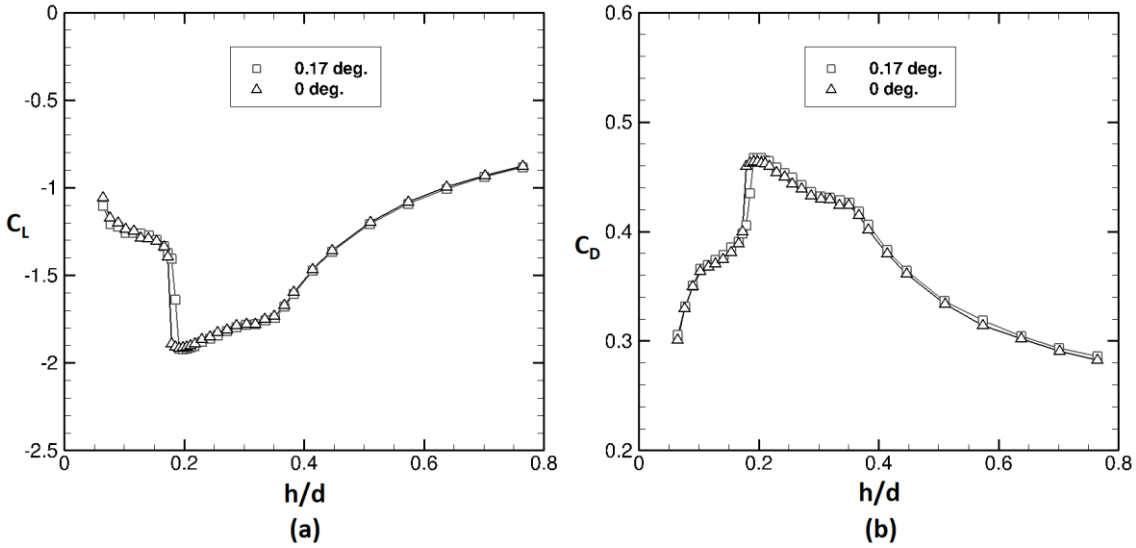

Figure 4-18: Force measurements (wind tunnel) across ride heights $(h/d = 0.764 \text{ to } 0.064)$ with bluff body positioned at pitch angle (nose down) of 0.17°: **(a)** Downforce **(b)** Drag

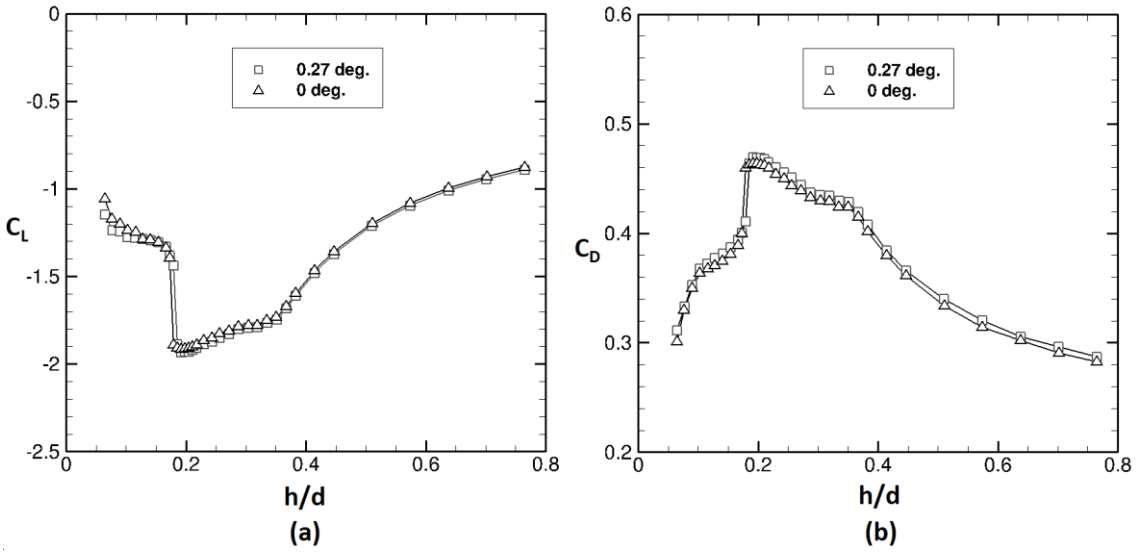

Figure 4-19: Force measurements (wind tunnel) across ride heights $(h/d = 0.764 \text{ to } 0.064)$ with bluff body positioned at pitch angle (nose down) of 0.27°: **(a)** Downforce **(b)** Drag

4.2.5 Effects of transition fixing

The downforce and drag effect of fixing transition to turbulent flow across the diffuser body was investigated using a 1.2 mm trip wire wrapped around the nose section at a location 100 mm from the leading face of the body (similar

to Senior, 2002). The selection of the transition point was chosen to prevent the formation of a laminar separation bubble around the nose and to induce a turbulent flow upstream of the flat section of the bluff body's underbody.

The comparisons of downforce and drag coefficients between fixed transition and natural transition are shown in Figures 4–20 and 4–21. These indicate that the fixing of transition marginally reduced downforce and increased drag. Also, the severe drop in downforce and drag occurred at a higher ride height relative to the case without transition. In addition, the respective marginal deficit and surplus offset in downforce and drag with the use of fixed transition remained, even at a bluff body (nose down) pitch angle of 0.08° (Figure 4–21a and 4–21b). This implies that the inducement of boundary layer turbulence through transition fixing also caused an increase in skin friction drag. As a result, there was a resultant increase in drag and a decrease in downforce.

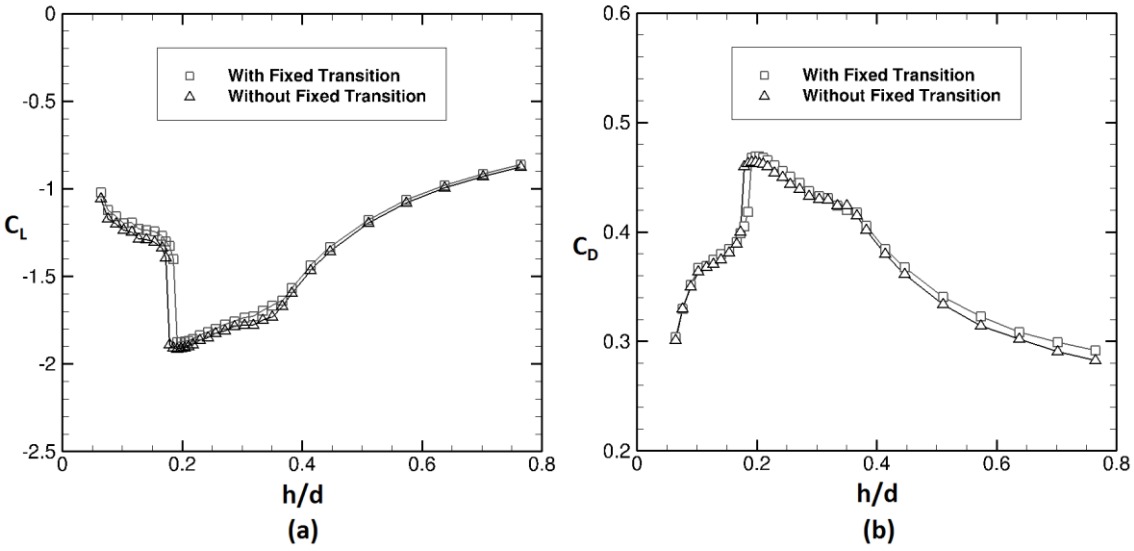

Figure 4-20: Force measurements (wind tunnel) comparison across ride heights $(h/d = 0.764 \text{ to } 0.064)$ between fixed and without fixed transition: **(a)** downforce **(b)** drag

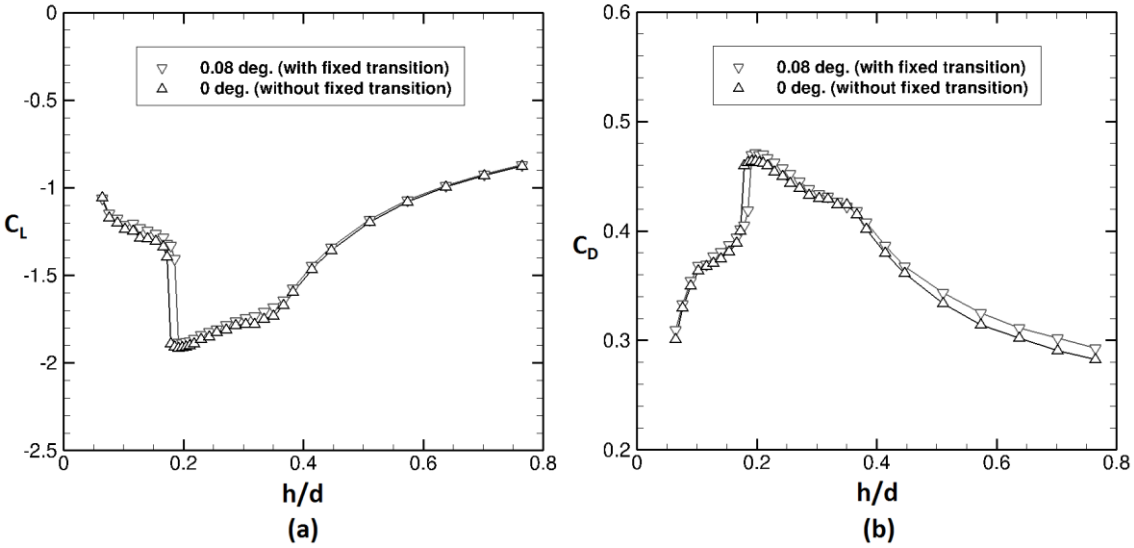

Figure 4-21: Force measurements (wind tunnel) comparison across ride heights ($h/d = 0.764$ to 0.064) between fixed transition (with bluff body positioned at a nose down pitch angle of 0.08°) and without fixed transition (with zero bluff body pitch): **(a)** Downforce **(b)** Drag

4.2.6 Base surface pressures

The dominant type of drag generated by a bluff body is pressure drag while a streamlined body such as an aerofoil generates less pressure drag (but more proportionally viscous drag) than a bluff body. The differing drag attributes is as a result of the shapes of both bodies — the streamline body has a decreasing cross-sectional area along its length than a bluff body. Thus, at a given flow velocity there is a pressure difference between the front surface and base surface of a bluff body because the wake of a bluff body induces a drop in the base surface pressures due to the eddy motions (vortices) formed in the wake. The investigations of Krajnovic and Davidson (2001) discovered that the near-wake of a 'bus-shaped' bluff body in ground effect was dominated by counter-rotating upper and lower vortices. Furthermore, the CFD investigations of Puglisevich and Page (2011), which were validated against the wind tunnel study of Jowsey (2013) indicated that the outflow from the diffuser enabled the lower vortex to dominate the upper vortex of a diffuser bluff body in ground effect.

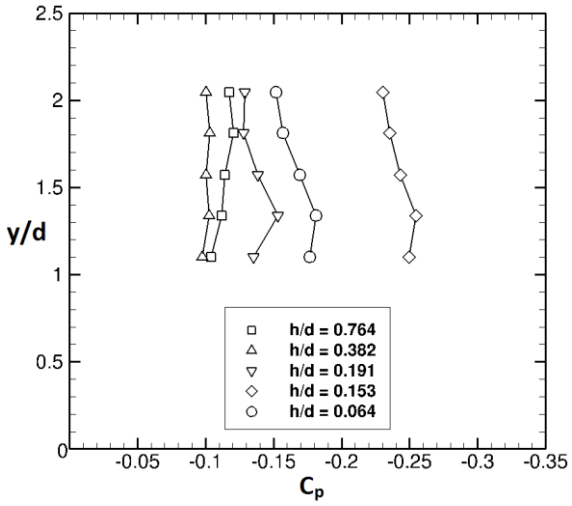

Figure 4-22: Surface pressure measurements (wind tunnel) along the vertical centreline of diffuser bluff body base plate at $h/d = 0.764,\ 0.382,\ 0.191,\ 0.153,$ and 0.064

Similar to the investigations by Senior (2002), the separated upsweeping outflow from the diffuser and the separated flow over the bluff body of this present study implied that the base surface pressures were kept low by the separated flows (see upper and lower vortices in Figure 4–23) within the bluff body near-wake. However, the varying ride height of the diffuser ensured that the outflow from diffuser which includes the diffuser longitudinal vortices dictated the levels of drag for the bluff body. As shown in Figure 4–22, the base surface pressure distribution along the vertical centreline of the base surface indicated a wavy-shaped pressure distribution for the four flow regime types represented by five ride heights ($h/d = 0.764,\ 0.382,\ 0.191,\ 0.153$ and 0.064). The base pressure distribution at $h/d = 0.764$ and 0.382 indicate a similar base pressure behaviour in the type A flow regime. The lowest C_p at $h/d = 0.764$ and 0.382 are -0.120 and -0.102 respectively. These pressures where measured at the location of the upper vortex (above $y/d = 1.57$), indicating that the strength of the upper vortex is more than the lower vortex (below $y/d = 1.57$). However at $h/d = 0.191$, the base pressures become more negative with the lowest C_p of -0.152 measured at the location of the lower vortex thus indicating an increase in strength of the lower vortex.

The strength of the low pressure core of the lower vortex has increased as a result of the enhanced longitudinal vortices of the diffuser in the maximum force flow regime. This ensured an increased velocity of the separated diffuser outflow. However, the base pressures at the force reduction and low force flow regimes (type C and D flows respectively) are lower than the type A and B flow regimes. The lowest C_p at $h/d = 0.153$ (type C flow) and $h/d = 0.064$ (type D flow) were measured at the lower region of the base surface are -0.254 and -0.181 respectively. In the type C and D flow regimes, a breakdown on one of the longitudinal vortices occurred and this caused a reduction in diffuser outflow. As a result, the near-wake of the diffuser bluff body is dominated by a solitary vortex which reverses the near-wake flow direction into the diffuser (as detailed in Chapter 5). This occurrence appeared to have been responsible for the lowest base pressures (-0.254 and -0.181 respectively) measured for the type C flow regime at $h/d = 0.153$ and the type D regime at $h/d = 0.064$. Figure 4–23 show the on-surface flow structures predicted with CFD on the base plate surface of the diffuser bluff body. Streamwise LDV surveys on off-surface planes in the near-wake of the diffuser body that present additional analysis on the near-wake flow characteristics are discussed in chapter 5.

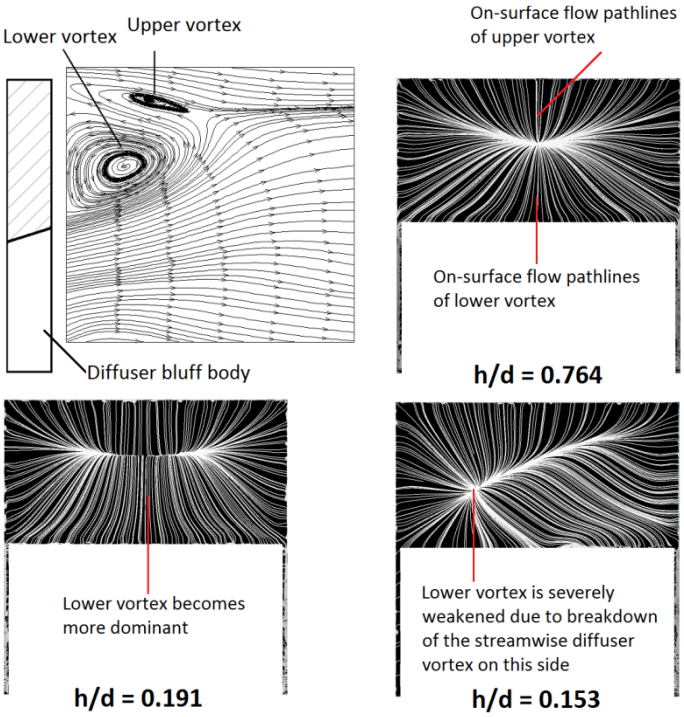

Figure 4-23: Near-wake (wind tunnel experiments) and flow pathlines on diffuser bluff body base plate (predicted with CFD) of the counter-rotating upper and lower near-wake vortices

4.3 Baseline Downforce and Drag (CFD vs. Experiments)

Computational modelling of the external flow around the diffuser bluff body was done to provide additional insight into the flow physics. The comparative CFD investigations as shown in Figure 4–24 indicated a similar downforce and drag behaviour across the ride heights of the flow regimes. As in the case of the wind tunnel results, downforce and drag increased from the highest ride height of the type A flow ($h/d = 0.764$) to maximum values at $h/d = 0.191$ of the type B flow. After which downforce and drag reduced sharply in the type C flow with further reduction in the type D flow regime.

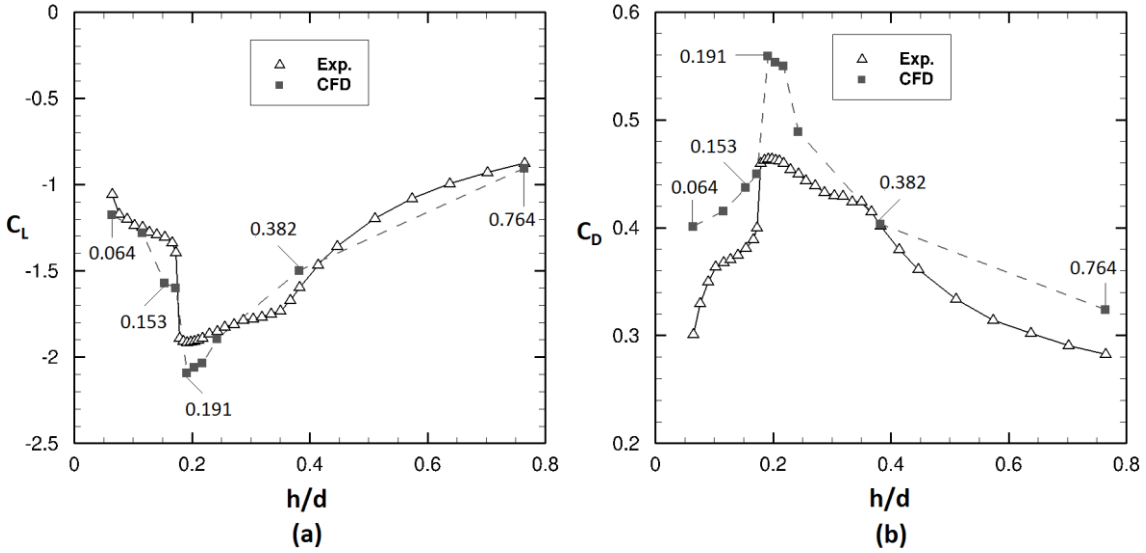

Figure 4-24: Measured (wind tunnel) and CFD-predicted force coefficients across ride heights and flow regimes: **(a)** downforce **(b)** drag

Within the type A flow regime at $h/d = 0.764$, CFD simulations (time-averaged IDDES) predicted -0.907 and 0.324 for C_L and C_D respectively thereby overpredicting C_L and C_D, by 3.53% and 14.89% respectively. At $h/d = 0.382$, the predicted values for C_L and C_D are -1.499 and 0.403 respectively thus underpredicting C_L and C_D by 6.07% and 0.49% respectively. Beyond the type A flow, CFD simulations predicted a similar further increase in downforce and drag trend as reported in the wind tunnel experiments of the type B flow regime. As seen in Figure 4–24, the CFD predicted a further increase in downforce and drag between $h/d = 0.255$ and $h/d = 0.191$ that was much greater than seen in the experiments. At $h/d = 0.191$, CFD (time-averaged URANS) predicted -2.092 and 0.560 respectively as the maximum coefficients for downforce and drag hence overpredicting C_L and C_D by 9.24% and 20.9% respectively. Furthermore at $h/d = 0.191$, the CFD simulations reveal a marginal $\pm 0.0004\%$ variation from the time-averaged C_L value and the power spectral density (PSD) estimated by Fourier transformation (Welch,1967) indicated no dominant frequency (Figure 4–25a and 4–25b). This means that at the maximum downforce and drag ride height ($h/d = 0.191$), the diffuser flow remains generally steady.

The type C flow in the CFD (time-averaged IDDES) investigations is represented at $h/d = 0.153$. At this ride height, CFD predicted the significant drop in C_L and C_D as reported in the wind tunnel experimental data. Between $h/d = 0.191$ to $h/d = 0.153$, CFD predicted a 24.90% and 21.82% drop in both C_L and C_D respectively. However, CFD overpredicted the experimental data for downforce and drag by 20.38% and 15% respectively. In (Figure 4–26a and 4–26b), the transient CFD investigation at $h/d = 0.153$, indicated a C_L variation of $\pm 14\%$ from the averaged C_L value of -1.571. Again, the power spectral density (PSD) does not reveal the presence of a dominant frequency. However, the increase in predicted C_L variation at $h/d = 0.153$ relative to that of $h/d = 0.191$ implies that at $h/d = 0.153$, the diffuser flow has become unsteady as a result of the breakdown of one of the diffuser's longitudinal vortex pair. In the type D (time-averaged URANS) diffuser flow regime represented at $h/d = 0.064$, the overpredicting trend of CFD remains present with predicted C_L and C_D values of -1.175 and 0.401 which implies that downforce was overpredicted by 11.05 %.

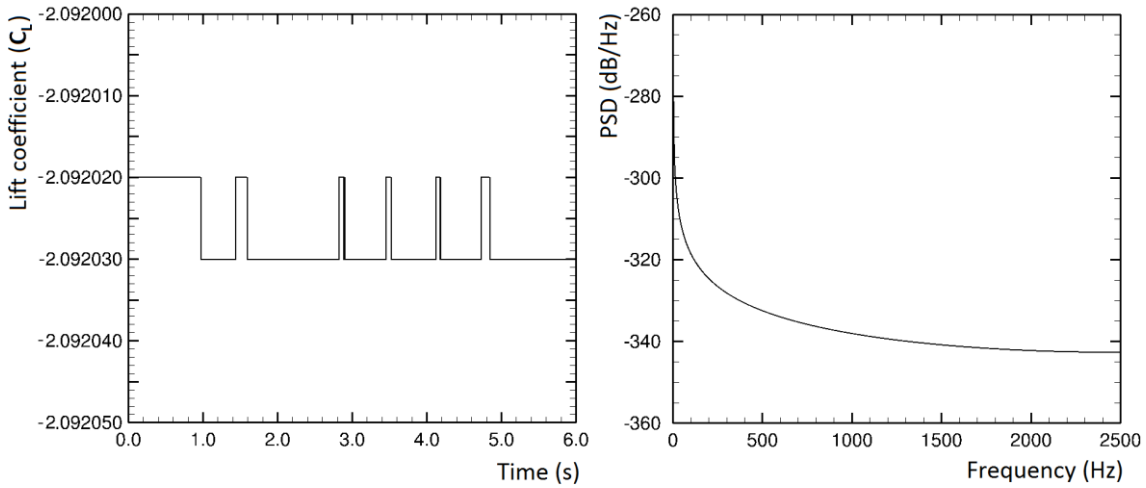

Figure 4-25: (a) Time history and **(b)** Power Spectral Density of downforce coefficient of diffuser bluff body at $h/d = 0.191$ using URANS

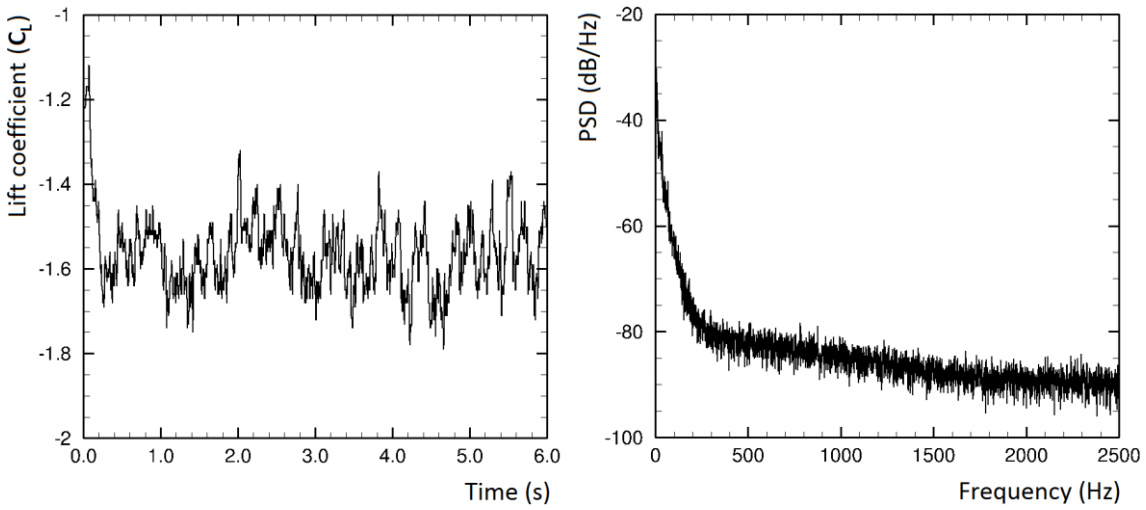

Figure 4-26: (a) Time history and **(b)** Power Spectral Density of downforce coefficient of diffuser bluff body at $h/d = 0.153$ using IDDES

4.4 Surface Pressure (CFD vs. Experiment)

The surface pressure distribution provided an insight into the flow and force behaviours across the flow regimes. The surface pressures predicted by CFD across the diffuser ramp also provided a local and detailed understanding of the over- or underpredictions of C_L and C_D. This is because the prediction deviation is reflected in the surface pressures at the diffuser inlet and across the diffuser ramp surface.

In the type A flow at $h/d = 0.764$, the percentage difference in C_L is reflected in the deviation in surface pressures predicted by the time-averaged CFD investigations at that ride height. As shown in the centreline pressure distribution (Figure 4–27a), at the locations ($x/d = 3.08$ and 3.19) proximate to the location of the diffuser inlet where peak suction occurs, the C_p values predicted by CFD are -1.055 and -1.116 respectively, while the wind tunnel experimental C_p data reveals -1.093 and -1.192 at those locations. The spanwise pressure distribution across the diffuser ramp as shown in Figures 4–27b, 4–27c, and 4–27d also revealed a similar marginal deviation in C_p between CFD and experimental data at $x/d = 3.63$, 5.02 and 6.29. At $x/d = 3.63$, 5.02, and 6.29 for $h/d = 0.764$, the lowest C_p values measured are:

$-0.794, -0.327$, and -0.157, respectively while the lowest C_p predicted at those locations are $-0.819,\ -0.303,$ and -0.137.

At $h/d = 0.382$, the underprediction of downforce is also reflected in the underprediction of the diffuser inlet peak suction and the surface pressures along the lengthwise sides of the diffuser where the longitudinal vortices are located. The centreline pressure distribution (Figure 4–28a) indicates that close to the diffuser inlet ($x/d = 3.19$), the measured and predicted peak suction has a C_p of -1.682 and -1.463 respectively. Figures 4–28b, 4–28c, and 4–28d show that the highest suction measured at $x/d = 3.63,\ 5.02,$ and 6.29 are: $C_p = -1.558,\ -0.557,$ and -0.195 while the CFD predicted surface pressures at those locations are: $C_p = -1.418,\ -0.471,$ and -0.168 respectively.

In the type B flow as represented at $h/d = 0.191$, the 9.24% overprediction of measured downforce is demonstrated in the overprediction in surface pressure distribution. At this ride height at which maximum downforce was measured and predicted, the diffuser inlet C_p at $x/d = 3.08$ as shown in Figure 4–29a is -2.057 and -2.199 for the measured and predicted values respectively. The overprediction in CFD data is also indicated in the lowest C_p measured at $x/d = 3.63$ and 5.02 with an underprediction at $x/d = 6.29$ as shown in Figures 4–29b to 4–29d. At $x/d = 3.63,\ 5.02,$ and 6.29, the lowest C_p measured are: $-1.850,\ -0.644,$ and -0.246 respectively while the lowest C_p predicted at those positions are $-2.075,\ -0.649,$ and -0.205 respectively.

The force reduction associated with the type C and D flow was also predicted by CFD and reflected in the reduced surface pressures from the maximum levels predicted in the type B flow regime at $h/d = 0.191$. However, the time-averaged CFD simulations for the type C flow regime at $h/d = 0.153$, indicated the overpredictions of surface pressures as in the case of the force predictions at this ride height. The measured peak suction close to the location of the diffuser inlet is -1.579 while the predicted suction value is -1.570 (Figure 4–30a). Measured and predicted spanwise pressure distribution are

presented in Figures 4–30b, to 4–30d and at $x/d = 3.63$, the highest suction measured on the end of the diffuser where the vortex remains present has a C_p of -1.280 and the predicted value is -1.556. On the other end of the surface pressure distribution at $x/d = 3.63$ where vortex breakdown occurred, the highest measured and predicted suction respectively are: $C_p = -0.512$ and -0.573.

At the type D flow ride height of $h/d = 0.064$, CFD also predicted the further reduction in the diffuser inlet peak suction from the higher level at $h/d = 0.153$. The overprediction trend is also present at $h/d = 0.064$ as shown in Figures 4–31a to 4–31d and as shown in Figure 4–31a where the measured and predicted C_p close to the diffuser inlet ($x/d = 3.08$) are: -1.315 and -1.538 respectively. Furthermore, at $x/d = 3.63$ (Figure 4–31b), the lowest measured C_p on the end of the diffuser ramp where the surviving vortex exists is -0.912 and the predicted value is -1.062 while on the other end of $x/d = 3.63$ where vortex breakdown occurred, the lowest measured and predicted C_p are: -0.352 and -0.399.

Similar to the underbody flat section and diffuser ramp, the base plate surface pressures (along $z/d = 0$) predicted by time-averaged CFD simulations generally agreed with the measured surface pressures (Figures 4–27e to 4–31e). However, distinct deviations between measured and predicted base plate pressures are present close to the trailing top edge of the diffuser bluff body ($y/d = 2.04$). This implied that the time-averaged CFD investigations did not adequately capture the low static pressures generated by the upper vortex induced by the off-surface flow over the body. In general, the overpredictions by CFD are as a result of the mesh insufficiency along the boundary layer of the bluff body to adequately resolve the wall flow physics. Thus further mesh refinement can enhance the resolution of the displacement thickness induced by boundary layer around the diffuser bluff body.

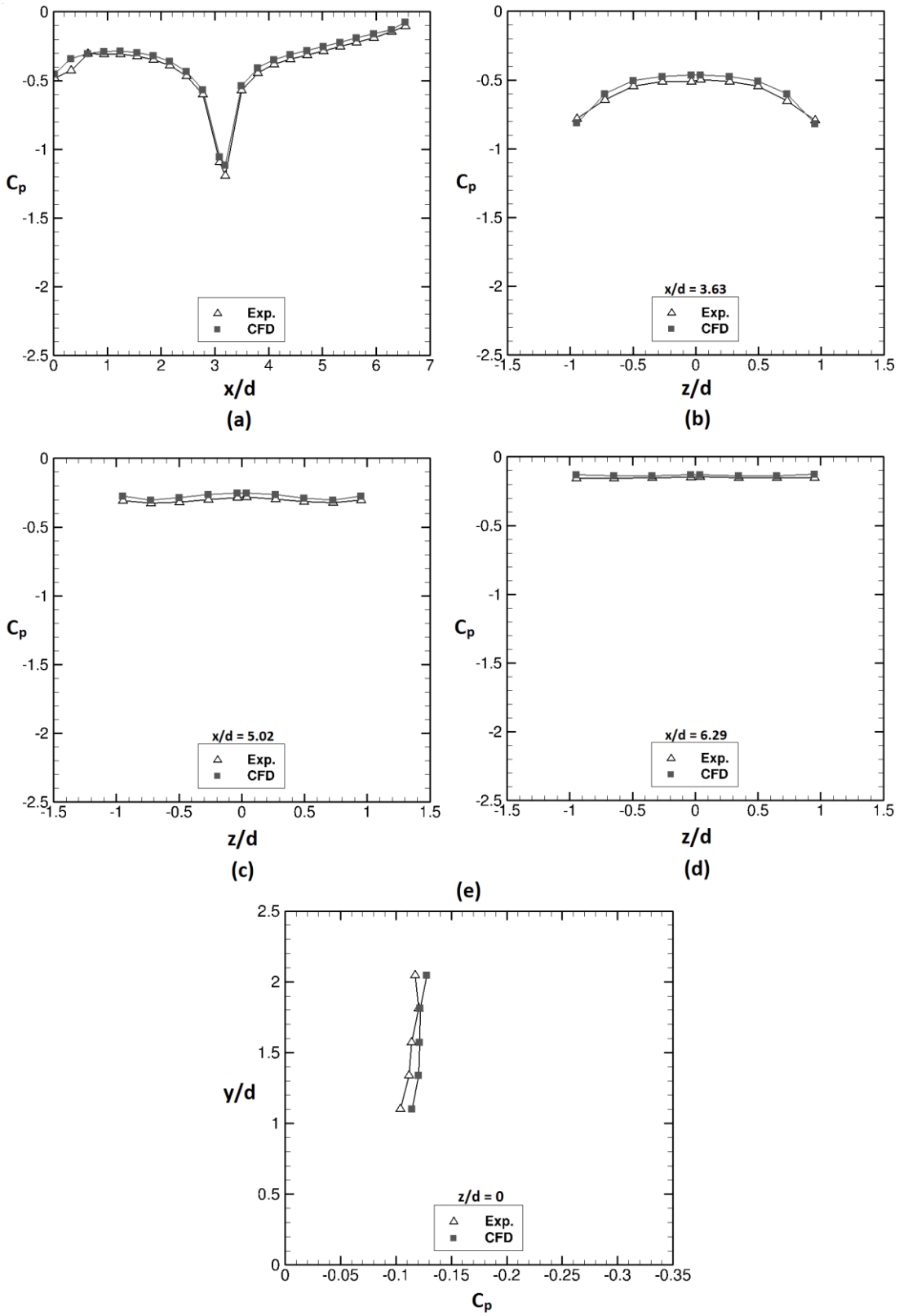

Figure 4-27: Measured (wind tunnel) and CFD-predicted surface pressure distributions for $h/d = 0.764$ along **(a)** underbody centreline **(b)** $x/d = 3.63$ **(c)** $x/d = 5.02$ **(d)** $x/d = 6.29$ **(e)** bluff-body base centreline $(z/d = 0)$

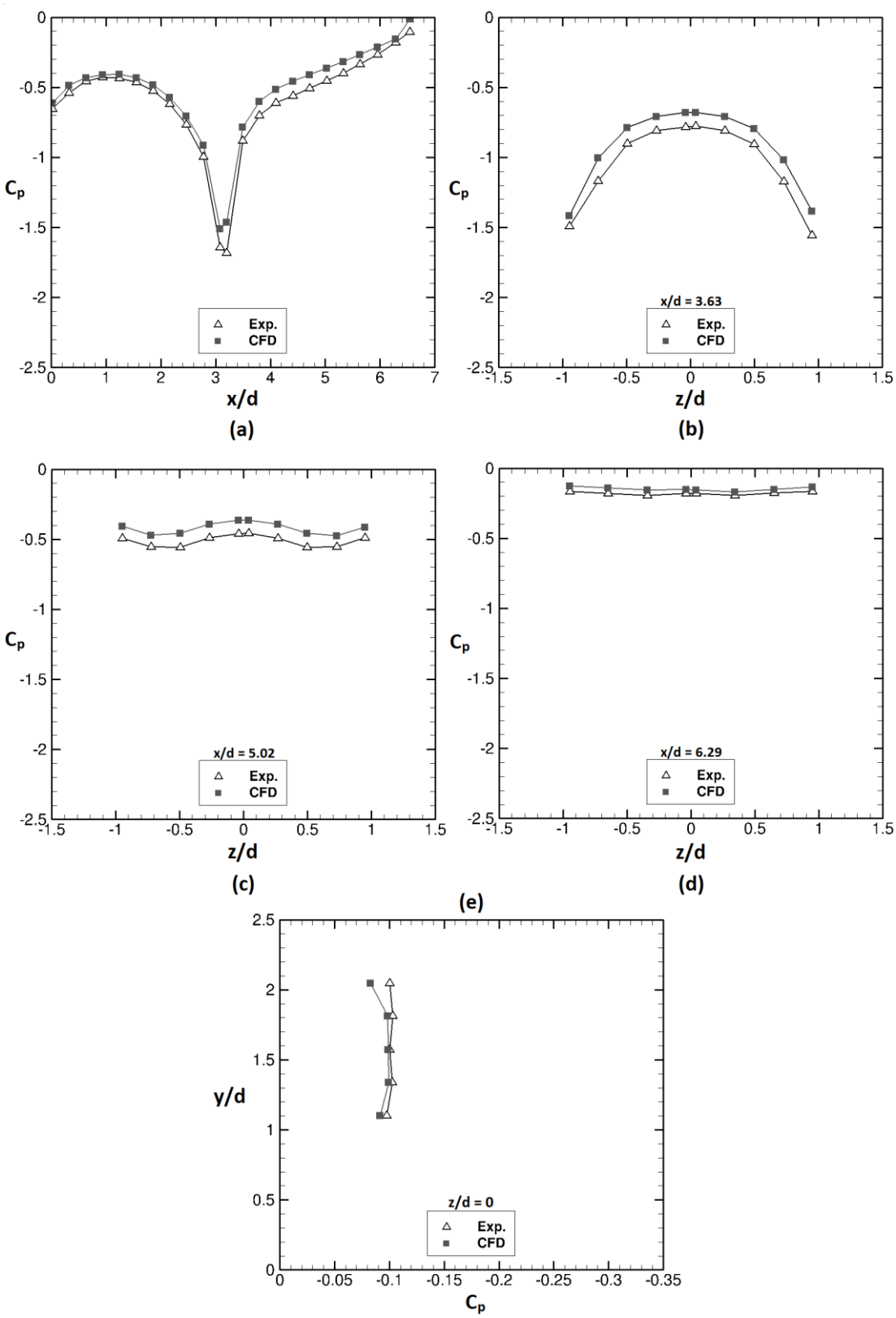

Figure 4-28: Measured (wind tunnel) and CFD-predicted surface pressure distributions for $h/d = 0.382$ along **(a)** underbody centreline **(b)** $x/d = 3.63$ **(c)** $x/d = 5.02$ **(d)** $x/d = 6.29$ **(e)** bluff-body base centreline $(z/d = 0)$

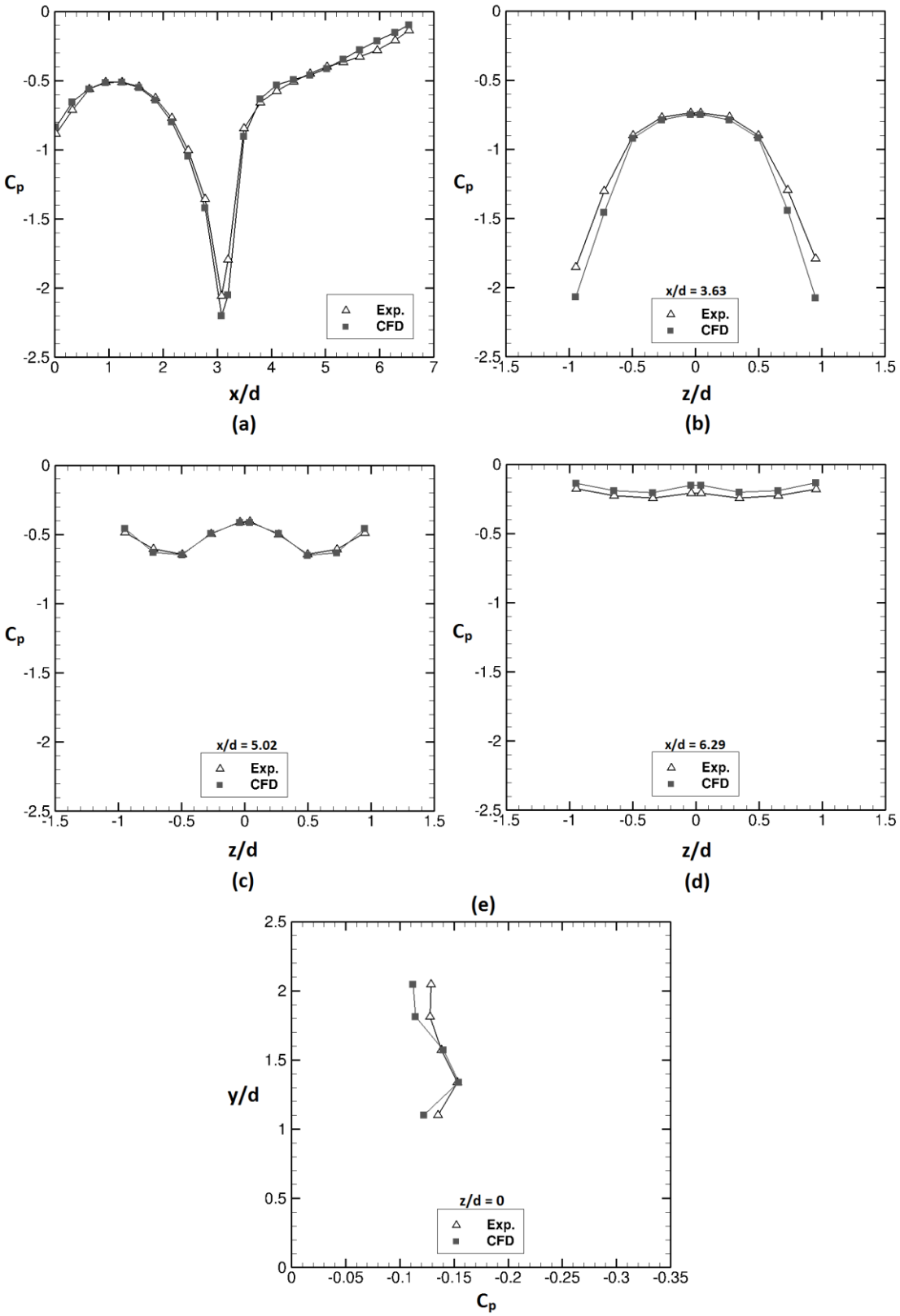

Figure 4-29: Measured (wind tunnel) and CFD-predicted surface pressure distributions for $h/d = 0.191$ along **(a)** underbody centreline **(b)** $x/d = 3.63$ **(c)** $x/d = 5.02$ **(d)** $x/d = 6.29$ **(e)** bluff-body base centreline $(z/d = 0)$

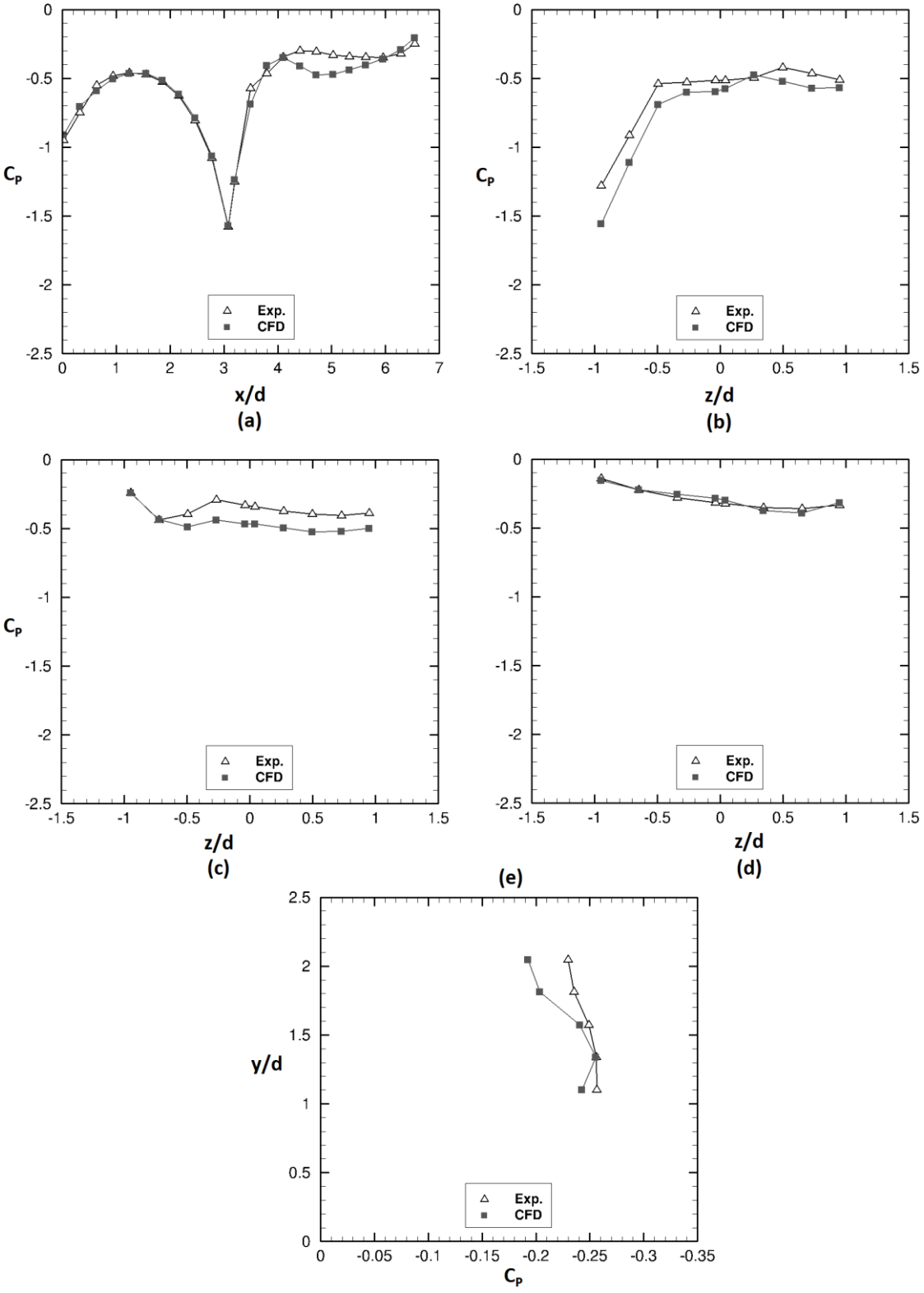

Figure 4-30: Measured (wind tunnel) and CFD-predicted surface pressure distributions for $h/d = 0.153$ along **(a)** underbody centreline **(b)** $x/d = 3.63$ **(c)** $x/d = 5.02$ **(d)** $x/d = 6.29$ **(e)** bluff-body base centreline $(z/d = 0)$

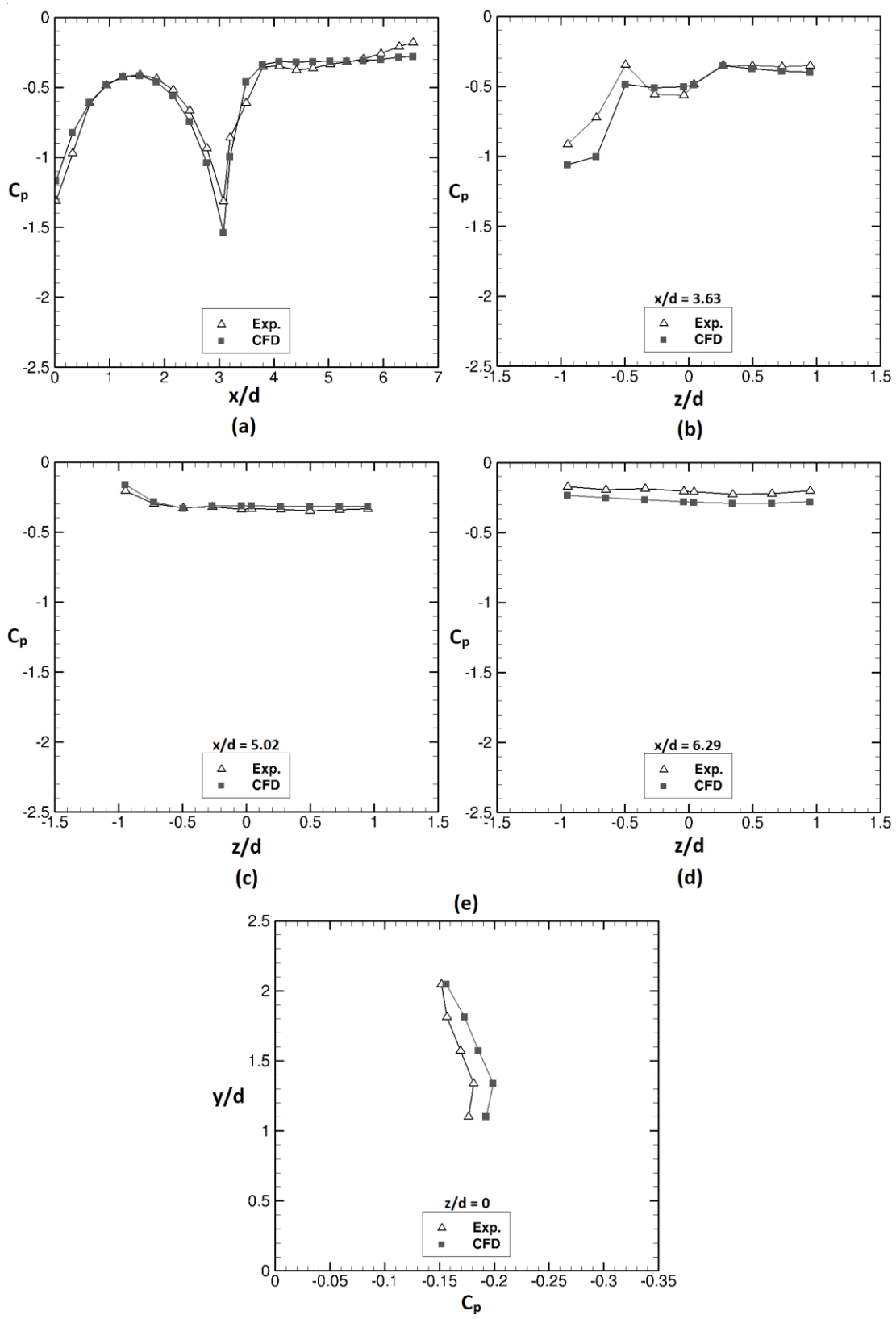

Figure 4-31: Measured (wind tunnel) and CFD-predicted surface pressure distributions for $h/d = 0.064$ along **(a)** underbody centreline **(b)** $x/d = 3.63$ **(c)** $x/d = 5.02$ **(d)** $x/d = 6.29$ **(e)** bluff-body base centreline $(z/d = 0)$

4.5 Surface Flow Features (CFD vs. Experiment)

In addition to the surface pressure distribution, the flow features on the diffuser ramp offers additional information on the downforce-generating behaviour of the diffuser. As in the case of the surface pressures, time-averaged CFD predicted the on-surface flow features captured in the wind tunnel experiments using fluorescent paint. Predicted surface flow features from the four flow regimes are represented by CFD investigations at $h/d = 0.764,\ 0.382,\ 0.191,\ 0.153$ and 0.064 .

In the force-enhancement (type A) diffuser flow as represented at $h/d = 0.764$ and 0.382 (Figures 4–32 and 4–33), the development of the longitudinal vortices are indicated by the predicted curved pathlines along both sides of the diffuser ramp. This implies that CFD (using IDDES) correctly predicted that the type A flow regime is symmetric. As in the equivalent wind tunnel flow visualisation case, the vortex pathlines predicted by CFD appear to have a stronger crossflow angle at $h/d = 0.382$ than at $h/d = 0.764$, hence indicating the increased vortex strength and flow velocity as ride height is reduced (as quantified with contour plots in Chapter 5). Downstream of the diffuser inlet, CFD predicted the detachment of the vortices from the diffuser side plates as indicated by the reversed curved lines between the streamwise curved lines of the vortices and the diffuser side plates (Figures 4–32 and 4–33). Also the weakening and separation towards the diffuser exit of the vortices from the diffuser ramp is predicted by the gradual straightening of the curvy vortex pathlines in the direction of the diffuser exit. The predicted flow features that indicate the separation and weakening of the longitudinal vortices as described are more distinguishable at $h/d = 0.382$ than at $h/d = 0.764$. This implies that the time-averaged CFD is correctly predicting the increasing adverse pressure encountered by the type A diffuser flow when ride height is reduced.

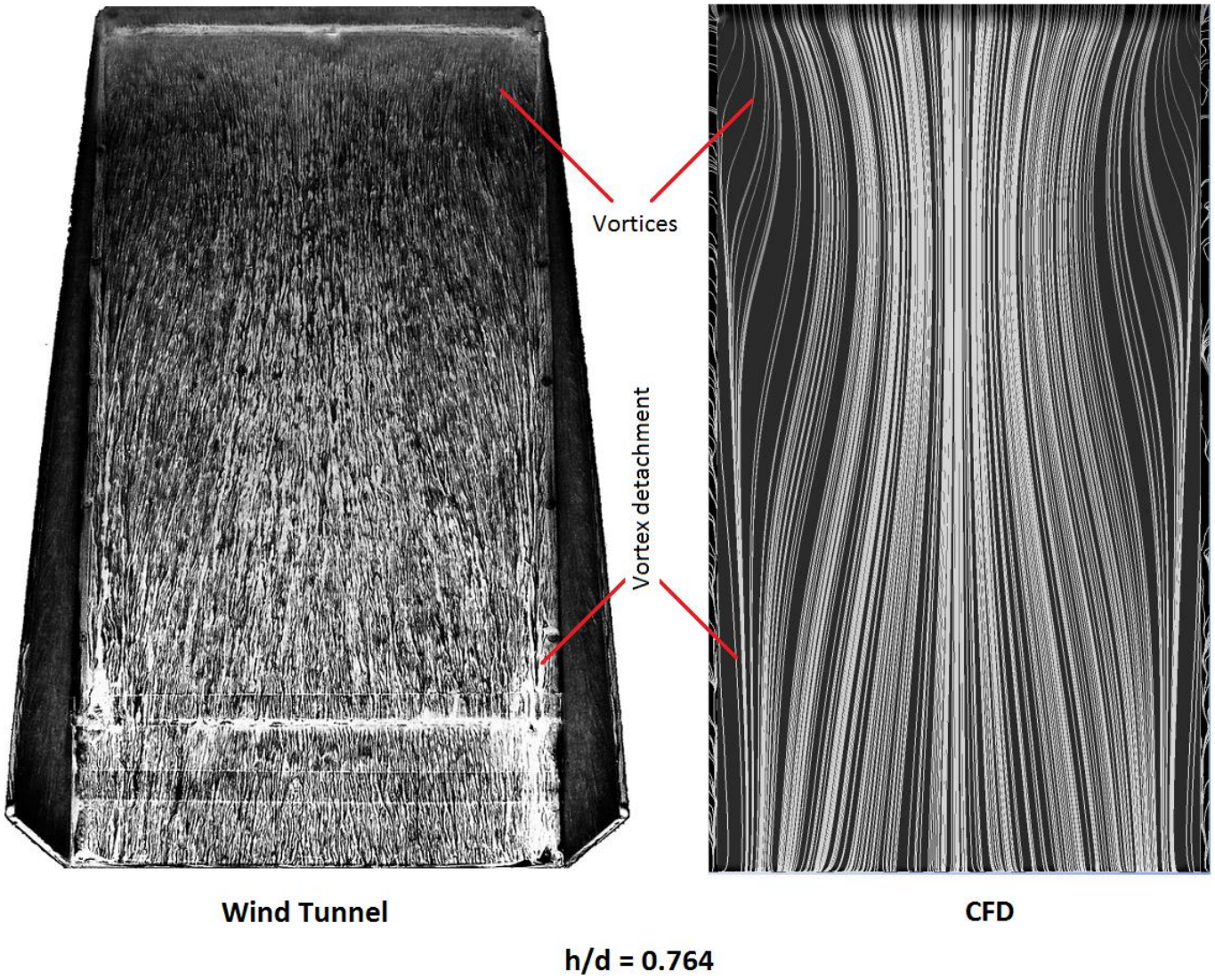

Figure 4-32: Experimental and CFD-predicted diffuser surface flow features for flow regime Type A (Flow direction from top to bottom)

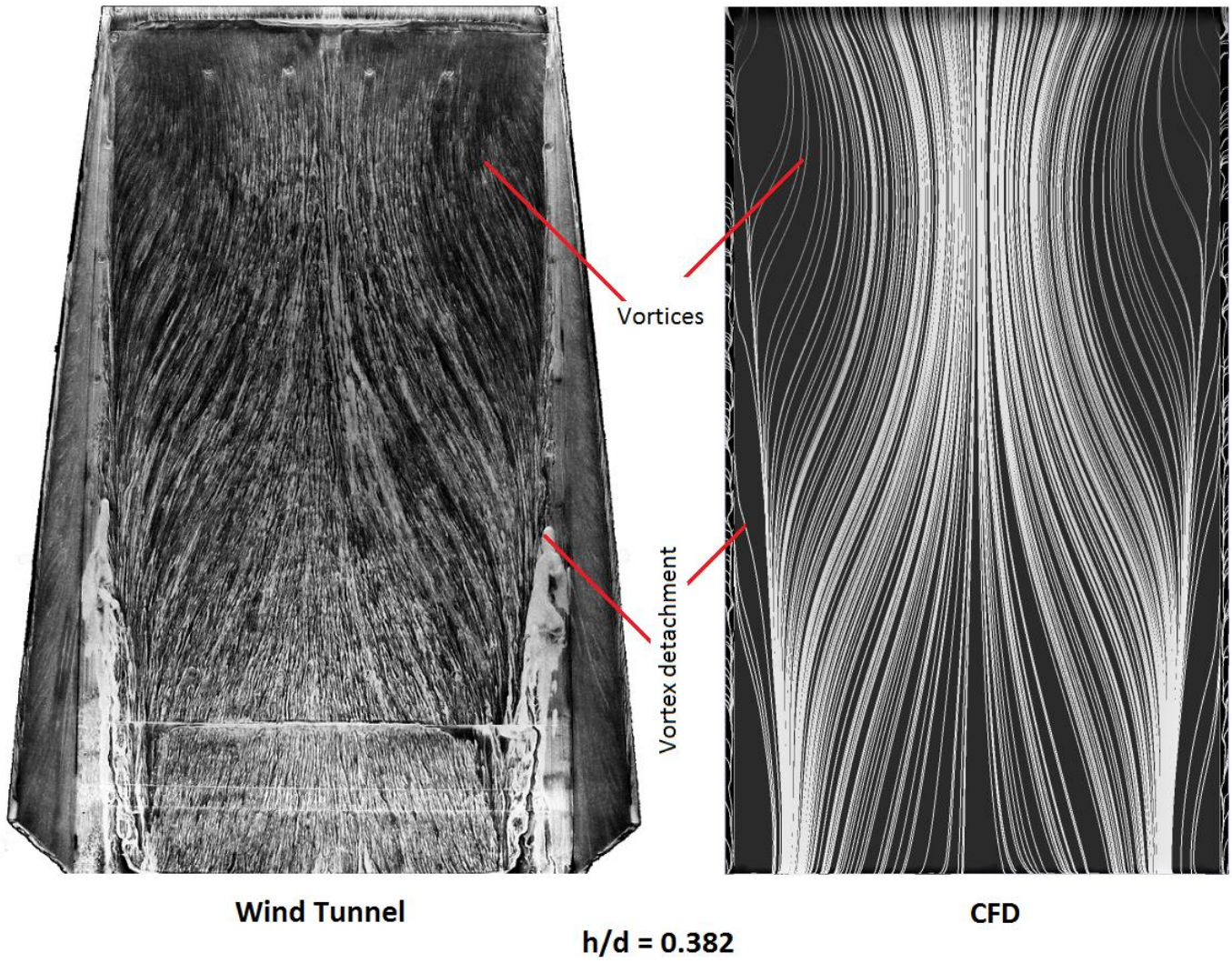

Figure 4-33: Experimental and CFD-predicted diffuser surface flow features for flow regime Type A (Flow direction from top to bottom)

At $h/d = 0.191$ (Figure 4–34) which represents the maximum force (type B) flow regime, the curvature of the predicted curved pathlines at the early part of the diffuser appear to be more profound relative to those at $h/d = 0.382$. Also, the predicted reversed curved pathlines and the diminishing curvature of the curved pathlines along both lengthwise sides of the diffuser are clearly visible. These predicted flow features support those of the equivalent surface flow features captured by fluorescent paint at $h/d = 0.191$. This implied that CFD (URANS) predicted the further increase in vortex strength, flow velocity and adverse pressure gradient associated with the symmetric flow at the maximum force ride height. However, the distinguishable separation bubble that originated from the centre of the diffuser inlet and traveled downstream of the inlet with diminishing presence is not clearly visible on the CFD representation of predicted flow pathlines. This means that although CFD predicted the further increase in flow velocity (as quantified with contour plots in Chapter 5) and suction distribution across the diffuser ramp, it underpredicted the further enhancement of adverse pressure gradient close to the centre of the diffuser inlet which induces the separation bubble.

For $h/d = 0.153$, the disappearance of the predicted curved pathlines along one side of the diffuser ramp surface as shown in the corresponding flow features captured by fluorescent paint (Figure 4–35) is clearly visible. The flow transformation indicated that CFD (IDDES) predicted the flow asymmetry associated with the flow reduction (type C) flow regime of $h/d = 0.153$. The predicted pathlines reveal a demarcation area (with reverse curved pathlines) along one side of the diffuser and this represents the separation of the flow from the diffuser endplates. On the side of the diffuser ramp surface where the surviving vortex is located, the predicted curved pathlines appear to be restricted close to the diffuser inlet. On the other side of the ramp, CFD predicted the diagonal pathlines as in the wind tunnel fluorescent paint case but the pathlines do not clearly represent a vortex breakdown. Nonetheless, the significantly curved pathlines of a vortex is not predicted on the stalled

side of the diffuser thus indicating the collapse of a vortex. Moreover, in the corresponding fluorescent paint case at $h/d = 0.153$, part of the predicted pathlines appeared to have reversed towards the diffuser inlet and the other part reversed around the side of the diffuser ramp where flow separation occurs. The predicted flow features as described, indicated that CFD predicted the separated and reversed diffuser flow responsible for the weakening of the surviving vortex and the collapse of the other vortex which previously existed in the type A and B flow regimes. As a result, CFD predicted the force reduction related to the type C flow regime.

In the low force (type D) flow regime represented at $h/d = 0.064$ and shown in (Figure 4–36), the flow pathlines predicted with CFD (URANS) was adequately validated by the equivalent flow features captured by fluorescent paint. The predicted pathlines captured the asymmetry of the flow through the predicted presence of a single vortex on one side of the diffuser ramp. The predicted curved pathlines that signified the presence of the surviving vortex remain restricted close to diffuser inlet and this indicated that the remaining vortex is severely weakened (as presented with contour plots in Chapter 5). Also, CFD predicted the severe adverse pressure gradient and flow separation induced across the diffuser ramp as represented by diagonal flow recirculation across the diffuser. As in the corresponding fluorescent paint case, the core of the predicted recirculation stretched diagonally across the diffuser and the profound recirculating pathlines which dominate the side of the diffuser where vortex breakdown occurred is clearly visible. As a result, the predicted flow features as described, are responsible for the reduced downforce predicted at $h/d = 0.064$.

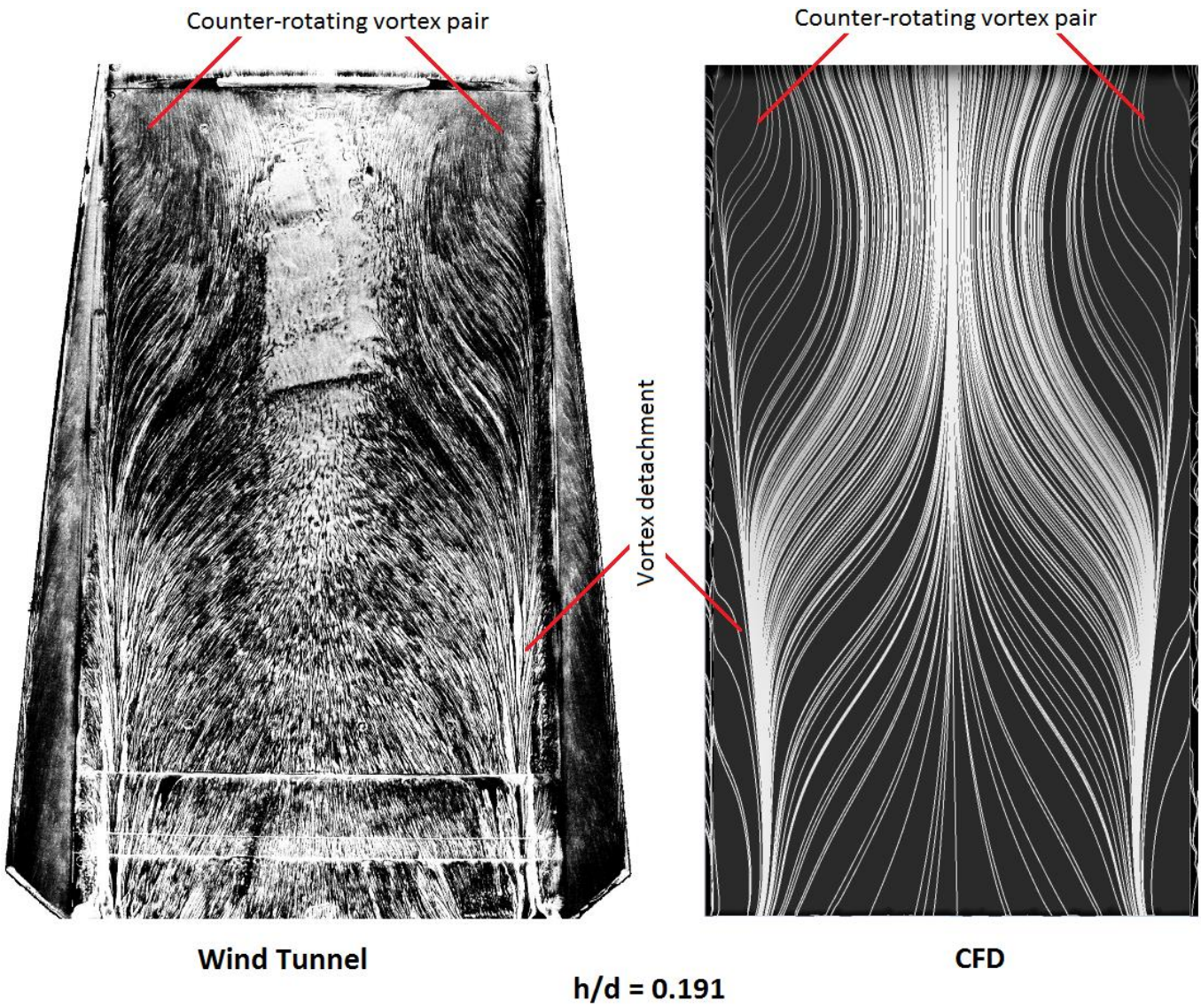

Figure 4-34: Experimental and CFD-predicted diffuser surface flow features for flow regime Type B (Flow direction from top to bottom)

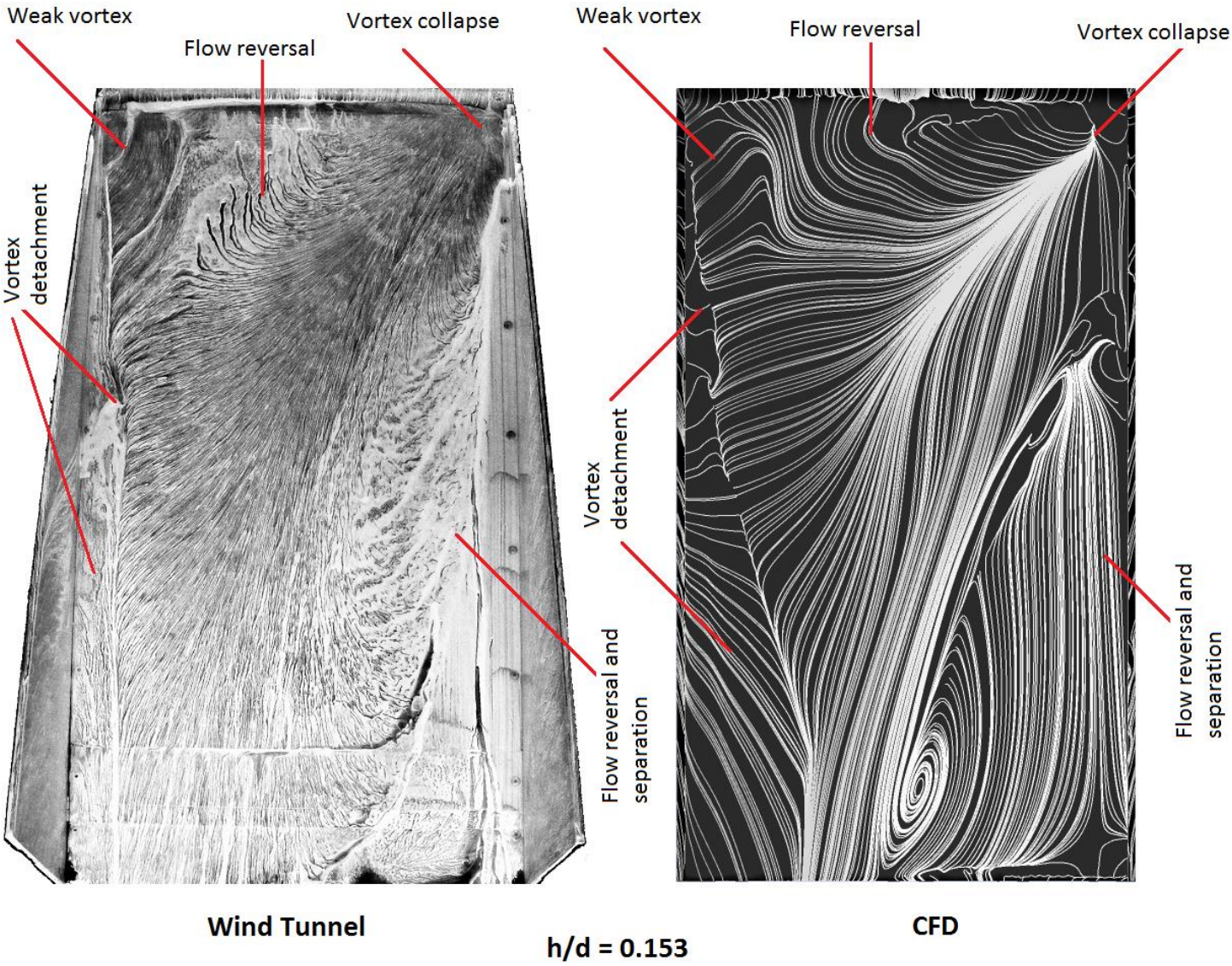

Figure 4-35: Experimental and CFD-predicted diffuser surface flow features for flow regime Type C (Flow direction from top to bottom)

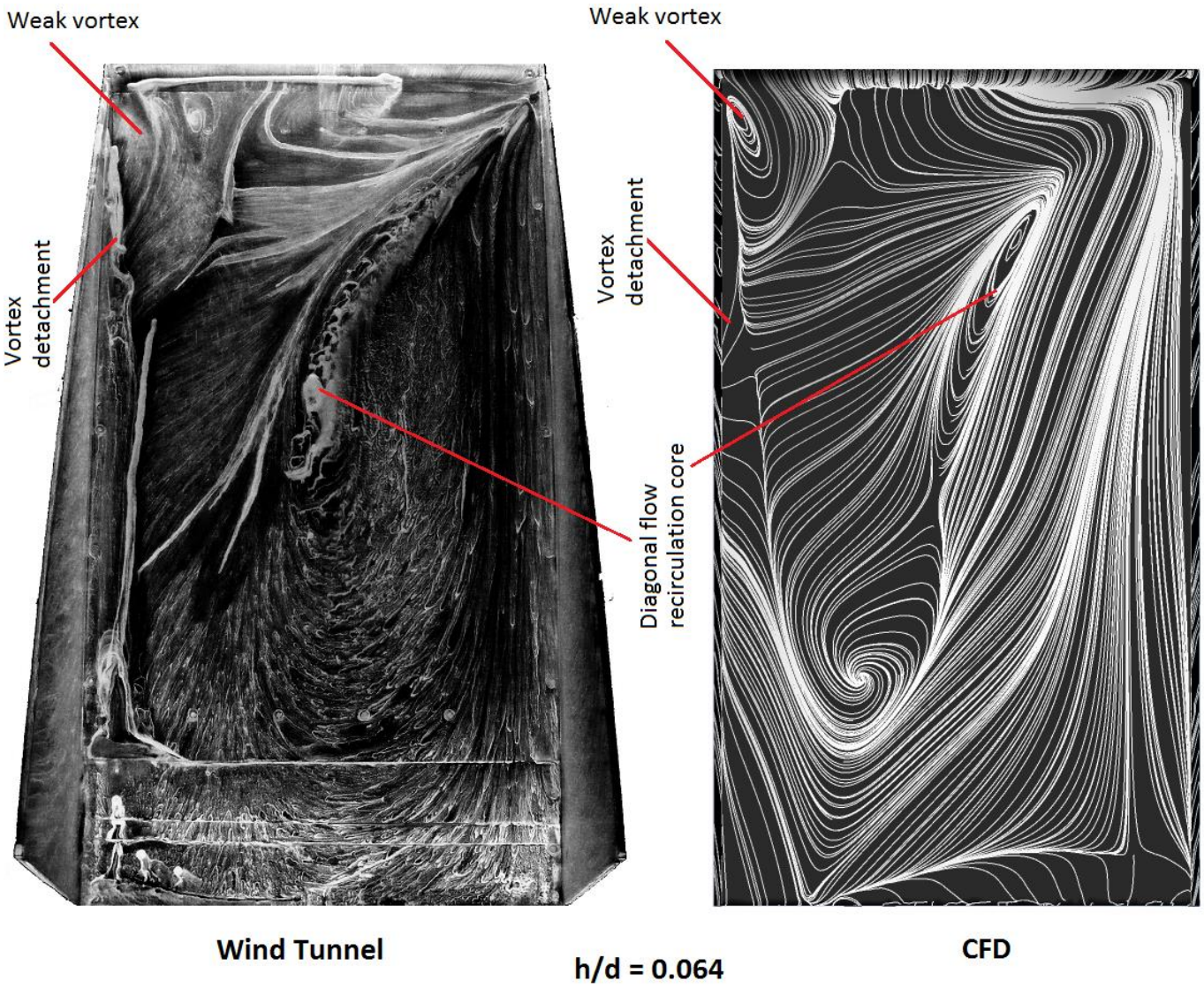

Figure 4-36: Experimental and CFD-predicted diffuser surface flow features for flow regime Type D (Flow direction from top to bottom)

4.6 Further Discussion

The surface flow visualization combined with the force and surface pressure measurements show that the complex flow physics of the diffuser has a significant aerodynamic impact. Across a wide range of ride heights, the diffuser was characterized by different flow characteristics that determined its aerodynamic performance. Notably, two major flow characteristics determine which of four flow types is prevalent: the peak suction at the diffuser inlet and the longitudinal vortices along both sides of the diffuser.

In the type A flow, the longitudinal vortex pair is formed when peak suction is established at the diffuser inlet feed by the diffuser pump down effect at the inlet (Cooper et al., 1998, 2000). The underbody centreline pressure measurements indicate that the intensity of the inlet suction increased with decreasing ride height until maximum downforce and drag is achieved at a critical ride height of the type B flow. Likewise, localised spanwise surface pressures and flow visualization indicated a similar increase in suction along both sides of the diffuser due to an increase in vortex strength. However, another flow characteristic that should be highlighted is the increasing adverse pressure gradient encountered by the flow as ride height is reduced. This was responsible for the detachment of the flow (including its vortical components) from the surface of the diffuser.

The flow physics observed under the type C and D flow regimes is the antithesis of the flow physics observed under the type A and B flow regimes. The diffuser flow of the type C and D flow regimes was asymmetric, as defined by the decrease in inlet peak suction and the complete breakdown of one of the longitudinal vortices. In addition, flow separation at the diffuser inlet and downstream flow recirculation were prevalent in the type C and D flow regimes. However, as observed under the type A regime to the B regime, the intensity of the flow characteristics increased when the ride height was reduced from the type C to the type D regime.

One phenomenon that generates further interest is the basis for the selection of one of the two longitudinal vortices for vortex breakdown. At the type C and more so the type D flow regimes, the boundary layer towards the diffuser inlet dominates the underbody flow entering the diffuser inlet with the boundary layer thickness reducing the effective ride height. This indicates that the boundary layer-dominated flow influences the flow asymmetry associated with the type C and D flow regimes. Even so, Senior & Zhang (2000) and Senior (2002) state that the thickness of the boundary layer ($\sim 15\, mm$) as estimated in their studies was smaller than the ride height at which the onset of flow asymmetry was observed. Therefore, the bi-stability of the asymmetric flow cannot be fully explained by the retardation of the boundary layer flow, an error in aligning the diffuser body model or the unevenness of the underbody of the model. Despite this, the spanwise surface pressures for the maximum downforce regime in the present study indicate that one of the vortices of the pair generated suction that was ~3.4% greater than the other vortex, despite the symmetry of the diffuser flow. Also, the stronger vortex appeared to be the surviving vortex in the type C and type D regimes, as reported by Senior & Zhang (2000). Thus the vortex strength (see velocity profiles, vorticity and streamwise velocity contours presented in Chapter 5) of the longitudinal vortex pair in the maximum-force flow regime (type B) determines which vortex survives in the type C and type D regimes. The flow visualization for the force-reduction and low-force regimes indicated that the stronger vortex appeared also to have pulled flow from the other side of the diffuser where vortex bursting occurred (hence the diagonal flow pathlines).

Time-averaged transient CFD employed in this study appeared to have generally predicted the flow physics across the four flow regimes. The use of the transition turbulence models enabled the prediction of the laminar-to-turbulent transition (separation bubble) around the location where the nose section merges with the rest of the bluff body (Figure 4–37). As a result, the flow physics downstream of that location were generally captured even though there were relative deviations in predicted force and surface pressures.

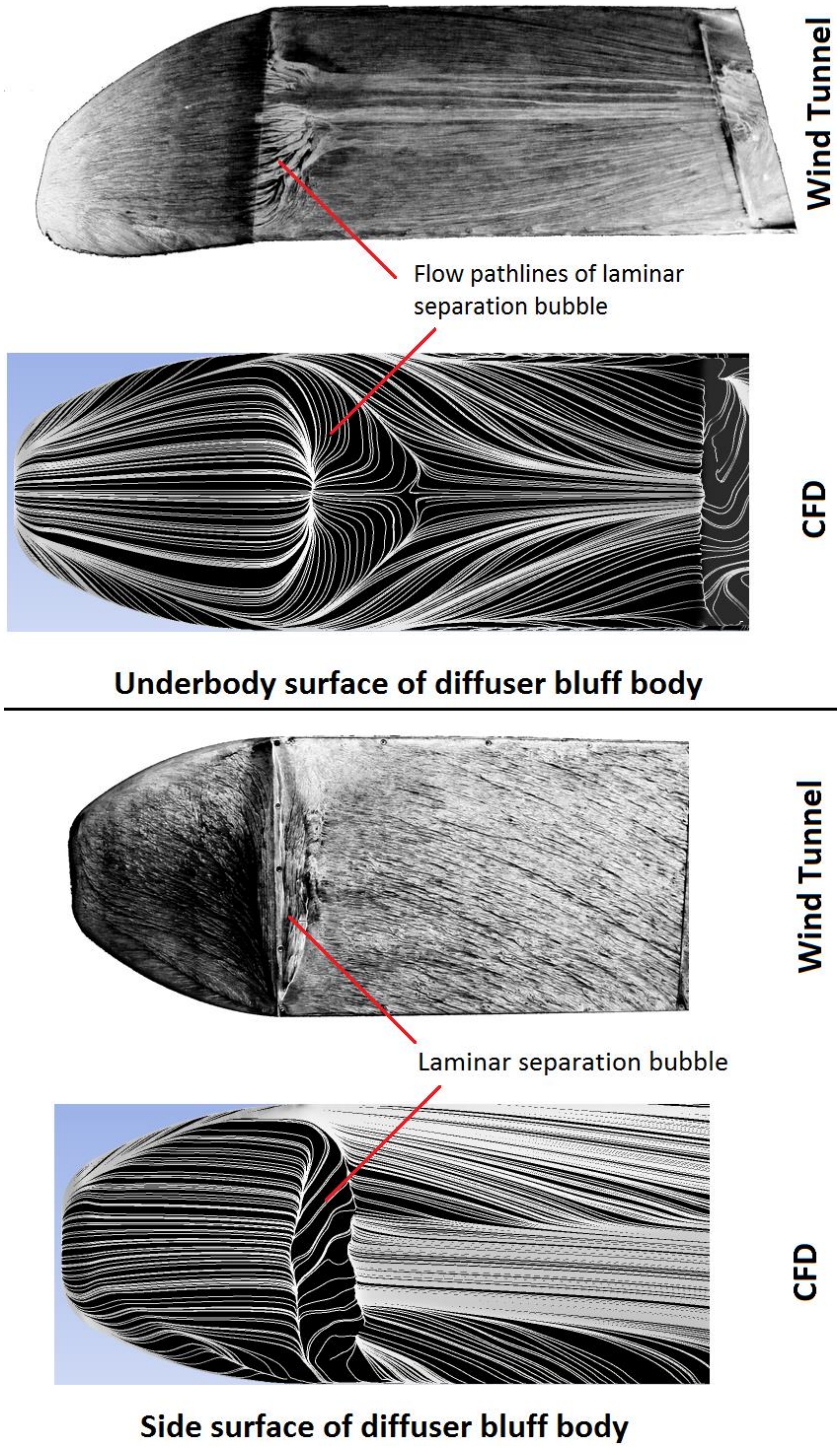

Figure 4-37: Experimental and CFD-predicted flow pathlines on underbody and side surfaces of the diffuser bluff body (Flow direction from left to right)

4.7 Summary

The experimental and computational investigations presented in this chapter validate in general terms, the findings established in previous research works on this subject. The flow physics of a baseline diffuser bluff body indicate that in ground effect, the diffuser is a downforce-generating device. In near proximity to the ground plane, the diffuser inlet converts high-velocity flow travelling through it to low static pressure and towards the diffuser exit the diffuser flow gradually transforms to a low-velocity flow with a static pressure recovery at the diffuser exit. Under a wide range of ride heights, the diffuser flow exhibits four distinct flow regimes.

In the force-enhancement (type A) flow regime, longitudinal counter-rotating vortices are formed and the adverse pressure gradient, encountered by the flow towards the diffuser exit, detaches the vortices from the diffuser ramp surface and endplates. In the maximum-force (type B) flow regime, the downforce produced by the diffuser reaches it maximum due to enhanced suction at the diffuser inlet. Also, the vortices are strengthened at the early part of the diffuser and the flow around the lengthwise centreline of the diffuser separates before reattaching towards the diffuser exit. The force-reduction (type C) flow regime induces a breakdown of one of the vortices, causing the 3—D diffuser flow to become asymmetric. In addition, the unsteady diffuser flow becomes increasingly separated from the diffuser ramp, flow reversal occurs and downforce reduces. In the low-force (type D) flow regime, the flow entering the diffuser is largely dominated by the boundary layer flow at the diffuser inlet. Also, the surviving vortex is severely weakened with flow separation and recirculation becoming increasingly prevalent. As a result, the flow is very unstable and a low amount of downforce is generated.

Chapter 5

Plane Diffuser (Baseline): Edge Vortex Behaviour and Velocity Profiles

In the previous chapter, the diffuser flow physics was presented and analysed in terms of the behaviour of force, surface pressure distribution and on-surface flow structure on the diffuser ramp. However, the flow physics that govern the development and breakdown of the longitudinal vortices and reveal further insights of the diffuser flow were not presented in a detailed analysis. Hence, this chapter is focused on delineating flow field quantities predicted by CFD that define the longitudinal vortex pair behaviour between the diffuser inlet and exit. CFD has been used due to the challenges in setting-up the LDV system in a three-component arrangement to measure non-intrusively the flow quantities within the diffuser section. Despite this, measured and predicted boundary layer profiles of the 3—D flow across the diffuser inlet and in the separated near-wake flow of the bluff body are also presented and discussed.

5.1 Diffuser Edge Vortex Development

The longitudinal vortex pair in the diffuser flow travel in the streamwise direction along the sides of the diffuser. The vortices develop at both sides of the diffuser inlet and are induced by the pressure difference inside and outside the diffuser. The progression of the vortices along the length of the diffuser is enhanced by the inward vortical roll-up of entrained flow underneath the diffuser endplates. The streamwise vortex pair rotates around their cores in counter rotating directions and similar to longitudinal wing-tip vortices, the axial speed and vorticity at the early part of the vortex core formation is stronger than at the latter part of the vortex development (as presented subsequently in this Chapter).

The vortex development along the diffuser sides determines suction levels in those locations. At the early part of the diffuser where the streamwise velocity induced by the vortices is higher than surrounding flow velocity, the surface pressures along the diffuser sides become increasingly negative. Also, the presence of both vortices and the breakdown of one of the vortices respectively determine the symmetry and asymmetry of the diffuser flow. In the types A and B diffuser flows, the presence of the vortex pair maintains the symmetry of the diffuser flow thus enhancing downforce. However, in the types C and D diffuser flows, breakdown of one of the longitudinal vortices causes the diffuser flow to become asymmetric and induces a loss in downforce.

In this chapter, the development of the counter-rotating vortex pair are presented on three measurement planes at the same streamwise locations of the spanwise surface pressure measurements in Chapter 4. The three spanwise planes include: a plane located close to the diffuser inlet ($x/d = 3.63$); a second plane close to the mid-section of the diffuser length ($x/d = 5.02$); and a third plane close to the diffuser exit ($x/d = 6.29$). Also, the spanwise planes are presented for all four flow regimes (A to D) represented by $h/d = 0.764$, 0.382, 0.191, 0.153, and 0.064. The counter-rotating directions of the longitudinal vortices within the diffuser for $h/d = 0.764$ remain present downstream of the diffuser inlet as seen by the total velocity vectors on the spanwise plane at $x/d = 5.02$ which is near the diffuser lengthwise mid-section (Figure 5—1). Near the diffuser inlet at $x/d = 3.63$ (Figure 5—2) the contour regions of positive and negative velocities on both sides of the diffuser show that the counter-rotating diffuser vortices induce a cross flow into the diffuser and the velocities of the inflow reduces towards the diffuser centre. The enhancement of the cross flow velocity contours from the type A to the type B flow regime indicates increased vortex strength and the reduced cross flow velocities of the asymmetric flow in the type C and D regimes indicates that the surviving vortex is weak.

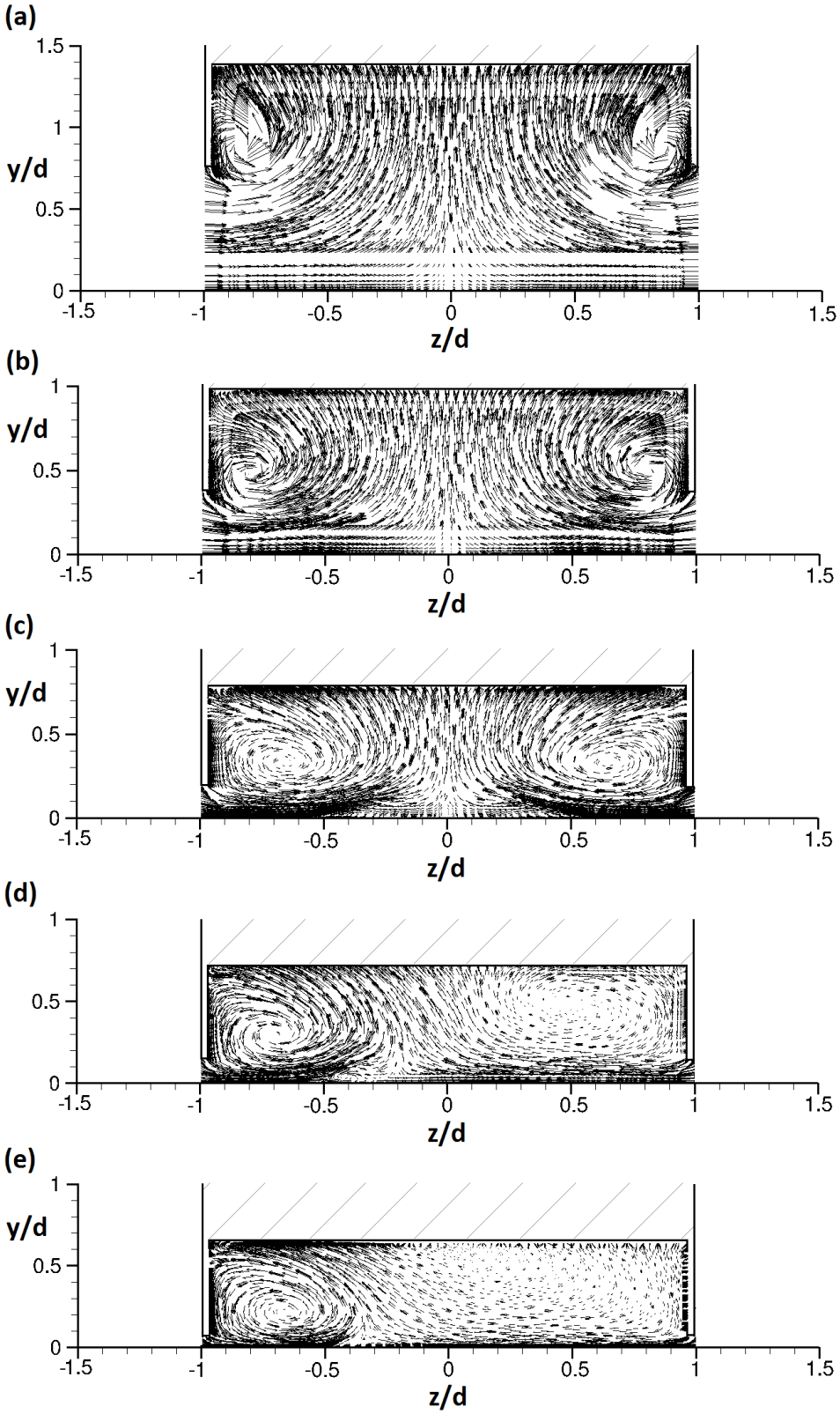

Figure 5-1: Total velocity vectors $\left(\vec{\boldsymbol{U}}\right)$ predicted with CFD on spanwise plane at $x/d = 5.02$ showing the counter-rotating directions of the diffuser vortices at: **(a)** $h/d = 0.764$ (flow regime A) **(b)** $h/d = 0.382$ (flow regime A) **(c)** $h/d = 0.191$ (flow regime B) **(d)** $h/d = 0.153$ (flow regime C) **(e)** $h/d = 0.064$ (flow regime D)

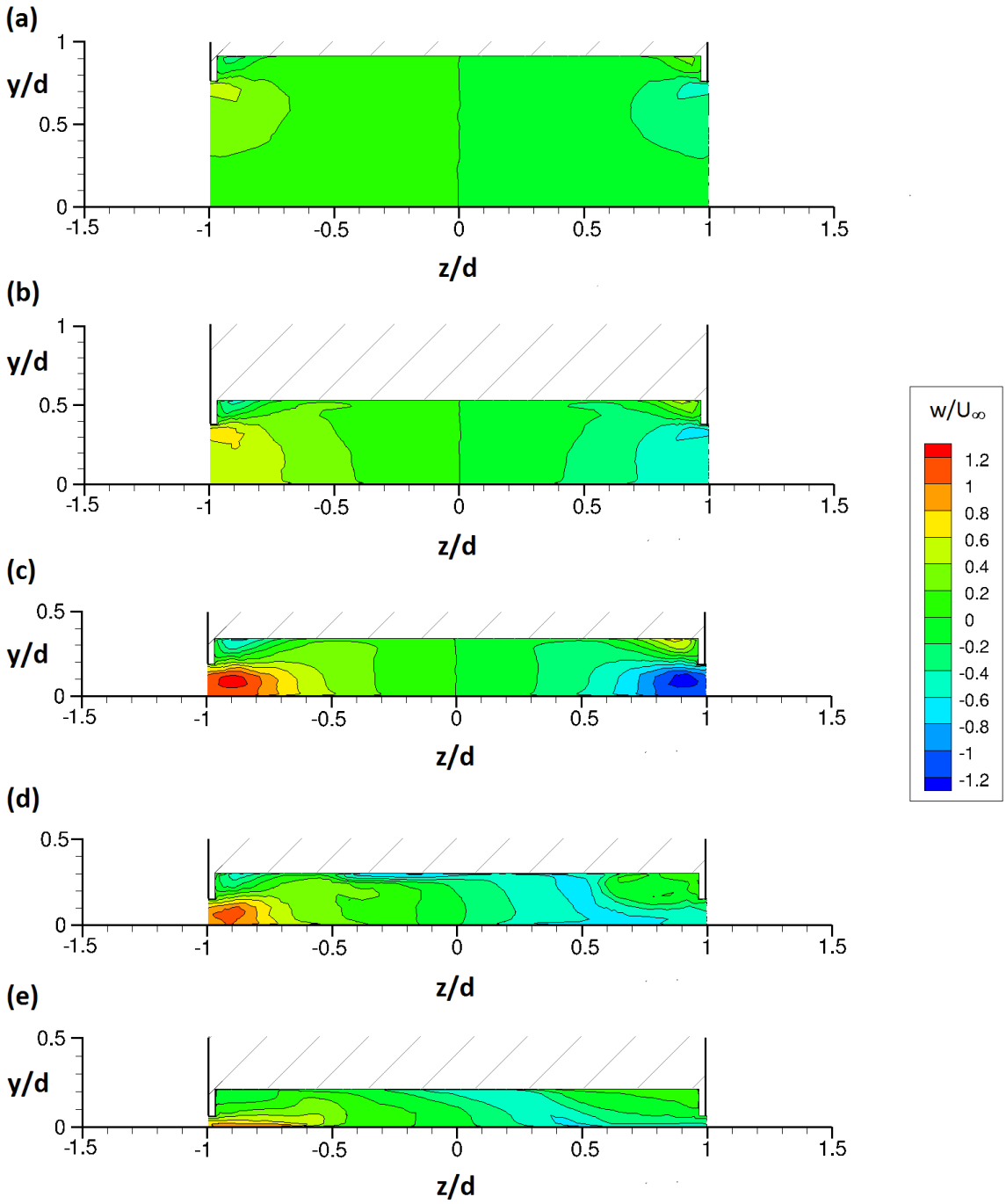

Figure 5-2: Crossflow velocity ($\boldsymbol{w}$) contours predicted with CFD on spanwise plane near the diffuser inlet ($x/d = 3.63$) highlighting the inflow induced by the counter-rotating vortices at: **(a)** $h/d = 0.764$ **(b)** $h/d = 0.382$ **(c)** $h/d = 0.191$ **(d)** $h/d = 0.153$ **(e)** $h/d = 0.064$

In the identification of the 3—D vortical flow structures, the symmetric and asymmetric components of the velocity gradient tensor ∇u are defined (Jeong & Hussain,1995). The symmetric S, and asymmetric Ω components of the velocity gradient tensor at any given point in the flow are expressed in Equation 5.1 to 5.3 as:

$$\nabla u = S + \Omega \tag{5.1}$$

Where,

$$S_{ij} = \frac{1}{2}\left(u_{i,j} + u_{j,i}\right) \tag{5.2}$$

$$\Omega_{ij} = \frac{1}{2}\left(u_{i,j} - u_{j,i}\right) \tag{5.3}$$

The decomposition of S and Ω can be described as the separation of the rate of strain tensor S_{ij}, and vorticity tensor Ω_{ij}. The criterion Q applies the decomposition to identify the vortices and is expressed in Equation 5.4 as a positive ($Q > 0$) second invariant of ∇u.

$$Q = \frac{1}{2}(\|\Omega\|^2 - \|S\|^2) \tag{5.4}$$

The $Q\text{–}criterion$ of the time-averaged velocity magnitude for the force-enhancement (type A flow regime) at $h/d = 0.764$ and 0.382 is shown in Figure 5−3 where $Q = 150{,}000$ to highlight clearly the features of the longitudinal vortices. The presence of the longitudinal counter-rotating vortex pair is distinct and is shown to originate from the lengthwise sides close to the diffuser inlet. Also, the detachment of the streamwise vortices from the side plates as indicated by the on-surface flow pathlines (Figure 5—3) is clearly visible. The velocity contours of the vortices indicate that the strength of the vortices gradually reduces downstream of the diffuser inlet. However, there is no occurrence of vortex breakdown within the diffuser. Relative to the vortices for $h/d = 0.764$, the vortices for $h/d = 0.382$ appear to be increased in size

and the velocities at the early part of the vortices close to the diffuser inlet are higher than those at the same location for $h/d = 0.764$. As a result, there is a corresponding increase in downforce as ride height is lowered within the type A flow regime. At the force-reduction (type C flow regime) ride height at $h/d = 0.153$ (as shown in Figure 5–4), the Q–$criterion$ of the time-averaged velocity magnitude at $h/d = 0.153$ indicates the presence of a solitary vortex that appears to gradually weaken downstream of the diffuser inlet.

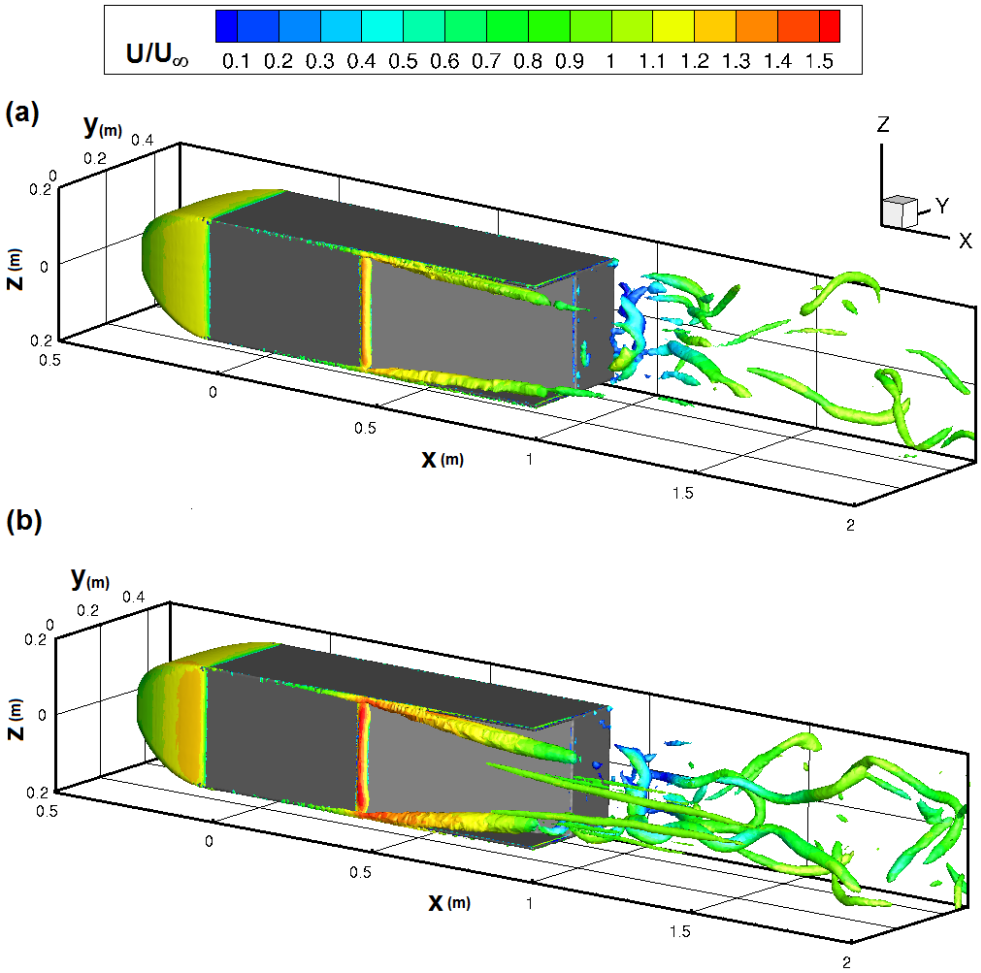

Figure 5-3: CFD iso-surface of the $\boldsymbol{Q}$–$\boldsymbol{Criterion}$ ($\boldsymbol{Q = 150,000}$) highlighting the longitudinal vortex pair formed within the diffuser at the normalised ride heights of the force-enhancement flow regimes: **(a)** $h/d = 0.764$ and **(b)** $h/d = 0.382$. The iso-surface is coloured by time-averaged total velocity $\left(\boldsymbol{U = \sqrt{u^2 + v^2 + w^2}}\right)$

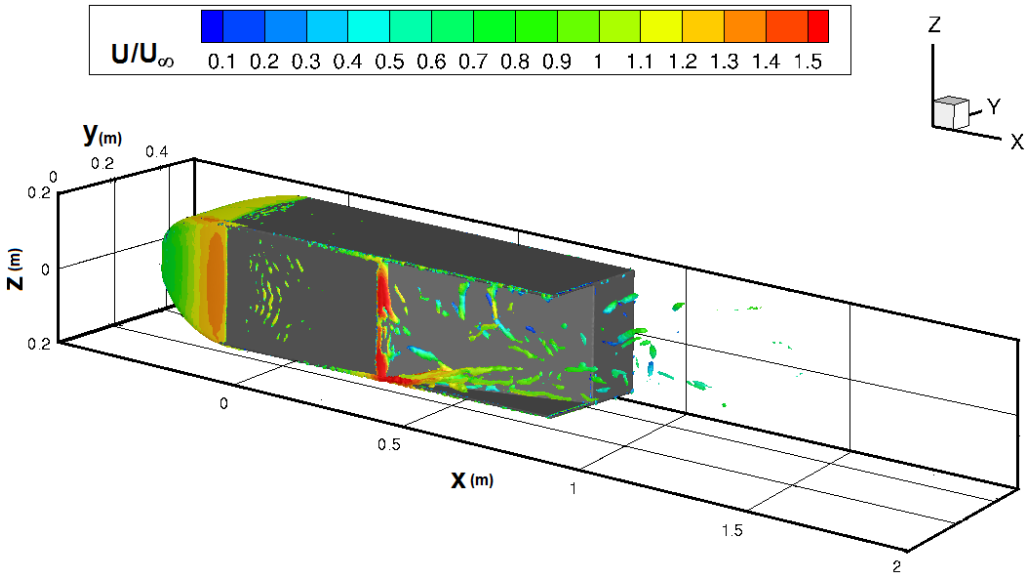

Figure 5-4: CFD iso-surface of the $\boldsymbol{Q}$–$\boldsymbol{Criterion}$ ($\boldsymbol{Q = 150,000}$) highlighting the solitary surviving longitudinal vortex within the diffuser at the normalised force-reduction flow regime ride height of $h/d = 0.153$. The iso-surface is coloured by time-averaged total velocity $\left(\boldsymbol{U = \sqrt{u^2 + v^2 + w^2}}\right)$

5.1.1 Vortex behaviour in flow regime A

The behaviour of the streamwise vortices for the type A flow regime ride heights at $h/d = 0.764$ and 0.382 is further highlighted on the spanwise planes (on $x/d = 3.63,\ 5.02,$ and 6.29) within the diffuser. At $h/d = 0.764$ (Figure 5–5), the velocity across the span of the diffuser inlet is above freestream, hence confirming the existence of peak velocity which in turn is responsible for the diffuser inlet peak suction captured by the surface pressure distribution measurements. The streamwise velocity contours show shear layers that roll up away from both end plates thus, indicating the presence of the vortex pair. The rolled-up shear layers appear to be small and concentrated. Above the area between both vortices (Figure 5–5), the horizontal shear layers indicate the presence of velocity gradient encountered by the streamwise flow. However, below the lateral shear layers, the streamwise flow velocity is above freestream velocity. From $x/d = 3.63$ to 6.29, the gradual velocity reduction which in turn is responsible for the pressure recovery downstream of the diffuser inlet is indicated with the reduction in the

size of the contour region with velocities above freestream velocity. The gradual reduction (from $x/d = 3.63$ to 6.29) in streamwise vorticity at the cores of the vortex pair confirms the reduction in strength of the vortices downstream of the diffuser inlet (Figure 5–6). However, the presence of the vortex pair vorticity contours from $x/d = 3.63$ to 6.29 indicates that vortices remained strong and concentrated within the diffuser. Towards the diffuser exit, the increase in the production of TKE (turbulent kinetic energy) from $x/d = 3.63$ to 6.29 (Figure 5–7) means that there is a gradual increase in turbulence as the vortices travel downstream of the diffuser inlet.

The vortex flow physics for $h/d = 0.382$ (from $x/d = 3.63$ to 6.29) appeared to be generally an enhancement of the characteristics for $h/d = 0.764$. This is indicative of the increase in downforce and suction accompanied with the reduction of ride height in flow regime A. The streamwise velocity (Figure 5–8) and vorticity (Figure 5–9) contours of the vortices for $h/d = 0.382$ relative to $h/d = 0.764$ indicate a general enhancement of diffuser flow velocity hence an increase in vortex strength. This also means that the axial velocity of the local counter-rotating vortices has gained strength relatively to that of $h/d = 0.764$. Furthermore, the relative increase (relative to $h/d = 0.764$) in vortex diffusion as the streamwise velocity of the vortices reduces towards the diffuser exit has induced a corresponding increase in TKE as shown in Figure 5–10.

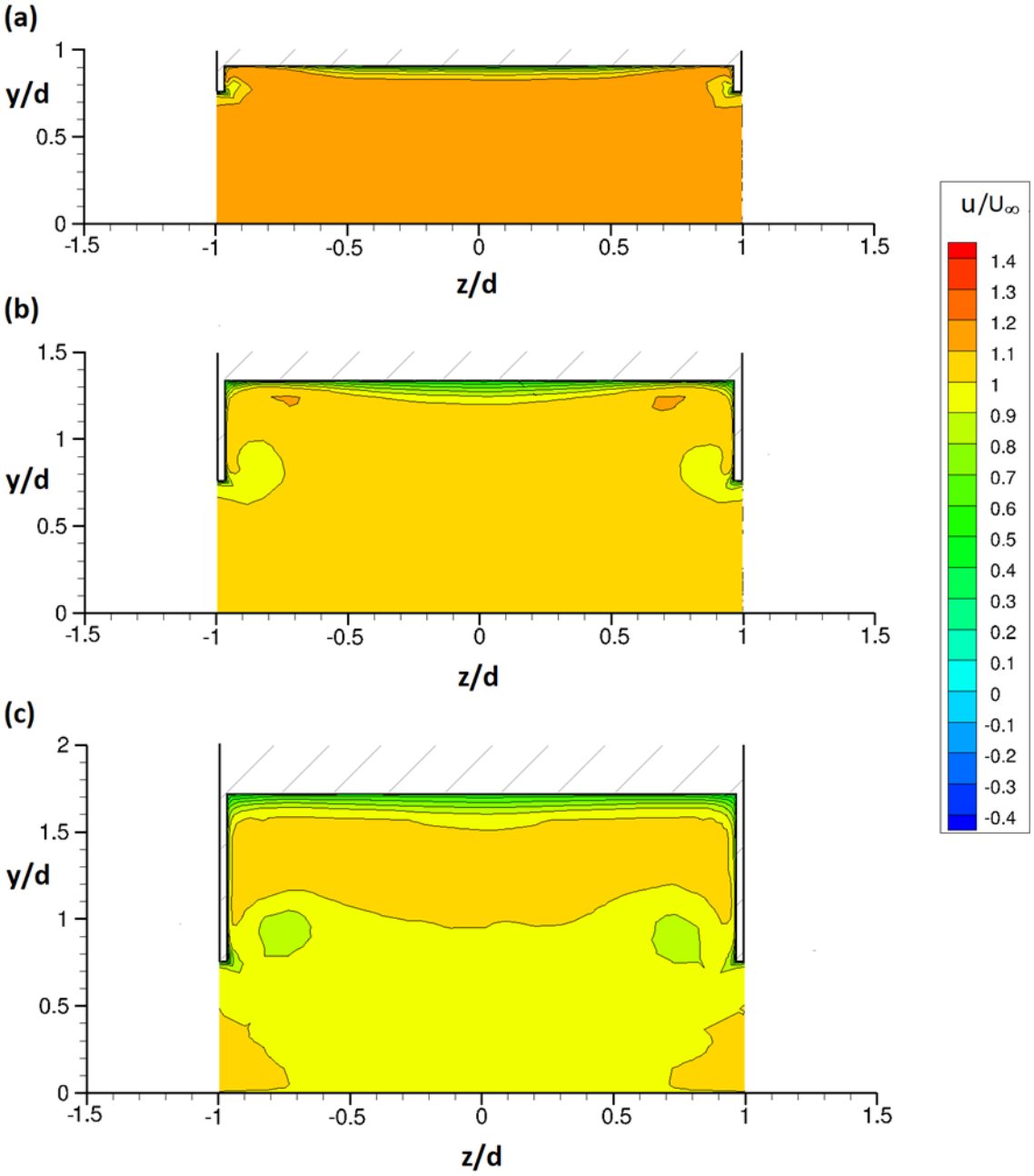

Figure 5-5: Streamwise velocity $(\boldsymbol{u})$ contours predicted with CFD at $h/d = 0.764$ for spanwise planes on: **(a)** $x/d = 3.63$ **(b)** $x/d = 5.02$ **(c)** $x/d = 6.29$

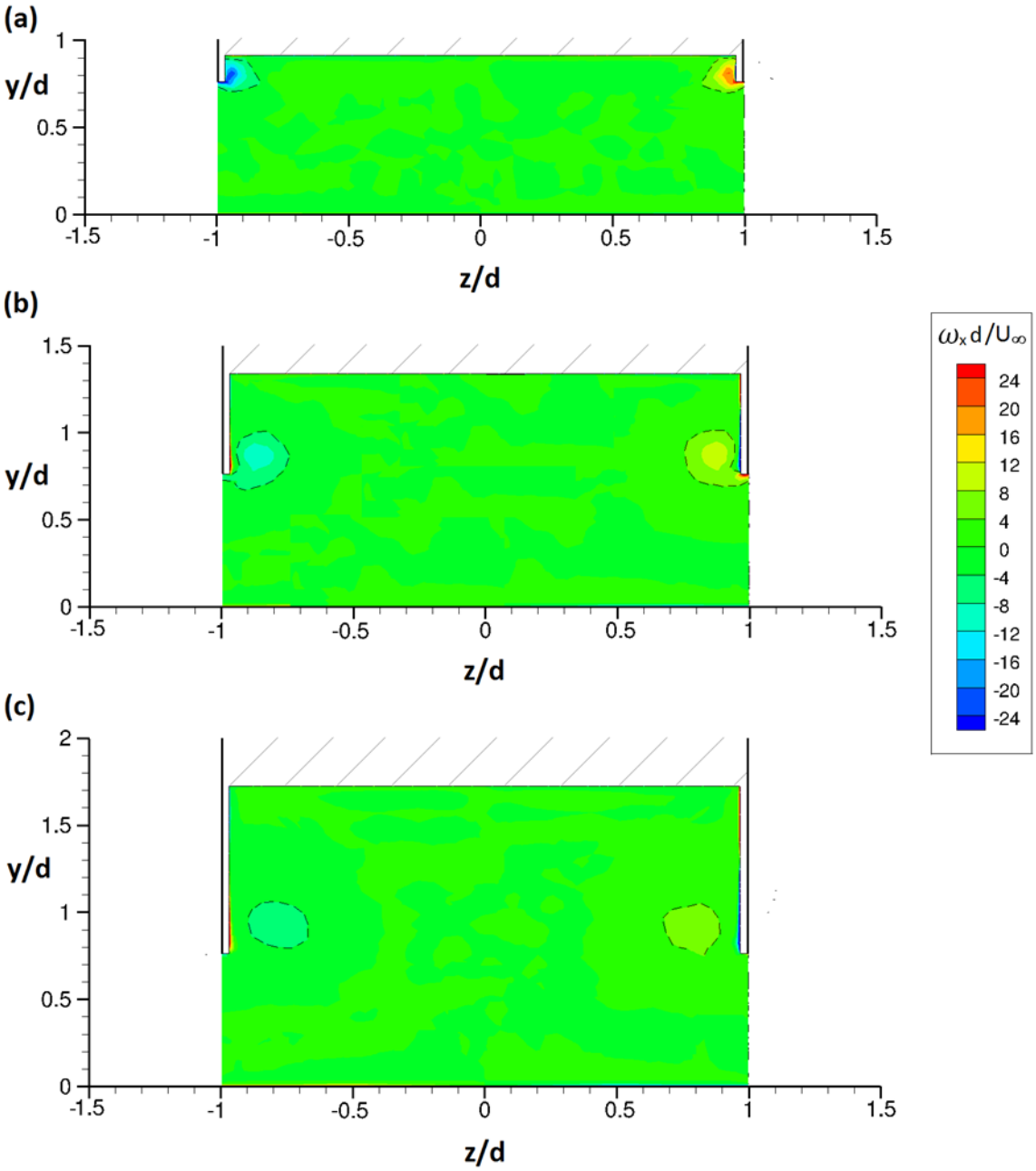

Figure 5-6: Streamwise vorticity ($\boldsymbol{\omega_x}$) contours predicted with CFD at $h/d = 0.764$ for spanwise planes on: **(a)** $x/d = 3.63$ **(b)** $x/d = 5.02$ **(c)** $x/d = 6.29$

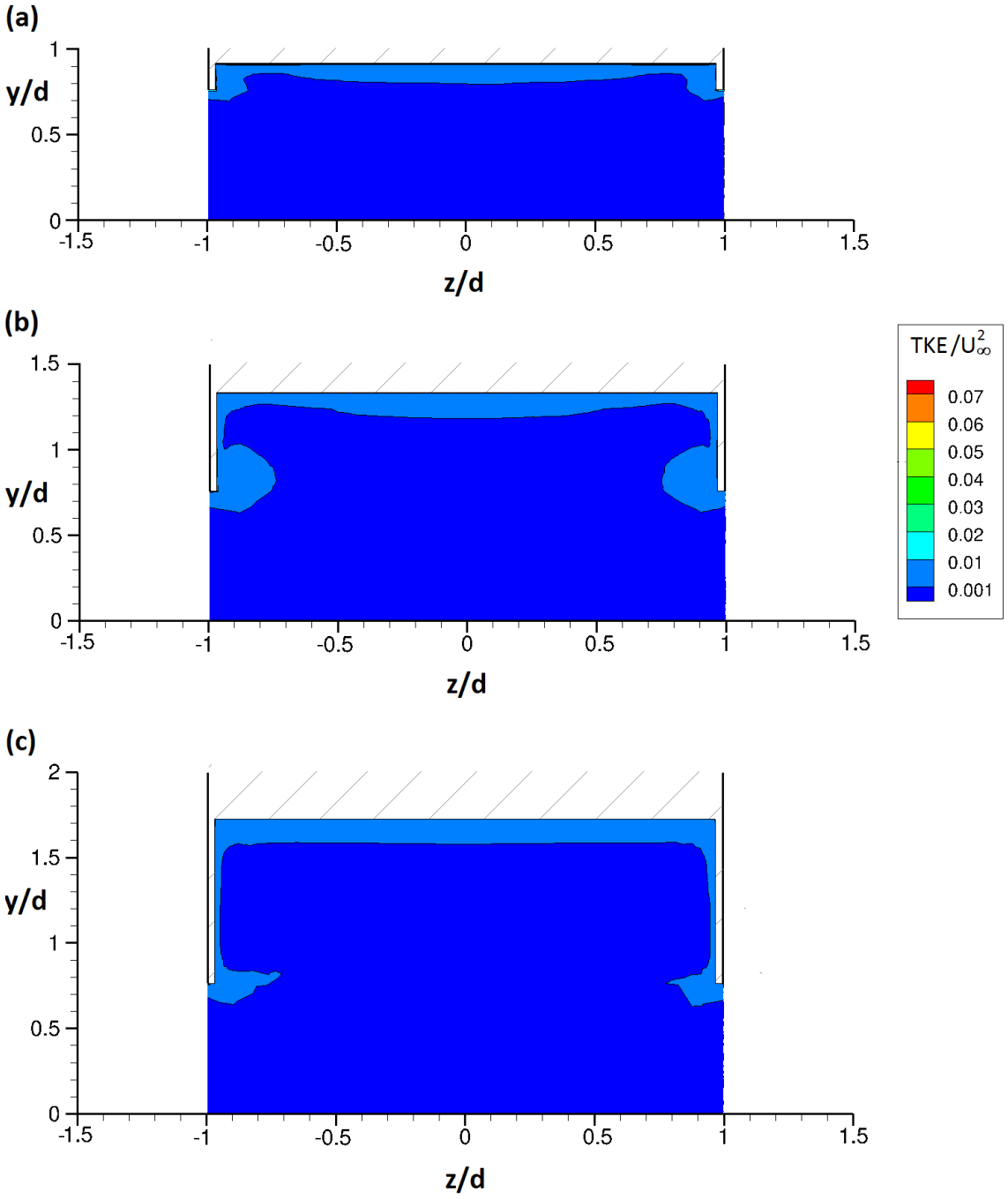

Figure 5-7: Turbulent kinetic energy (**TKE**) contours predicted with CFD at $h/d = 0.764$ for spanwise planes on: **(a)** $x/d = 3.63$ **(b)** $x/d = 5.02$ **(c)** $x/d = 6.29$

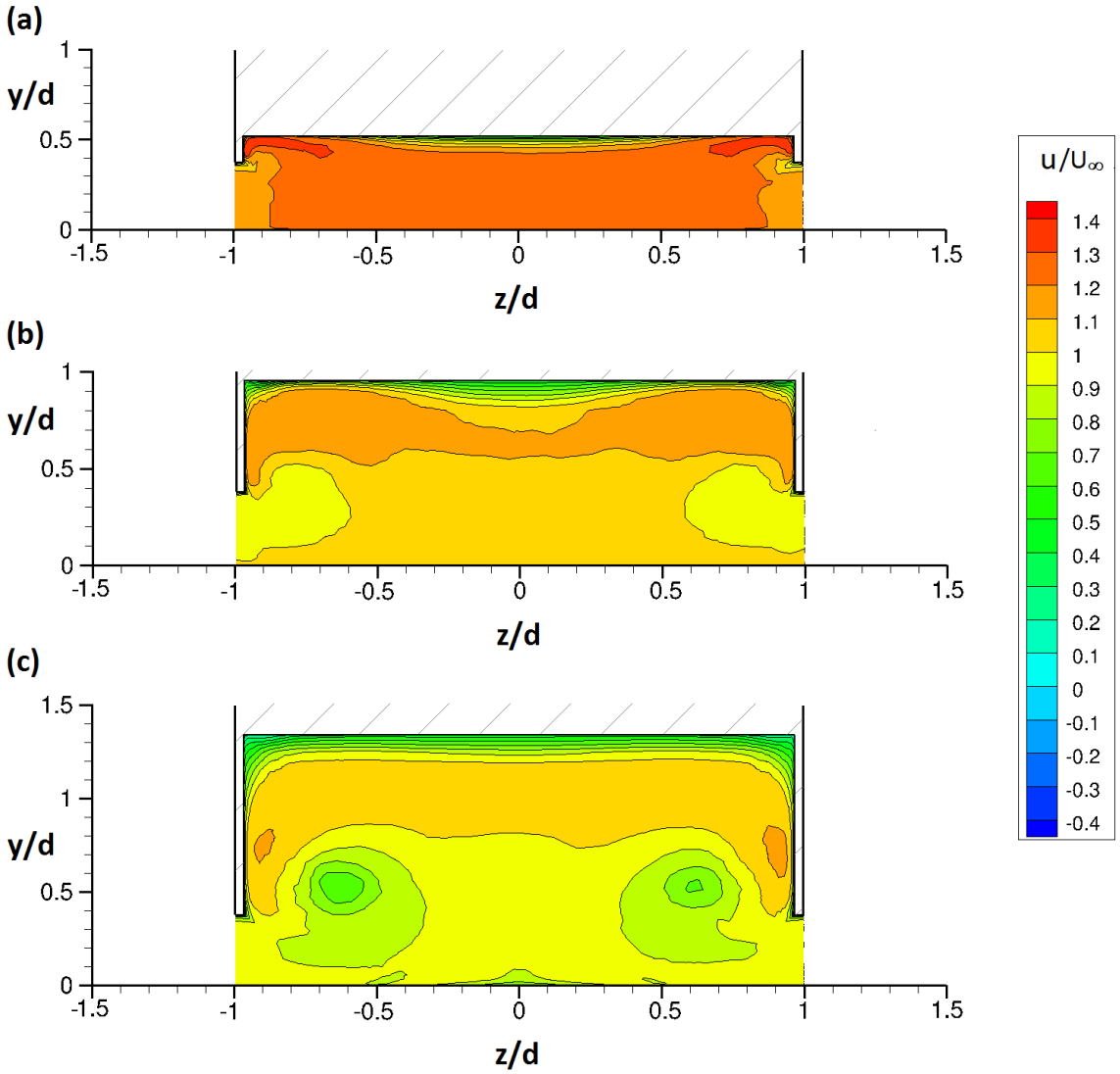

Figure 5-8: Streamwise velocity $(\boldsymbol{u})$ contours predicted with CFD at $h/d = 0.382$ for spanwise planes on: **(a)** $x/d = 3.63$ **(b)** $x/d = 5.02$ **(c)** $x/d = 6.29$

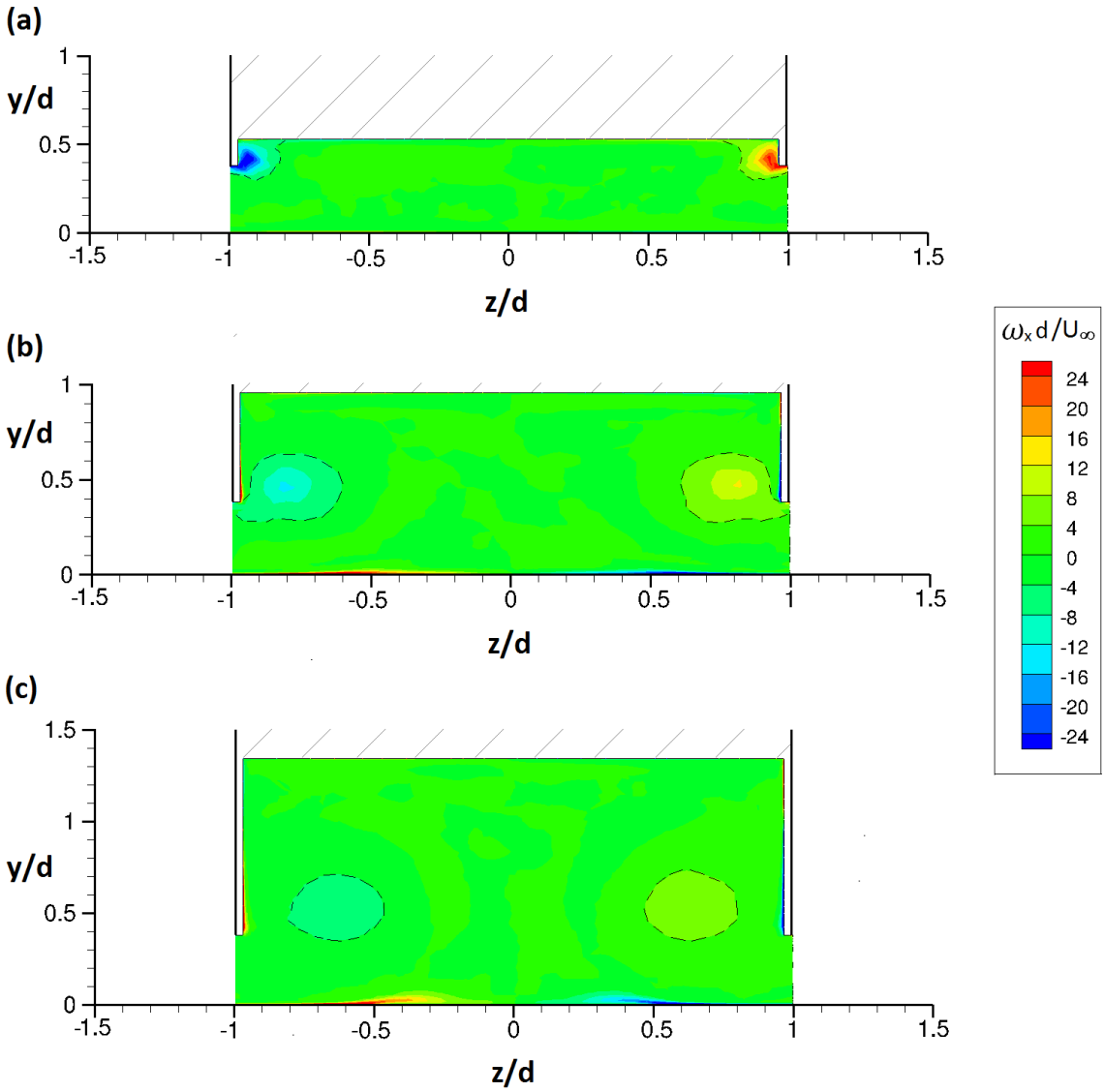

Figure 5-9: Streamwise vorticity ($\boldsymbol{\omega_x}$) contours predicted with CFD at $h/d = 0.382$ for spanwise planes on: **(a)** $x/d = 3.63$ **(b)** $x/d = 5.02$ **(c)** $x/d = 6.29$

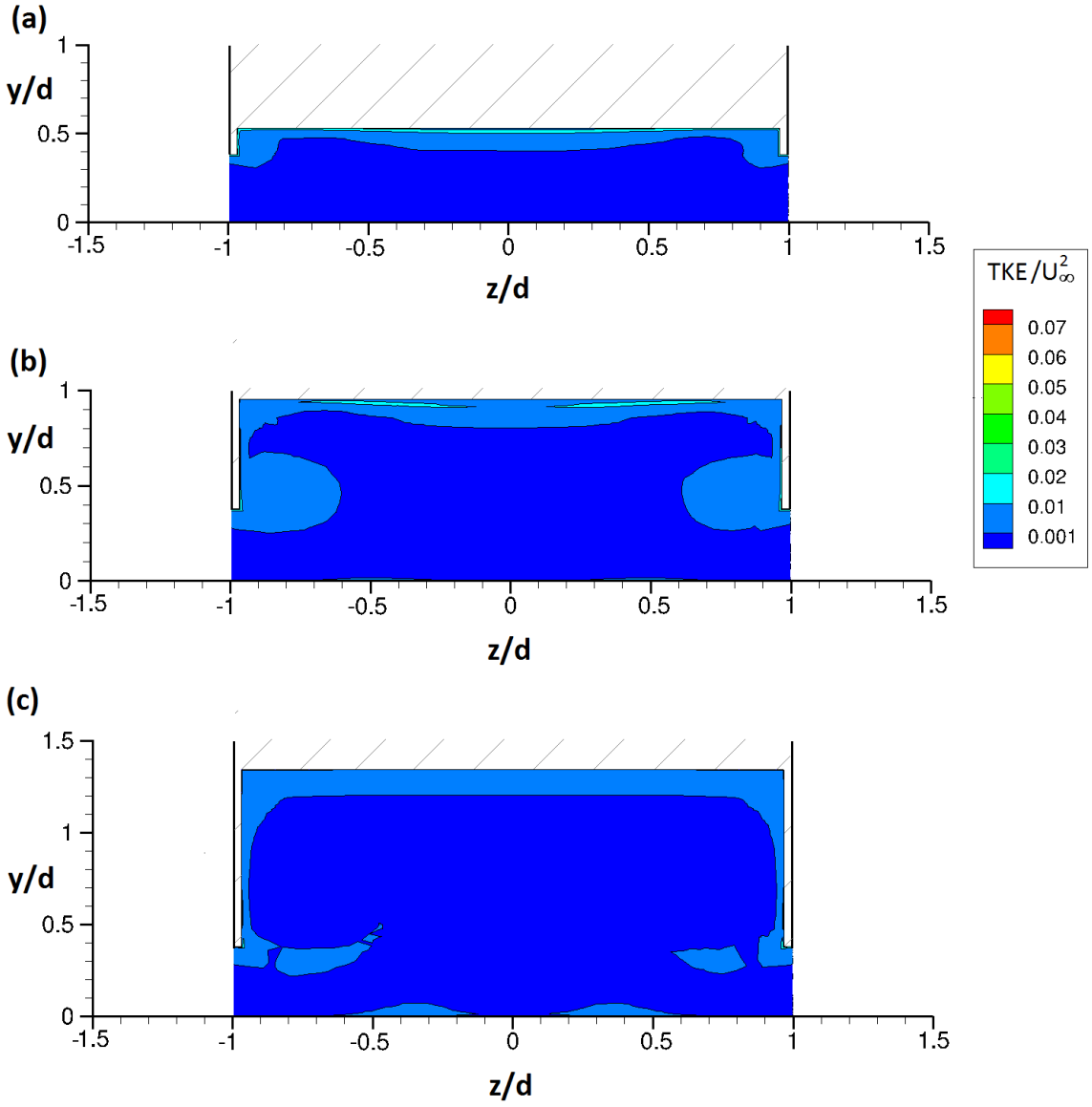

Figure 5-10: Turbulent kinetic energy (**TKE**) contours predicted with CFD at $h/d = 0.382$ for spanwise planes on: **(a)** $x/d = 3.63$ **(b)** $x/d = 5.02$ **(c)** $x/d = 6.29$

5.1.2 Vortex behaviour in flow regime B

The vortex development for the type B flow is represented at the maximum downforce ride height of $h/d = 0.191$. The streamwise flow physics at this ride height indicate that the vortex behaviour is similar to that of the type A flow regime even though the vortex features are relatively enhanced. The further increase in downforce associated with the reduction of ride height from the type A to the type B flow regime is due to the enhanced vortex properties. Relative to the type A flow regime ride height of $h/d = 0.382$, the streamwise flow velocities between the vortices for $h/d = 0.191$ has increased as shown on the spanwise plane at $x/d = 3.63$. (Figure 5−11) However, on the downstream planes of $x/d = 5.02$ and 6.29, the contours of the streamwise velocity (Figure 5−11), the low-pressure vortex core (Figure 5−12) and vorticity (Figure 5−13) of the vortices indicate reducing vortex strength and appear to be larger in size and more diffused than those of the type A ride heights. The visible flow separation (as captured by the flow features on the diffuser ramp surface in Figure 4−7) that begins close to the centre of the diffuser inlet and extends downstream is confirmed by the increased shear layer formation above and between both vortices at $x/d = 3.63$ and 5.02 (Figure 5−11). Also the diffuser vortex pair appears to have induced a separation off the ground plane in the form of secondary counter-rotating vortices (Figure 5−13).

At the approximate location of the vortices, the size of the contour region of high TKE (Figure 5−14) expands gradually from $x/d = 3.63$ to 6.29. Furthermore at $x/d = 6.29$, the outer rolled-up velocity shear layers of the vortices are merged. Both occurrences imply that close to the diffuser exit, there is severe vortex diffusion and increased turbulence with the vortices becoming unsteady. Hence, the axial velocities of the vortices are weakened due to the breakdown of the vortices at the latter part of the diffuser towards the diffuser exit. The low streamwise velocities of the vortex cores confirm that the swirling flow gradually weakens as it travels towards the centre of the diffuser exit.

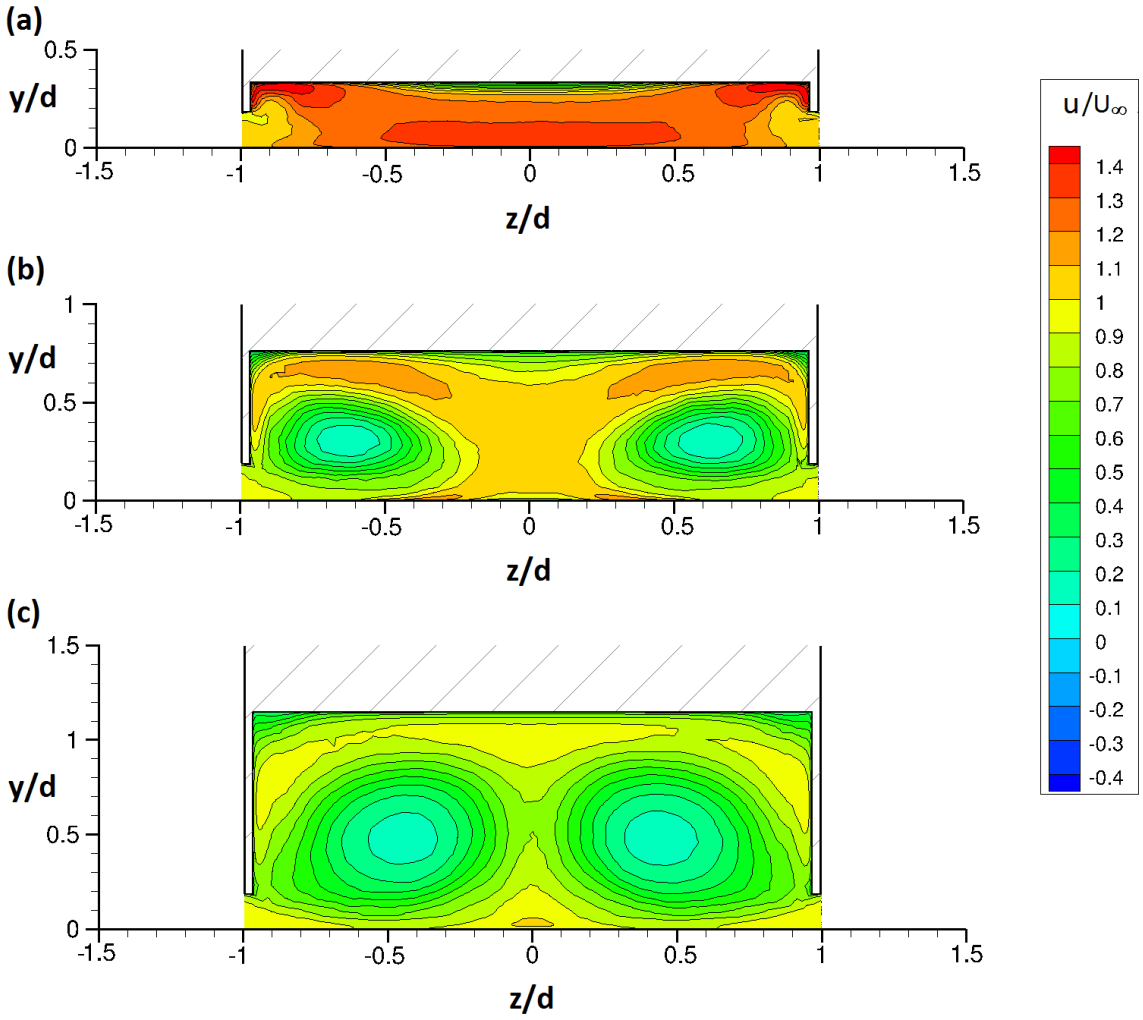

Figure 5-11: Streamwise velocity ($\boldsymbol{u}$) contours predicted with CFD at $h/d = 0.191$ for spanwise planes on: **(a)** $x/d = 3.63$ **(b)** $x/d = 5.02$ **(c)** $x/d = 6.29$

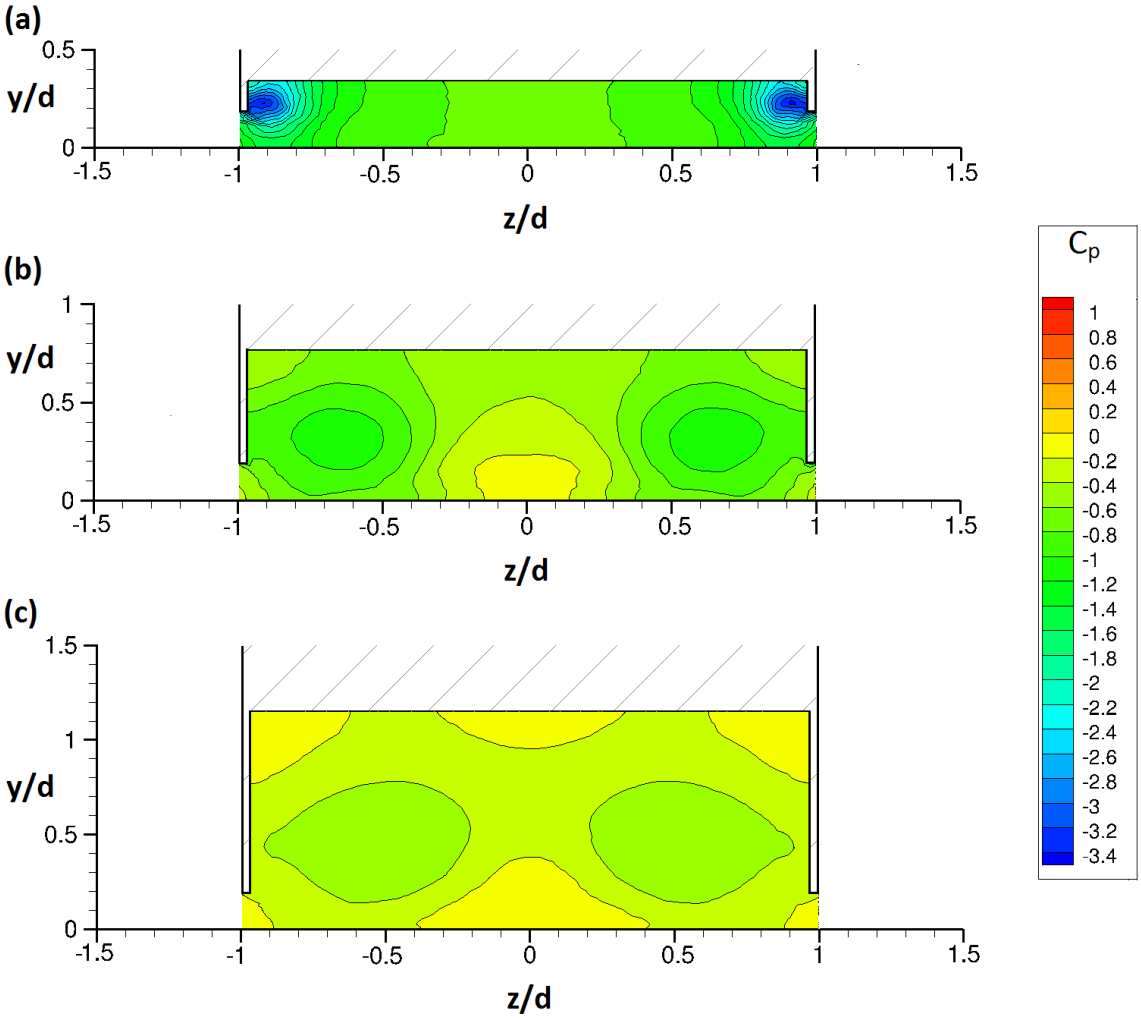

Figure 5-12: Streamwise pressure coefficient (C_p) contours predicted with CFD at $h/d = 0.191$ for spanwise planes on: **(a)** $x/d = 3.63$ **(b)** $x/d = 5.02$ **(c)** $x/d = 6.29$

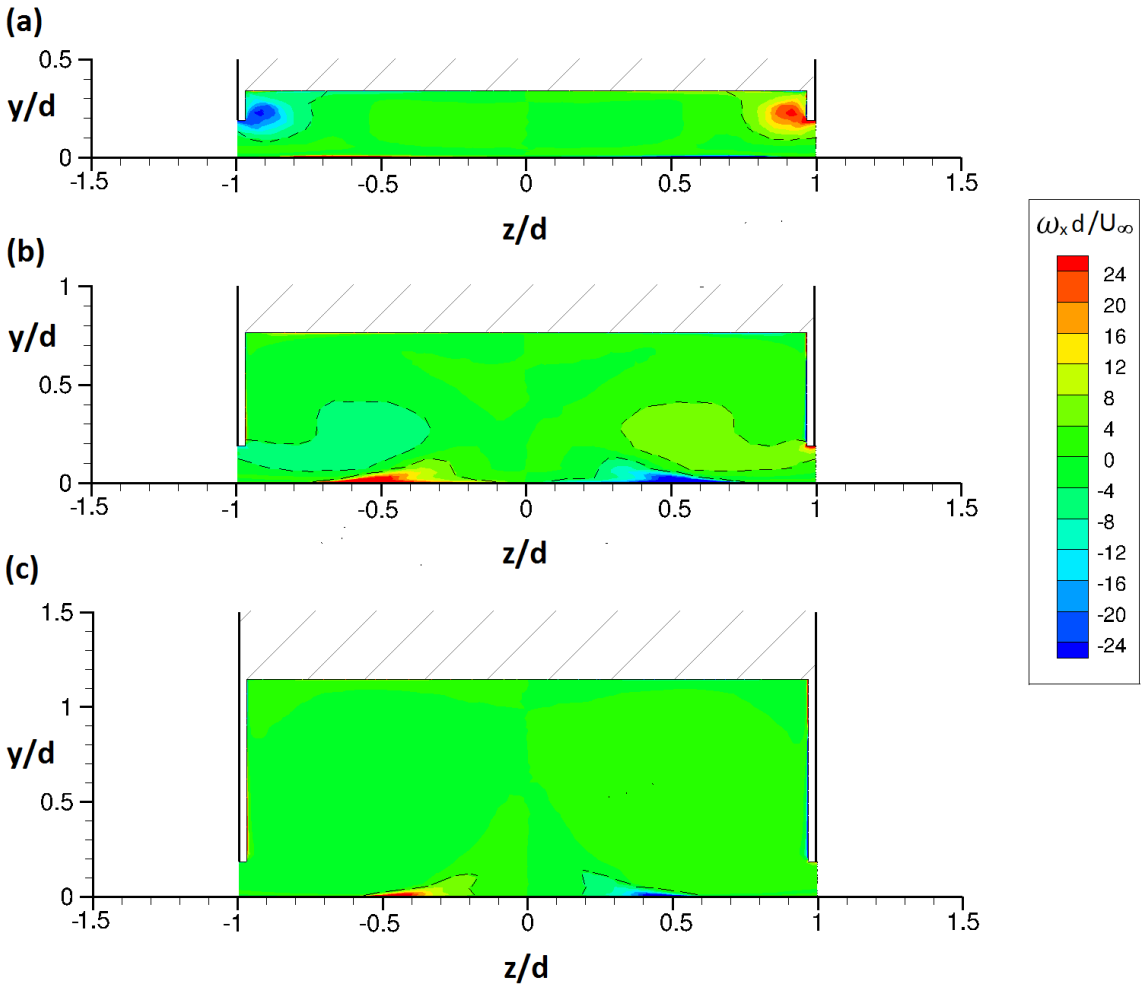

Figure 5-13: Streamwise vorticity ($\boldsymbol{\omega_x}$) contours predicted with CFD at $h/d = 0.191$ for spanwise planes on: **(a)** $x/d = 3.63$ **(b)** $x/d = 5.02$ **(c)** $x/d = 6.29$

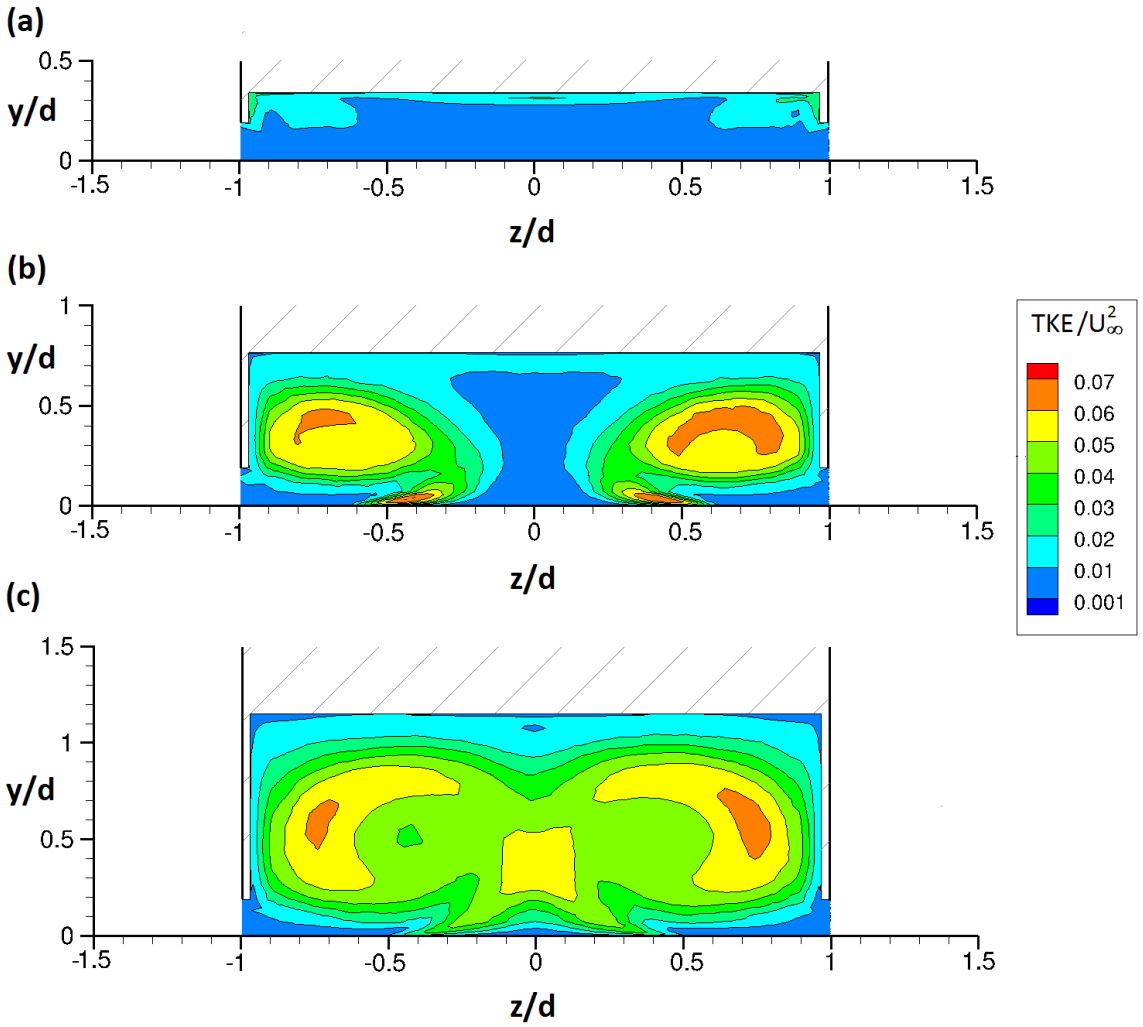

Figure 5-14: Turbulent kinetic energy (**TKE**) contours predicted with CFD at $h/d = 0.191$ for spanwise planes on: **(a)** $x/d = 3.63$ **(b)** $x/d = 5.02$ **(c)** $x/d = 6.29$

5.1.3 Vortex behaviour in flow regime C

The type C flow regime as represented by $h/d = 0.153$ indicates a fundamental change in the diffuser flow. In this flow regime, the diffuser flow is asymmetric as a result a breakdown of one the vortex pair. The streamwise velocity (Figure 5–15) contours at $x/d = 3.63$ show a high-velocity rolled-up shear layer on one side of the diffuser and low-velocity shear layer on the other side. Between both rolled-up shear layers, the region of high velocity associated with the peak velocity at the diffuser inlet is still present. However, the low-velocity shear layer across the diffuser span and above the contour region of high velocity has increased in size relative to those at the same location for $h/d = 0.191$. This implies that as the ride height is lowered from $h/d = 0.191$, the flow entering the diffuser is gradually dominated by boundary layer flow. Further downstream at $x/d = 5.02$ and $x/d = 6.29$, the strength of the surviving vortex reduces as indicated by the decrease in velocity at its core. Also, the velocity of the low-velocity contour region on the other side of the diffuser reduces and its size increases as a result of increased flow separation from the diffuser ramp surface.

Vorticity contours (Figure 5—16) indicate the presence of the solitary strong vortex close to the diffuser inlet ($x/d = 3.63$) and the vortex diffuses downstream at $x/d = 5.02$. At $x/d = 6.29$ (close to the diffuser exit), the vorticity contours indicates that the vortex strength has waned. On the other side of the diffuser where vortex breakdown occurred vorticity contours generally indicate the non-presence of high vorticity. At $x/d = 3.63$, the high TKE regions appear at the locations (as seen on the streamwise velocity contours Figure 5 – 17) of the vortex breakdown and the slow-moving boundary layer flow across the diffuser span. This occurrence implies that the separated flows at those locations are inducing turbulence in the inflow. Towards the diffuser exit, the surviving vortex diffuses thus increasing TKE at its location at $x/d = 5.02$, and at $x/d = 6.29$, the region of low TKE between both sides of the diffuser has disappeared. This is as a result of the merger between the relative higher TKE generated by the diffusing vortex and that generated by the increasingly dominant separated and reversing flow on the other side of the diffuser.

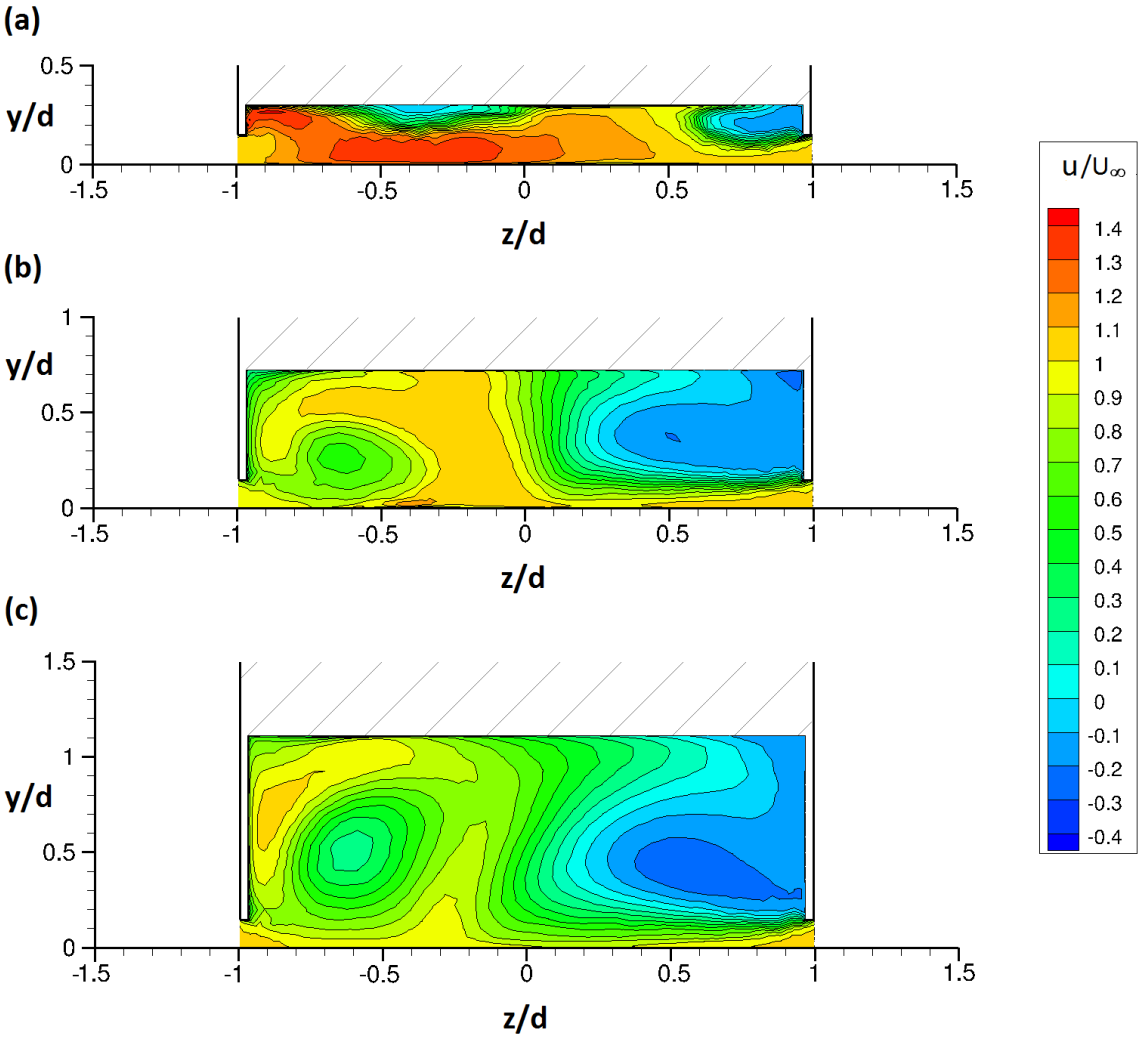

Figure 5-15: Streamwise velocity ($\boldsymbol{u}$) contours predicted with CFD at $h/d = 0.153$ for spanwise planes on: **(a)** $x/d = 3.63$ **(b)** $x/d = 5.02$ **(c)** $x/d = 6.29$

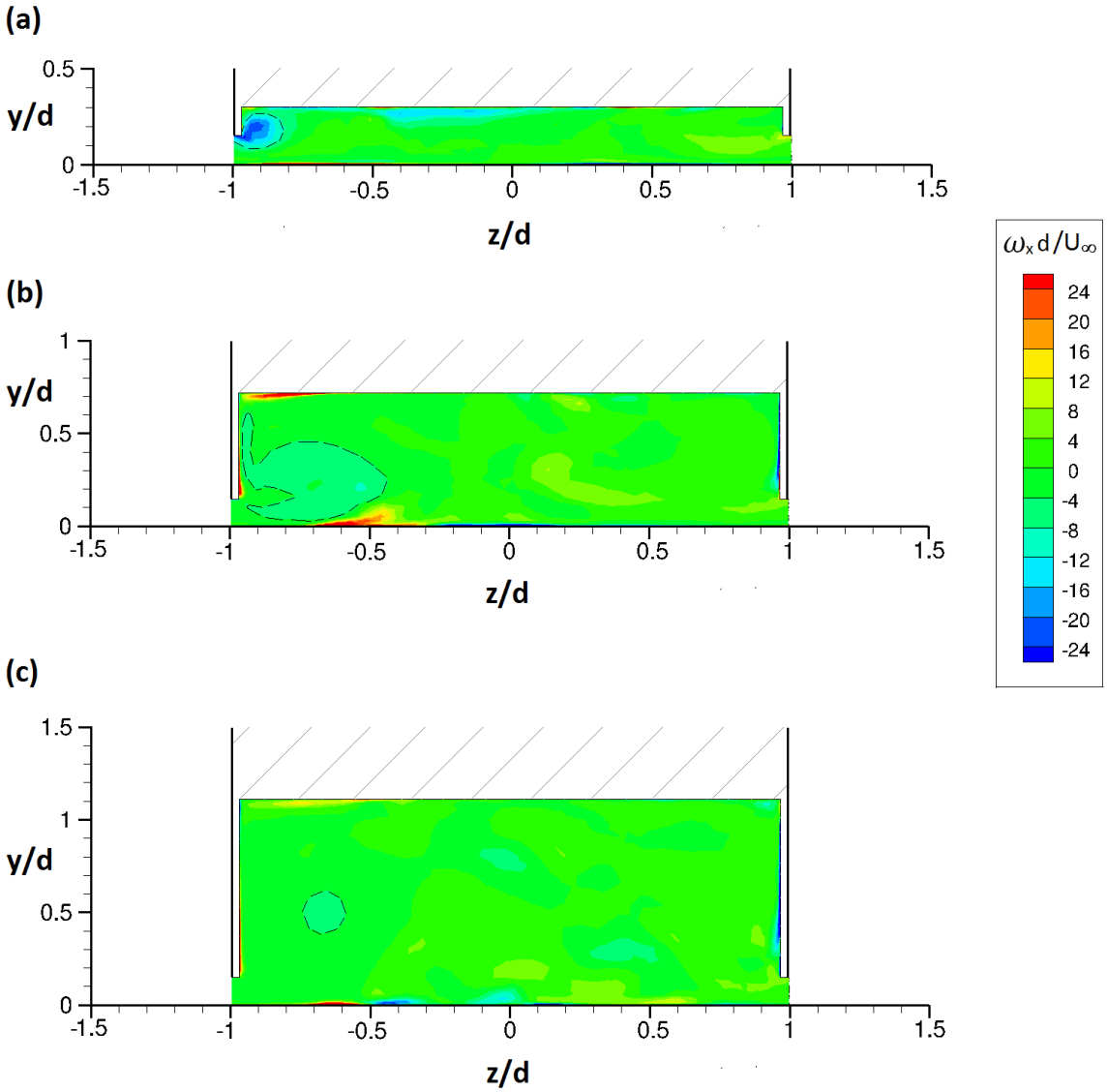

Figure 5-16: Streamwise vorticity ($\boldsymbol{\omega_x}$) contours predicted with CFD at $h/d = 0.153$ for spanwise planes on: **(a)** $x/d = 3.63$ **(b)** $x/d = 5.02$ **(c)** $x/d = 6.29$

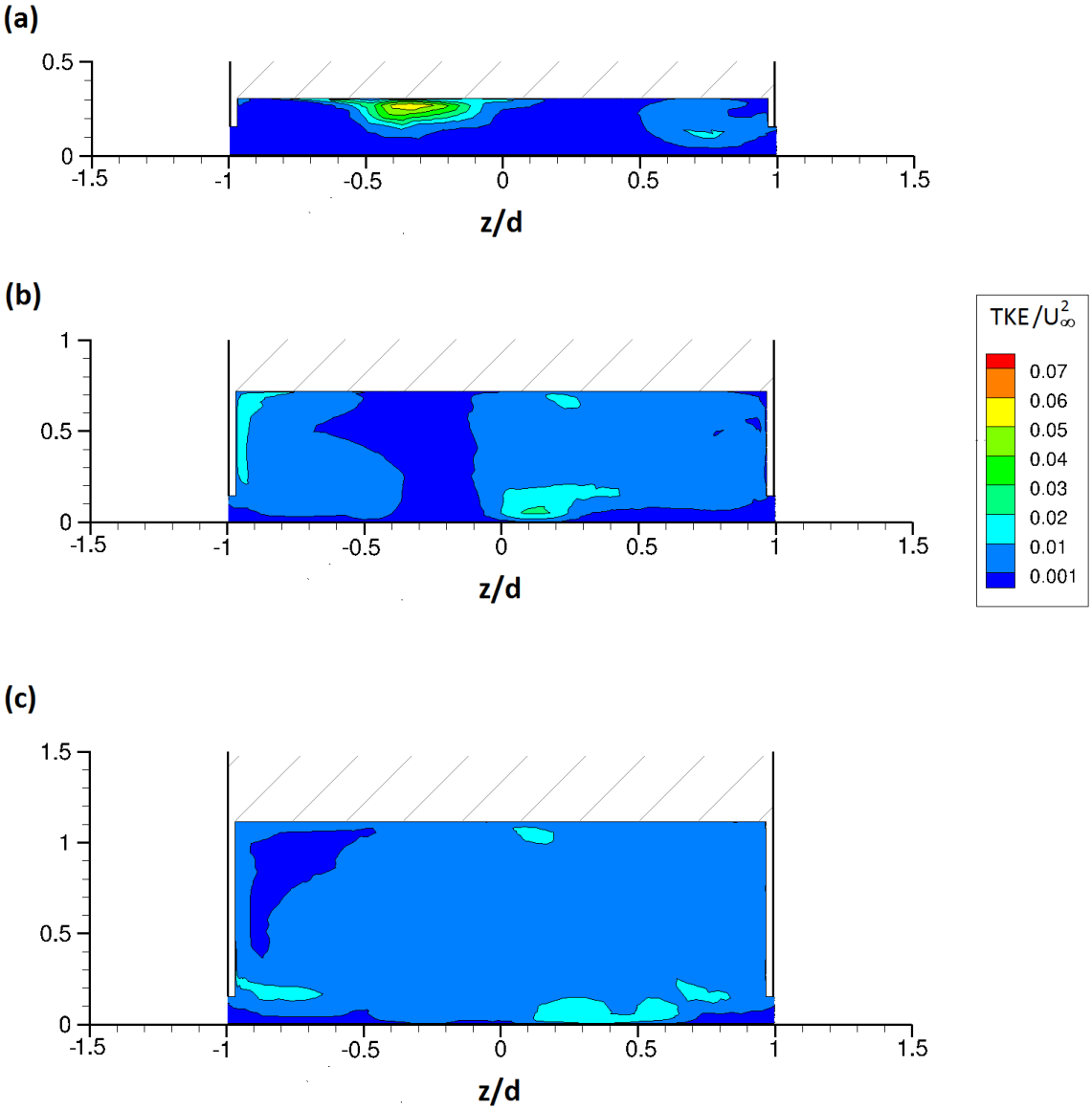

Figure 5-17: Turbulent kinetic energy (**TKE**) contours predicted with CFD at $h/d = 0.153$ for spanwise planes on: **(a)** $x/d = 3.63$ **(b)** $x/d = 5.02$ **(c)** $x/d = 6.29$

5.1.4 Vortex behaviour in flow regime D

The type D is represented by the lowest ride height investigated in this study ($h/d = 0.064$). The vortex flow physics from $x/d = 3.63$ to 6.29 indicates that it maintains similar asymmetric flow behaviour to the type C flow regime at $h/d = 0.153$. The roll-up streamwise velocity shear layer that represents the vortex flow is only present on one side of the cross-planes. The streamwise velocity contours (Figure 5–18) of the single vortex indicate that the surviving vortex strength has further weakened relative to that of the type C flow. On the other half of the diffuser, the low velocity shear layers that dominate that half area of the diffuser represents the separated and recirculating flow attributed to breakdown of vortex.

The streamwise vorticity at $x/d = 3.63$ and 5.02 (Figure 5–19) show a region of separation induced secondary vortex off the ground plane on the side of the surviving vortex. However, the core of the surviving primary diffuser vortex is not visible from $x/d = 3.63$ to 6.29 thus indicating that the vorticity of the surviving vortex has severely weakened.Furthermore, regions of high TKE dominate the cross flow from $x/d = 3.63$ to 6.29 which means that flow turbulence is profound within the diffuser (Figure 5–20).The high TKE through the length of the diffuser is a result of the diffusion of the surviving vortex on one side of the diffuser and the recirculating flow dominating the other side of the diffuser.

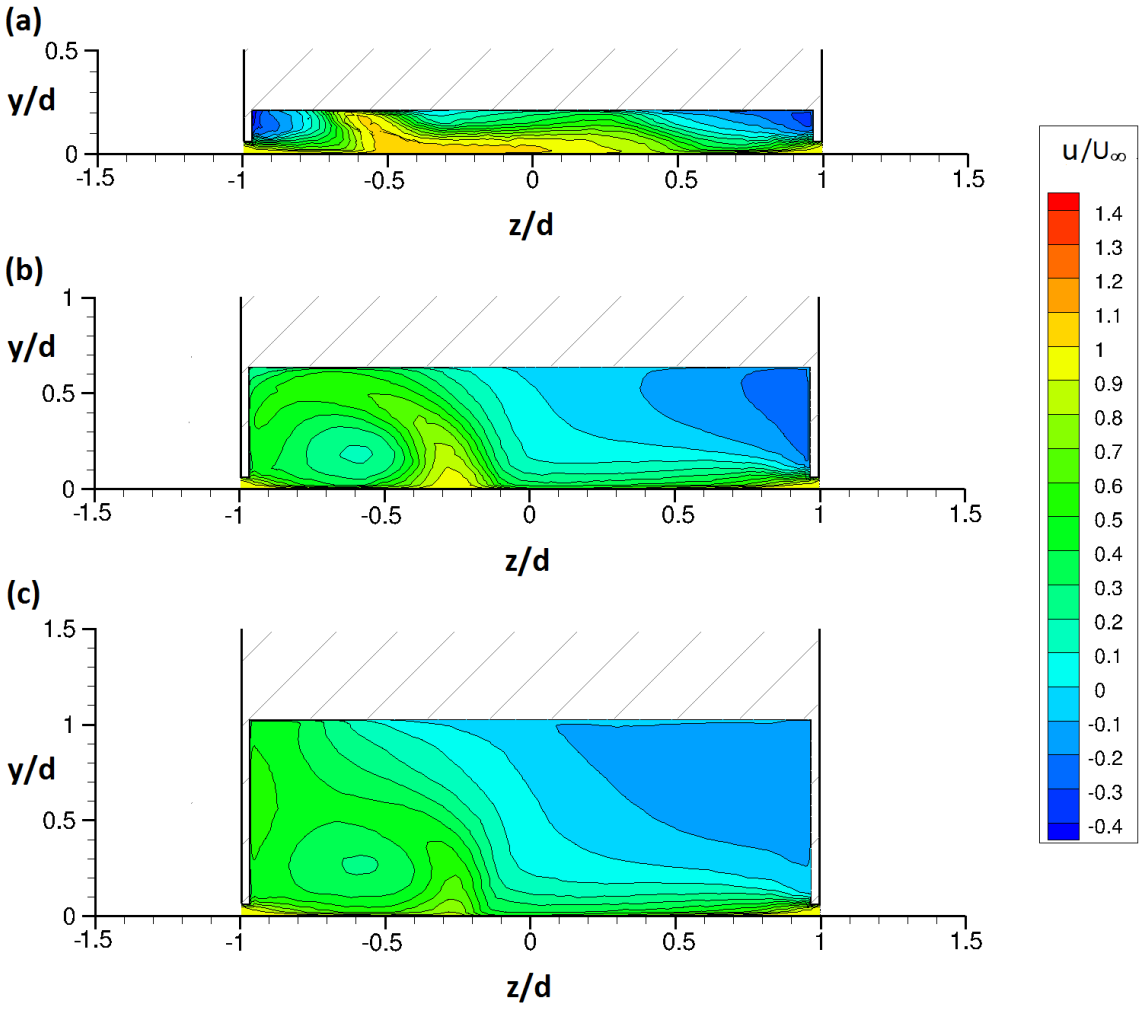

Figure 5-18: Streamwise velocity ($\boldsymbol{u}$) contours predicted with CFD at $h/d = 0.064$ for spanwise planes on: **(a)** $x/d = 3.63$ **(b)** $x/d = 5.02$ **(c)** $x/d = 6.29$

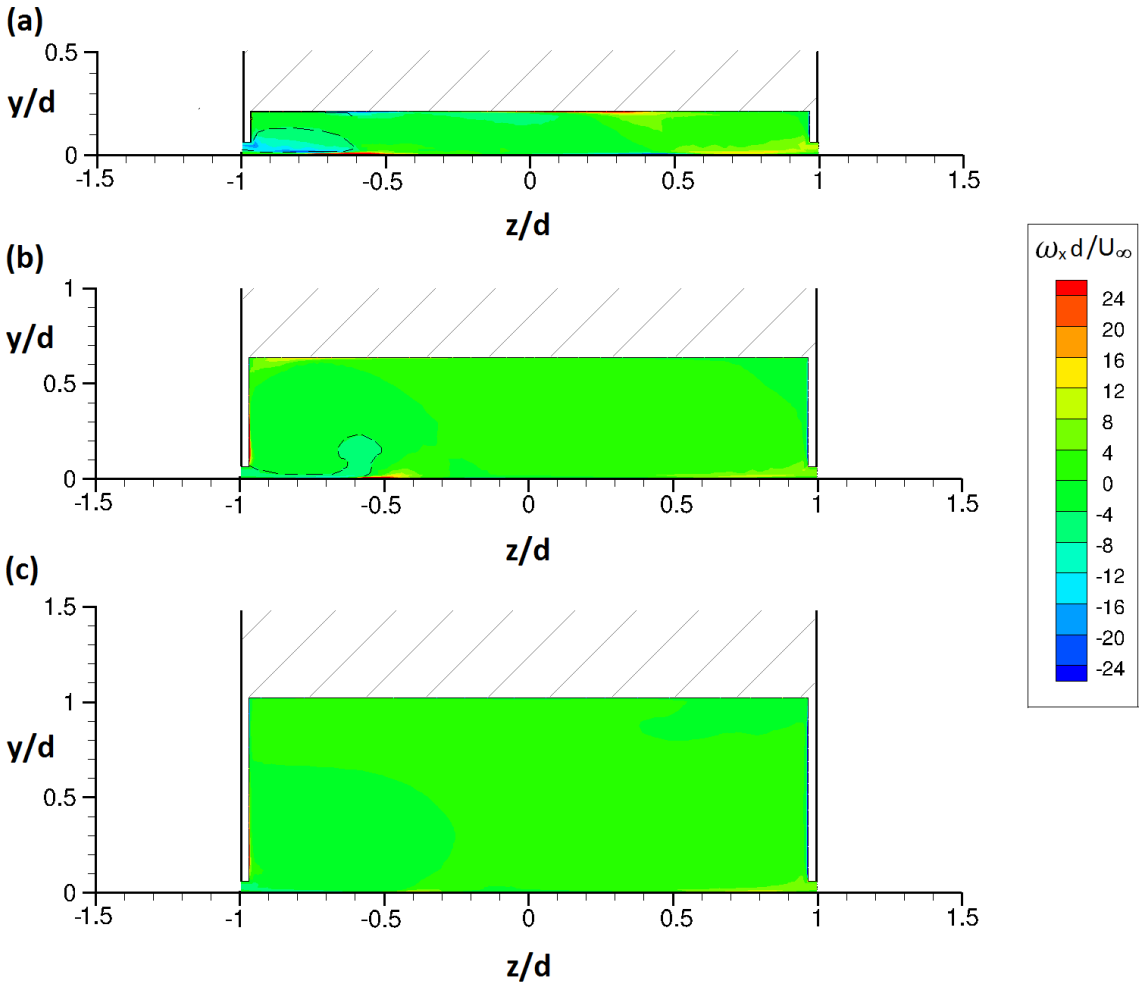

Figure 5-19: Streamwise vorticity ($\boldsymbol{\omega_x}$) contours predicted with CFD at $h/d = 0.064$ for spanwise planes on: **(a)** $x/d = 3.63$ **(b)** $x/d = 5.02$ **(c)** $x/d = 6.29$

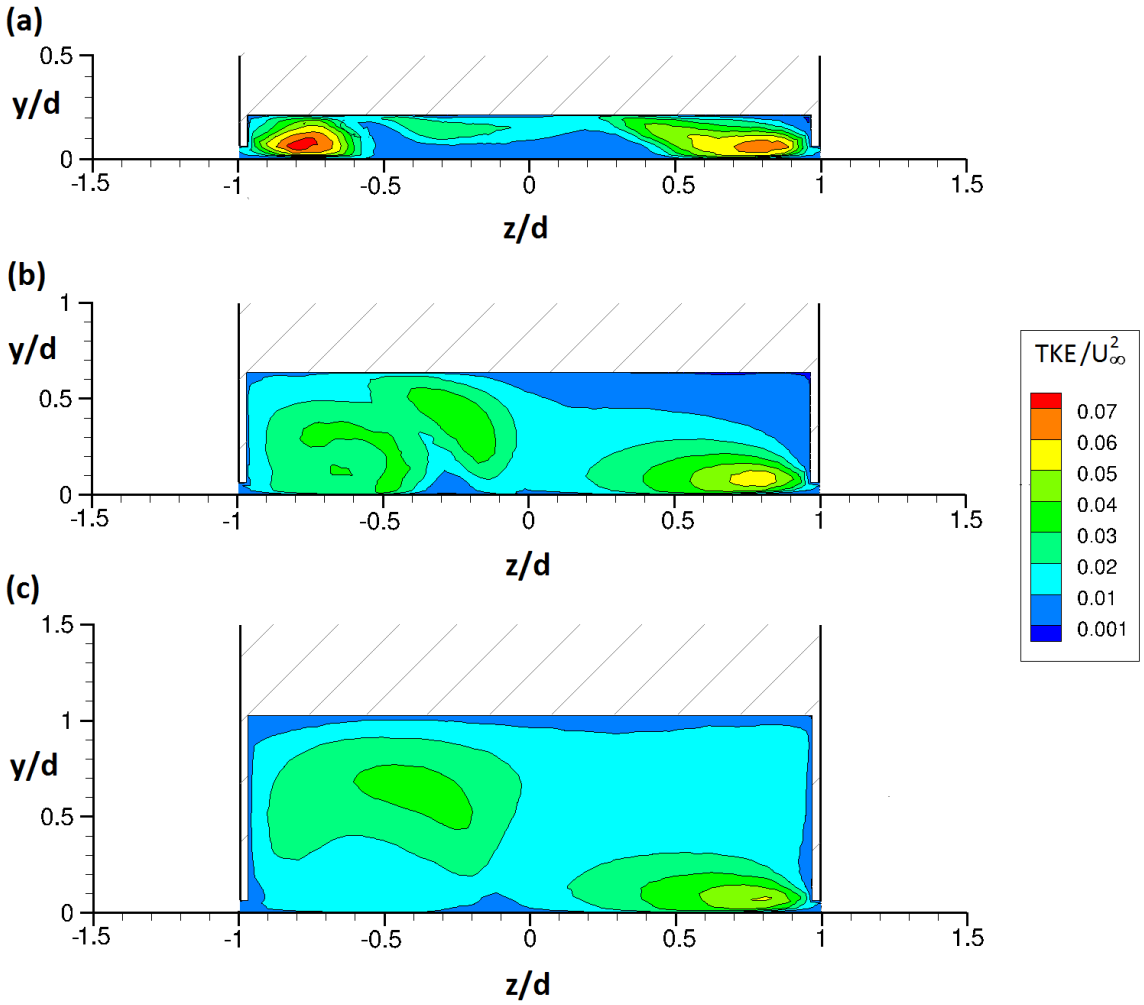

Figure 5-20: Turbulent kinetic energy (**TKE**) contours predicted with CFD at $h/d = 0.064$ for spanwise planes on: **(a)** $x/d = 3.63$ **(b)** $x/d = 5.02$ **(c)** $x/d = 6.29$

5.2 Velocity Profile Development

At the maximum downforce ride height of $h/d = 0.191$, streamwise velocity contour distribution over the diffuser bluff body (on longitudinal planes at $z/d = 0$ and 0.490) are shown in Figure 5—21a and 5—21b. The velocity distribution at the centreline plane ($z/d = 0$) Figure 5—21a shows regions of low velocity in front of the nose section, and at the near-wake of the bluff body base plate induced by the separated flow downstream of the body. The centreline plane also shows a region of relatively high velocity around the top of the nose section (see dashed lines in 5—21a). As indicated in Chapter 4 (Figure 4—33), a laminar separation bubble occurs around the sides of the bluff body where the nose section merges with the rest of the body. This occurrence is induced by the flow curvature acceleration at this region where laminar-to-turbulent flow transition develops. Underneath the body, high flow velocities are dominant at the location where the underbody flat section merges with the nose section and at the location of the diffuser inlet (see dashed lines in 5—21a). At these respective locations, the high velocity is as a result of the curvature around the nose section which accelerates the flow at the early part of the underbody and the 'pump down' effect of the diffuser inlet. The streamwise plane ($z/d = 0.490$) representing the approximate location of one of the diffuser vortices for the maximum downforce ride height ($h/d = 0.191$) and the equivalent plane at the downforce reduction height ($h/d = 0.153$) is respectively shown in Figures 5—21b and 5—21c. The streamwise velocities in the diffuser section shows a region of relative high velocity at the early part of the diffuser and lower velocities towards the diffuser exit (see dashed lines in 5—21b). The flow behaviour at $h/d = 0.191$ is as a result of the gradually waning strength of the vortices as they travel towards the diffuser exit and at $h/d = 0.153$ (Figure 5—21c), the diffuser is largely dominated by relative lower velocities due to flow reversal into the diffuser exit.

The total flow energy of the airflow across the diffuser bluff body can be quantified by the total pressure which is equal to the sum of freestream static

and dynamic pressures. Total pressure contours on the streamwise planes (Figure 5—22) indicate a relatively constant freestream pressure distribution over the diffuser body with lower total pressure distribution near the surface or boundary layer of the body. This means that the relatively low total pressure close to the surface of the body is as a result of the flow energy spent (flow energy losses) to overcome the boundary layer viscous forces along the surface of the body. However the diffuser low-velocity regions on the plane, $z/d = 0.490$ for $h/d = 0.191$ and 0.153 are largely dominated by low total pressure. The low total pressure is due to the significant flow energy expended in overcoming the diffuser adverse pressure gradient by the longitudinal vortex for $h/d = 0.191$ and the flow reversal for $h/d = 0.153$. At the diffuser bluff body near-wake region for all three streamwise planes, the remaining flow energy is minimal, depleted by the turbulent eddies of the separated flow of the near-wake region. The flow energy losses induced by the diffuser longitudinal vortices and the bluff body near-wake enables the identification flow regions associated with vortex drag and base drag (Chometon & Gilliéron, 1996).

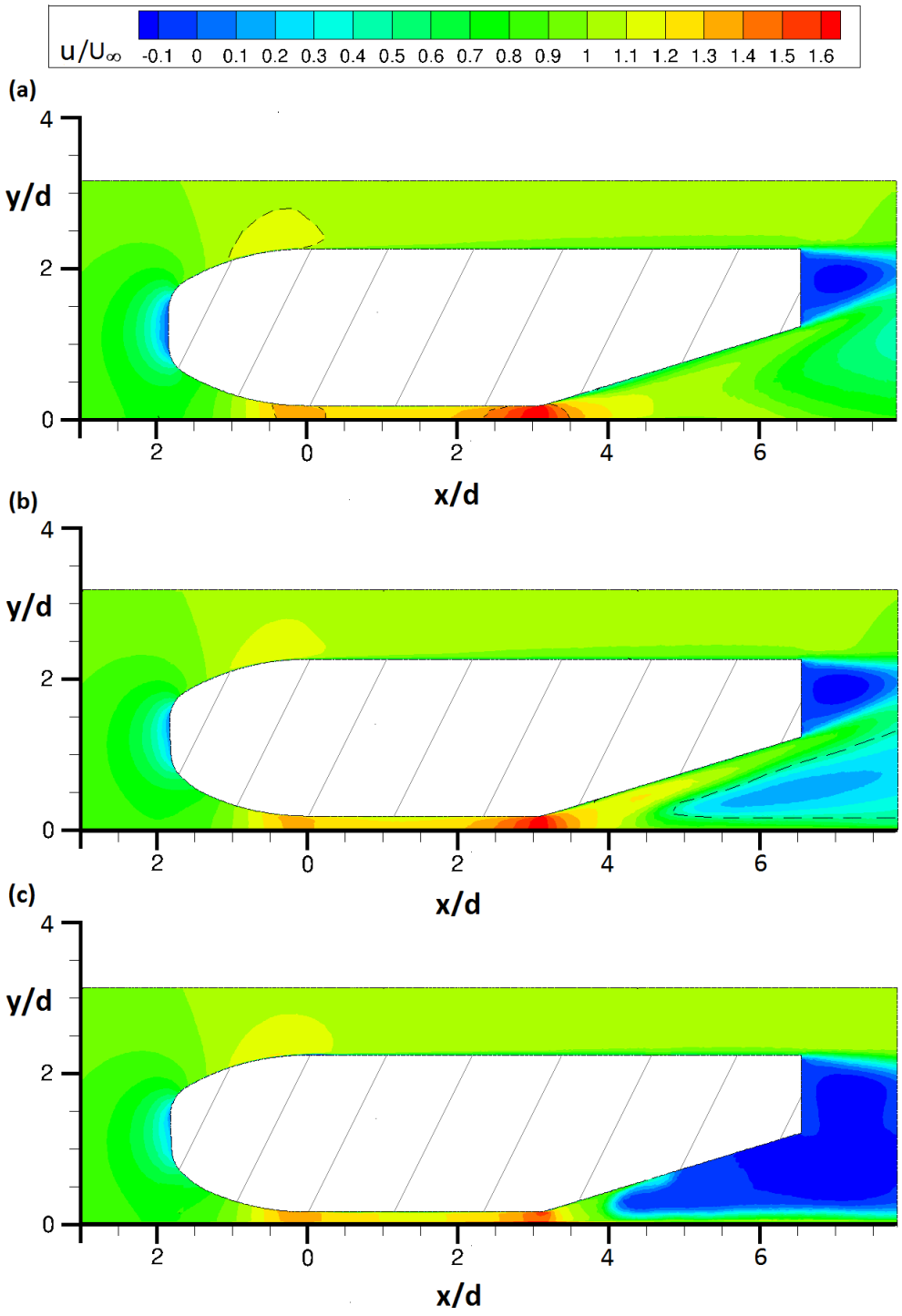

Figure 5-21: Streamwise velocity ($\boldsymbol{u}$) contours predicted with CFD at: **(a)** $h/d = 0.191$ for streamwise centreline plane on $z/d = 0$ **(b)** $h/d = 0.191$ for streamwise plane on $z/d = 0.490$ **(c)** $h/d = 0.153$ for streamwise plane on $z/d = 0.490$

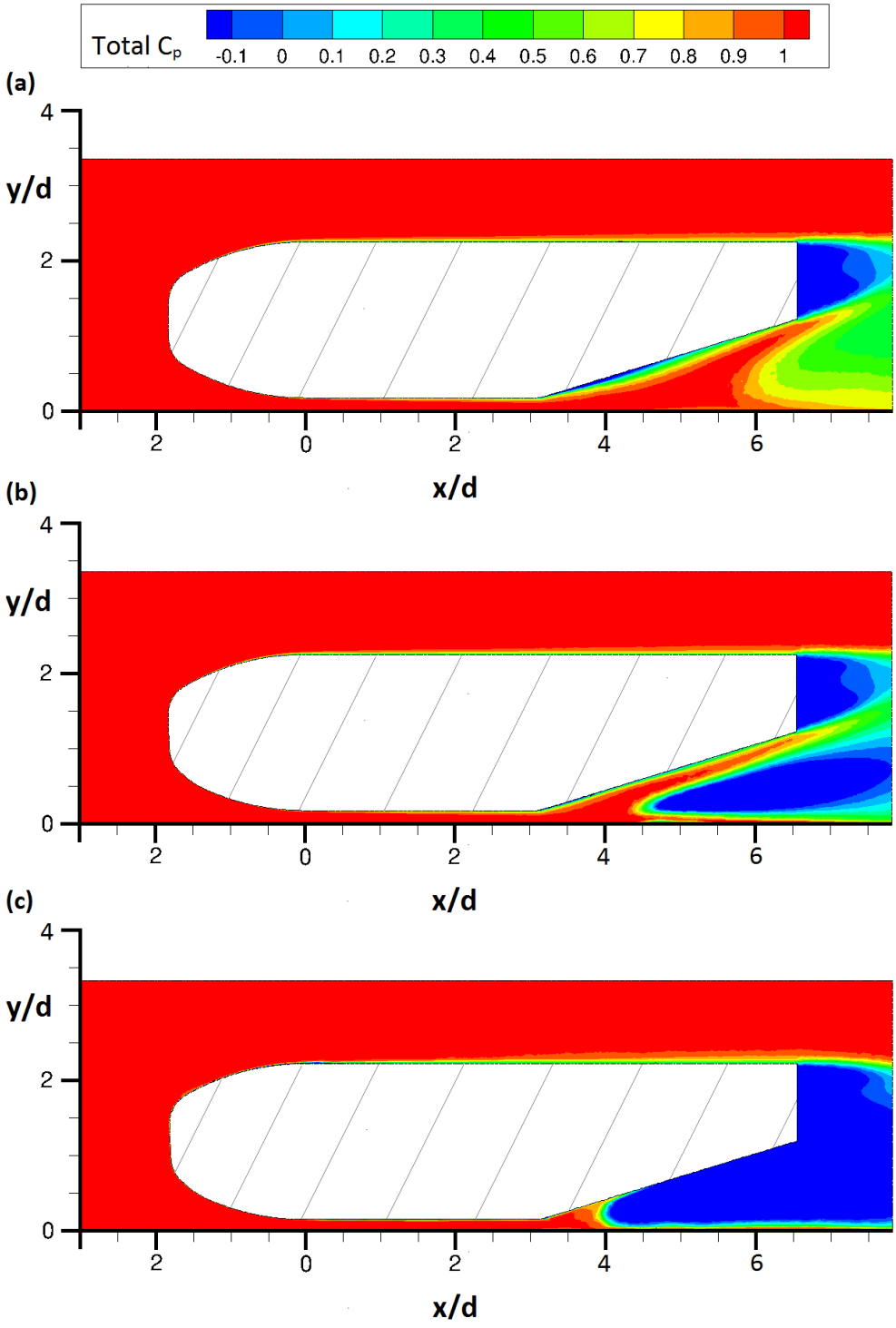

Figure 5-22: Total pressure coefficient contours predicted with CFD at: **(a)** $h/d = 0.191$ for streamwise centreline plane on $z/d = 0$ **(b)** $h/d = 0.191$ for streamwise plane on $z/d = 0.490$ **(c)** $h/d = 0.153$ for streamwise plane on $z/d = 0.490$

5.2.1 Underbody boundary layer profiles

The velocity profiles (U/U_∞) of the boundary layer were measured and predicted at the diffuser inlet $(x/d = 3.14)$. The boundary layer velocity profiles were taken on the diffuser centreline $(z/d = 0)$ and on either side of the diffuser centreline $(z/d = 0.363 \text{ and } -0.363)$. The locations on either side of the centreline are approximately outside the core region of the counter-rotating longitudinal vortices of the diffuser and correspond to distances $100\ mm$ from the spanwise sides of the diffuser.

The velocity gradients at the top and bottom of the velocity profiles as shown in Figure 5—23 indicate the presence of boundary layer development on the diffuser inlet and on the moving ground. The shape of the boundary layer profiles measured in the wind tunnel experiments are correctly predicted with time-averaged CFD, although with a degree of underprediction and overprediction. At the type A flow represented at $h/d = 0.382$, the diffuser centreline inlet flow reaches a measured and predicted velocity of $U/U_\infty = 1.6 \text{ and } 1.51$ respectively at $y/d = 0.324$. At the maximum downforce ride height of $h/d = 0.191$, the measured and predicted velocity at the centreline increases to $U/U_\infty = 1.71 \text{ and } 1.70$ at $y/d = 0.133$, hence reflecting the increase in diffuser inlet suction due to an increase in inlet flow velocity. However, at the respective downforce-reduction and low-downforce ride heights represented by $h/d = 0.153$ and 0.064, the measured and predicted peak flow velocities reduce to $U/U_\infty = 1.48 \text{ and } 1.571$ at $y/d = 0.089$ for $h/d = 0.153$, with a further reduction of measured and predicted peak flow velocities to $U/U_\infty = 1.32 \text{ and } 1.43$ at $y/d = 0.015$ for $h/d = 0.064$. Unlike the diffuser inlet centreline boundary layer profiles of the types A to C regimes, the velocity gradients for (both the diffuser inlet and corresponding ground location) of the type D flow are significantly diminished thus indicating that the boundary layers are merged (Figure 5—23). Even so, centreline velocity profiles from types A to D regimes also show that the boundary layer growth from both the diffuser inlet and the moving ground thickens with reducing ride height. The

increasing boundary layer thickness is as a result of the gradual reduction in flow-turning at the diffuser inlet due to the gradual reduction of the diffuser inlet flow area – thus enlarging the thickness and length of the separation line along the diffuser inlet (Figure 4–8).

At both sides of the centreline, the velocity profiles at $z/d = 0.363$ and -0.363 for the type A flow ($h/d = 0.382$) shown in Figure 5—24, the peak flow velocity on either side of the centreline is about 4.3% lower than that of the centreline. This implies that flow velocity before the diffuser inlet region is lower away (in the spanwise direction) from the centreline of the bluff body underbody. At the maximum downforce ride height ($h/d = 0.191$), measured boundary layer profiles at $z/d = 0.363$ and -0.363 for the type B flow indicate a degree of asymmetry at the diffuser inlet highlighted by a significant region ($y/d = 0.031$ to 0.165) of lower velocities for the profile at $z/d = 0.363$ relative to the profile at $z/d = -0.363$ (1.43% lower between highest velocities measured in the region). However, the pressure distribution (presented in Chapter 4) at $h/d = 0.191$ indicated a reasonable existence of flow symmetry within the diffuser. Moreover, as in the case in $h/d = 0.191$ where measured boundary layer velocities are lower at $z/d = 0.363$ comparatively to those at $z/d = -0.363$, a similar occurrence is present in $h/d = 0.153$. However, in the case of $h/d = 0.153$ the boundary layer velocities on the side of the diffuser where vortex breakdown occurred (at $z/d = 0.363$) is significantly lower than the velocities at the other side (at $z/d = -0.363$) where there is a surviving vortex (12.88% lower between measured peak velocities). This signifies that the onset of vortex breakdown responsible for downforce loss in the force reduction and low downforce ride heights begins to occur at the maximum downforce ride height.

Despite these occurrences, the velocity profiles at $h/d = 0.191$ and 0.153 suggest the presence of a region of relative constant velocity within the distance between the boundary layers of the diffuser inlet and the ground plane. This occurrence indicate that although the reduction of ride height

beyond that of maximum downforce enhances flow separation at the diffuser inlet, the merging of the boundary layers does not occur at $h/d = 0.153$ (more so on the stalled side at $z/d = 0.363$). Hence, the merging of the boundary layers is not entirely responsible for the flow asymmetry associated with the force reduction and low downforce ride heights. However, below the maximum downforce ride height boundary layer profiles for $h/d = 0.153$ and 0.064 indicates that peak flow velocity at the diffuser inlet reduces with decreasing ride height. Furthermore, the relative slower boundary layer flow velocities on the side of the diffuser inlet where vortex breakdown occurs appear to have induced the vortex breakdown on that side.

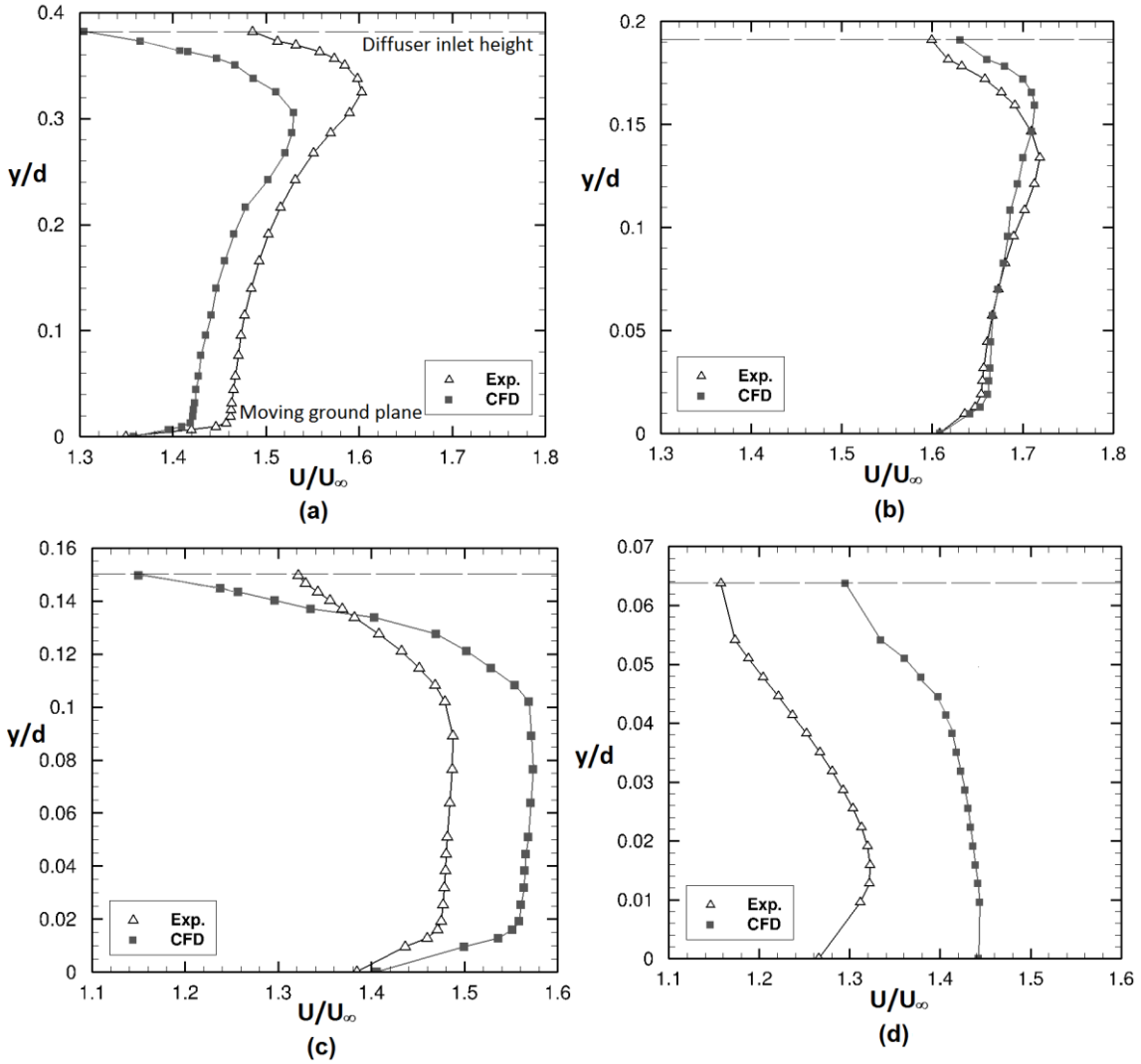

Figure 5-23: LDV-measured and CFD-predicted boundary layer profiles at diffuser inlet $(x/d = 3.14)$ centre point $(z/d = 0)$ for: **(a)** $h/d = 0.382$ **(b)** $h/d = 0.191$ **(c)** $h/d = 0.153$ **(d)** $h/d = 0.064$

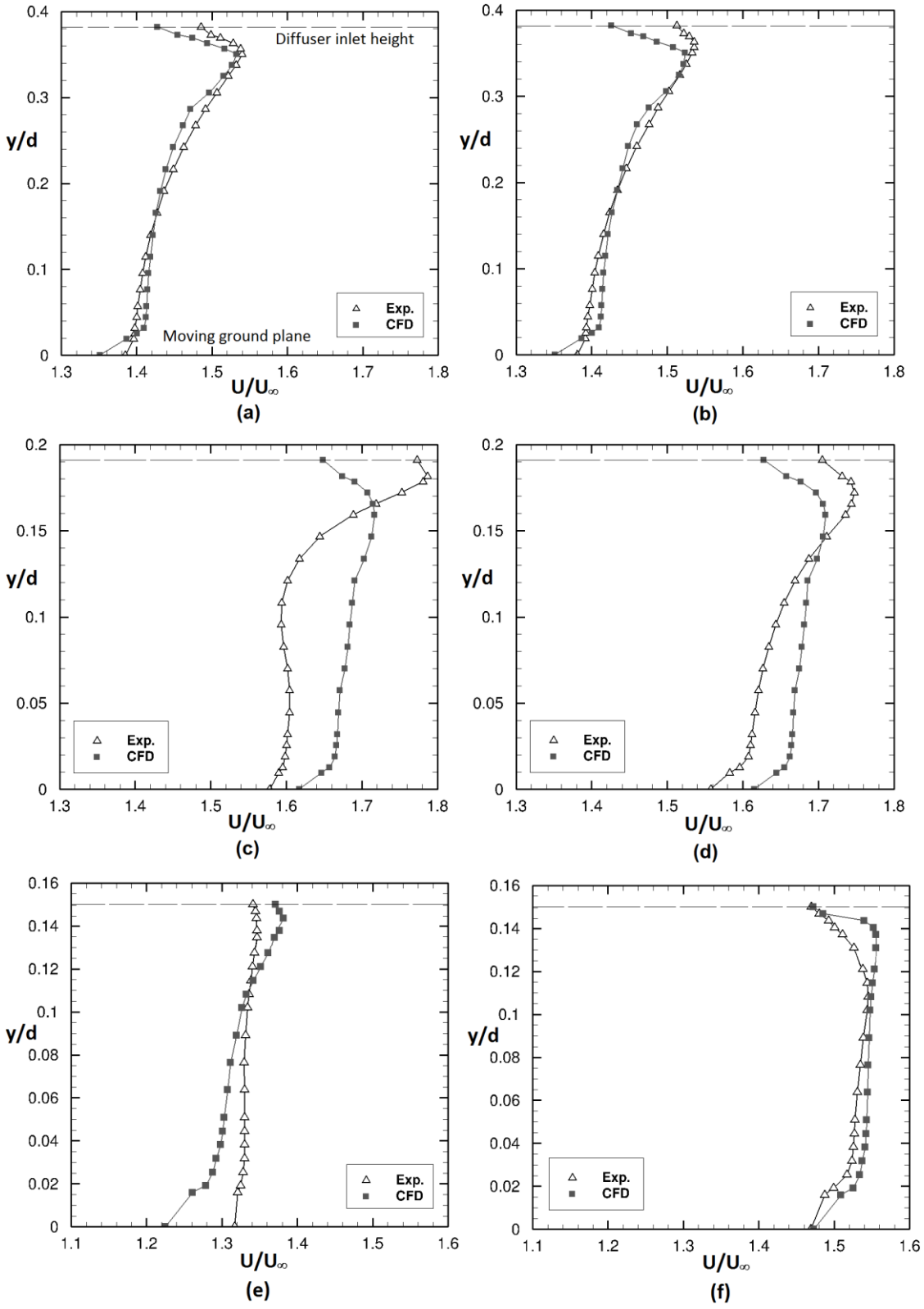

Figure 5-24: LDV-measured and CFD-predicted boundary layer profiles at either side $(z/d = 0.363$ and $-0.363)$ of diffuser inlet centre point $(x/d = 3.14$ at $z/d = 0)$ for: **(a)** $h/d = 0.382$ at $z/d = 0.363$ **(b)** $h/d = 0.382$ at $z/d = -0.363$ **(c)** $h/d = 0.191$ at $z/d = 0.363$ **(d)** $h/d = 0.191$ at $z/d = -0.363$ **(e)** $h/d = 0.153$ at $z/d = 0.363$ **(f)** $h/d = 0.153$ at $z/d = -0.363$

5.2.2 Velocity profiles of diffuser near-wake region

The flow physics in the near-wake region of the diffuser bluff body was investigated on longitudinal planes at the approximate locations of the vortex cores ($z/d = 0.490$ and -0.490) for the maximum downforce ride height of $h/d = 0.191$ and force-reduction ride height of $h/d = 0.153$.

At $h/d = 0.191$, the similarities in near-wake velocity magnitude profiles (Figure 5—25) indicate that the diffuser flow is reasonably symmetric. Also, low velocities in the triangular region within the upper part of the near-wake planes infer the presence of the anticipated base flow recirculation. These low velocities are induced by the separated flow region near the base surface of the bluff body. Low velocities also dominate within the lower part of the near-wake planes. This implies that the cores of the vortex pair are diffused at the diffuser exit as reported by Senior (2002) and that the diffused vortices shown in Figure 5—25 have induced low velocities with increased turbulence in this region, as shown in Figure 5—26. Low turbulence was present on both planes in the immediate wake region (labelled 'Q') of the bluff body back plate, which indicated that the wake vortices are steady at that region (Figure 5—26). In addition, the higher-velocity region (labelled 'P') above the low-velocity region at the lower part of the wake planes induced by the diffused vortices indicated that, towards the diffuser exit, the vortices have separated from the diffuser ramp (Figure 5—25).

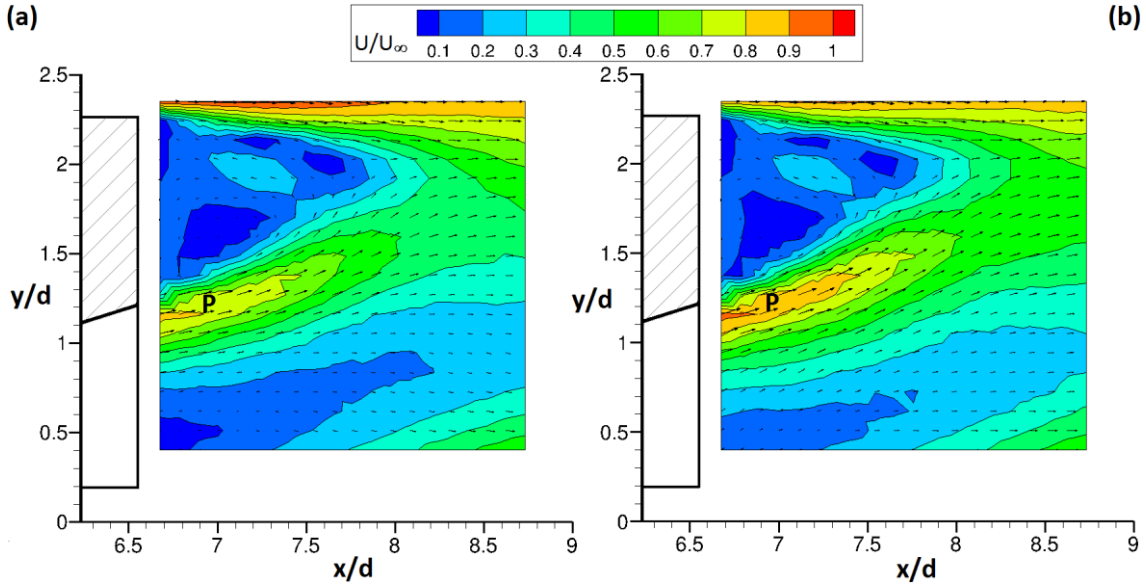

Figure 5-25: Near-wake non-dimensionalised $\boldsymbol{U}$ contours for the diffuser body measured with LDV at $h/d = 0.191$ on: **(a)** plane at $z/d = 0.490$ and **(b)** plane at $z/d = -0.490$

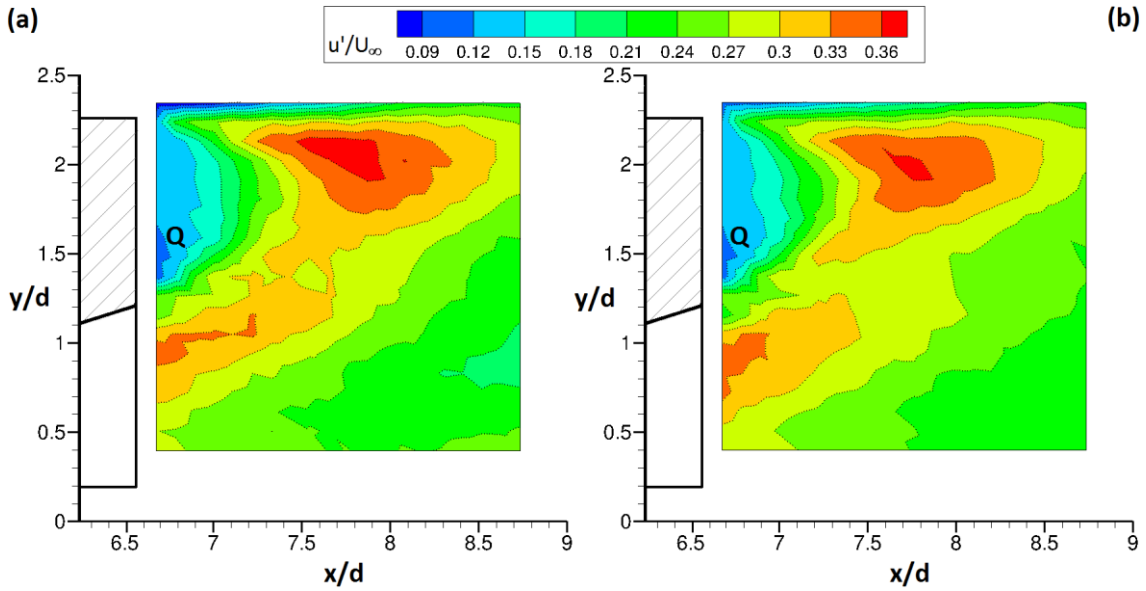

Figure 5-26: Near-wake non-dimensionalised turbulence intensity $(\boldsymbol{u'/U_\infty})$ contours for the diffuser body measured with LDV at $h/d = 0.191$ on: **(a)** plane at $z/d = 0.490$ and **(b)** plane at $z/d = -0.490$

At $h/d = 0.153$, velocity measurements reveal a different velocity contour plot on planes at $z/d = 0.490$ and -0.490, indicating that the diffuser flow is substantially asymmetric as shown in Figure 5–27. The asymmetric flow can be attributed to the breakdown of one of the longitudinal vortices as shown

at $z/d = 0.490$ in Figure 5—27a. As reported by Senior (2002), the loss of downforce coincided with the development of flow asymmetry and the asymmetric 3—D boundary layer at the diffuser inlet induced a breakdown of one of the vortices. The breakdown of the vortex shown for at $z/d = 0.490$ in Figure 5—27a allowed the low velocities of the upper separated flow region to dominate a large area of the diffuser near-wake. As a result, separated flow is prevalent over a substantial area of the near wake at $z/d = 0.490$ and flow turbulence is enhanced further downstream of the wake as shown in Figure 5—28a. However, higher velocities (close to freestream velocity) are prevalent near the diffuser exit at $z/d = -0.490$ in Figure 5—27b even though the separated flow region close to the base surface of the bluff body is still present. Despite the higher velocities near the diffuser exit at $z/d = -0.490$, Figure 5—28b indicates a significant reduction in turbulence levels in the vortex close to the diffuser exit, as observed at $h/d = 0.191$ in Figure 5—26b. Senior (2002) observed that this was because the surviving vortex had separated from the diffuser ramp and side walls and is less diffused towards the diffuser exit than the type B flow hence the reduced level of turbulence. In addition, the near-wake of the bluff body base plate was dominated by low turbulence on the streamwise planes on both sides of the bluff body centreline indicating a low turbulent flow in the region.

Notably, the higher velocities between the upper and lower low-velocity regions on the streamwise near-wake plane at $z/d = -0.490$ in Figure 5—25b reached a peak velocity approximately 11.1% higher than that of the corresponding measurement in the same area on the near-wake plane at $z/d = 0.490$, as shown in Figure 5—25a. Low velocities within the lower part of the planes at $z/d = -0.490$ and $z/d = -0.490$ can be attributed to the diffused and turbulent part of the vortex at the diffuser exit. However as shown in Figure 5—25, lowest velocity measured at $z/d = -0.490$ is about 100% higher than the corresponding measurement in the same region at $z/d = 0.490$. Furthermore, the surviving vortex of the pair is on the side of

the diffuser represented by the near-wake contours at $z/d = -0.490$ at a ride height of $h/d = 0.153$ as shown in Figure 5–27b. These observations suggest that at $h/d = 0.191$, the vortex at $z/d = -0.490$ is stronger than that at $z/d = 0.490$, and for this reason the vortex at $z/d = -0.490$ in the asymmetric flow at a ride height of $h/d = 0.153$ is still present.

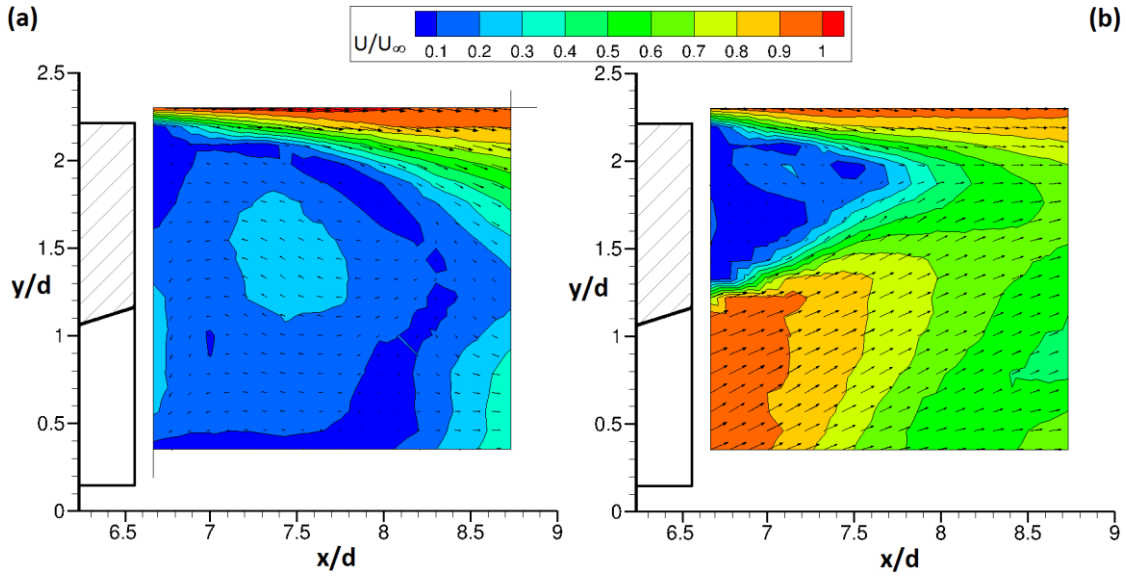

Figure 5-27: Near-wake non-dimensionalised $\boldsymbol{U}$ contours for the diffuser body measured with LDV at $h/d = 0.153$ on: **(a)** plane at $z/d = 0.490$ and **(b)** plane at $z/d = -0.490$

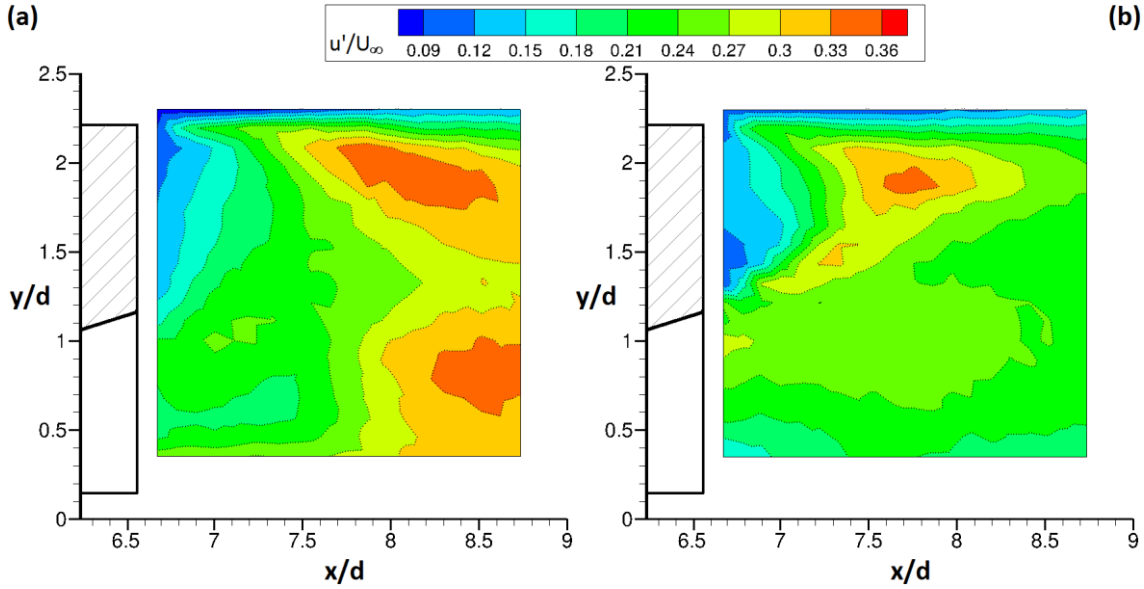

Figure 5-28: Near-wake non-dimensionalised turbulence intensity ($\boldsymbol{u'/U_\infty}$) contours for the diffuser body measured with LDV at $h/d = 0.153$ on: **(a)** plane at $z/d = 0.490$ and **(b)** plane at $z/d = -0.490$

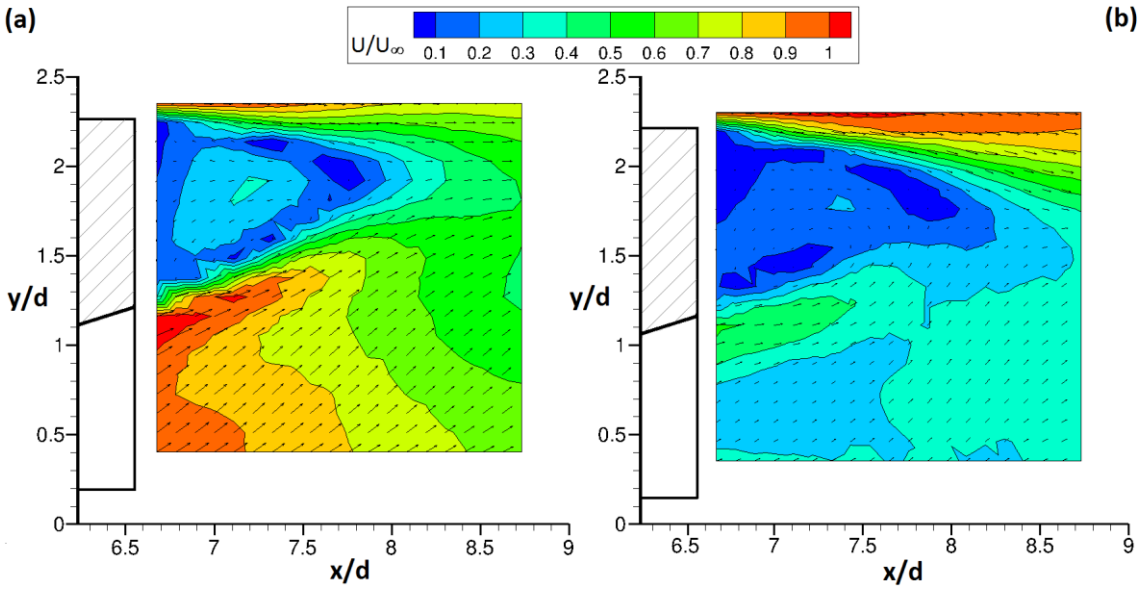

Figure 5-29: Near-wake non-dimensionalised $\boldsymbol{U}$ contours for the diffuser body measured with LDV at centreline plane $(z/d = 0)$ for: **(a)** $h/d = 0.191$ and **(b)** $h/d = 0.153$

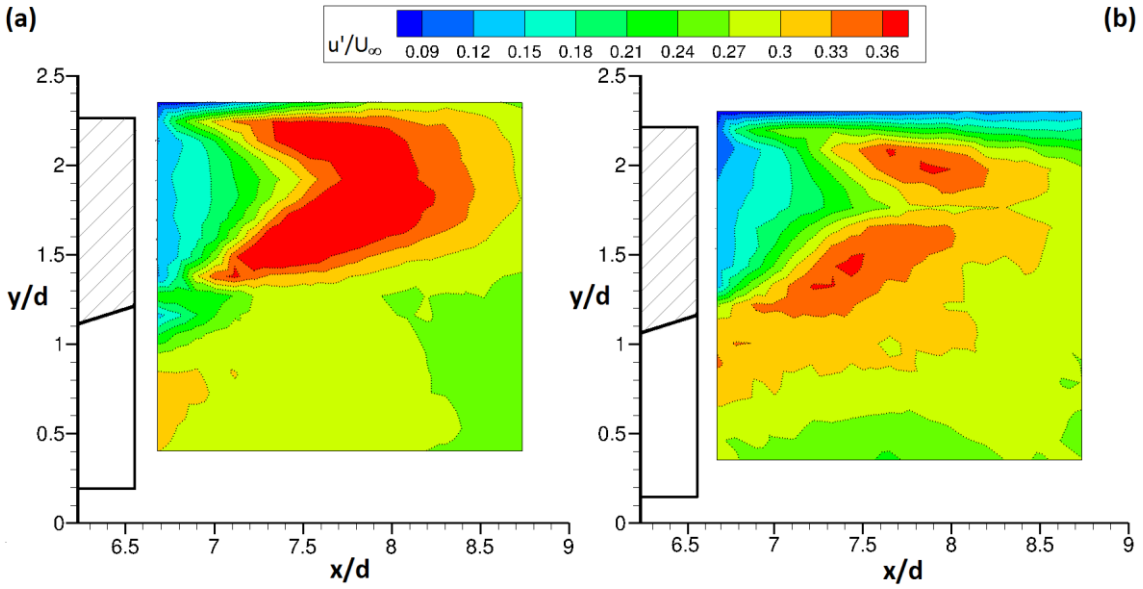

Figure 5-30: Near-wake non-dimensionalised turbulence intensity $(\boldsymbol{u'/U_\infty})$ contours for the diffuser body measured with LDV at centreline plane $(z/d = 0)$ for: **(a)** $h/d = 0.191$ and **(b)** $h/d = 0.153$

The centreline $(z/d = 0)$ velocity magnitude and turbulence contours for $h/d = 0.191$ and 0.153 are shown in Figure 5—29 and 5—30. In Figure 5—29a, the centreline plane for $h/d = 0.191$ show a region of low velocity at the near-

wake of the base plate of the body above a region of high velocity at the near-wake of the diffuser exit. For $h/d = 0.153$ (Figure 5—29b), the near-wake of the entire body is largely dominated by low velocities with a diminished region of relative high velocity close to the diffuser exit. The centreline wake behaviour at the type B ($h/d = 0.191$) and type C ($h/d = 0.153$) flow regimes indicates that the outflow of the type B regime remains strong. In the type C regime, the vortex breakdown and the flow reversal it induces on one side of the diffuser is also impeding the diffuser outflow away from the spanwise location of vortex breakdown towards the diffuser centreline at $z/d = 0$. The centreline near-wake turbulence contours at $h/d = 0.191$ (Figure 5—30a) indicate that the turbulence induced by the diffusing vortices on either side of the centreline plane merge at the centre of the diffuser together with the turbulence generated above the diffuser exit and downstream of the base plate of the buff body. In the case of the centreline plane for $h/d = 0.153$ (Figure 5—30b), the interaction between the reverse flow on one side of the diffuser centre plane and the diffusing vortex on the other side has enhanced centre plane turbulence at the bluff body near-wake.

Velocity power spectral densities (Figures 5—31) in the near wake at a location on the centreline plane underneath the region of low velocity and above the region of high velocity ($y/d = 1.6$ and $x/d = 7.84$) of Figure 5—29 (shown for only $h/d = 0.191$ and 0.153) indicate a similar time history behaviour for u and v. A dominant frequency of ~$36Hz$ (for type A flow at $h/d = 0.382$); ~$34Hz$ (for type B flow at $h/d = 0.191$); and broadband frequencies within <$20Hz$ (for type C flow at $h/d = 0.153$). This implies that a dominant frequency exists in the types A and B where the diffuser outflow is strong and steady but in the type C flow regime where flow reversal due to vortex breakdown and flow separation at the diffuser inlet occurs, the frequency is lower and exists over a wide range distribution. Time-averaged CFD flow velocity predictions on the streamwise near-wake planes for $h/d = 0.191$ and 0.153 indicate a reasonable agreement with wind tunnel

measurements (Figures 5–32 to 5–34). However, noticeable differences occur largely in the high velocity contour region of the diffuser exit (for $h/d = 0.191$) where CFD appeared to have underpredicted the higher velocities within the region by about 10% (Figures 5–32 and 5–33). At $h/d = 0.153$ (Figure 5–34), CFD predicted the dominant low velocity of the reversed flow in the diffuser near-wake but there is a region of overpredicted velocities (by as much as 33%) in the near-wake.

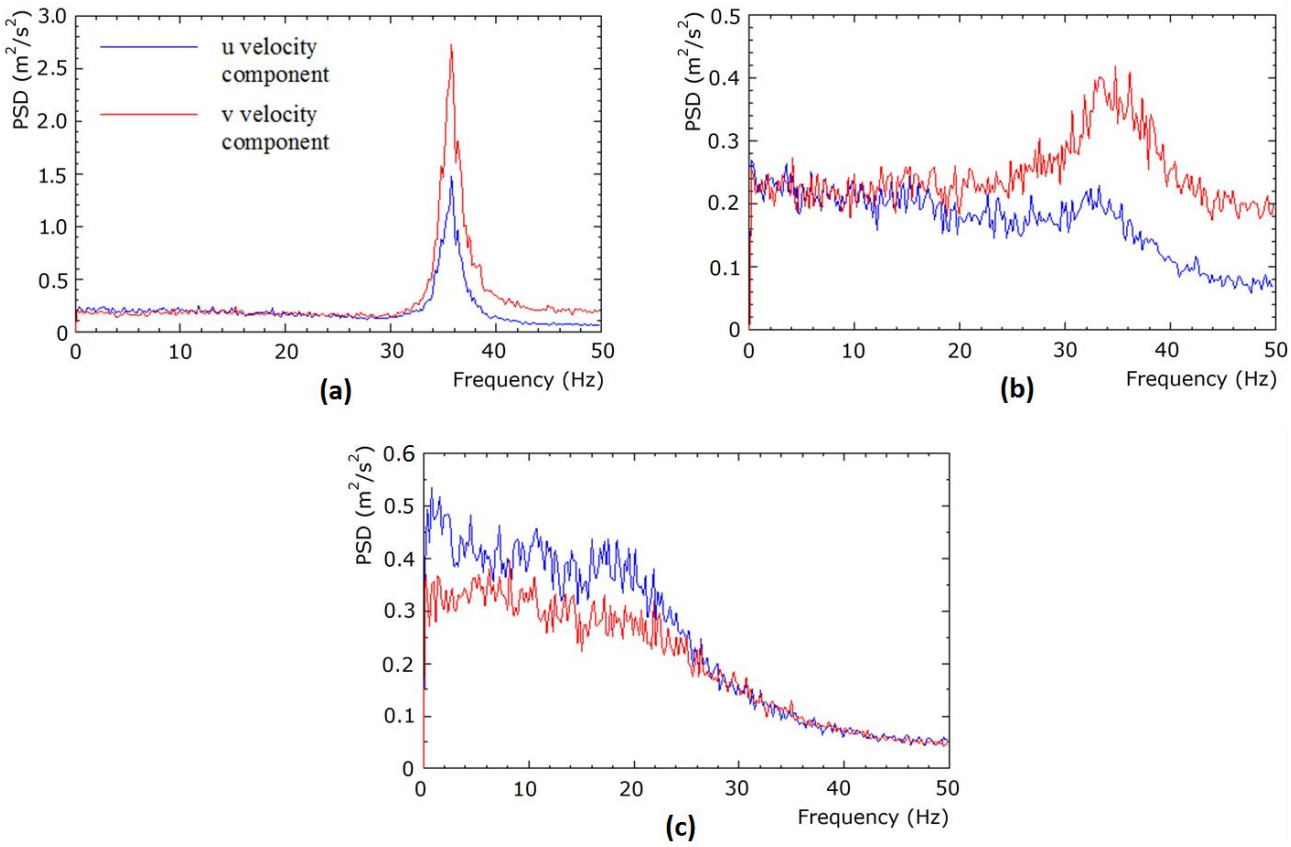

Figure 5-31: Velocity power spectral densities for $\boldsymbol{u}$ and $\boldsymbol{v}$ measured by LDV at the near wake location ($y/d = 1.6$ and $x/d = 7.84$) for: **(a)** $h/d = 0.382$ **(b)** $h/d = 0.191$ and **(c)** $h/d = 0.153$

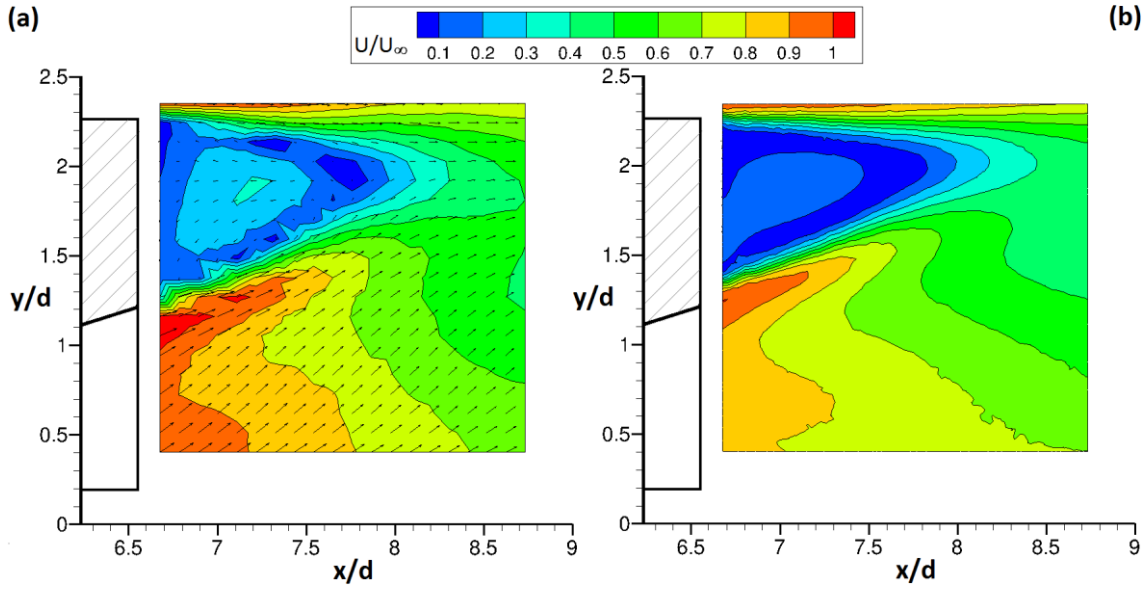

Figure 5-32: Near-wake non-dimensionalised $\boldsymbol{U}$ contours for the diffuser body at $h/d = 0.191$ and on the centreline plane at $z/d = 0$ for: **(a)** Wind tunnel LDV measurements **(b)** time-averaged URANS predictions

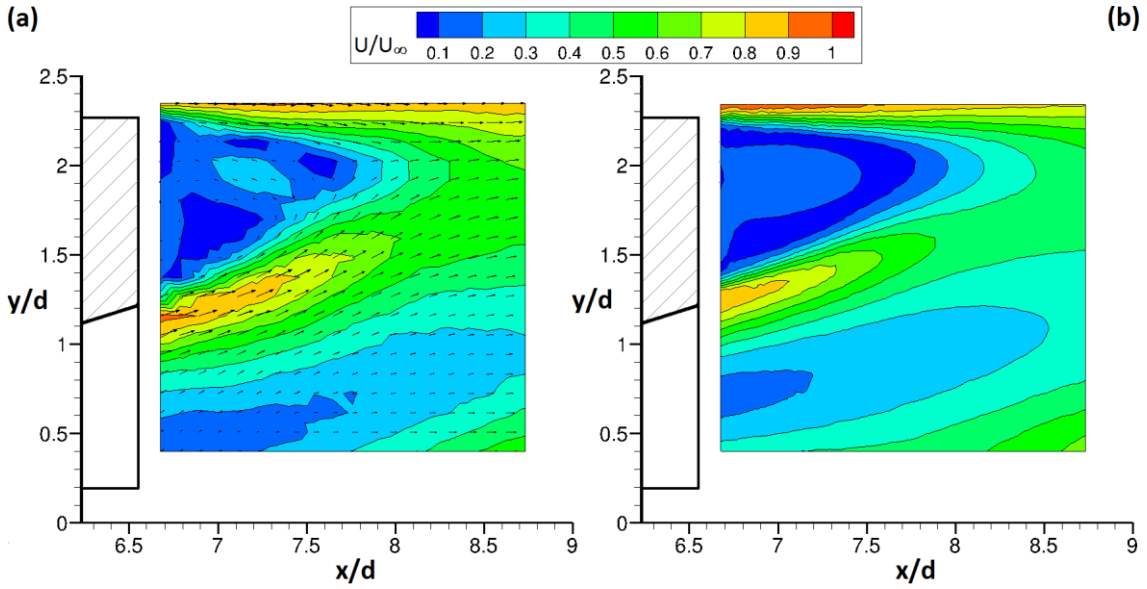

Figure 5-33: Near-wake non-dimensionalised $\boldsymbol{U}$ contours for the diffuser body at $h/d = 0.191$ and on the plane at $z/d = 0.490$ for: **(a)** Wind tunnel LDV measurements **(b)** time-averaged URANS predictions

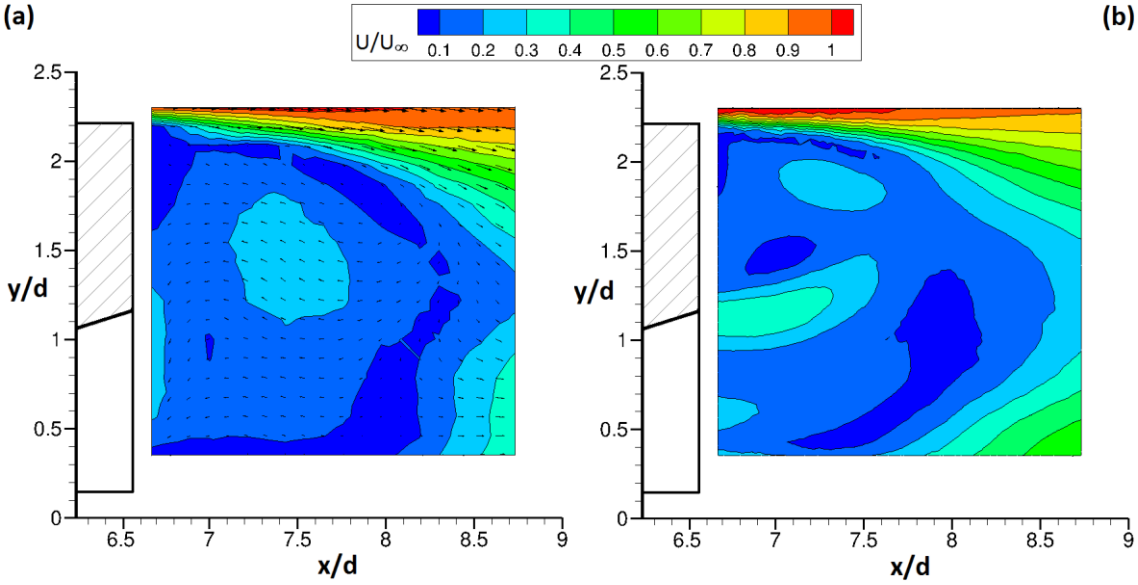

Figure 5-34: Near-wake non-dimensionalised $\boldsymbol{U}$ contours for the diffuser body at $h/d = 0.153$ and on the plane at $z/d = 0.490$ for: **(a)** Wind tunnel LDV measurements **(b)** time-averaged IDDES predictions

5.2.3 Flow structures of diffuser near-wake region

The near-wake of bluff bodies is dominated by separated flow. The separated flow of the near-wake region in turn dominates the aerodynamic drag of bluff bodies, the pressure drag component of which can be attributed to the pressure difference between the high pressure (stagnation point) on the front surface of the bluff body and the low pressure on the base surface induced by the separated flow at that region. The flow structures on the planes at $z/d = 0.490$ and -0.490 in the near-wake of the diffuser bluff body (Figures 5—35 to 5—37) indicated the presence of the separated and recirculating flow in this region. Also, the flow exiting the diffuser was found to shape the recirculating flow in the near-wake region of the bluff body.

These observations agree with earlier reports that the near-wake at the centreline of a 'bus-shaped' bluff body was dominated by upper and lower counter-rotating vortices (Krajnovic and Davidson, 2001). In addition, the lower vortex was found to have originated from the underbody flow traveling through the ground clearance of the bluff body. Likewise, Puglisevich (2011) discovered that for a bluff body with a diffuser, the lower vortex of the near-

wake generated by the flow exiting the diffuser dominated the near-wake region of the bluff body, reducing the size of the upper vortex generated by the separated flow over the end of the bluff body top surface.

Figure 5—35 shows the flow structure at the maximum downforce ride height of $h/d = 0.191$, suggesting that the lower vortex induced by the upward diffuser exit flow dominated the near-wake region of the baseline diffuser. This lower vortex is larger in size and appeared to have suppressed the size of the upper vortex. The recirculating flows of the upper and lower vortices meet at a saddle point located at a height of approximately $y/d = 2.00$ and a streamwise distance of approximately $x/d = 7.65$. Figure 5—35 also reveals flow angularity differences between the planes at $z/d = 0.490$ and at $z/d = -0.490$ even though the corresponding velocities in Figure 5—25 reveal reasonable flow symmetry. In contrast, a different near-wake flow structure appeared at$z/d = 0.490$ for $h/d = 0.153$ confirming the asymmetry of the diffuser flow in the force reduction flow regime (Figure 5—36).

On the plane at $z/d = 0.490$ in Figure 5—36, the lower vortex induced by the flow exiting the diffuser flow is non-existent, indicating that there is no streamwise vortex on that side of the diffuser. The upper near-wake vortex is shown to dominate the wake of the bluff body. Furthermore, the upper vortex dominance appears to transform into a reverse flow which travels into the diffuser exit to replace the non-existing streamwise flow. The saddle point, where the upper and lower vortices meet, is no longer visible and has been replaced by a flow boundary that separates the reversed flow of the upper vortex and the streamwise wake downstream of the reversed flow. The flow boundary stretches downwards from the upper vortex by a significant fraction of the bluff body height. Due 2—D planar set-up of the LDV experiments, 3—D flow behaviour was not captured. Nonetheless, CFD simulations indicate that solitary wake vortex only stretches across the half span of diffuser body near-wake where the diffuser streamwise vortex has collapsed, and on the other half, the upper and lower wake vortices are present. The flow structure

at $z/d = -0.490$, however, did not change by comparison with the higher ride height, with the lower vortex remaining dominant over the upper vortex. In Figure 5—37, the centreline flow structures for $h/d = 0.191$ and 0.153 show a similar flow direction with the presence of the upper and lower vortices, however, the lower vortex for $h/d = 0.153$ is relatively larger in size to that of $h/d = 0.191$. This further explains the obstruction of the diffuser exit flow by the reversed and recirculating near flow on the side of vortex breakdown up to the centreline of the diffuser exit span (hence the low velocities in the near-wake of the diffuser exit in Figure 5—29b). However, it is noteworthy to indicate that although bi-stability of the type C flow regime at $h/d = 0.153$ did not occur in this present study, Senior (2002) reported the occurrence of this flow behaviour.

Bi-stable flow can be described as a flow behaviour characterized by two stable states of equilibrium which are usually asymmetric (Schewe,1983). However the asymmetric configurations can occur and stabilize around symmetric structures like single circular cylinders and circular cylinders in pairs (Lupi et al., 2013). Flow bi-stability examples include the flow field around offshore structures, axisymmetric slender bodies, and missiles. As stated in Section 4.1.3, Senior (2002) found that between $h/d = 0.204$ to $h/d = 0.159$ of the type C flow regime the breakdown of the vortex randomly switched from one side to the other. This bi-stable flow behaviour was attributed to errors in bluff body yaw settings and an uneven flat section of the underbody surface. The bi-stable behaviour of the diffuser flow was non-existent in the wind tunnel experiments in this present study even though yaw sensitivity was also investigated. However, it was observed in the CFD investigations at $h/d = 0.153$ (type C regime) that a change of the intermittency settings of the γ–Re_θ transition SST turbulence model (as detailed in Section 3.3.4) between a fully turbulent and a fully laminar mode induced flow bi-stability. Also with the k–kl–ω transition model at $h/d = 0.064$, flow bi-stability was grid sensitive. This because a change in the grid

size of the unstructured tetrahedral cells or y^+ of the wall-bounded prism layers automatically alters the grid distribution between both spanwise ends of the diffuser body.

The computational attributes implies that although the vortex breakdown and near-wake flow reversal as documented in this study consistently occurred at the port side $(+z/d)$ of the diffuser body, these flow characteristics can be bi-stable. Thus, bi-stability can also occur for the static pressure distribution on the diffuser ramp induced by the asymmetric flow characteristics associated with the type C and D regimes.

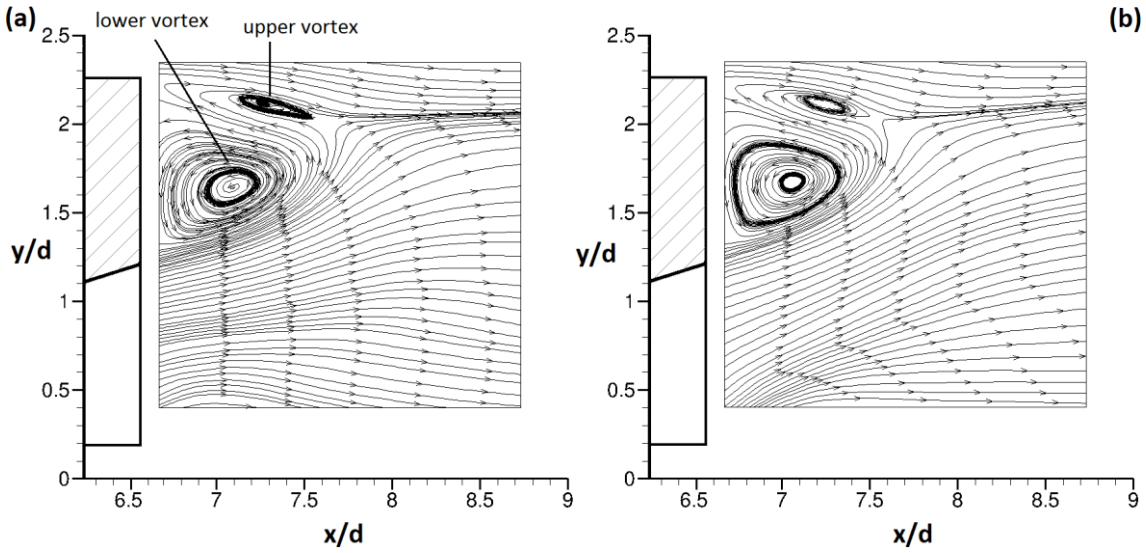

Figure 5-35: Near-wake $\boldsymbol{U}$ flow structures for the diffuser body measured with LDV at $h/d = 0.191$ on **(a)** plane at $z/d = 0.490$ and **(b)** plane at $z/d = -0.490$

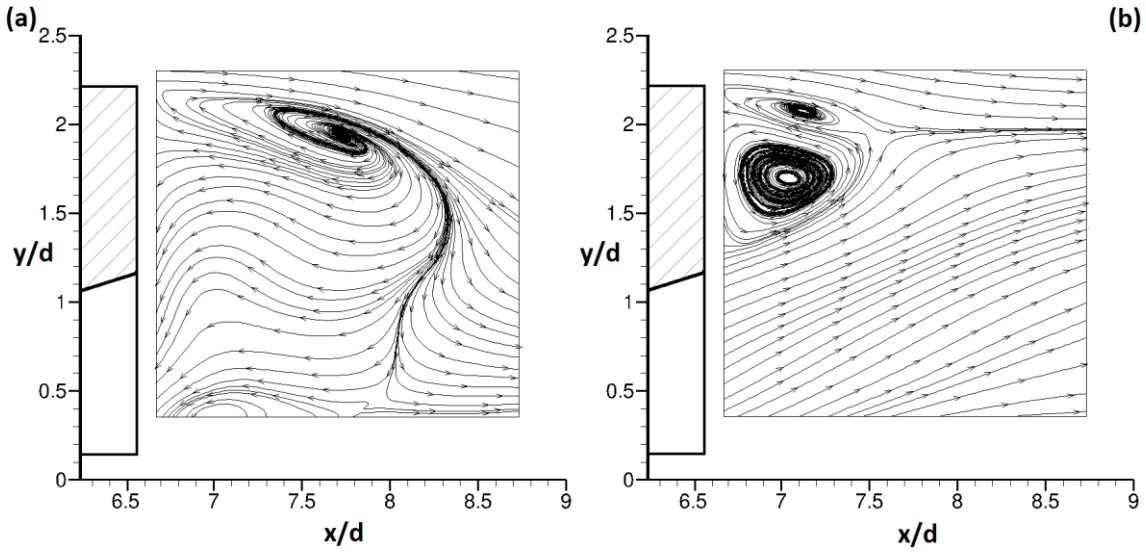

Figure 5-36: Near-wake $\boldsymbol{U}$ flow structures for the diffuser body measured with LDV at $h/d = 0.153$ on: **(a)** plane at $z/d = 0.490$ and **(b)** plane at $z/d = -0.490$

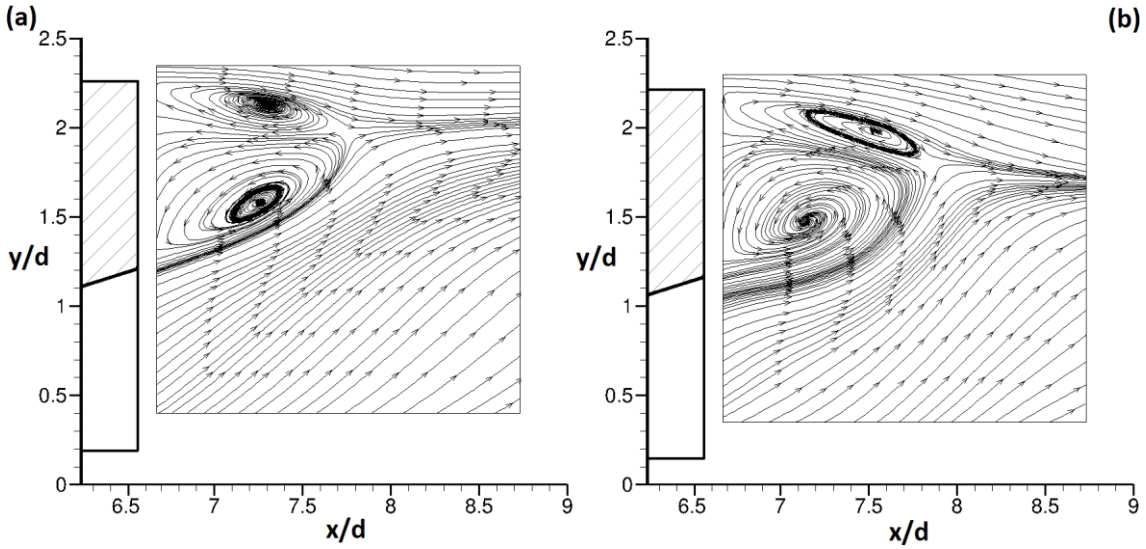

Figure 5-37: Near-wake $\boldsymbol{U}$ flow structures for the diffuser body on centreline plane $(z/d = 0)$ measured with LDV at: **(a)** $h/d = 0.191$ and **(b)** $h/d = 0.153$

5.3 Further Discussion

The flow physics within and in the near wake of the diffuser provides not only a validation to the information described by Senior (2002) but also, additional understanding of the diffuser flow. Downforce is generated in the type A and B flow regimes due to the high-velocity flow at the diffuser inlet and the additional streamwise velocity of the longitudinal counter-rotating vortex pair. Notably, the counter-rotating vortices traveling in the streamwise

direction enhance downforce by increasing flow velocity above the vortex core or by the added suction produced by the low pressure vortex core. However, downforce loss occurs in the type C and D flow regimes as a result of the decreased, boundary layer-dominant, flow velocity at the diffuser inlet created by the reduced diffuser inlet area. In addition, the severe adverse pressure gradient that induces flow separation at the diffuser inlet prevents adequate flow-turning to occur and deprives one of the vortices of the flow velocity and vorticity it requires to survive in the type C and D flows.

The flow within the type A flow regime as illustrated at $h/d = 0.764$ and 0.382 is comprised of a vortex pair with concentrated vorticity, thus high axial speed. The strength of the vortex pair remains strong along the diffuser length, as indicated by the visible concentrated vorticity and relatively reduced turbulent kinetic energy in comparison to subsequent flow regime types. In the type B flow regime, the vorticity at the vortex core is present from the diffuser inlet to a lengthwise distance about half of the diffuser length. The vortex cores up to that point increase in size, and beyond that half-way distance towards the diffuser exit the disappearance of the vortex core (even though velocity vectors show the presence of a rotating flow) indicates the occurrence of a vortex breakdown.

The high turbulent kinetic energy close to the diffuser exit combined with low streamwise velocity, and high turbulence intensity at the near-wake of the diffuser suggest that the breakdown of the vortex pair began inside the diffuser. Senior (2002) suggested that the breakdown of the vortex may have been induced by vortex wandering generated by the Kelvin-Helmholtz instability of the vortex shear layer. Gursul and Xie (2000) stated that the random displacement of the vortex core associated with trailing wing-tip vortices increased swirl velocities and this was as a result of shear layer instability around the vortex core. Also, the PIV investigations by Edstrand et al. (2016) indicated that the trailing vortex core structure of an airfoil diffused as it travels downstream with increased kinetic energy and turbulence levels

related to shear layer instabilities. Notwithstanding, the type B flow appeared to have generated more downforce than the type A flow not only because of relative increased diffuser inlet flow velocity but also because at the early part of the diffuser, the larger vortex core generated increased suction.

In the type C flow regime, the vorticity of the surviving vortex remains present in the early part of the diffuser before it breaks down later towards the diffuser exit. This increased turbulent kinetic energy towards the diffuser exit. In addition, the respective flow separation and reverse flow indicated by the low velocity shear layers on the other side of the diffuser and at the diffuser near-wake where vortex breakdown occurred appear to have generated high turbulent kinetic energy inside the diffuser. Hence, the vortex breakdown and low streamwise flow velocity are responsible for the loss of downforce. The type D flow is largely dominated by low velocity flow due to increased flow separation, recirculation and a merged boundary layer at the diffuser inlet. The invisibility of vorticity contours in the early part of the diffuser indicates that the surviving vortex is severely weakened and unsteady although the velocity vectors indicate the vortex remains present. Also, the high turbulence energy generated by the weak surviving vortex on one side of the diffuser and the separated and recirculating flow on the other side of the diffuser has merged across the diffuser span. As a result of the flow physics described, low downforce is associated with the type D flow regime.

5.4 Summary

In conclusion, the type A and B flows are reasonably symmetric with the presence of a counter-rotating vortex pair. The vortices in the type A flow sustain a coherent vorticity region from the diffuser inlet to the diffuser exit. However in the case of the type B flow, its larger vortices diffuse towards the diffuser exit with increased turbulence. Near-wake flow structures for the type A and B flow regimes includes an upper vortex produced by the off-surface separated flow above the diffuser body and a lower vortex induced by the separated upwash from the diffuser exit.

The type C and D flows are asymmetric due to the existence of a single surviving vortex. The surviving vortex is weaker than in the type A and B flow regimes and the diffuser flow synonymous with the type C and D flow regimes is largely unsteady. Unlike the type A and B flows, flow reversal dominates the diffuser near-wake of the type C and D flow regimes on the side where vortex breakdown occurred. Also, it was confirmed as detailed by Senior (2002) that the boundary layers at the diffuser inlet in the type C do not merge although in the type D regime, the amalgamation of the boundary layers is more apparent. However, the selection of the particular vortex for breakdown does not appear to be random as suggested by Senior (2002) but rather on the side of the diffuser with the weaker velocity (thus vorticity) as the flow velocity of the diffuser inlet boundary layer reduces with decreasing ride height. This selection begins in the type B flow where the diffuser flow appears reasonably symmetric but the inlet boundary layer, although not predicted by time-averaged CFD, is measured in the wind tunnel to have a degree of asymmetry (with one side having lower inlet velocity).

Lastly, the diffuser vortices, recirculating flow, and near-wake flow turbulence induced flow energy losses (Figure 5—22) on the freestream flow traveling around the diffuser body as indicated by the total pressure distribution.

Chapter 6

Flow Physics of Diffuser with Passive Flow Control

In the previous chapters (4 and 5), the flow physics of the plane diffuser (baseline) have been discussed with analysis of the on-surface flow features, time-averaged flow quantities within the diffuser, force and surface pressure measurements. The analysis of the baseline diffuser was also presented in terms of the four distinct flow regimes. In this chapter, the focus of the results analysis is on passive flow-control methods that enhance the aerodynamic performance of the diffuser. The flow control methods enhance downforce by inducing changes in the diffuser flow velocity as detailed in the velocity profiles subsequently presented in this Chapter. In addition, surface pressure and force measurements from wind tunnel experiments and time-averaged CFD together with on-surface flow features from ride heights representing the four flow regimes are all presented comparatively with the plane diffuser (baseline).

6.1 Flow Control Methods: Introduction

As detailed in Chapter 2 (Section 2.3.1), flow control methods exist as passive and active devices. Passive flow control devices are mainly geometric modifications of an aerodynamic surface while active devices involve the application of an external energy source to alter the flow behaviour. In this study, passive methods are investigated due to their dependability and cost savings relative to active methods, which require expensive energy resources (electrical or mechanical) to function. Geometric modifications such as vortex generators that do not require an energy resource to function, have been

established as efficient devices on a high-lifting aeroplane wing that re-energise slow-moving boundary layer on the suction surface of the wing through the inducement of a vortex. As a result of this action, aerodynamic performance of the wing is enhanced due to a delay in local flow separation.

However in this study, the novel passive methods employed to enhance the downforce generated by the diffuser apply the aerodynamic principle of flow curvature effect. Flow over the curved surface of a convex shaped body or top side of an aerofoil alters the shape of the straight-line freestream to a curved flow and the flow curvature introduces a pressure drop to the flow. Therefore to achieve the static pressure drop at the diffuser inlet and pressure rise downstream of that point, flow curvature can be applied at a location near the diffuser exit. A second-stage pressure drop and congruent pressure recovery as delineated in Section 2.3 of Chapter 2, lowers the average pressures across the diffuser ramp surface, thus increasing downforce. The application of flow curvature on a convex bump, an inverted wing and a combination of the two is explored and analysed in this chapter.

6.1.1 Convex bump

The convex bump passive flow control method as shown in Figure 3—4, involves the positioning of a bump near the end of the diffuser ramp surface. The curvature of the bump increases flow velocity along its surface because the flow requires a favourable pressure gradient to accelerate over the convex surface of the bump. Therefore, the flow reattaches to the curved surface of the bump due to a radial pressure gradient normal to the bump curvature. The consequence of this action is a static pressure drop near the diffuser exit followed by an increase to freestream static pressure (Figure 2—15), thus increasing downforce across a wide range of ride heights. The static pressure drop induced by wall-bounded flows over convex surfaces has been found to be accompanied with a reduction in wall friction, turbulence intensity and shear stress as the static pressure subsequently recovers (So & Mellor, 1973; Gibson et. al., 1984; Muck et al., 1985). However, even though the convex surface

generates a low skin friction drag, the increase in static pressure at the leading surface of the convex surface on the diffuser ramp means that there is an increase in profile drag.

Initial investigations with CFD as shown in Figure 6—1 indicated that the aerodynamic performance of the convex bump is dependent on its length and thickness. An increase in bump length will increase downforce, however, an increase in bump thickness will increase downforce up to a critical point after which further increase in thickness will reduce the lift-to-drag ratio of the bump as a result of increased profile drag. This is because the curvature has become too steep (inducing a significant adverse pressure gradient) for the flow to remain attached to the bump surface. Downforce, drag, and lift-to-drag ratio of five bump sizes are presented in Table 6—1. Among the bump sizes investigated in Figure 6—1, an effective bump thickness ($5.6\,mm$) was discovered to be within ~20% of the plane diffuser ramp boundary layer thickness (low-velocity shear layers near the diffuser exit) of Figure 6—1a. In addition, to maximize the flow curvature effect and the aerodynamic performance of the second-stage pressure recovery region in delaying pressure recovery near the diffuser exit, it was discovered that the length of the bump should be about 25% to 30% of the diffuser ramp length.

As shown in Figure 6—1b, the diffuser flow over the surface of a convex bump, $50\,mm$ long and $10\,mm$ thick, increased boundary layer thickness upstream of the bump in comparison to that of the plane diffuser (Figure 6—1a). This is because the bump thickness and length is too high and small respectively to induce the flow acceleration associated with flow curvature even though the velocity contours in Figure 6—1b indicates a small region of flow attachment towards the bottom of the bump. More so, the high bump thickness is obstructing the flow along the diffuser ramp surface therefore increasing profile drag. The predicted downforce (C_L) and drag (C_D) with the bump at $h/d = 0.764$ are -0.797 and 0.290 respectively, while for the baseline case, predicted C_L and C_D are -0.907 and 0.324

respectively. The reduction in drag with the bump relative to the baseline case indicates that although profile drag may have increased, skin friction drag may have reduced due to a significantly low flow velocity close to the diffuser ramp surface (slow-moving boundary layer) induced by the bump (Figure 6—1b). However in Figure 6—1c, where the thickness of the bump is reduced to 5.6 mm and the length is increased to 92 mm, C_L increased to 0.964 and C_D to 0.327. A further elongation of bump length to 25% and 30% of the diffuser ramp length (with bump thickness remaining at 5.6 mm as shown in Figures 6—1d and 6—1e) also increased C_L and C_D (Table 6—1). The increase in downforce by a longer bump is not only as a result of a reduced bump thickness which allows the flow to travel over the bump with increased streamwise velocity but also due to an increased surface curvature area (longer bump) which provides a larger surface area of low static pressure. Therefore, the flow attachment over the bump is enhanced as a result of the increased radial pressure gradient induced by the longer bump. However, flow velocity induced by the flow curvature effect is diminished with further elongation of the bump beyond 25% to 30% of the diffuser ramp length (Figure 6—1f). As a consequence, aerodynamic efficiency (lift-to-drag) ratio reduces as in the case of a bump that is 50% of the diffuser ramp length (Table 6—1).

Notably when the surface of a bump with a length 15% of the diffuser ramp length and 5.6 mm thick (Figure 6—2), is defined in the CFD boundary conditions as a moving wall traveling in the streamwise direction at 20 m/s (same as freestream velocity), the lift-to-drag ratio generated is the largest among other bump configurations (Table 6—1). This is because the moving bump surface further diminishes the boundary layer growth (near-wall velocity shear layers) near the diffuser exit and extends the higher velocity flow region towards the diffuser exit (Figure 6—2). However, a rolling convex surface as shown in Figure 6—2 is an active flow control system because it requires an energy resource to move the convex surface.

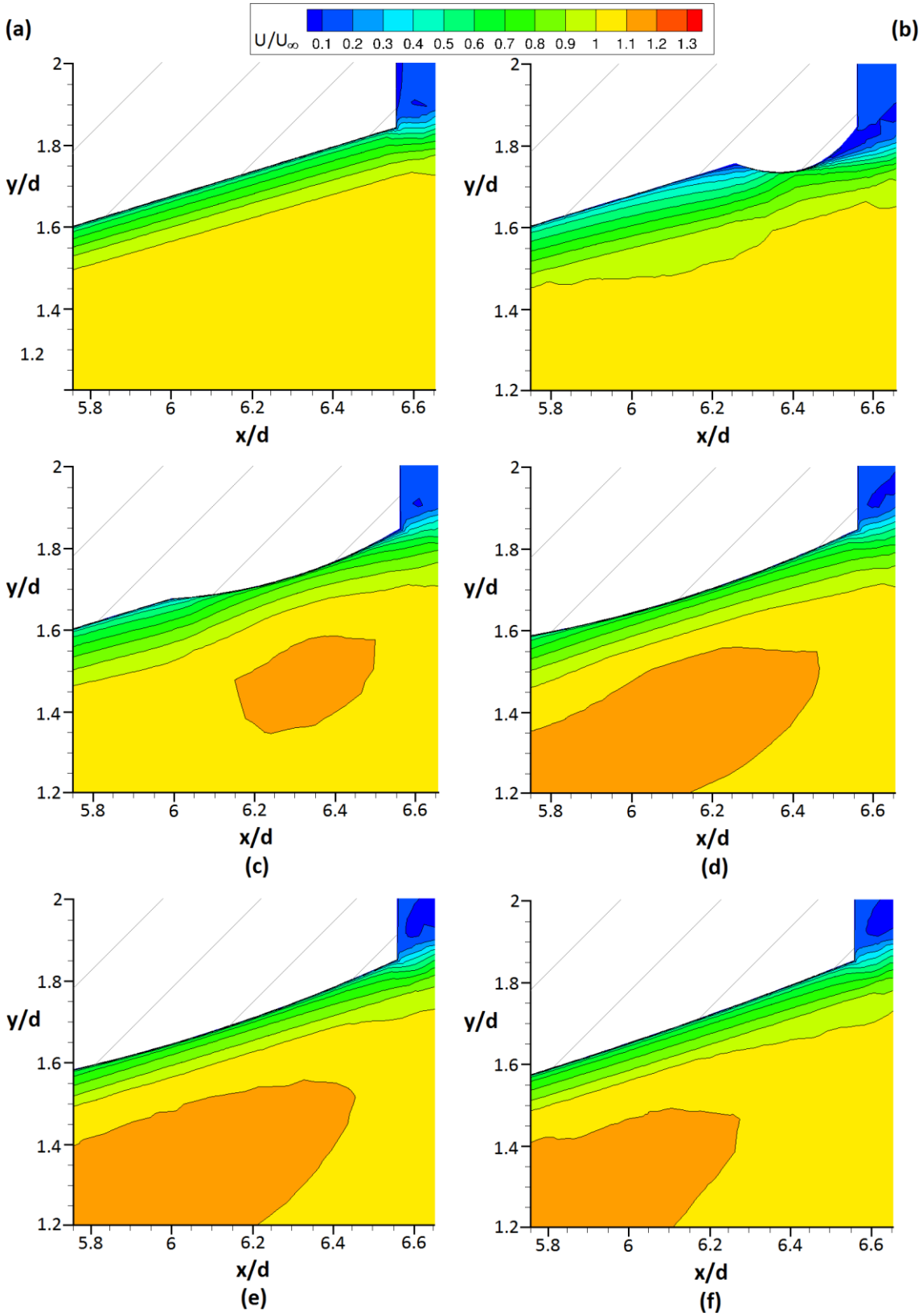

Figure 6-1: CFD total velocity contours on centreline plane $(z/d = 0)$ of the diffuser bluff body at $h/d = 0.764$ for: **(a)** plane diffuser **(b)** a convex bump 50 mm long and 10 mm thick **(c)** a convex bump 92 mm long and 5.6 mm thick **(d)** a convex bump 150 mm long and 5.6 mm thick **(e)** a convex bump 170 mm long and 5.6 mm thick **(f)** a convex bump 280 mm long and 5.6 mm thick

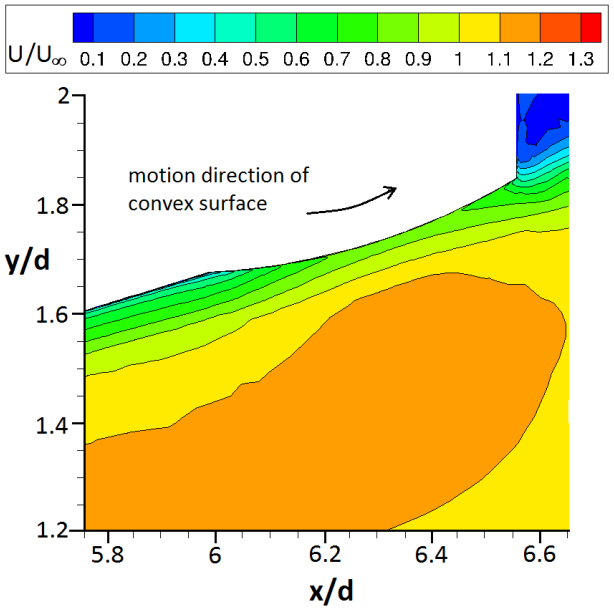

Figure 6-2: CFD total velocity contours on centreline plane $(z/d = 0)$ of the diffuser bluff body at $h/d = 0.764$ with a moving convex bump wall 92 mm long and 5.6 mm thick, travelling in the streamwise direction at $20\ m/s$

Table 6-1: CFD predictions of downforce, drag, and lift-to-drag ratio at $h/d = 0.764$ (type A regime) for the baseline plane diffuser, and the diffuser with a bump of varied dimensions

	$\boldsymbol{h/d = 0.764}$		
Diffuser Type	$\boldsymbol{C_L}$	$\boldsymbol{C_D}$	$\boldsymbol{\lvert C_L/C_D \rvert}$
Plane Diffuser (Baseline)	-0.907	0.324	2.799
Diffuser with bump ~9% of diffuser ramp length (50mm long and 10 mm thick)	-0.797	0.290	2.748
Diffuser with bump ~15% of diffuser ramp length (92 mm long and 5.6 mm thick)	0.964	0.327	2.948
Diffuser with bump ~25% of diffuser ramp length (150 mm long 5.6 mm thick)	-0.978	0.323	3.027
Diffuser with bump ~30% of diffuser ramp length (170 mm long 5.6 mm thick)	-0.979	0.322	3.040
Diffuser with bump ~50% of diffuser ramp length (280 mm long 5.6 mm thick)	-0.971	0.320	3.034
Diffuser with moving bump wall ~15% of diffuser ramp length (92 mm long 5.6 mm thick)	-1.023	0.333	3.072

6.1.2 Inverted wing in diffuser

The downforce-generating characteristics of an inverted 2—D aerofoil have been detailed in Chapter 1. When inverted, the suction side of the aerofoil is parallel to the ground plane, and as airflow travels between the suction side and the ground plane, the constrained flow accelerates and generates low pressure. Similar to the convex surface, the low static pressure induced by the aerofoil suction side is as a result of the introduction of curved streamlines by the curvature of the suction side. Thus for a 3—D flow, a pressure gradient is induced over the curvature of the aerofoil suction surface to enable the flow accelerate over the curved suction surface, and in turn the flow is attached to the surface.

Thus, an inverted wing can be applied within the diffuser (as shown in Figure 3—5) as a passive flow control device to induce a second-stage pressure drop and recovery region close to the diffuser exit. The occurrence of the secondary pressure recovery region close to the diffuser exit lowers average static pressure before the flow exits the diffuser at the higher atmospheric pressure. As a result of this action downforce may be increased. Notably the gap (g_p) between the pressure surface (top side) of the wing and the ramp surface is critical to the performance of the inverted wing as a passive flow control device. This is because the diffusing flow of the diffuser follows the trajectory of the upwardly inclined diffuser ramp. Hence, if the wing is not at an equal angle of attack (α) as the diffuser angle (θ), the wall-bounded airflow between the diffuser ramp and the pressure side of wing separates from the pressure surface of the wing. As a consequence, the aerodynamic performance of the wing declines due to a loss in downforce.

Preliminary investigations with CFD indicated an unperturbed flow towards the diffuser exit (Figure 6—3a), but at $\alpha = 0°$ (Figure 6—3b), airflow separated from the pressure surface of the inverted wing, thus producing a C_L and C_D of -0.748 and 0.280 respectively at $h/d = 0.764$. This implies that at

zero angle of attack, C_L reduced by ~18% and C_D reduced by ~14 % relative to the coefficients predicted for the baseline diffuser (Table 6—2). Also flow velocity upstream and at the early part of the wing appeared to have reduced (Figure 6—3b) because the wing is not aligned with the upward-inclined flow direction, therefore inhibiting the higher flow velocities induced by the suction surface of wing when $\alpha = 17°$ (Figure 6—3c). As a result, downforce is reduced. Notably, drag appeared to have reduced due to the loss of downforce induced by the separated flow above the wing, thus decreasing the accompanying lift-dependent drag. However in Figure 6—3c, where α of the inverted wing is increased from 0° (in Figure 6—3b) to 17° (equal to the diffuser angle) and $g_p = 14.35\,mm$ (50% of diffuser ramp approximate boundary layer thickness), flow separation over the pressure surface is removed. As a result, there is an increase in C_L to -1.040 (+39%) and an increase in C_D to 0.343 (+23%) relative to the zero angle of attack values. When the gap g_p between the ramp and the wing is increased by positioning the wing (with $\alpha = 17°$) at about three times the boundary layer thickness $(g_p = \sim 82\,mm)$ of the ramp (Figure 6—3d), the flow separation over the pressure surface is also removed. However, flow velocity over the pressure surface of the wing is substantially significant than in the case of Figure 6—3c because the pressure difference between the pressure and suction surfaces of the wing is smaller in comparison. Therefore, the diffuser body with the increased gap wing generated a C_L and C_D (-0.963 and 0.324 respectively) that is more (+6% for C_L and 0% for C_D) than the corresponding values for the baseline diffuser, but less (-7.5% for C_L and -5.5% for C_D) than the corresponding values for the wing with a decreased gap.

The velocity contours also indicate that in comparison to the convex bumps (Figure 6—1), the suction surface of the inverted wing (Figure 6—3c) induced an increased region of higher flow velocity. For that reason, the inverted wing as a passive device generates more downforce than the convex bump. Furthermore, an increase in chord length of the inverted wing will further extend the higher

flow velocity region underneath the wing towards the higher velocity region generated by the diffuser inlet. Nonetheless, a second-stage pressure drop close to the primary pressure drop of the inlet can present a steep pressure recovery gradient between both pressure drop locations, thus disrupting the aerodynamic performance of the diffuser pump-down effect. As shown in Figure 6—4, if the wing chord length c is further elongated from 15% (Figure 6—3c) to 25% of diffuser ramp length (Figure 6—4a), downforce and lift-to-drag ratio increases (Table 6—2) due to the extension of contour regions of higher flow velocity induced by the wing suction surface. In contrast, a further increase in c to 40% and 65% of diffuser ramp length further increases downforce but reduces lift-to-drag ratio (Table 6—2) because the leading edge of the wing is increasingly too large to accelerate the upward-inclined diffuser flow as shown in (Figures 6—4b and 6—4c). Therefore, a significant extension of the wing can inhibit the peak flow velocity at the diffuser inlet that produces a corresponding low-pressure peak at the same location. This suggests that a steep secondary static pressure drop close to the primary static pressure drop at the diffuser inlet can induce a significant adverse pressure gradient, thus inhibiting the pump-down effect (as detailed in Section 1.2 of Chapter 1) between the diffuser inlet and exit.

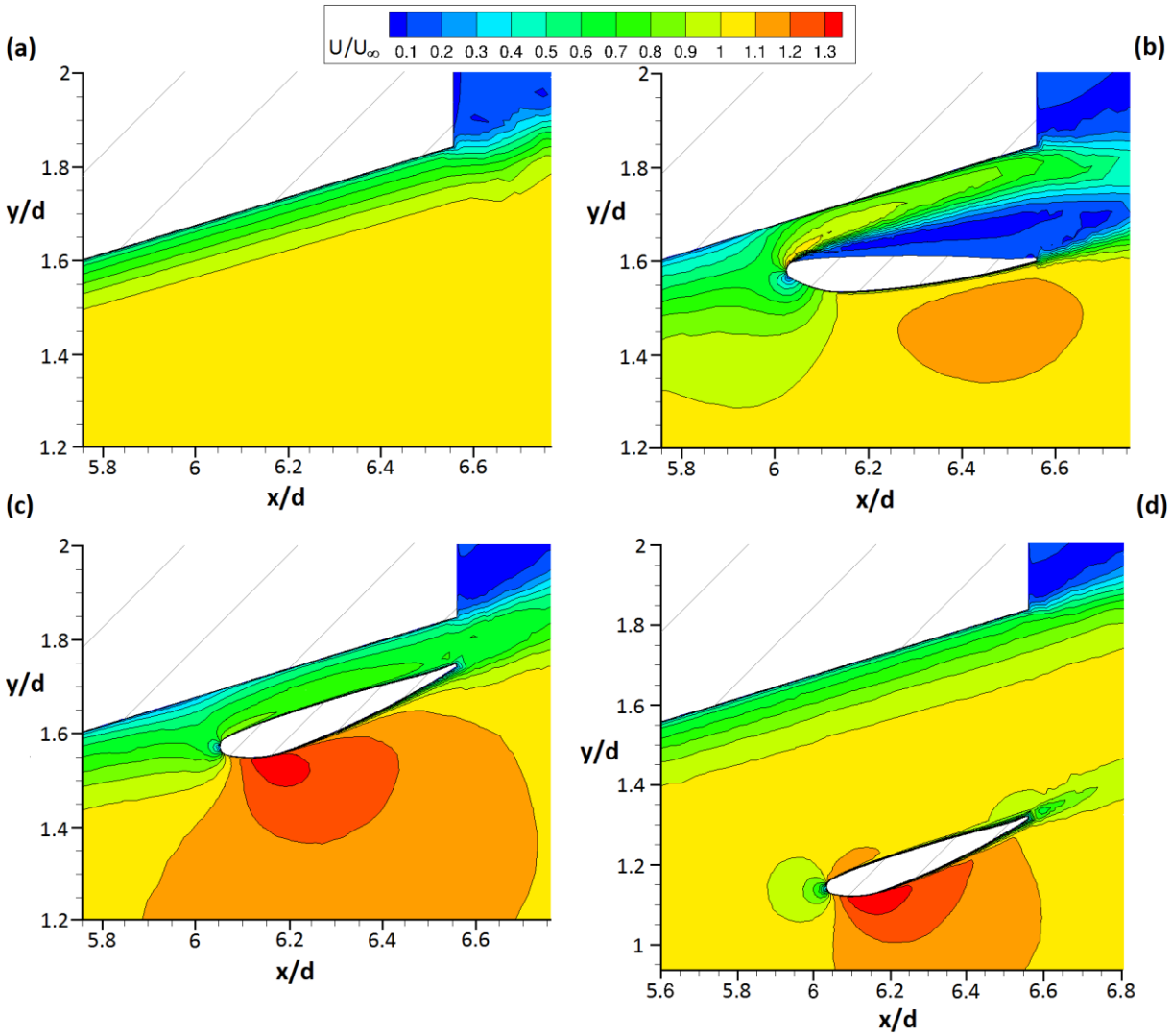

Figure 6-3: CFD total velocity contours on centreline plane $(z/d = 0)$ of the diffuser bluff body at $h/d = 0.764$ for: **(a)** plane diffuser **(b)** diffuser with an inverted wing at $\alpha = 0°$ (diverging gap g_p), and $c = 83.7\,mm$ **(c)** diffuser with an inverted wing at $\alpha = 17°$, $g_p = 14.35\,mm$ and $c = 83.7\,mm$ **(d)** diffuser with an inverted wing at $\alpha = 17°$, $g_p = \sim 82\,mm$ and $c = 83.7\,mm$

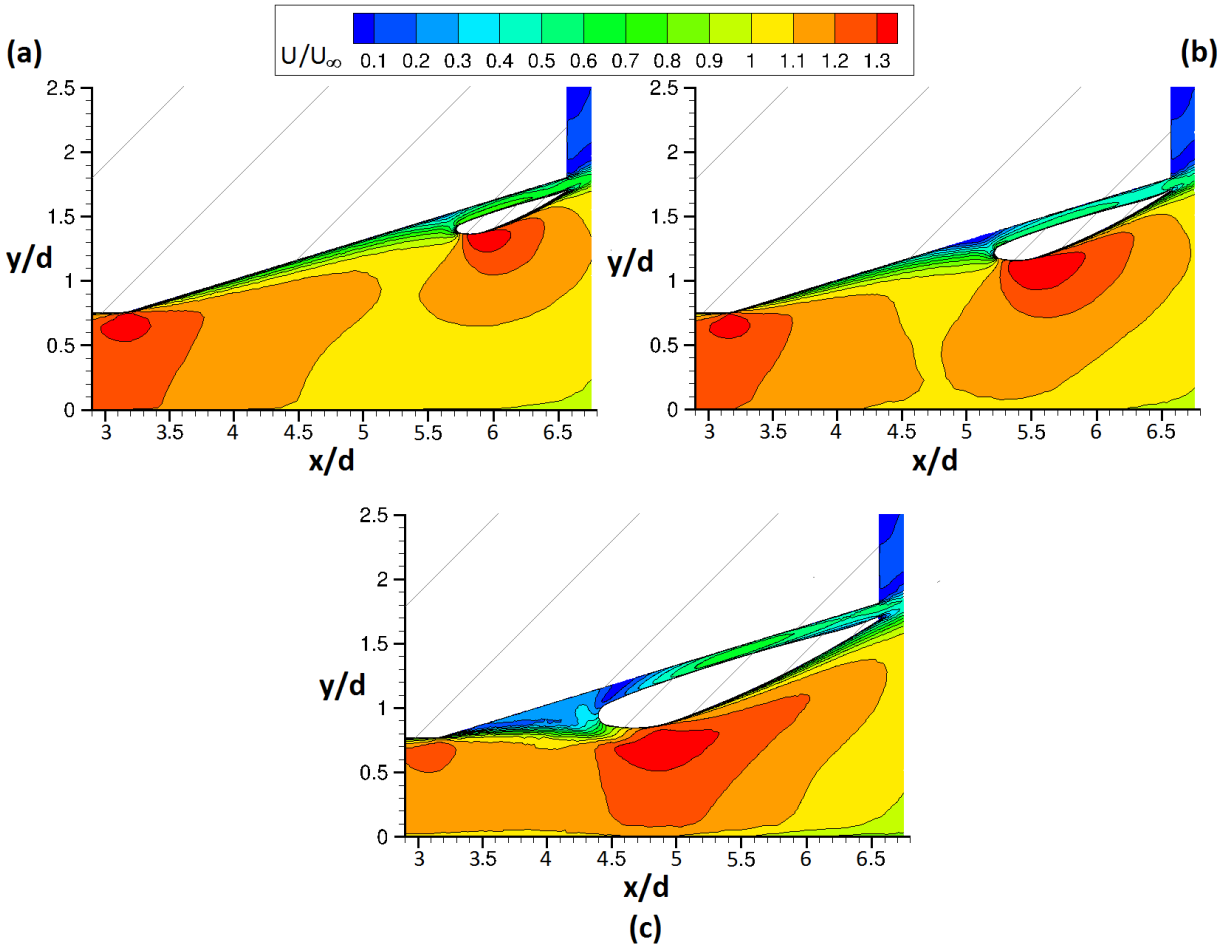

Figure 6-4: CFD total velocity contours on centreline plane $(z/d = 0)$ of the diffuser bluff body with an inverted wing at $\alpha = 17°$, $g_p = 14.35\,mm$ and different chord lengths c at $h/d = 0.764$ for: **(a)** $c = 140\,mm$ **(b)** $c = 225\,mm$ **(c)** $c = 365\,mm$

Table 6-2: CFD predictions of downforce, drag, and lift-to-drag ratio at $h/d = 0.764$ (type A regime) for the baseline plane diffuser; and the diffuser with a wing ($\alpha = 17°$, $g_p = 14.35\,mm$) with varied chord lengths c

	$h/d = 0.764$		
Diffuser Type	C_L	C_D	$\lvert C_L/C_D \rvert$
Plane Diffuser (Baseline)	-0.907	0.324	2.799
Diffuser with wing ~15% of diffuser ramp length (c = 83.7 mm)	-1.040	0.343	3.032
Diffuser with wing ~25% of diffuser ramp length (c = 140 mm)	-1.097	0.340	3.226
Diffuser with wing ~40% of diffuser ramp length (c = 225 mm)	-1.154	0.359	3.214
Diffuser with wing ~65% of diffuser ramp length (c = 365 mm)	-1.188	0.391	3.038

6.1.3 Combination of convex bump and inverted wing

In the case of the 17° angle of attack inverted wing as a passive flow control device, there is a low airflow velocity above the pressure surface of the wing. As a means of increasing the flow above the wing, the convex bump positioned above the wing was explored in preliminary CFD investigations.

As shown in Figure 6—5, flow velocity between the bump and the pressure surface of the inverted wing has increased in comparison to the flow between the wing and the diffuser ramp (Figure 6—3c). This is due to the flow curvature effect of the bump surface. Consequently, static pressure on the bump surface is lowered as airflow passes through the decreased gap between the wing's pressure surface and the bump ($g_p = 8.75\,mm$, which is about 30% of the diffuser ramp boundary layer thickness), before exiting the diffuser at freestream pressure. Furthermore, as shown in Figure 6—5, the suction surface of the wing also induces an increase in flow velocity, which in turn leads to increased suction. As a result of the passive flow control actions of both devices together, downforce is further increased relative to when the inverted wing or convex bump is used individually. At $h/d = 0.764$, the predicted C_L and C_D for the inverted wing and bump configurations are -0.999 and 0.338 respectively but at the maximum-force ride height ($h/d = 0.191$), the use of the bump and wing together generated the most downforce. At the maximum-force flow regime (type B) ride height of $h/d = 0.191$, predicted C_L and C_D for the various diffuser types are respectively: -2.092 and 0.559 (baseline); -2.187 and 0.578 (diffuser with $5.6\,mm$ thick bump); -2.217 and 0.568 (diffuser with wing at $\alpha = 17°$); -2.236 and 0.568 (diffuser with bump and wing at $\alpha = 17°$) (see Table 6—3). Tunnel measurements at $h/d = 0.191$ also indicate that the diffuser with bump and wing generated the most downforce (C_L) among the various diffuser types (see Appendix D).

The flow velocity changes induced by the passive flow control methods are further highlighted in the expanded velocity contours from inlet to exit. In Figure 6—6a, there is a gap between the higher velocities induced by the

diffuser inlet and the bump. When the bump is further elongated (Figure 6–6b), the contour regions of higher flow velocity between the diffuser inlet and the bump are merged. Furthermore, when the wing and bump are used in combination, flow velocity is further increased around the wing near the diffuser exit thus inducing lower static pressures and consequently producing a further increase in downforce.

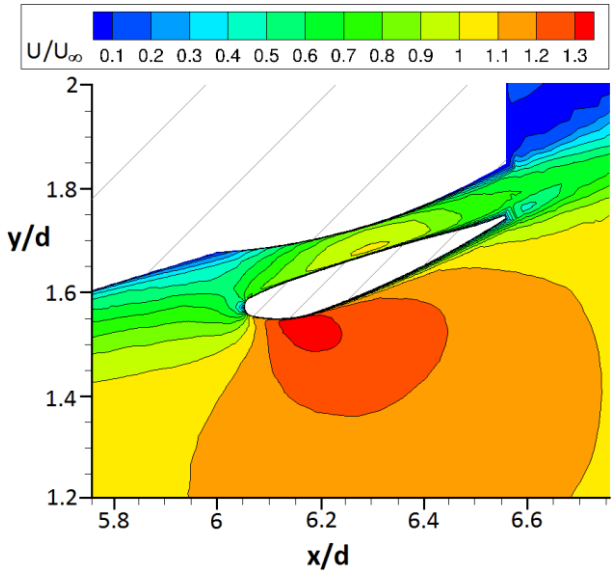

Figure 6-5: CFD total velocity contours on centreline plane $(z/d = 0)$ of the diffuser bluff body at $h/d = 0.764$ for diffuser with a convex bump $92\ mm$ long, $5.6\ mm$ thick; and an inverted wing with $\alpha = 17°$, $g_p = 8.75\ mm$ and $c = 83.7\ mm$

Table 6-3: CFD predictions of downforce and drag coefficients at $h/d = 0.764$ (type A regime) and at $h/d = 0.191$ (type B regime) for the baseline diffuser, and the diffuser with passive flow control methods of varied dimensions

	$h/d = 0.764$			$h/d = 0.191$		
Diffuser Type	C_L	C_D	$\lvert C_L/C_D \rvert$	C_L	C_D	$\lvert C_L/C_D \rvert$
Plane Diffuser (Baseline)	-0.907	0.324	2.799	-2.092	0.559	3.742
Diffuser with bump ~15% of diffuser ramp length (92 mm long and 5.6 mm thick)	-0.964	0.327	2.948	-2.187	0.578	3.783
Diffuser with wing ~15% of diffuser ramp length (α = 17°, g_p = 14.35 mm, c = 83.7 mm)	-1.040	0.343	3.032	-2.217	0.568	3.903
Diffuser with bump (92 mm long and 5.6 mm thick) and wing (α = 17°, g_p = 8.75 mm, c = 83.7 mm); both ~15% of diffuser ramp length	-0.999	0.338	2.955	-2.236	0.568	3.936

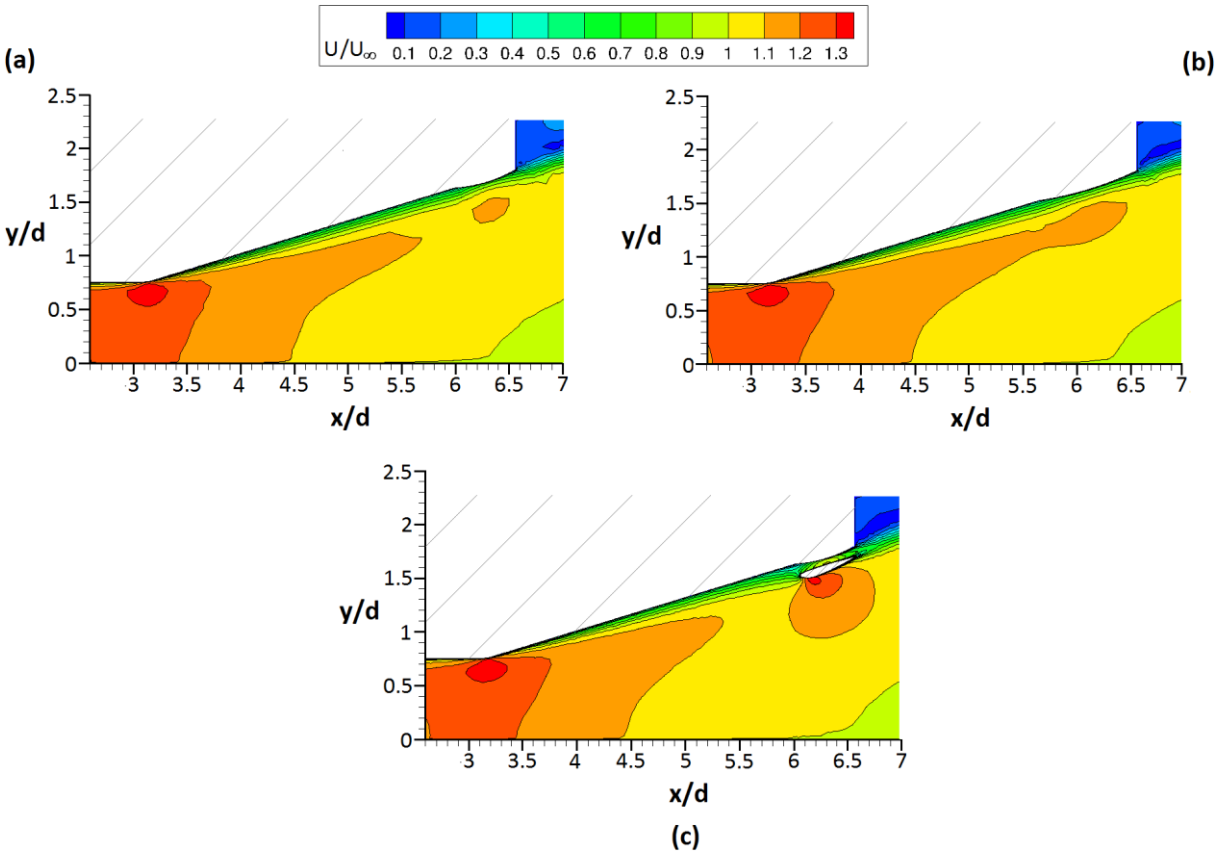

Figure 6-6: An expanded view of CFD total velocity contour profiles from inlet to exit of the diffuser on centreline plane $(z/d = 0)$ of the diffuser bluff body at $h/d = 0.764$ with: **(a)** a convex bump 92 mm long and 5.6 mm thick **(b)** a convex bump 150 mm long and 5.6 mm thick **(c)** a convex bump 92 mm long and 5.6 mm thick; and an inverted wing with $\alpha = 17°$, $g_p = 8.75\ mm$ and $c = 83.7\ mm$

6.2 Flow Characteristics: Baseline and Passive Flow Control Methods

The flow control qualities of the passive control methods as described are ascertained by force and surface pressure measurements and also by the diffuser surface flow features they induce. The aerodynamic effectiveness of the flow control methods is underlined not only by their inducement of flow acceleration through the application of flow curvature effect. Their beneficial aerodynamic impact also includes the conversion of the flow acceleration into incremental downforce by effecting a second-stage pressure drop and recovery close to the diffuser exit across a wide range of ride heights.

6.2.1 Diffuser body downforce and drag measurements

Similar to the plane diffuser case, force measurements with the passive flow control methods were taken for the range of normalized ride heights from $h/d = 0.764$ to 0.064. As shown in the comparative force curves of Figure 6—7, there is a similar trend in force behavior between the passive methods and the plane diffuser. Across the range of ride heights tested, the force curves with the passive methods generally fall within the A to D flow regimes defined with the plane diffuser. However, there are marginal differences with the passive methods on the ride height of maximum downforce or the ride height where the onset of force reduction occurs.

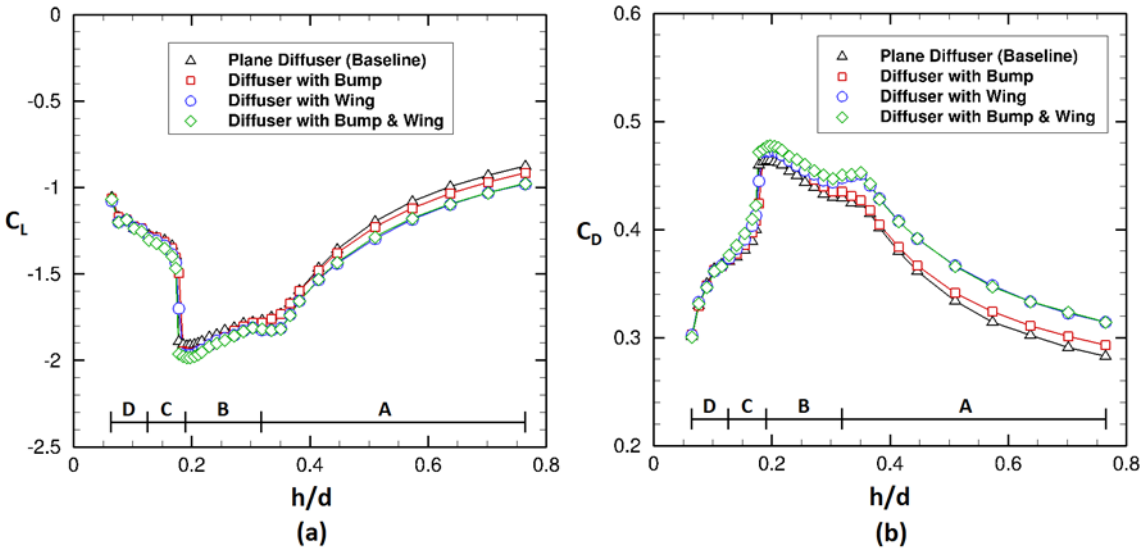

Figure 6-7: Force measurement (wind tunnel) comparison between plane diffuser (baseline) and diffuser with passive flow control methods: **(a)** downforce coefficients **(b)** drag coefficients

In the case of the plane diffuser, flow regime A (force-enhancement) occurred between $h/d = 0.764$ to 0.318 and this is the same with the passive methods. Flow regime B (maximum-downforce) lies within $h/d = 0.318$ to 0.191 for the plane diffuser and this is the same for the diffuser with the inverted wing and the diffuser with both the inverted wing and the convex bump. However, maximum downforce C_L occurs at a higher ride height ($h/d = 0.204$) than $h/d = 0.191$ for the diffuser with the convex bump (see Appendix D). This is because as the diffusing longitudinal vortices travel

across the convex surface they generate small recirculation regions (see Section 6.2.5 of this Chapter) at both sides of the surface. The recirculation regions increase in size with reducing ride height and are adverse to the additional downforce generated by the convex surface suction because they increase static pressure on the suction surfaces of the bump and wing. Thus the recirculation becomes detrimental to further increments of downforce before the ride height reduction gets to $h/d = 0.191$. However the difference in downforce at $h/d = 0.204$ and $h/d = 0.191$ is marginal with C_L measured as -1.957 and -1.954 respectively. Flow regimes C (force-reduction) and D (low-force) occurred between $h/d = 0.191$ to 0.127 and $h/d = 0.127$ to 0.064 respectively for the plane diffuser and this is also the same with the passive methods. However, for the convex bump diffuser, regime C falls within $h/d = 0.204$ to 0.127 as a result of the early attainment of maximum downforce at $h/d = 0.204$.

Also, the comparative force curves (Figure 6–7) indicate a reasonably steady region within the force-enhancement regime (Regime A) between $h/d = 0.350$ to 0.318 for the diffuser with a wing and the diffuser with both the convex bump and wing. As in the case with the convex bump, the diffusing longitudinal vortices generate adverse small recirculation regions at both sides of the wing surface and they increase in size with reducing ride height. However between $h/d = 0.350$ to 0.318, the recirculation regions remain steady in size and therefore the downforce and drag produced remained marginally steady (with $\pm C_L$ of 0.006%). Another notable behavior of the force curves is the differences in the ride height within the force reduction regime (Regime C) where the steep gradient of the drop in forces occurs. In the case of the plane diffuser, the sharp drop occurred at $h/d = 0.172$. The occurrence is also the same for all the passive methods except for the convex bump case. The drop occurred at $h/d = 0.178$ with the convex bump and the early occurrence is because maximum downforce is reached at $h/d = 0.204$ rather than at $h/d = 0.191$ as in the case of other diffuser types. In addition, although the

steep drop in forces occurred at $h/d = 0.172$ for the diffuser with the wing, the force drop is 54% (for C_L) and 45% (for C_D) of that of the plane diffuser. The disparity is also due to the recirculation on both lengthwise sides of the wing surface induced by the streamwise vortices. However, the recirculation in the case of the diffuser with the wing was less profound to inhibit the additional downforce generated by the inverted wing.

As also indicated by the force curves in Figure 6—7, the passive methods generally enhanced downforce and the accompanying drag across the ride heights of the four flow regimes. Between the ride height interval of flow regime A ($h/d = 0.764$ to 0.318), C_L and C_D measured for the plane diffuser increased from -0.876 to -1.769 and 0.282 to 0.429 respectively. In the case of the diffuser with the convex bump and the diffuser with the wing, C_L increased from -0.919 to -1.782 and -0.981 to -1.824 respectively while C_D increased from 0.292 to 0.434 and 0.313 to 0.447 respectively. For the diffuser with both the bump and the wing, C_L increased from -0.978 to -1.820 and C_D increased from 0.314 to 0.450.

In the ride height interval of flow regime B ($h/d = 0.318$ to 0.191), C_L and C_D measurements increased from 1.769 to -1.915 and 0.429 to 0.463, respectively for the plane diffuser. For the diffuser with the bump and the diffuser with the wing, C_L increased from -1.782 to -1.954 and -1.824 to -1.973 respectively while C_D respectively increased from 0.434 to 0.472 and 0.447 to 0.472. In the case of the diffuser with both the bump and wing, C_L increase from -1.820 to -1.983 and C_D increased from 0.450 to 0.476.

For the force-reduction regime (Regime C), the diffusers with the passive methods still maintained higher downforce than the plane diffuser despite the severe force reduction associated in this flow regime. From the ride height interval $h/d = 0.191$ to 0.127, C_L and C_D measurements for the plane diffuser decreased from -1.915 to -1.276 and 0.463 to 0.370 respectively. For the diffuser with the bump and the diffuser with the wing, C_L reduced from -1.954

to −1.284 and −1.973 to −1.295 respectively with C_D reducing from 0.472 to 0.371 and 0.472 to 0.373 respectively. For the diffuser with both the bump and the wing, C_L decreased from −1.983 to −1.307 and C_D decreased from 0.476 to 0.375.

For the ride height interval from $h/d = 0.127$ to 0.064 which represents regime D, C_L and C_D measurements further reduced for the plane diffuser from −1.276 to −1.058 and from 0.370 to 0.300, respectively. The diffuser with the bump and the diffuser with the wing both had a C_L reduction from −1.284 to −1.064 and −1.295 to −1.078 respectively and a C_D reduction from 0.371 to 0.302 and 0.373 to 0.301 respectively. In the case of the diffuser with the bump and wing, C_L reduced from −1.307 to −1.068 and C_D reduced from 0.375 to 0.300.

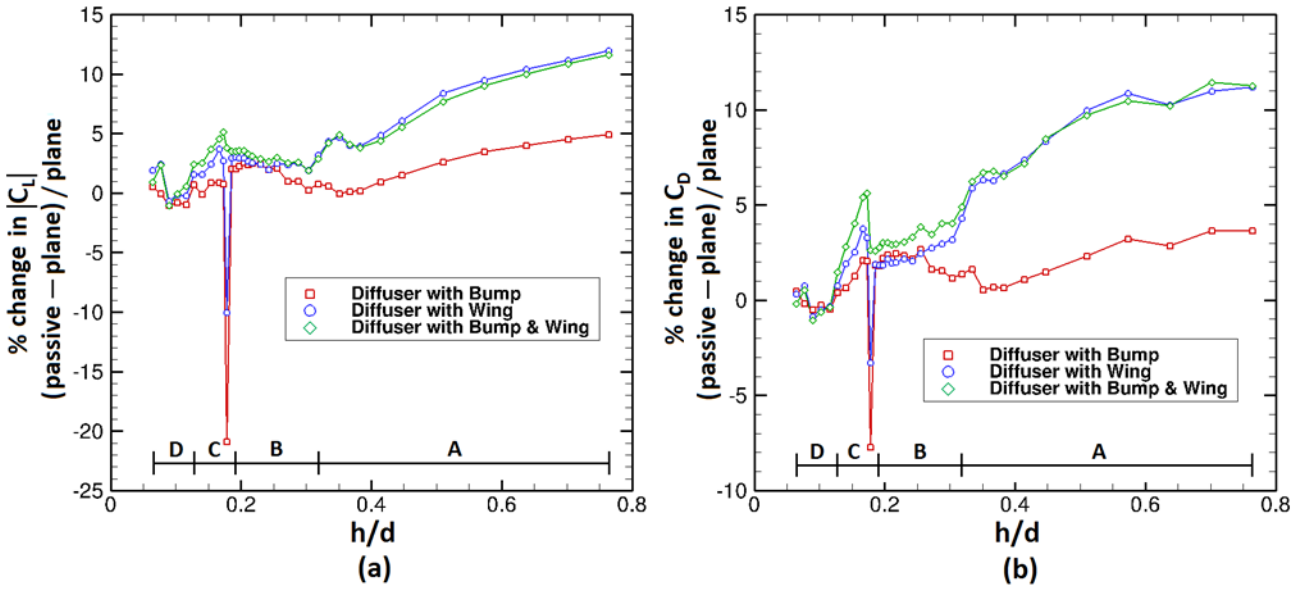

Figure 6-8: Percentage difference in force coefficients across the range of ride heights ($h/d = 0.764$ to 0.064) between the plane diffuser and the diffuser with the wing for: **(a)** C_L ; **(b)** C_D

The percentage changes in downforce and drag are shown in Figure 6–8. Increase in downforce leads to a similar increase in drag, thus, as shown in Figure 6–8, the percentage differences in downforce correspond to similar percentage differences in drag. The percentage change in C_L and C_D between the diffusers with passive flow control and plane diffuser, is highest at the type

A flow regime ride height of $h/d = 0.764$. The diffusers with passive flow control generally generated an increase in downforce across the ride heights even though the percentage increase in force coefficients gradually reduces from flow regime A to B. However, as a result of the severe drop in downforce and drag at the force-reduction (type C regime) ride height of $h/d = 0.178$, there is a corresponding large negative change at that ride height.

6.2.2 Reynolds number sensitivity

As in the case of the plane diffuser, three Reynolds numbers, $1.35\,x\,10^6$, $1.8\,x\,10^6$ and $2.25\,x\,10^6$ (representing freestream velocities of $15\,m/s$, $20\,m/s$ and $25\,m/s$) were investigated for the both the diffuser with the convex bump and the diffuser with the wing. Figure 6—9 shows a similarity in force curves for the three Reynolds numbers. However, as indicated with the Reynolds number sensitivity analysis (within measurement repeatability) of the plane diffuser in Section 4.2.3 of Chapter 4, the force-reduction flow regime is sensitive to low Reynolds number as a result of boundary layer blockage. This analysis also holds for both the diffuser with the bump and the diffuser with the wing. At the lower Reynolds numbers (Re = $1.3\,x\,10^6$ and $1.8\,x\,10^6$), the severe gradient in force reduction occurred at $h/d = 0.178$ for the diffuser with the bump and the diffuser with the wing. However for the diffuser with the bump and the diffuser with the wing, at Re = $2.25\,x\,10^6$, the sharp drop in downforce occurred at $h/d = 0.172$ and $h/d = 0.166$ (a difference of $1\,mm$ and $2\,mm$ from that of the plane diffuser respectively).

As observed with the plane diffuser (Figure 4—14), the severe drop in forces occurred earlier at $h/d = 0.178$ for Re = $1.3\,x\,10^6$ and Re = $1.8\,x\,10^6$, while for $2.25\,x\,10^6$, the significant force reduction occurred at $h/d = 0.172$. Although there are differences between the plane diffuser and the diffuser with the passive methods in terms of varying Reynolds numbers at which the severe loss in forces occurs at the higher ride height, the trend remains fundamental. This infers that low Reynolds number flow induces boundary

layer blockage thus causing the severe drop in lift and drag forces to occur at higher ride heights, and with increasing Reynolds number, the severe drop in forces occurs at a lower ride height. However at the same Reynolds number, the differences in the ride height of severe force reduction between the plane diffuser and the diffusers with passive methods, as earlier explained, is due to the adverse flow recirculation regions present at both lengthwise sides of the wing and bump.

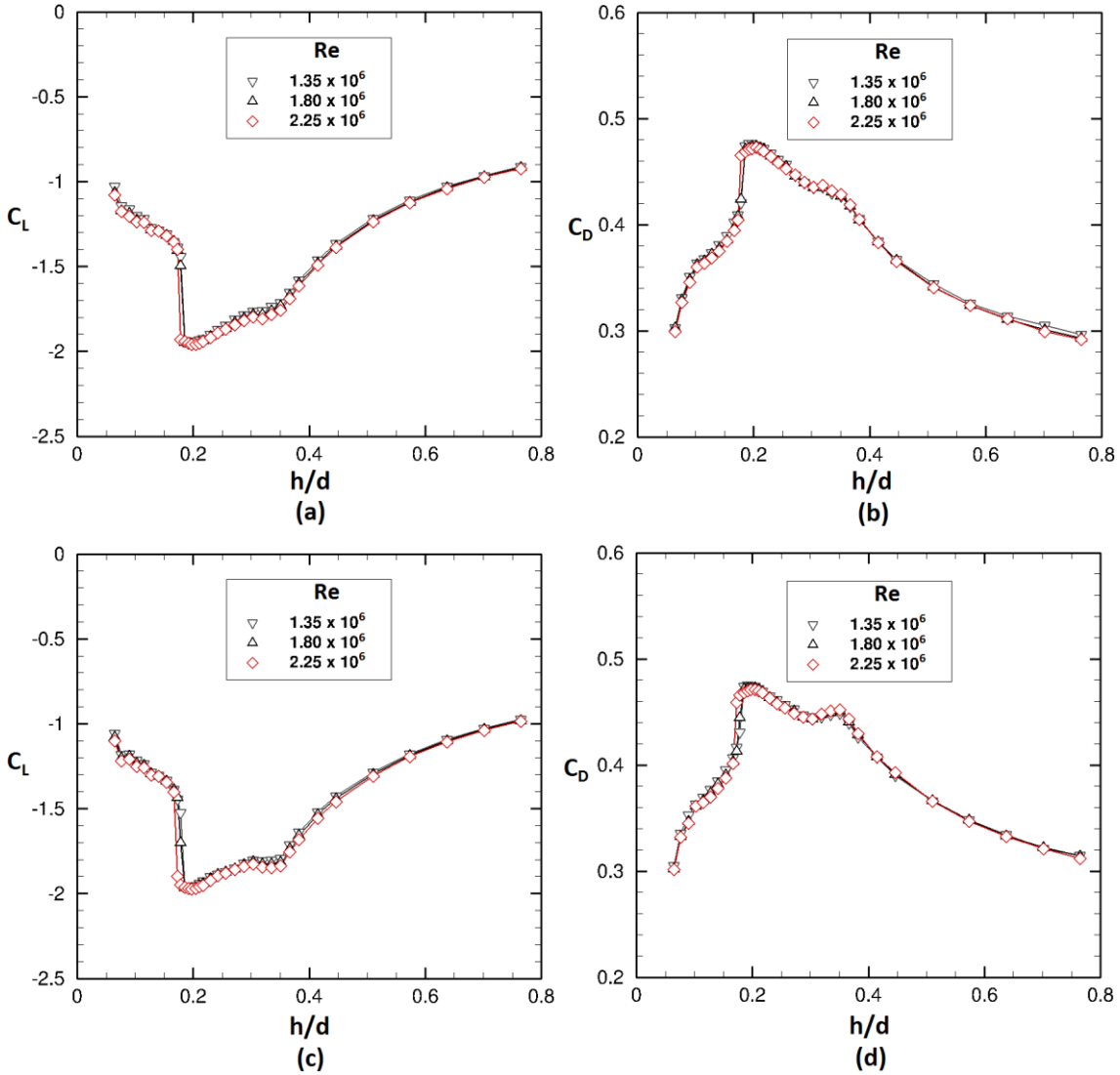

Figure 6-9: Reynolds number sensitivity across ride heights ($h/d = 0.764$ to 0.064): **(a)** Downforce coefficients for diffuser with bump **(b)** Drag coefficients for diffuser with bump **(c)** Downforce coefficients for diffuser with wing **(d)** Drag coefficients for diffuser with wing

6.2.3 Aerodynamic efficiency (lift-to-drag ratio)

In the design of aerodynamic vehicles such as aircraft, a design measure is needed to ascertain their ability to produce aerodynamic loads to suit the defined flight parameters. Likewise in a racing car, the aerodynamic forces generated by its aerodynamic devices needs to act on the car efficiently so as to enable the racing car travel quicker on the race track with less air resistance. In Section 4.2.3 of Chapter 4 the lift-to-drag curves indicated that the maximum (C_L/C_D) increases with an increase in Re. However, the lift-to-drag ratio is also a defined measure of aerodynamic efficiency. A high lift-to-drag ratio is desirable in aircraft because a major flight parameter is an aircraft's ability to generate a lift force greater than its weight. Also, in the case of racing cars, a high lift-to-drag ratio is favourable in enabling the race car to generate downforce that allows it to travel faster on corners at the expense of higher drag, which slows it on the straights of a race track.

The aerodynamic efficiency of the plane diffuser and the diffusers with passive flow-control methods were plotted in Figure 6—10a to ascertain their efficiency across the range of ride heights investigated. As indicated in Figure 6—10a, the diffuser with both the bump and wing has the lowest lift-to-drag ratio from $h/d = 0.764$ to 0.318 (flow regime A) and at $h/d = 0.318$, the plane diffuser still maintains the highest lift-to-drag ratio of 4.123. At the maximum downforce ride height $(h/d = 0.191)$, the plane diffuser has the lowest lift-to-drag ratio of 4.131 while the diffuser with the wing has the highest lift-to-drag ratio of 4.178. At $h/d = 0.127$ where the force-reduction (flow regime C) ride height interval ends, the diffuser with both the bump and wing generated the highest lift-to-drag ratio of 3.477 and the lowest ratio is 3.445 for the plane diffuser. When the ride height was lowered to the last ride height of flow regime D $(h/d = 0.064)$, the plane diffuser, diffuser with the bump, diffuser with the wing and diffuser with both the bump and wing produced a ratio of 3.518, 3.521, 3.574, and 3.558 respectively. This implies that within the type A flow regime, the plane diffuser and the convex bump

generated less drag than the diffuser with the wing, and the diffuser with both the bump and wing (even though the latter two generated more downforce). However, from the maximum downforce regime to the low-force regime, the diffuser with the wing and the diffuser with both the bump and wing were more efficient because the additional downforce generated was more than the additional drag produced.

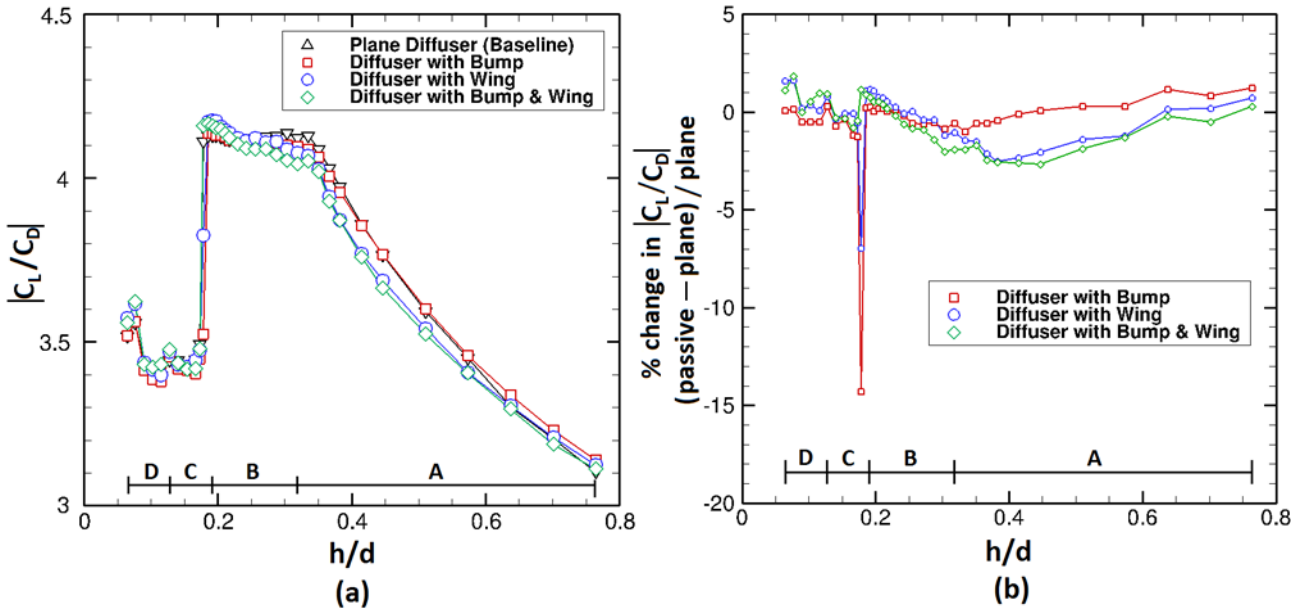

Figure 6-10: (a) Lift-to-drag ratio magnitude measured (wind tunnel) across ride heights $h/d = 0.764$ to 0.064 for plane diffuser (baseline) and diffuser with passive flow control methods; **(b)** Percentage difference in lift-to-drag ratio magnitude between the plane diffuser (baseline) and diffuser with passive flow control methods

Figure 6—10b shows the lift-to-drag ratio and its percentage change between the modified and plane diffusers. It can be seen that there is a similar trend for the diffusers with respect to the overall change in C_L/C_D across the ride heights. In general, there is a slight reduction over much of regime A and half of regime B. However, at the maximum-force flow regime (type B), peak C_L/C_D occurs at the ride height of $h/d = 0.191$. This means that for a high-downforce aerodynamic setup, a racing car with a diffuser that includes the passive flow control devices will have an increased aerodynamic "efficiency" (higher C_L/C_D).

6.2.4 Underbody and diffuser surface pressure measurements

Further flow physics that illustrates the enhanced downforce produced by the diffuser with passive methods is exhibited by the surface pressure distribution. As in the case of the plane diffuser as analysed in Chapter 4, the centreline underbody surface pressure distributions for the diffuser with passive methods also share similar attributes at each of the five ride heights representing the four distinct flow regimes (Figure 6—11). This includes the pressure drop at the start of the underbody flat section as a result of flow curvature of the upstream nose section and the peak suction at the diffuser inlet due to the diffuser pump-down effect. However, the distinct behaviour that underlines the increased downforce generated by the diffuser with passive methods is the second-stage pressure drop present close to the diffuser exit and downstream of the pressure drop at the diffuser inlet. Hence, as established in Section 2.3 of Chapter 2, the second-stage pressure drop introduces a reduction in average pressures close to the diffuser exit and, consequently, downforce is enhanced.

In Figure 6—11, the centreline (along $z/d = 0$) pressure distributions at $h/d = 0.764,\ 0.382,\ 0.191,\ 0.153,$ and 0.064 are shown for the plane diffuser and diffuser with the various passive methods. In the case of the diffuser with the wing and the diffuser with both the bump and wing, surface pressures were not measured on the suction surface of wing. However, the pressure measurements on the diffuser surface (on the plane surface in the case of the diffuser with the wing and on the bump as in the case of the diffuser with both the bump and wing) above the wing also show a pressure drop and recovery close to the diffuser exit.

In the force-enhancement flow regime represented at $h/d = 0.764$ (Figure 6—11a), on $x/d = 6.29$ the C_p for the plane diffuser, diffuser with the bump and diffuser with the wing are: -0.147, -0.430, and -0.109 respectively. At $h/d = 0.382$ (Figure 6—11b) the C_p measured on $x/d = 6.29$ are: -0.180, -0.462 and -0.182 respectively. At the maximum-downforce flow regime

reflected at $h/d = 0.191$ (Figure 6—11c), measured C_p on $x/d = 6.29$ for the plane diffuser, diffuser with the bump, diffuser with the wing and diffuser with both the bump and wing are: -0.21, -0.473, -0.242 and -0.882 respectively. In the force-reduction flow regime as represented at $h/d = 0.153$ (Figure 6—11d), C_p on $x/d = 6.29$ for the plane diffuser, diffuser with the bump and diffuser with the wing are: -0.319, -0.404 and -0.347 respectively while in the low-force regime ($h/d = 0.153$ in Figure 6—7d), the respective C_p measured are: -0.209, -0.216 and -0.220.

The spanwise pressure distributions (Figure 6—12) also reflect the relatively lower pressures associated with the second-stage pressure drop induced by the passive flow-control methods along $x/d = 6.29$. For the highest ride height of flow regime A ($h/d = 0.764$ in Figure 6—12a), the lowest C_p for the plane diffuser, diffuser with the bump and diffuser with the wing are: -0.157, -0.444 and -0.114 respectively. When the ride height is lowered within regime A to $h/d = 0.382$ (Figure 6—12b), the lowest C_p measured for the plane diffuser, diffuser with the bump and diffuser with the wing are: -0.195, -0.454 and -0.182 respectively. At the maximum downforce ride height ($h/d = 0.191$ in Figure 6—12c) which represents regime B, the respective lowest C_p for the plane diffuser, diffuser with the bump, diffuser with the wing and diffuser with both the bump and wing are: -0.246, -0.483, -0.242 and -0.878. In regime C ($h/d = 0.153$ in Figure 6—12d) and regime D ($h/d = 0.064$ in Figure 6—12e), the spanwise pressure distributions of the diffuser with the passive methods become asymmetrical along $x/d = 6.29$ as in the case of the plane diffuser. For the plane diffuser, diffuser with the bump and diffuser with the wing, at $h/d = 0.153$, the lowest C_p measured along $x/d = 6.29$ are: -0.359, -0.539 and -0.345 respectively while at $h/d = 0.064$, the lowest C_p are: -0.227, -0.231 and -0.219 respectively.

In terms of the base pressures (Figure 6—13), the centreline pressure distribution along $z/d = 0$ for the diffuser with passive methods share a similar behaviour with the plane diffuser as documented in Section of 4.2.6 of Chapter 4.

At $h/d = 0.764$ and 0.382, the strength of the upper near-wake vortex is stronger than the lower near-wake vortex thus the lowest static pressures are measured above $y/d = 1.57$. However at $h/d = 0.191$, 0.153, and 0.064, the strength of the lower near-wake vortex is enhanced and the lowest static base pressure for all diffusers are measured below $y/d = 1.57$. For the plane diffuser, diffuser with the bump and diffuser with the wing, at $h/d = 0.764$, the lowest measured C_p on the vertical centreline of the base plate are: -0.120, -0.113 and -0.120 respectively and at $h/d = 0.382$ lowest C_p are: -0.102, -0.114 and -0.129 respectively. At $h/d = 0.191$, the respective lowest C_p for the plane diffuser, diffuser with the bump, diffuser with the wing and the diffuser with both the bump and wing are: -0.152, -0.151, -0.139 and -0.136 respectively. In the case of the plane diffuser, diffuser with the bump and diffuser with the wing, at $h/d = 0.153$, the lowest measured C_p are: -0.254, -0.256 and -0.255 respectively and at the smallest ride height ($h/d = 0.064$) the lowest C_p are: -0.181, -0.176 and -0.180 respectively.

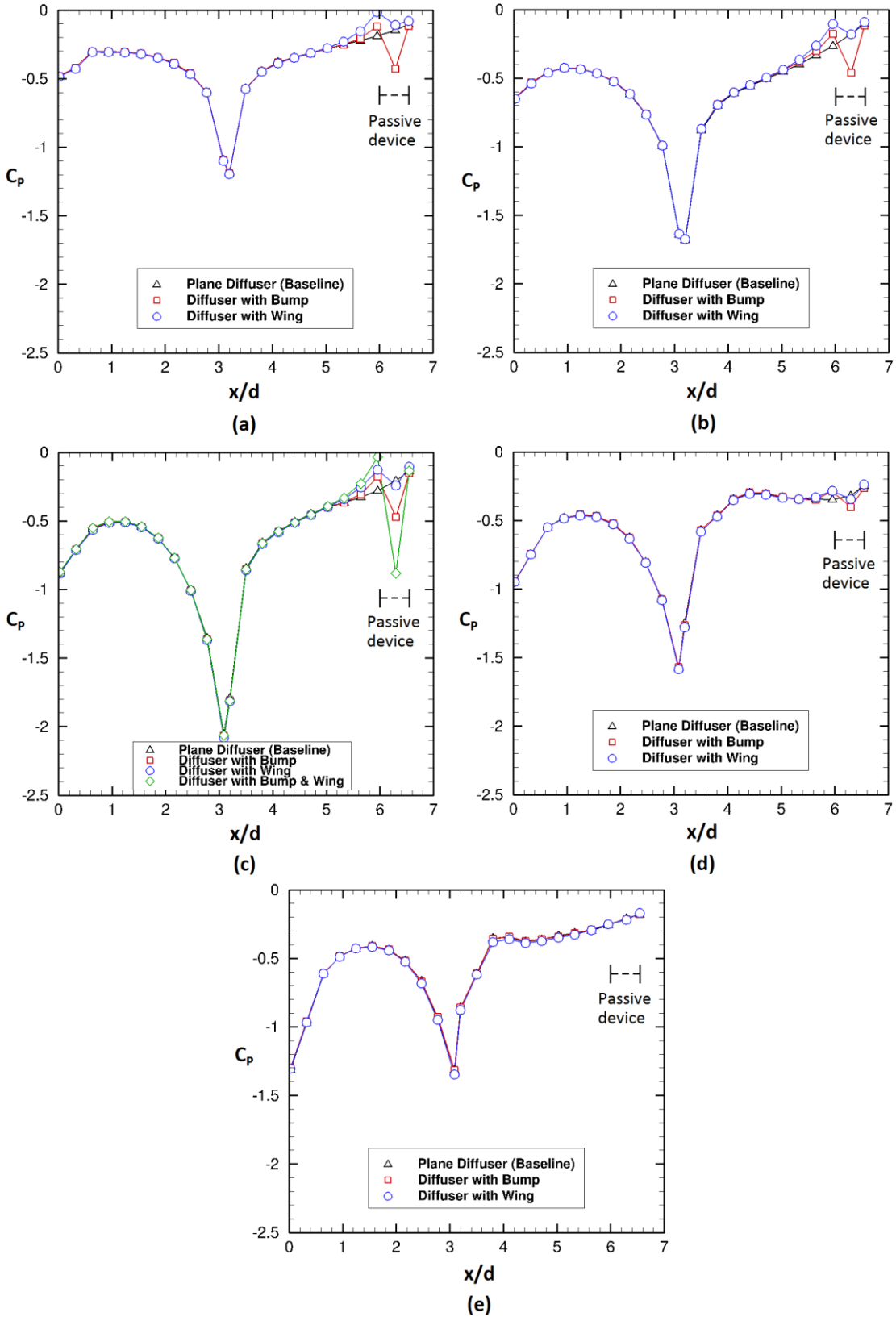

Figure 6-11: Underbody centreline pressure distribution measurements (wind tunnel) for the plane diffuser and diffuser with passive flow control methods at: **(a)** $h/d = 0.764$ **(b)** $h/d = 0.382$ **(c)** $h/d = 0.191$ **(d)** $h/d = 0.153$ **(e)** $h/d = 0.064$

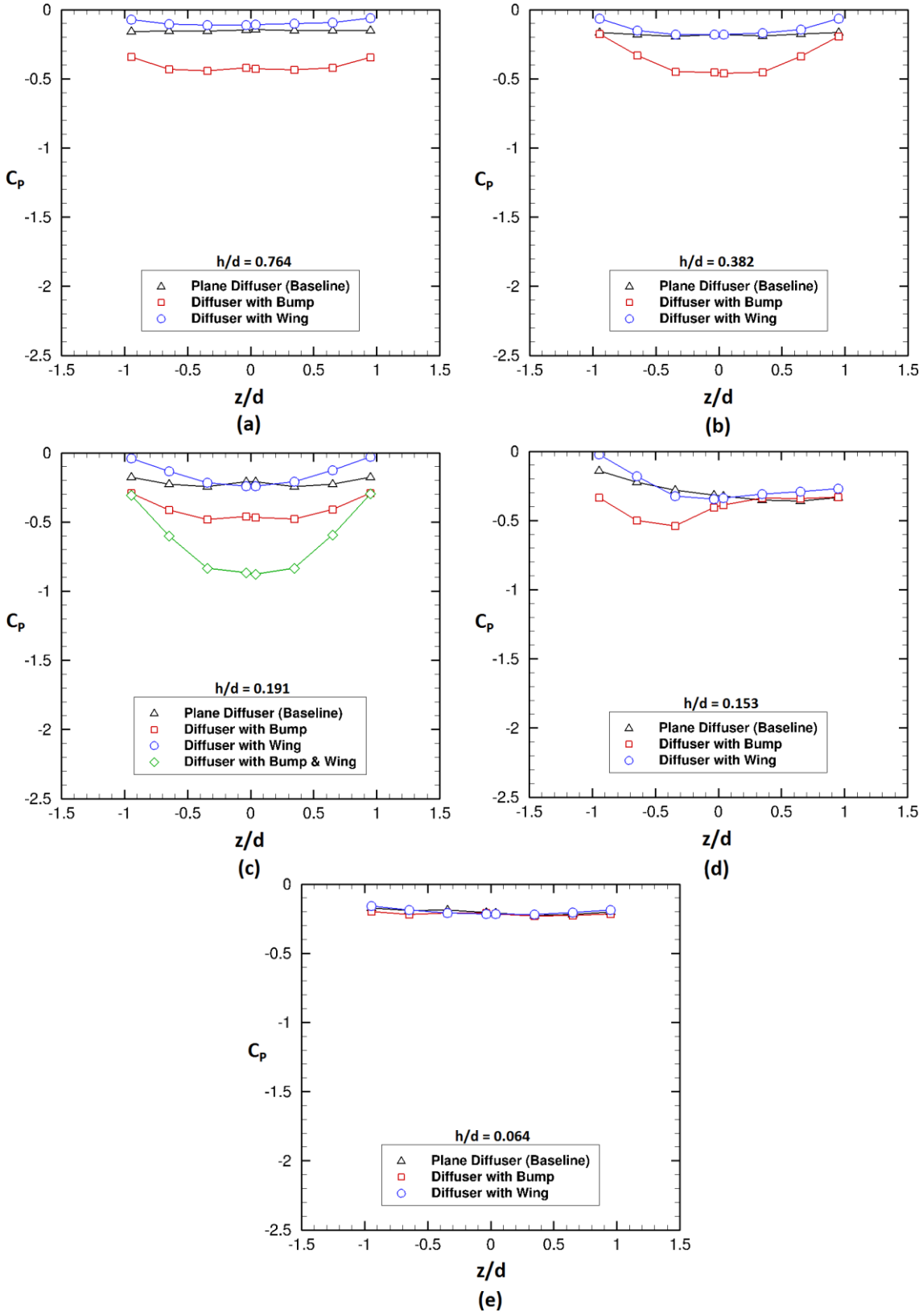

Figure 6-12: Spanwise surface pressure distribution measurements (wind tunnel) on $x/d = 6.29$ for the plane diffuser and diffuser with passive flow control methods at: **(a)** $h/d = 0.764$ **(b)** $h/d = 0.382$ **(c)** $h/d = 0.191$ **(d)** $h/d = 0.153$ **(e)** $h/d = 0.064$

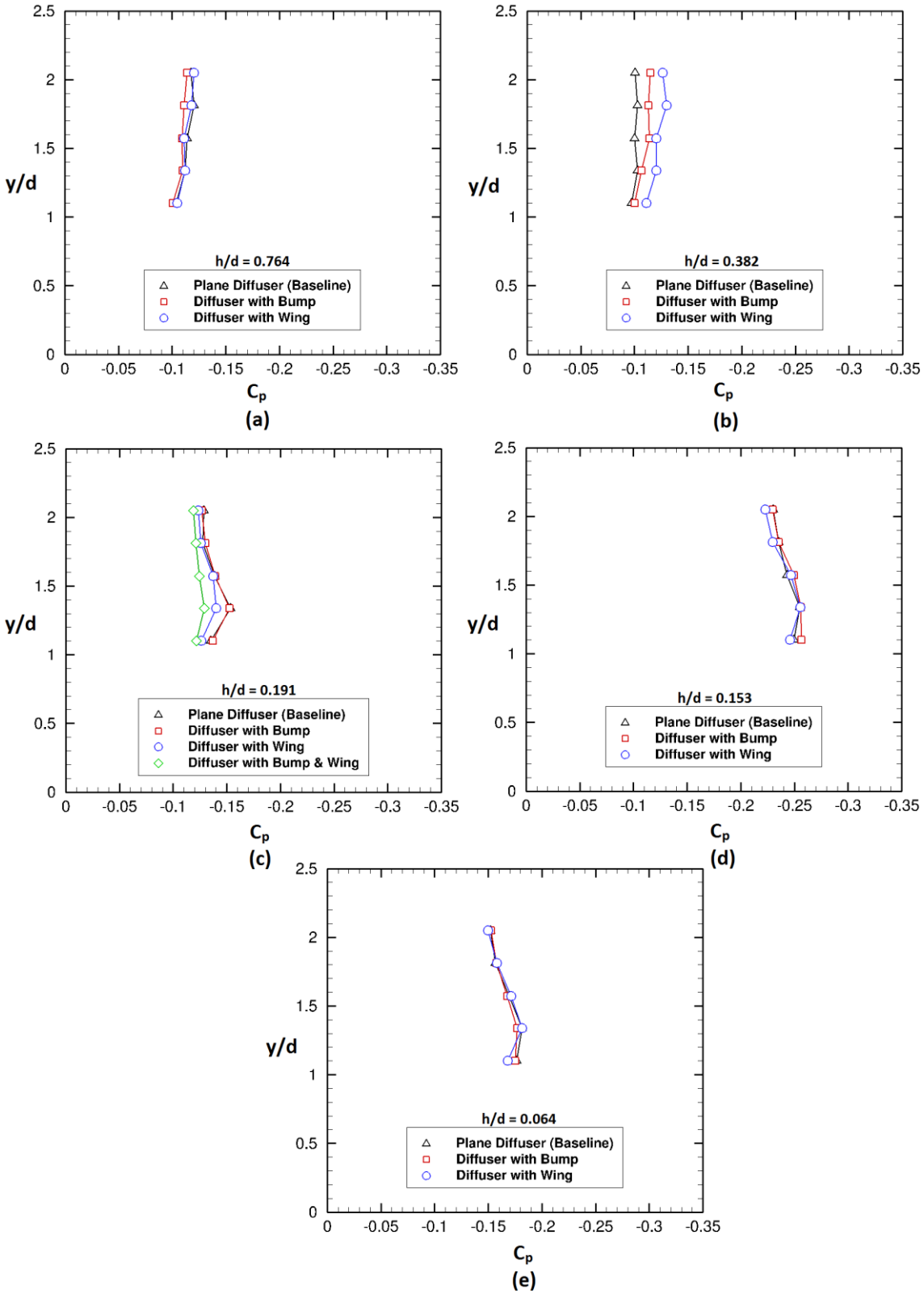

Figure 6-13: Surface pressure distribution measured (wind tunnel) along $z/d = 0$ of the base plate of the diffuser body with and without the passive flow control methods at: **(a)** $h/d = 0.764$ **(b)** $h/d = 0.382$ **(c)** $h/d = 0.191$ **(d)** $h/d = 0.153$ **(e)** $h/d = 0.064$

6.2.5 Diffuser ramp surface flow features

The diffusers with the various passive flow-control methods possess similar surface flow features as those of the plane diffuser. As shown in Figures 6—14 to 6—18, the surface flow features remain distinct for ride heights $h/d = 0.764$, 0.382, 0.191, 0.153, and 0.064 representing the four force regimes (A to D). At $h/d = 0.764$ and 0.382 (Figures 6—14 and 6—15), which both represent flow regime A, the flow is symmetrical with the curved pathlines on both sides of the centreline ($z/d = 0$) representing the longitudinal vortices that detach from the diffuser surface and travel downstream towards the diffuser exit. With a reduction in ride height to $h/d = 0.191$ (Figure 6—16), the vortex strength increased as represented by the stronger crossflow seen in the pathlines, with the appearance of the separation bubble along the diffuser centreline, which indicates an enhancement in adverse pressure gradient. A further reduction in ride height to $h/d = 0.153$ and 0.064 (Figures 6—17 and 6—18), which both represent flow regime C and D, the flow becomes asymmetric with a single surviving vortex. In addition, the diffuser flow on the side of vortex breakdown is dominated by flow reversal and recirculation.

However, there were also differences in the surface flow features between the plane diffuser and the diffuser with the passive methods at the location of the bump and the wing, which further explains their improved aerodynamic performance relative to the plane diffuser. At $h/d = 0.764$ (Figure 6—14) for both the diffuser with the bump and the diffuser with the wing, there was a small recirculation region at each side where the bump merges with the side plates and at each side near the leading edge of the wing. However, the flow over the bump and wing suction surface appeared mostly attached, except for a region along each side of the bump and wing close to the edge of the diffuser exit. Along those regions, the weakened vortex was detached from the diffuser surface and replaced by flow recirculation. At $h/d = 0.382$ (Figure 6—15), the recirculation region on each side close to where the bump meets the plane

diffuser ramp and at each side near the leading edge of the wing were more pronounced due to the greater vortex strength. However, the flow over the bump and wing suction surface was increasingly attached to the bump and wing, except along the sides of the bump and wing surface where recirculation was more distinct.

On the suction surface of the bump and wing at $h/d = 0.191$ (Figure 6—16), the flow appeared to be largely attached. However, the recirculation regions on each side of the bump and wing remained visible and appeared close to the edge of the diffuser exit. The undisturbed flow pathlines for both diffusers at the site corresponding to the position of the bump and wing indicated that the flow was attached. Flow attachment was more prevalent around the central area of the bump and wing relative to the same location of the plane diffuser. Notably, surface pressures measured at $x/d = 6.29$ indicated that the lower pressures are present on the central area of the bump (Figure 6—12c) and wing (see predicted pressures presented in subsequently in Figure 6—24) thus indicating relatively higher flow velocity at that region.

At $h/d = 0.153$ (Figure 6—17), the flow patterns remained broadly similar but the attachment of the flow on about half of the bump and wing suction surface area, particularly on the side featuring the surviving vortex appeared to have generated more suction. This was supported by the lower surface pressures ($x/d = 6.29$) on this half of the bump (Figure 6—12d) and wing suction surface (see predicted pressures presented subsequently in Figure 6—24e) compared to the corresponding half of the plane diffuser. As a result, the diffuser generated more downforce than the baseline diffuser. At $h/d = 0.064$ (Figure 6—18), the diffuser with the bump and diffuser with the wing generated only ~0.56% and 1.89% more downforce ($-C_L$) respectively than the plane diffuser because the flow on one-third of the bump and wing suction surface areas (on the side of the surviving vortex) was still attached.

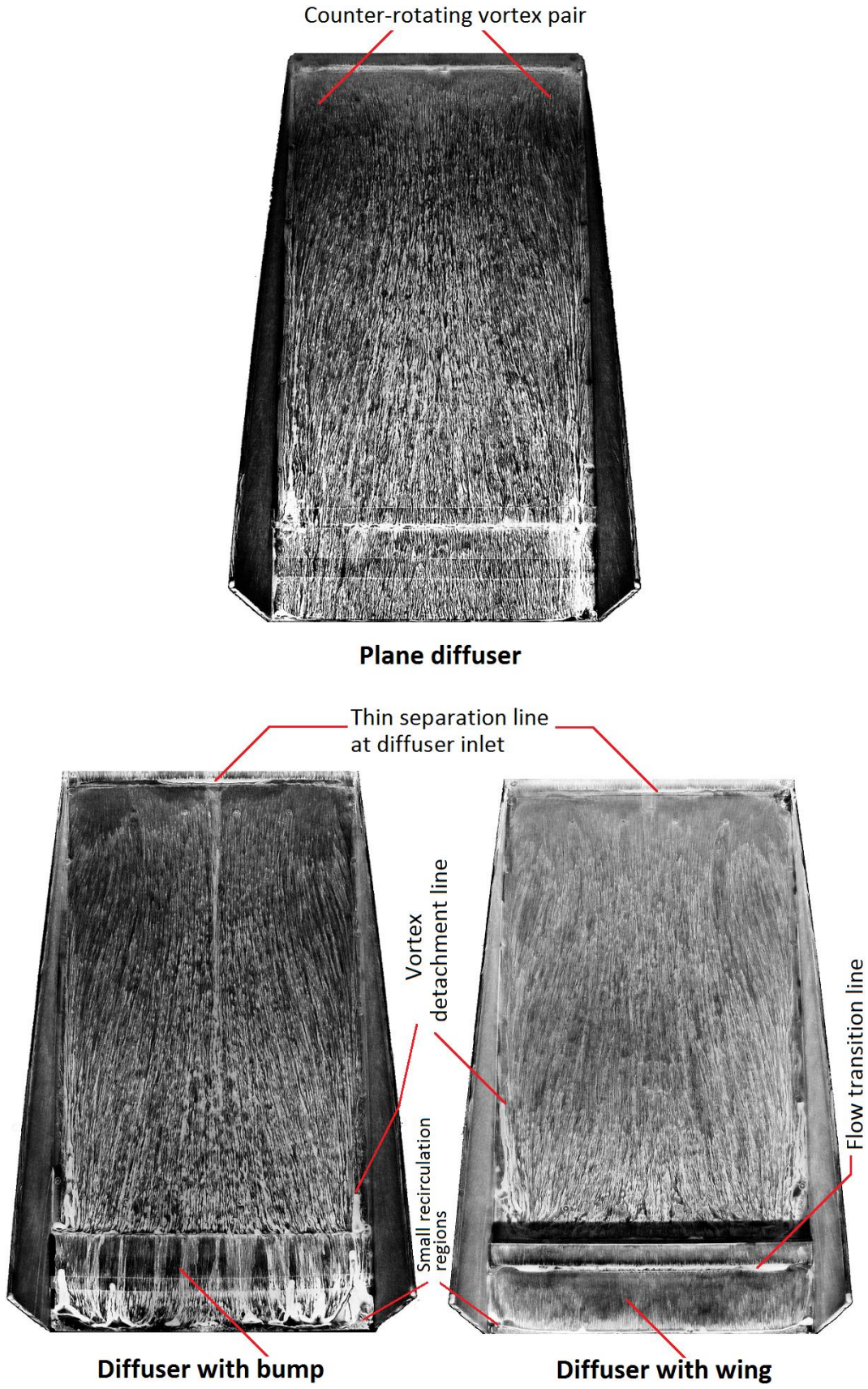

Figure 6-14: Diffuser surface flow features with flow visualisation paint for the Type A flow regime (force-enhancement) at $h/d = 0.764$ (Flow direction from top to bottom)

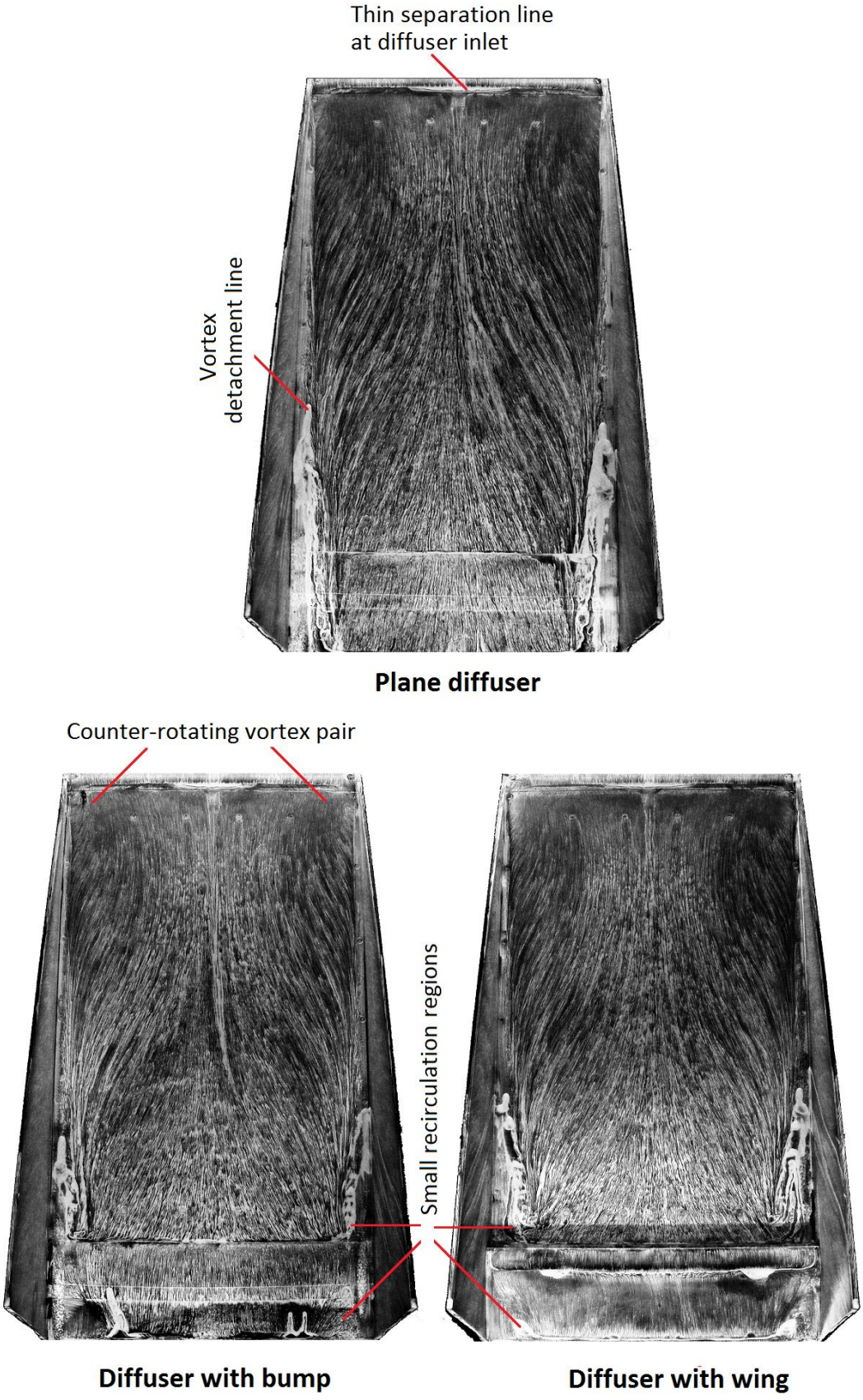

Figure 6-15: Diffuser surface flow features with flow visualisation paint for the Type A flow regime (force-enhancement) at $h/d = 0.382$ (Flow direction from top to bottom)

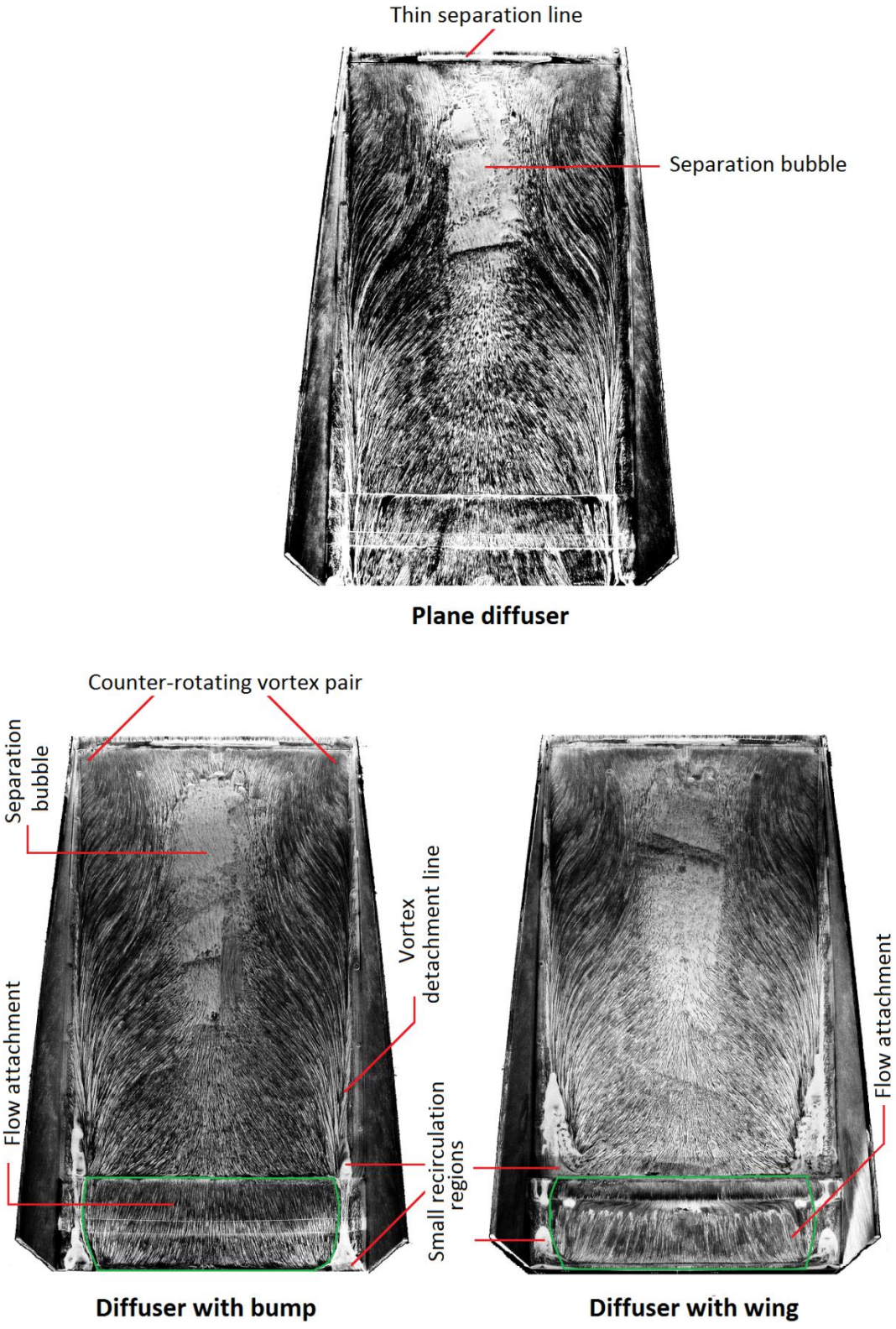

Figure 6-16: Diffuser surface flow features with flow visualisation paint for the Type B flow regime (maximum-force) at $h/d = 0.191$ (Flow direction from top to bottom)

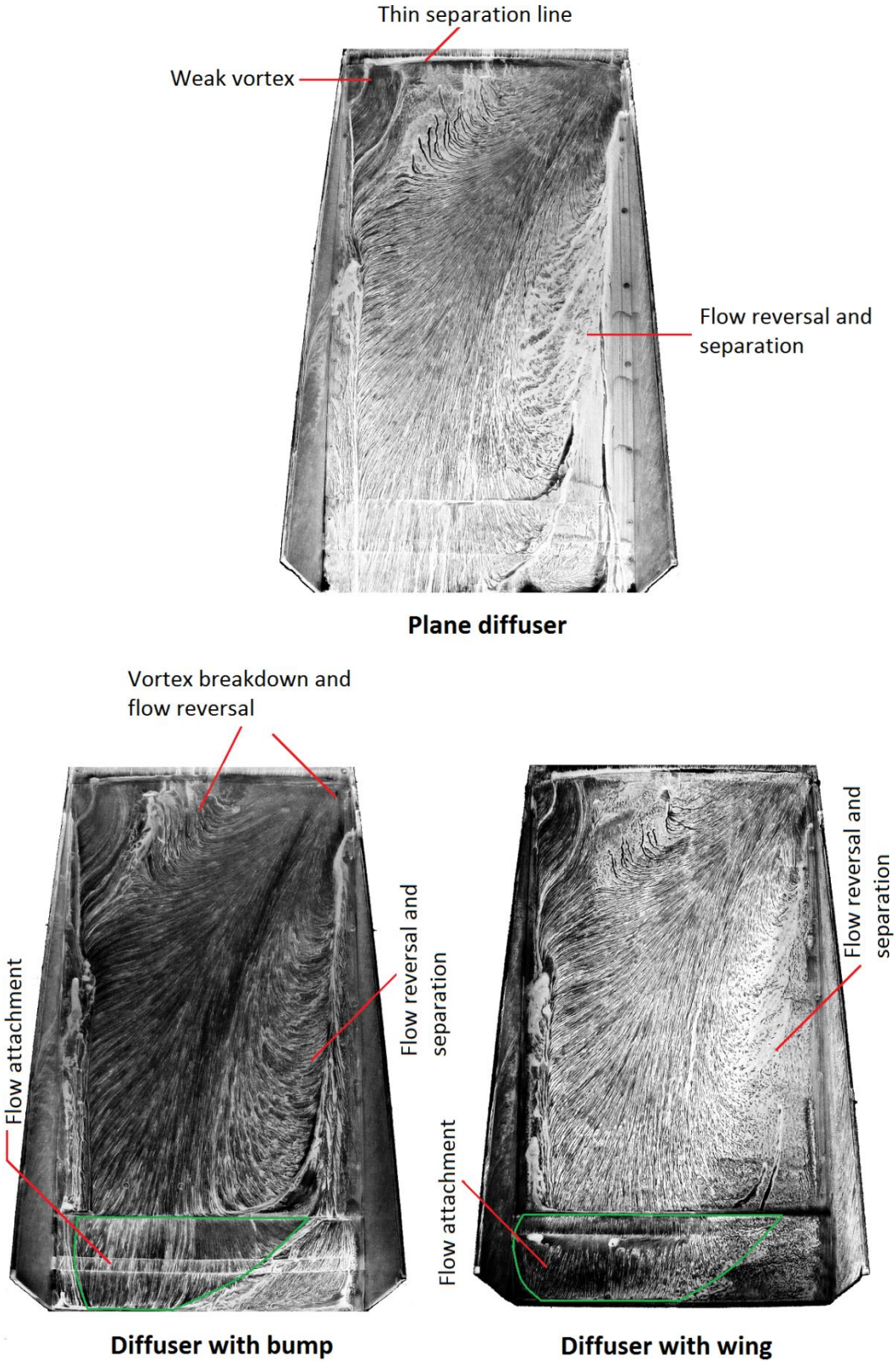

Figure 6-17: Diffuser surface flow features with flow visualisation paint for the Type C flow regime (force-reduction) at $h/d = 0.153$ (Flow direction from top to bottom)

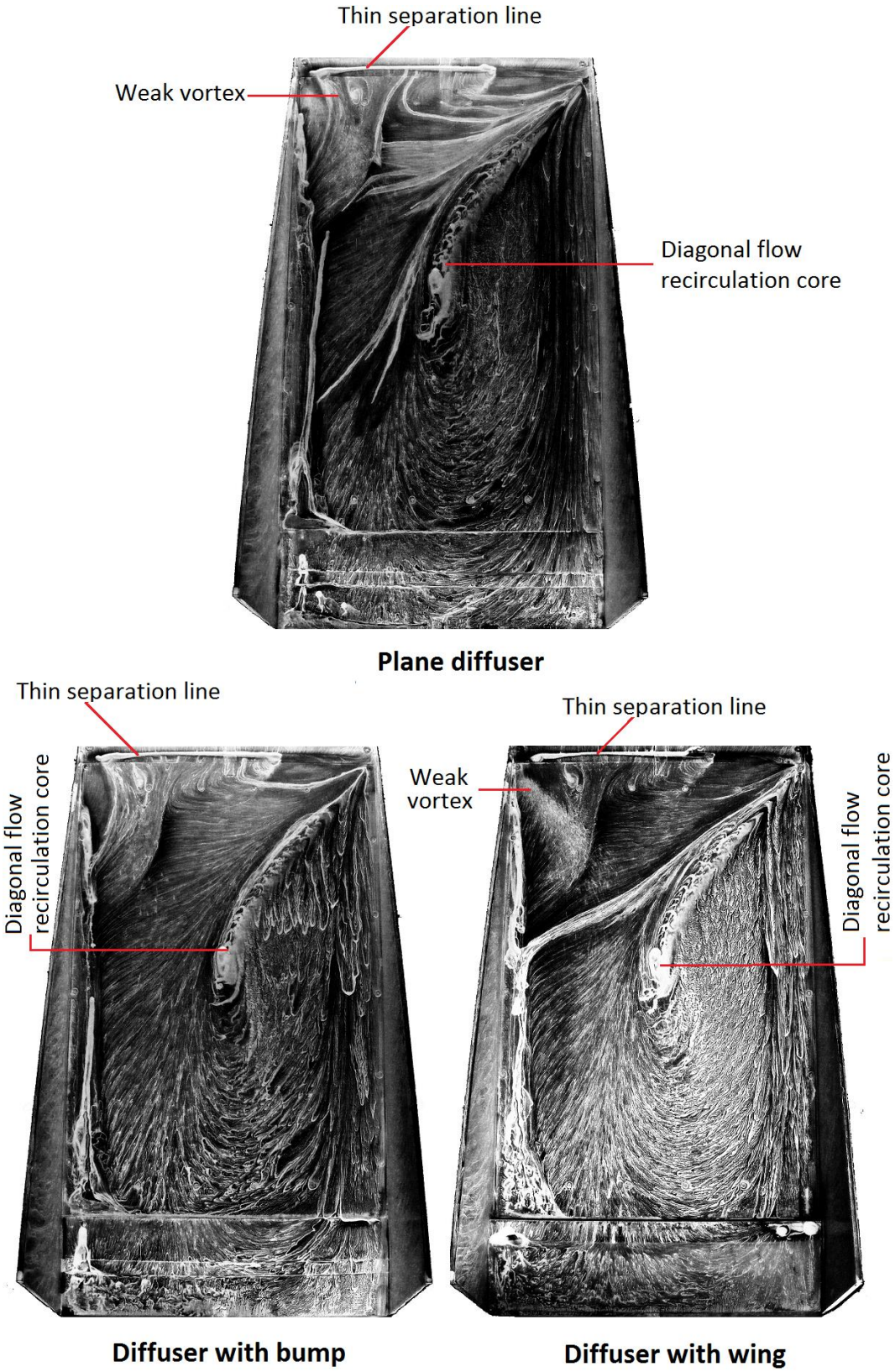

Figure 6-18: Diffuser surface flow features with flow visualisation paint for the Type D flow regime (low-force) at $h/d = 0.064$ (Flow direction from top to bottom)

6.3 Flow Characteristics: CFD vs. Experiments

As in the case of the plane diffuser in the previous chapters, a parallel CFD investigation was implemented to ascertain the efficacy of the computational grid and turbulence modelling employed in predicting the flow physics of the diffuser with passive flow control methods. The computational simulations were done for the five ride heights (h/d = 0.764, 0.382, 0.191, 0.153, and 0.064) representing the distinct flow regimes A to D. As in the baseline diffuser case, the IDDES methodology was used at h/d = 0.764, 0.382, and 0.153 while URANS was employed at h/d = 0.191 and 0.064. Comparative analysis between experimental and computational are presented subsequently in terms of force measurements, surface pressure measurements and surface flow visualization.

6.3.1 Force measurements (downforce and drag)

Time-averaged computations generally overpredicted downforce and drag coefficients across the five ride heights investigated for the diffuser with the bump, diffuser with the wing and the diffuser with both the bump and wing. For the diffuser with the bump (Figure 6–19), at h/d = 0.764, C_L and C_D was predicted to be −0.964 and 0.324 respectively which implies a respective 4.89% and 10.95% overprediction from experimental measurements. At h/d = 0.382 for the bump diffuser, C_L and C_D were respectively predicted to be −1.531 and 0.413 and this means a 4.25% and 2.22% respective underpredictions from the equivalent experimental measurements. At the maximum downforce flow regime ride height of h/d = 0.191, predicted C_L and C_D increased to −2.187 and 0.578 and in comparison to respective experimental measurements, C_L and C_D were overpredicted by 11.92% and 22.45%. For h/d = 0.153, the respective predicted values for C_L and C_D are: −1.598 and 0.448 and for h/d = 0.064, C_L and C_D are predicted as: −1.156 and 0.396. In comparison to experimental measurements, at h/d = 0.153 there are overpredictions of C_L and C_D by 21.4% and 16.36% respectively and at h/d = 0.064, the respective overpredictions are: 8.64% and 31.12%.

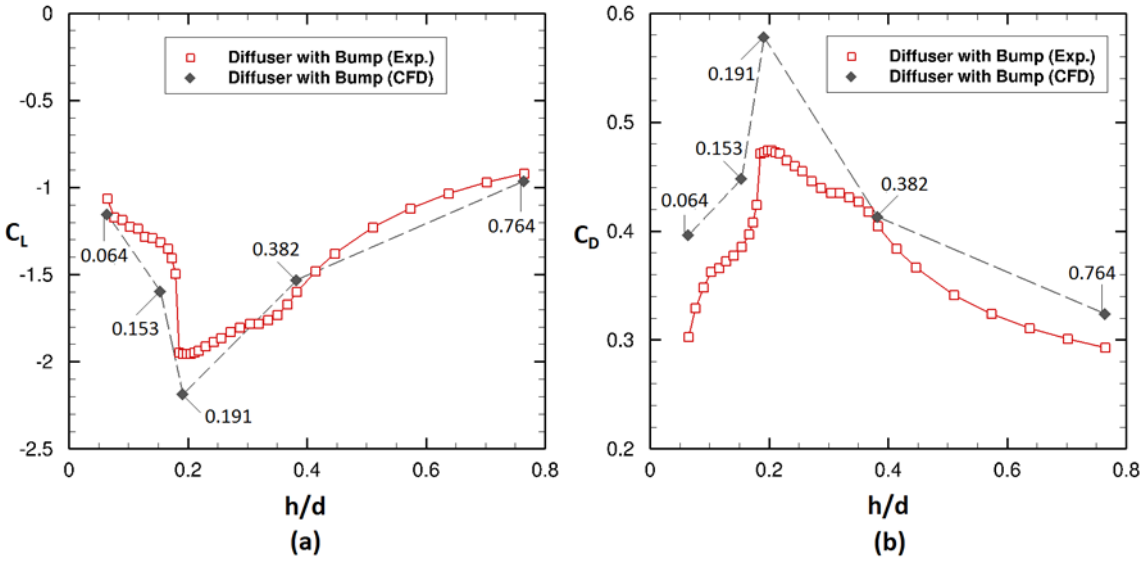

Figure 6-19: Measured (wind tunnel) and CFD-predicted force coefficients across ride heights and flow regimes for the diffuser with the bump: **(a)** downforce **(b)** drag

In the case of the diffuser with the wing (Figure 6–20), at $h/d = 0.764$ there is an over prediction of 6.01% and 9.58% as a result of CFD respectively predicting C_L and C_D as: -1.040 and 0.343. When the right height is reduced to $h/d = 0.382$, predicted values of C_L and C_D has increased to -1.553 and 0.419 respectively and this in turn implies a respective underprediction of 6.38% and 2.10%. At $h/d = 0.191$, time-averaged CFD predictions of C_L and C_D for the diffuser with the wing are: -2.217 and 0.568 respectively and for the diffuser with both the bump and wing, predicted values of C_L and C_D are: -2.236 and 0.568. This indicates a 12.36% and 20.33% C_L and C_D overprediction for the diffuser with the wing and a 12.75% and 19.32% respective overprediction for the diffuser with both the bump and the wing. For the type C ($h/d = 0.153$) flow regime, C_L and C_D predicted for the diffuser with wing are: -1.629 and 0.442 respectively and at the type D regime ($h/d = 0.064$), the respective C_L and C_D predicted are: -1.180 and 0.394. As a result there is an overprediction of 21.93% and 13.33% for C_L and C_D respectively at $h/d = 0.153$ and 9.46% and 30.89% at $h/d = 0.064$.

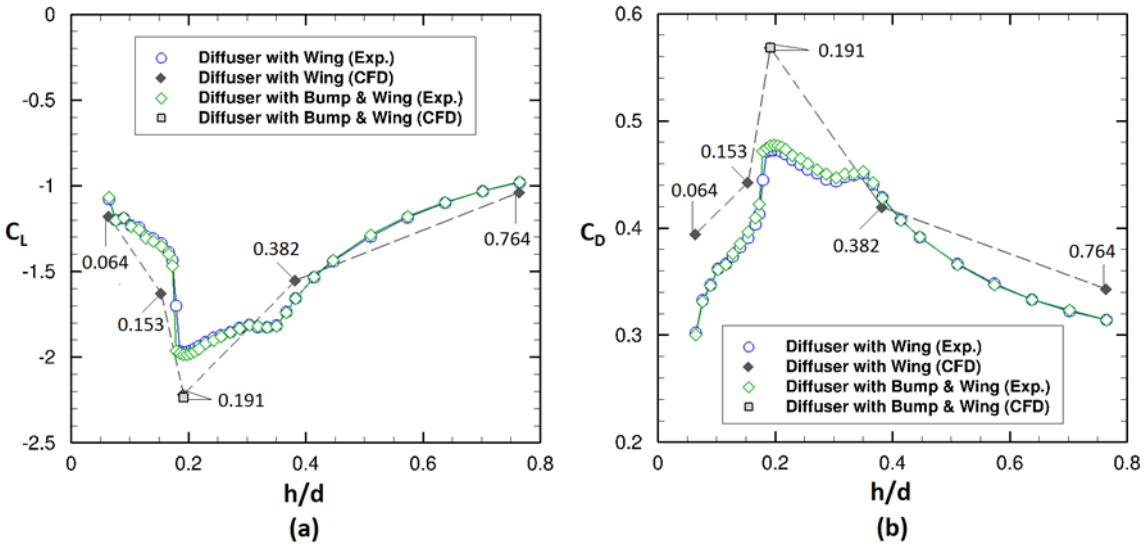

Figure 6-20: Measured (wind tunnel) and CFD-predicted force coefficients across ride heights and flow regimes for the diffuser with the wing, and with both bump and wing: **(a)** downforce **(b)** drag

The percentage deviation is observed to be larger for drag coefficients which imply that the turbulence modelling using the transitional turbulence models and the IDDES turbulence modelling approach did not adequately predict the flow physics in the diffuser near-wake. Within the force-enhancement ride heights of $h/d = 0.764$ and 0.382, the time-averaged predictions of C_L and C_D were within ~10%, however, further ride height reductions into the maximum-force, force-reduction and low-force flow regimes where the turbulence of the separated near-wake flow physics enhances, the percentage deviations increased.

6.3.2 Surface pressure measurements

The comparative centreline and spanwise pressure distributions (Figures 6–21 and 6–22) for the diffuser with the bump indicate that the time-averaged CFD investigations predicted the suction peaks at the start of the flat underbody, diffuser inlet and the second-stage suction peak close to the diffuser exit. In the type A flow regime (Figures 6–21a and 6 – 21b), the C_p predicted at the suction peak of the second-stage pressure recovery region ($x/d = 6.29$) are: -0.419 at $h/d = 0.764$ and -0.381 at $h/d = 0.382$ while the

respective experimental measurements are: -0.430 and-0.462. At the maximum downforce ride height ($h/d = 0.191$, Figure 6—21c), the predicted C_p at $x/d = 6.29$ is the same as the measured value ($C_p = -0.473$). However in the force-reduction ($h/d = 0.153$, Figure 6—21d) and low-force ($h/d = 0.064$, Figure 6—21e) regimes, there are respective overpredictions of 5.94% and 27.31% from the experimental measurements of -0.404 and -0.216. Spanwise pressure distributions for the diffuser with the bump (Figure 6—22) show that CFD predicted the pressure drop from the plane diffuser levels and the reasonable symmetric pressure distributions along $x/d = 6.29$ for the type A and B regimes at $h/d = 0.764$, 0.382 and 0.191 (Figures 6—22a, 6—22b, 6—22c). Also in the type C ($h/d = 0.153$, Figure 6—22d) and type D ($h/d = 0.064$, Figure 6—22e) regimes, the respective spanwise distributions along $x/d = 6.29$ for $h/d = 0.153$ and 0.064 indicates that the predictions capture the asymmetric pressure distributions and the pressure drop from the levels of the plane diffuser. The highest suction (lowest C_p) predicted along $x/d = 6.29$ for $h/d = 0.764$, 0.382, 0.191, 0.153 and 0.064 are respectively: -0.444, 0.461, -0.483, -0.539 and -0.231 while the respective measurements are: -0.465, -0.414, -0.505, -0.539 and -0.297.

Predictions of C_p along the underbody centreline for the diffuser with the wing and diffuser with both the bump and wing also indicate that the second-stage pressure drop at $x/d = 6.29$ were generally captured on the diffuser surface and on the suction surface of the wing. However as in the case with the diffuser bump there are percentage deviations (both under- and overpredictions) from the experimental measurements. For the diffuser with the wing, the centreline C_p predicted on the diffuser surface at $x/d = 6.29$ for $h/d = 0.764$, 0.382, 0.191, 0.153 and 0.064 (Figures 6—23 a, b, c, e and f) are respectively: -0.083, -0.147, -0.241, -0.362 and -0.269 while the respective experimental measurements are: -0.109, -0.182, -0.242, -0.347 and -0.220. In the case of the diffuser with both the bump and wing for $h/d = 0.764$

(Figure 6—23d), there is 39.90% overprediction on the surface of the bump on $x/d = 6.29$ from the experimental C_p measurement value of -0.882.

The additional downforce generated by the inverted wing is highlighted by the second-stage pressure drop and recovery also induced on its suction surface. Experimental pressure measurements were not taken on the suction surface of the wing but CFD predictions reasonably reproduces the pressure drop and recovery along the centreline of the wing's suction surface. Static pressures prediction indicates that peak suction on the wing exist along its centreline where the flow across the wing suction surface is undisturbed and attached to the surface. For the diffuser with the wing, the highest suction (lowest C_p) at $x/d = 6.29$ on the wing centreline, respectively for $h/d = 0.764$, 0.382, 0.191, 0.153 and 0.064 (Figure 6—24a, b, c, e and f) are: -0.460, -1.242, -0.966, -0.795 and -0.296. At $h/d = 0.191$ (Figure 6—24d) for the diffuser with both the bump and wing, the lowest C_p value predicted is -1.045. In the case of the diffuser with the wing, the lowest C_p values predicted on the wing suction surface show that within the type A flow, peak suction increases with reducing ride height, however, when the ride height is lowered beyond the type A regime, peak suction on the wing gradually reduces. This because with reducing ride height the diffuser flow underneath the wing suction surface encounters an increasing adverse pressure gradient.

Across the span of the diffuser at $x/d = 6.29$, the predicted pressure measurements also generally correlate the reasonable symmetry for $h/d = 0.764, 0.382, 0.191$ and the asymmetry for $h/d = 0.153$, and 0.064. In comparison between the highest suction (lowest C_p) measured across the span of the plane diffuser surface at $x/d = 6.29$ and the equivalent predicted C_p on the wing suction surface, the suction on the wing is higher. On the wing suction surface for the diffuser with the wing, the highest predicted suction (lowest C_p) values for $h/d = 0.764$, 0.382, 0.191, 0.153 and 0.064 are respectively: -0.799, -0.752, -0.628, -0.633 and -0.303. Comparatively, the

respective suction predictions are: 408.91%, 285.64%, 155.28%, 76.32%, and 33.48% higher than the equivalent C_p or suction measurements on the plane diffuser surface. For the diffuser with the bump and wing, the lowest C_p predicted on the suction surface of the wing at $h/d = 0.191$ is -0.671 and this 172.76% lower than equivalent measurement at the same location on the surface of the plane diffuser. These significant comparative surface pressure suction increments thus further underlines the enhanced downforce induced by the inverted wing as a passive flow-control device.

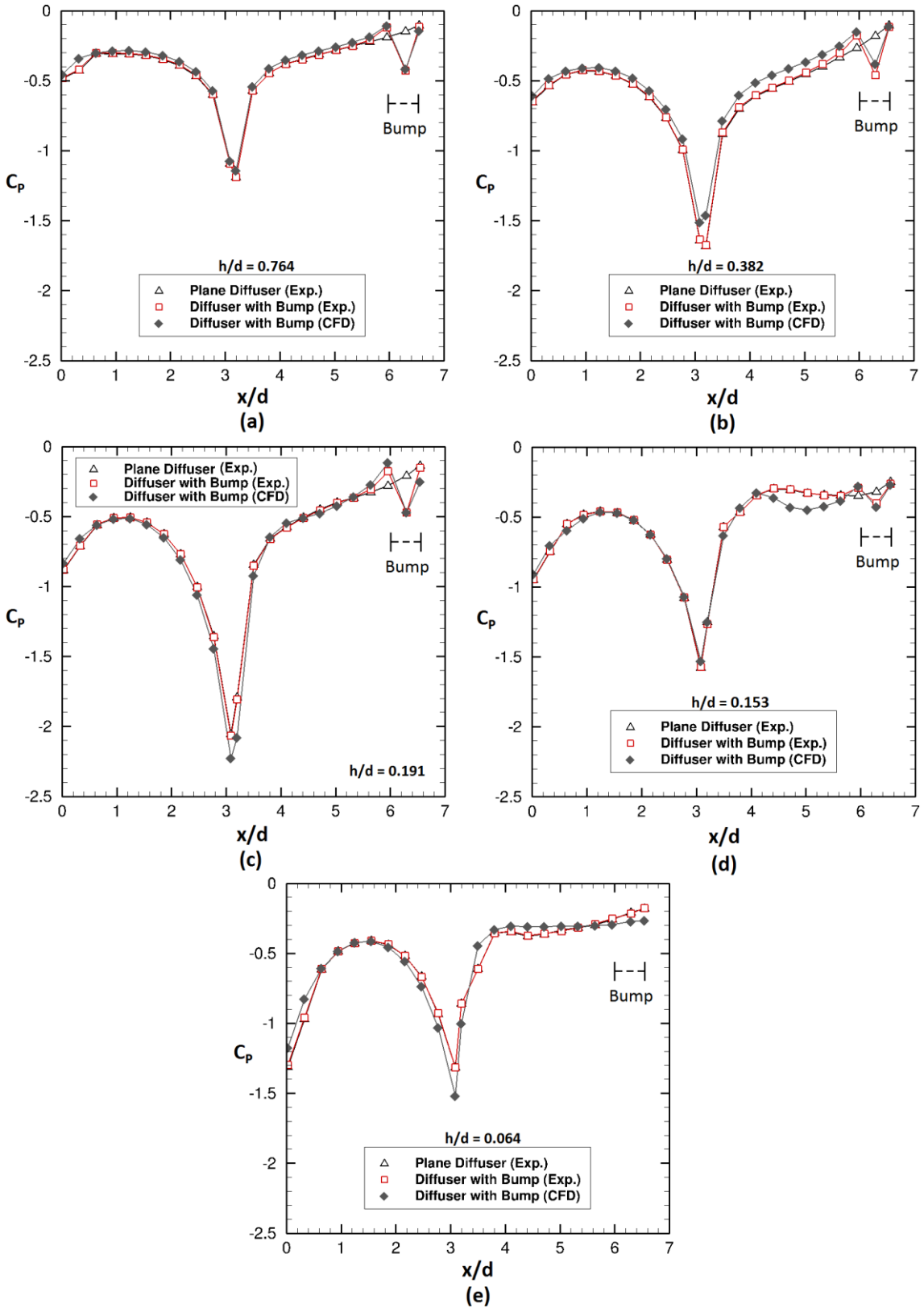

Figure 6-21: Measured (wind tunnel) and CFD-predicted underbody surface pressure distributions on centreline $(z/d = 0)$ for plane diffuser and diffuser with bump at: **(a)** $h/d = 0.764$ **(b)** $h/d = 0.382$ **(c)** $h/d = 0.191$ **(d)** $h/d = 0.153$ **(e)** $h/d = 0.064$

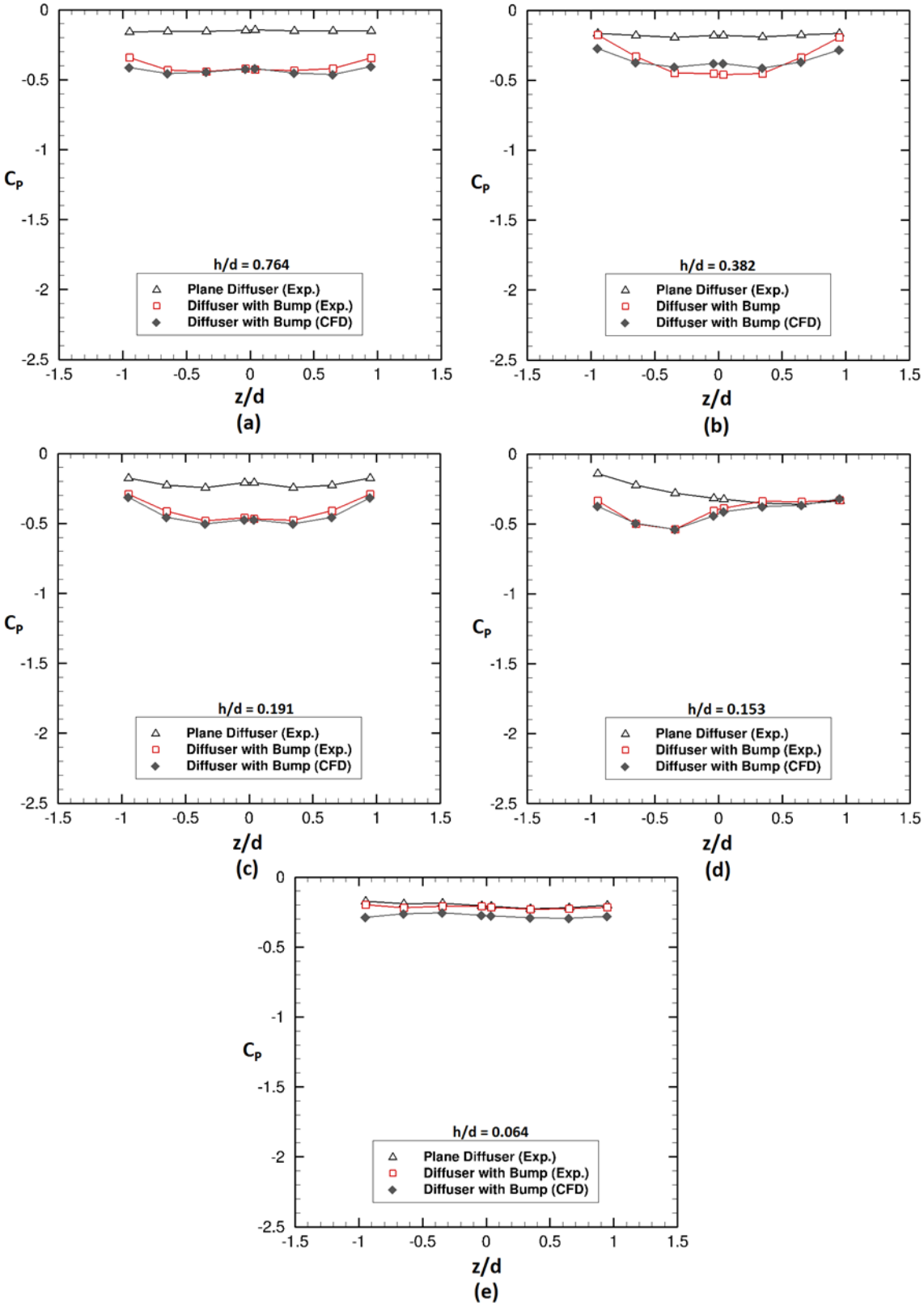

Figure 6-22: Measured (wind tunnel) and CFD-predicted diffuser spanwise surface pressure distributions on $x/d = 6.29$ for plane diffuser and diffuser with bump at: **(a)** $h/d = 0.764$ **(b)** $h/d = 0.382$ **(c)** $h/d = 0.191$ **(d)** $h/d = 0.153$ **(e)** $h/d = 0.064$

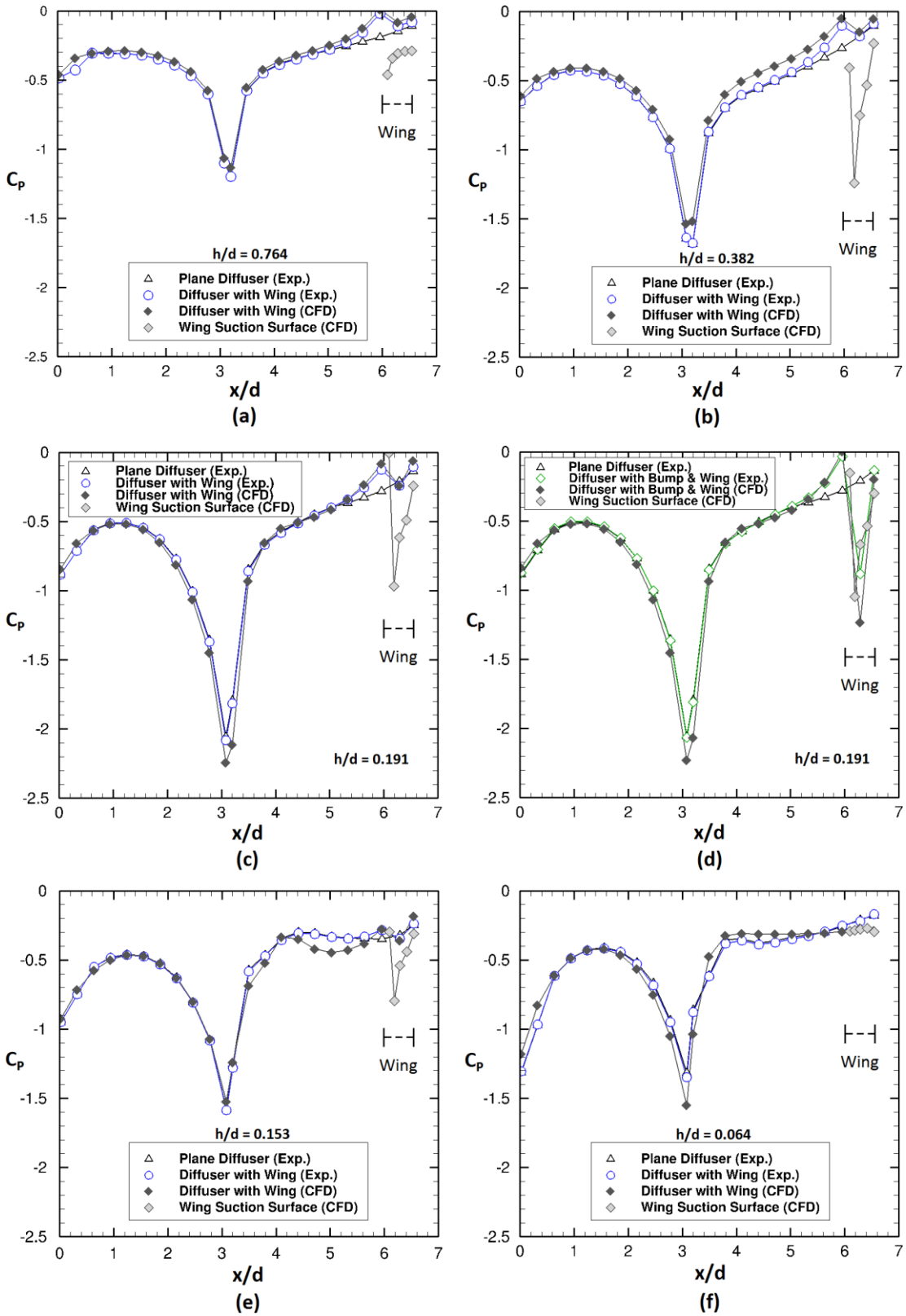

Figure 6-23: Measured (wind tunnel) and CFD-predicted underbody surface pressure distributions on centreline $(z/d = 0)$ for plane diffuser and diffuser with the wing at: **(a)** $h/d = 0.764$ **(b)** $h/d = 0.382$ **(c)** $h/d = 0.191$ **(d)** $h/d = 0.191$ (with both the wing and bump) **(e)** $h/d = 0.153$ **(f)** $h/d = 0.064$

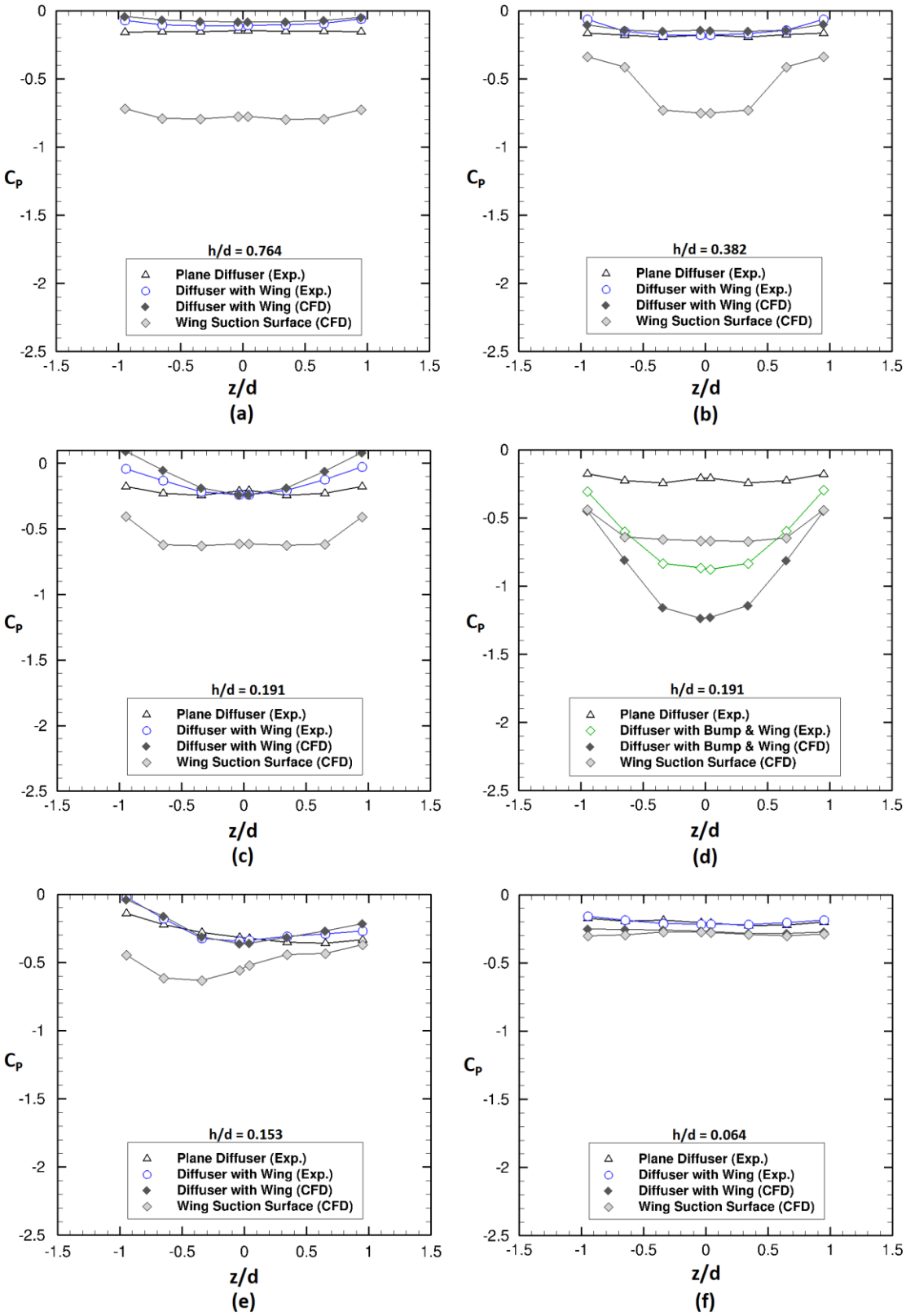

Figure 6-24: Measured and CFD-predicted diffuser spanwise surface pressure distributions on $x/d = 6.29$ for plane diffuser and diffuser with the wing (and both the wing and bump) at: **(a)** $h/d = 0.764$ **(b)** $h/d = 0.382$ **(c)** $h/d = 0.191$ **(d)** $h/d = 0.191$ (with both the wing and bump) **(e)** $h/d = 0.153$ **(f)** $h/d = 0.064$

6.3.3 Surface flow features

The predicted pathlines on the diffuser ramp surface for the five ride heights that represents the four distinct flow regimes not only agree with the on-surface flow visualizations captured in the wind tunnel investigations but also provide further clarity to the diffuser flow for the various diffuser types. In Figures 6—25 and 6—26, the vortex pair pathlines are visible for both $h/d = 0.764$ and 0.382 and increase in size from the lower to the higher ride height thus indicating an increase in vortex strength. At $h/d = 0.191$ (Figure 6—27), the predicted curved pathlines of the vortex pair further increase but the central separation bubble region as captured in the experimental flow visualization (Figure 6—16) is not apparent at this ride height. This is because the numerical solution appears not to adequately model the severe adverse pressure gradient and the resultant flow separation at that location. However at $h/d = 0.153$ and 0.064 (Figures 6—28 and 6—29), the flow asymmetry as indicated by the solitary weak vortex curved pathlines together with the flow recirculation and reversal pathlines are adequately captured by the turbulence modeling of the numerical solution.

The bump and wing as flow modification devices also induced visible surface flow features of the diffuser flow as indicated by the predicted flow pathlines. These include the small recirculation regions on both sides of the suction surfaces of the passive devices. The regions appear to increase in size with reducing ride height from $h/d = 0.764$ to 0.191 as indicated by the predicted pathlines shown in Figures 6—25 to 6—27 and the experimental pathlines in Figures 6—14 to 6—16. When the longitudinal vortices of the diffuser travel towards the diffuser exit their rotating structures generate the recirculation regions on the surfaces of the bump and wing. In addition, with reducing ride height from the type A to the type B diffuser flow regimes, the vortices increase in size thus enhancing the recirculation region on both sides of the suction surfaces of the passive flow-control devices. Another visible flow feature as adequately captured by the numerical simulations at $h/d = 0.153$

(Figure 6—28) is the undisturbed pathlines on a portion of the surface area of the bump and wing suction surfaces. This flow feature as predicted conforms to the experimental surface flow visualization in Figure 6—17 and the non-disturbed pathlines on that surface area of the passive devices which lies on the side of the diffuser where the solitary vortex still exist implies that that flow is attached. As further referenced by the enhance suction (Figures 6—22d and 6—24e) on the area of attached flow (Figure 6—17), the suction surfaces of the passive devices generate additional downforce relatively to the plane diffuser by inducing flow attachment which in turn leads to the increased suction. At $h/d = 0.064$ (Figure 6—29), the computations provide a reasonable capture (as with the experimental case in Figure 6—18) of the largely disturbed pathlines on the suction surfaces of the passive devices which are induced by significant diagonal flow recirculation across the diffuser ramp surface.

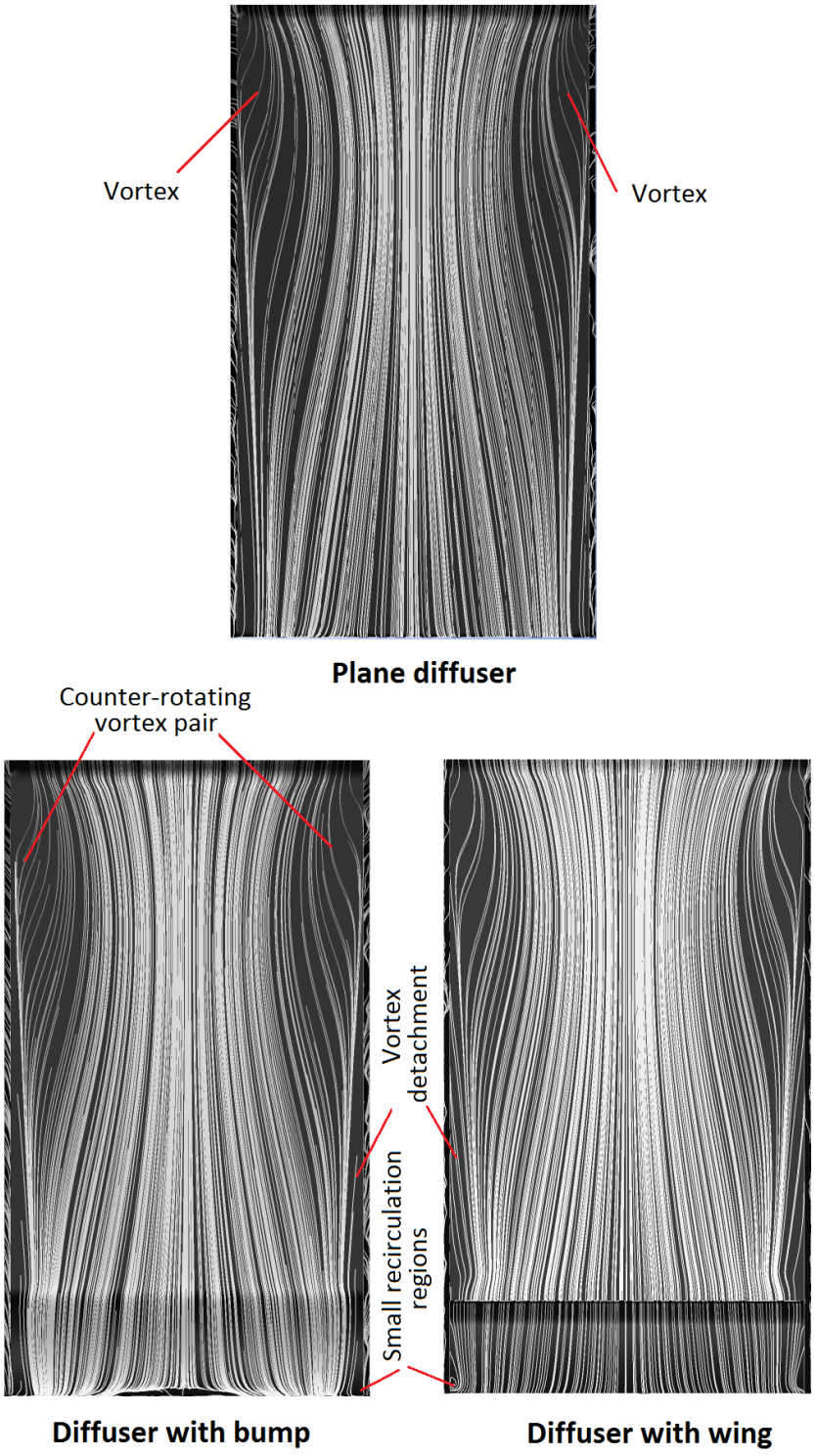

Figure 6-25: Predicted surface flow features (using CFD) for plane diffuser and diffuser with flow control methods for flow regime A at $h/d = 0.764$ (Flow direction from top to bottom)

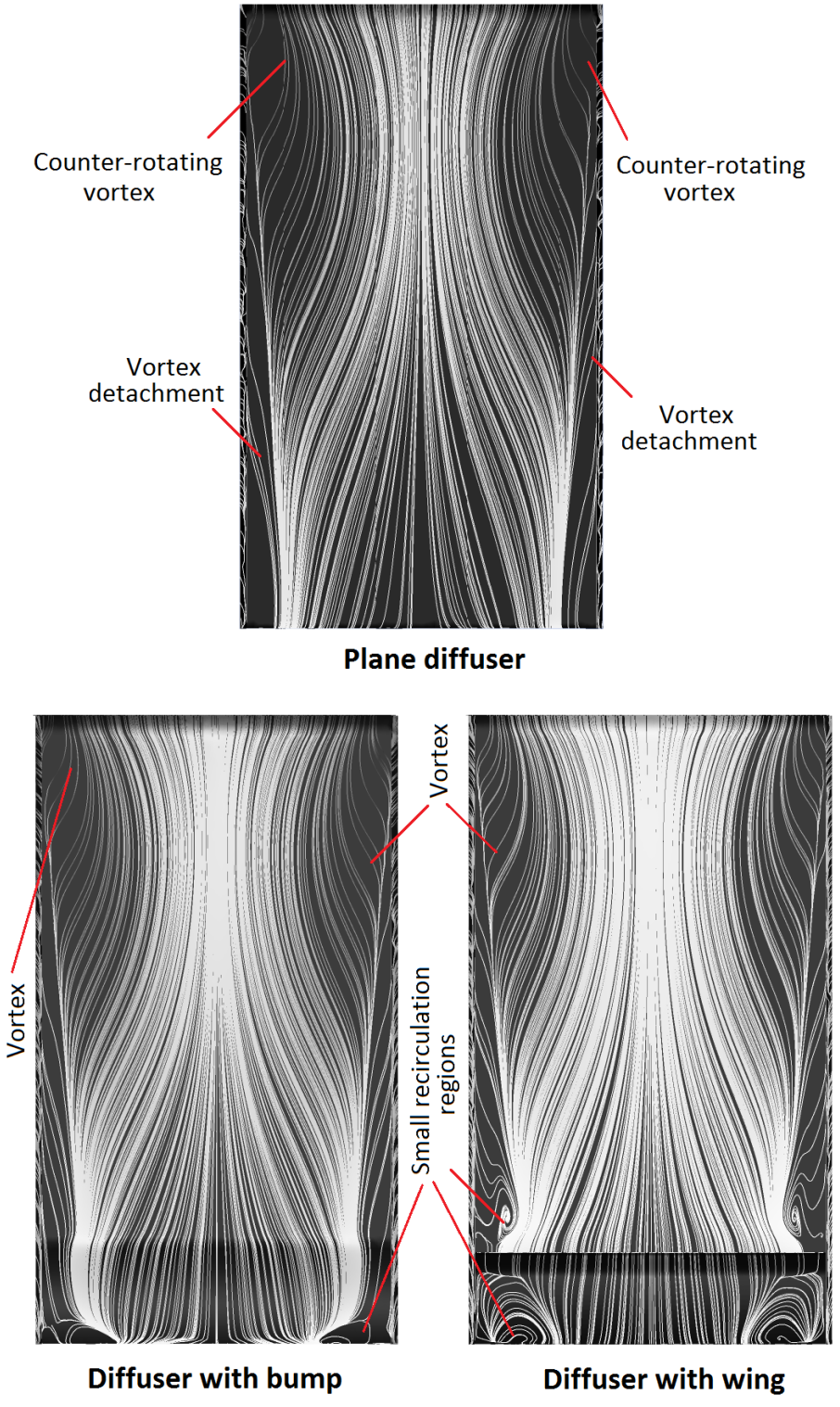

Figure 6-26: Predicted surface flow features (using CFD) for plane diffuser and diffuser with flow control methods for flow regime A at $h/d = 0.382$ (Flow direction from top to bottom)

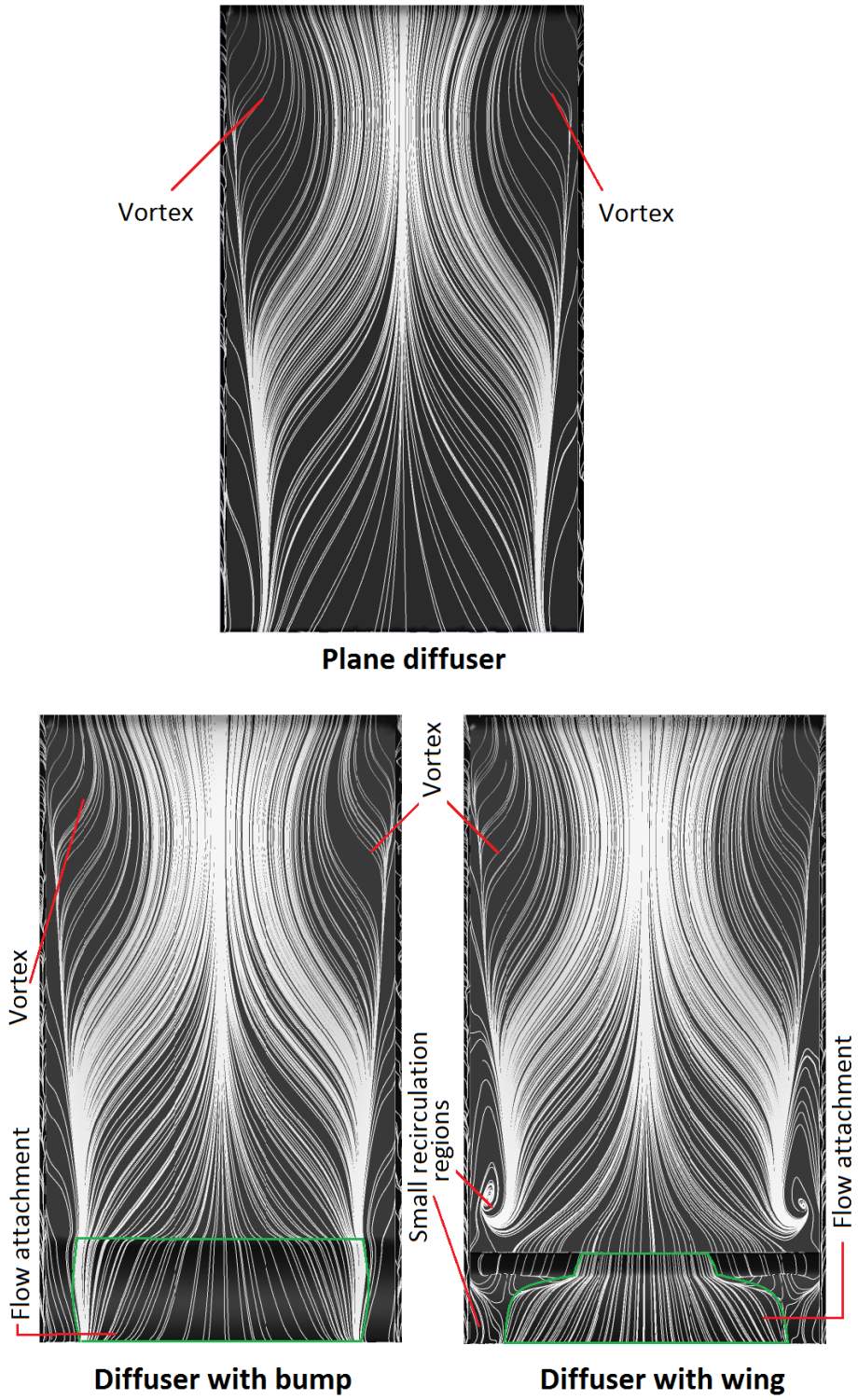

Figure 6-27: Predicted surface flow features (using CFD) for plane diffuser and diffuser with flow control methods for flow regime B at $h/d = 0.191$ (Flow direction from top to bottom)

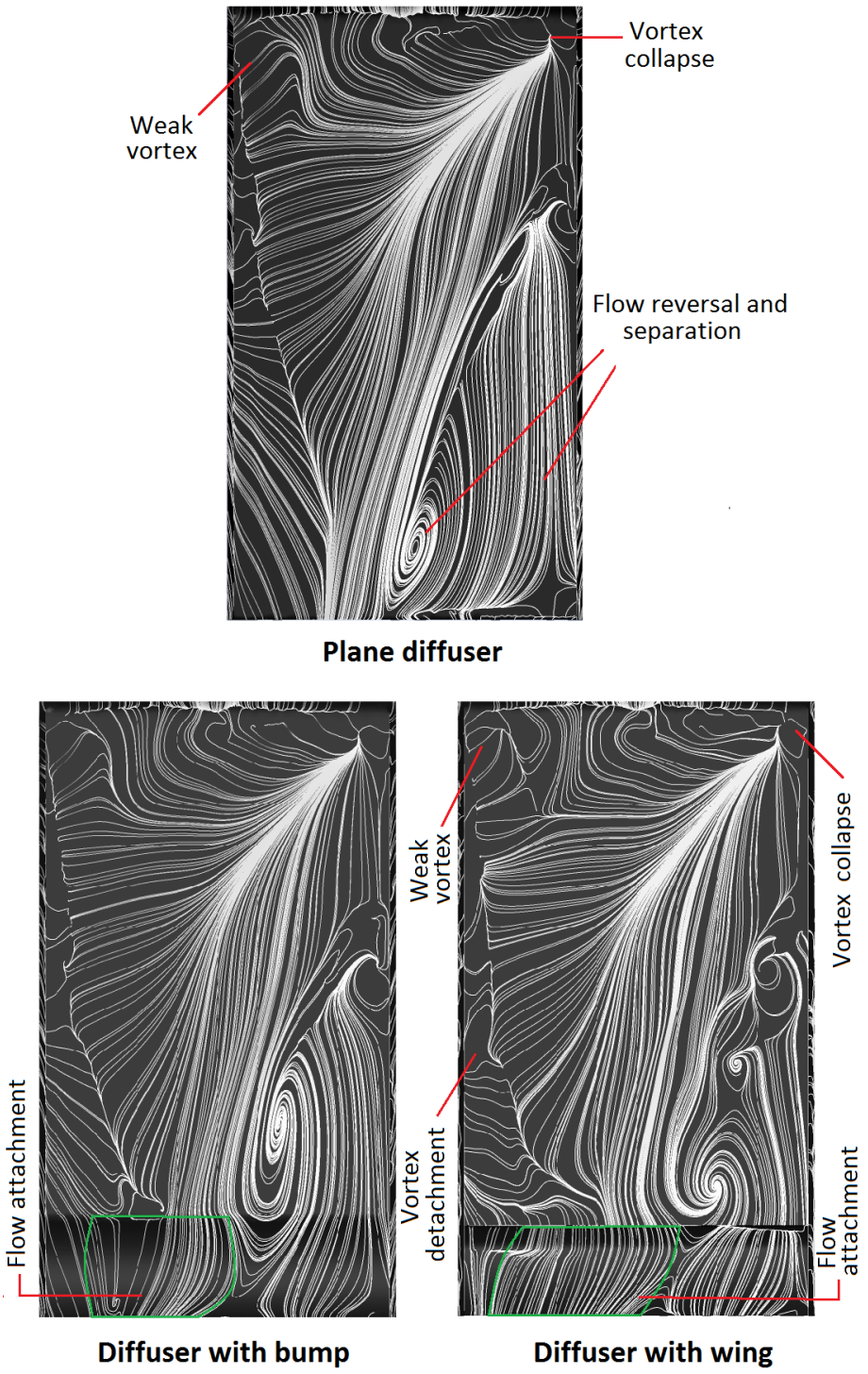

Figure 6-28: Predicted surface flow features (using CFD) for plane diffuser and diffuser with flow control methods for flow regime C at $h/d = 0.153$ (Flow direction from top to bottom)

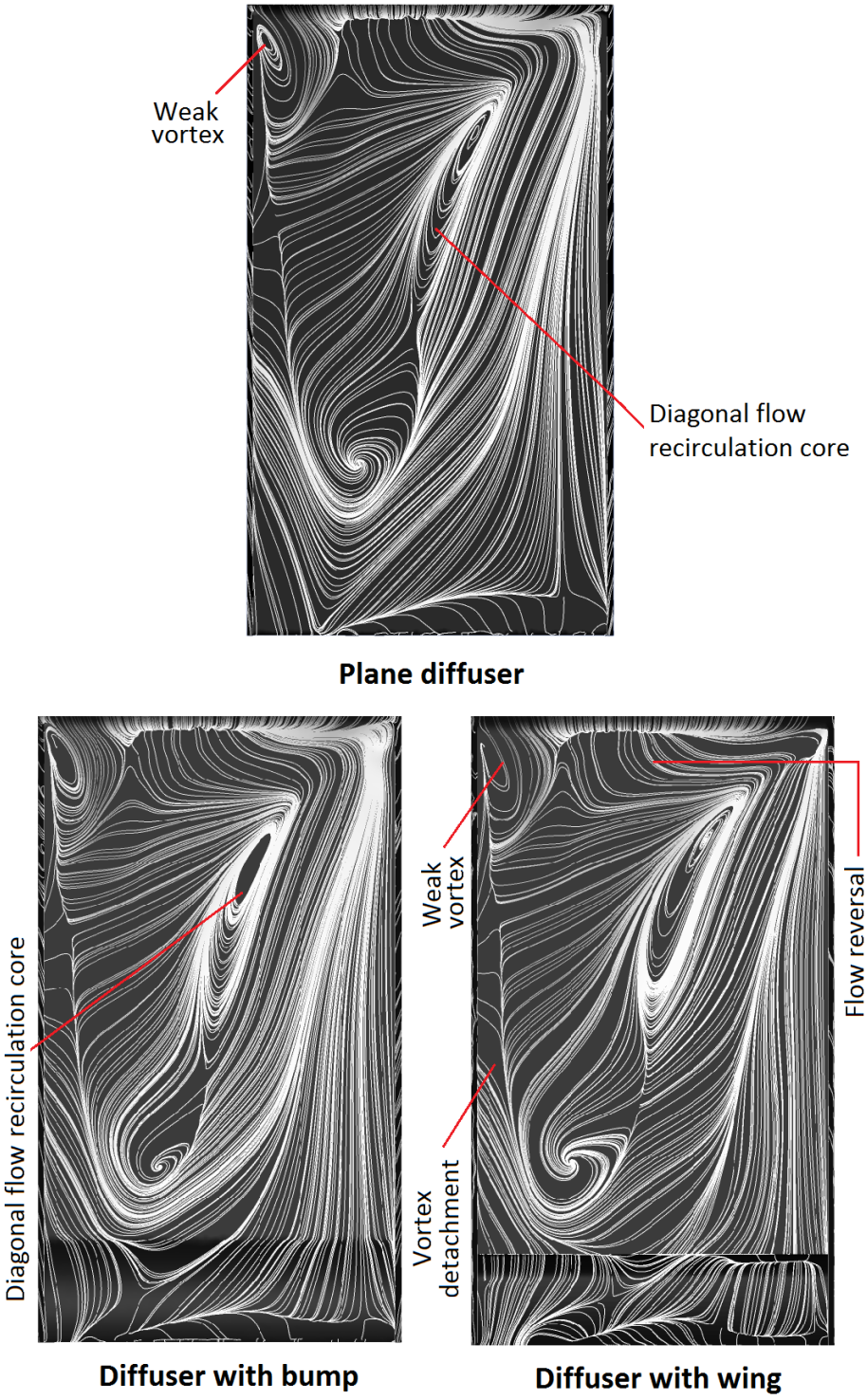

Figure 6-29: Predicted surface flow features (using CFD) for plane diffuser and diffuser with flow control methods for flow regime D at $h/d = 0.064$ (Flow direction from top to bottom)

6.3.4 Skin friction drag

As earlier stated in this chapter the additional downforce generated by the passive devices comes with an increase in drag. The additional drag induced is as a result of the geometrical profile or form of the devices. Thus the increment in drag can be described as profile drag which in turn comprises of pressure drag and skin friction drag. Skin friction is the dominant type of drag generated by streamlined bodies and is induced as a result of the frictional shearing forces (wall shear stress τ_w as defined in Equation 6.1) between the surface and the flow traveling over the surface (distance to the wall y). In the diffuser flow where there is the presence of longitudinal vortices traveling along the length of the diffuser, the increase or decrease of skin friction drag along the diffuser ramp surface is partly dictated by the strength of these vortices.

Where,

$$\tau_w = \mu\left(\frac{\partial u}{\partial y}\right)_{y=0} \tag{6.1}$$

$$C_f = \frac{\tau_w}{q_\infty} \tag{6.2}$$

The skin friction coefficient (C_f as defined in Equation 6.2) distributions for the plane diffuser along the lengthwise centreline ($z/d = 0$) of the diffuser and on both sides ($z/d = 0.490$ and -0.490) of the centreline, where the longitudinal vortices are located, are presented in Figure 6–30. The initial observation is that the reasonable symmetry associated with the maximum-downforce flow regime (type B) ride height of $h/d = 0.191$ at $z/d = 0.490$ and -0.490 is still existent with the respective C_f distributions. However at the ride height representing the force-reduction (type C) diffuser flow regime ($h/d = 0.153$), the C_f distribution at $z/d = -0.490$ where the solitary vortex is present is different to that at $z/d = 0.490$ where vortex breakdown occurred.

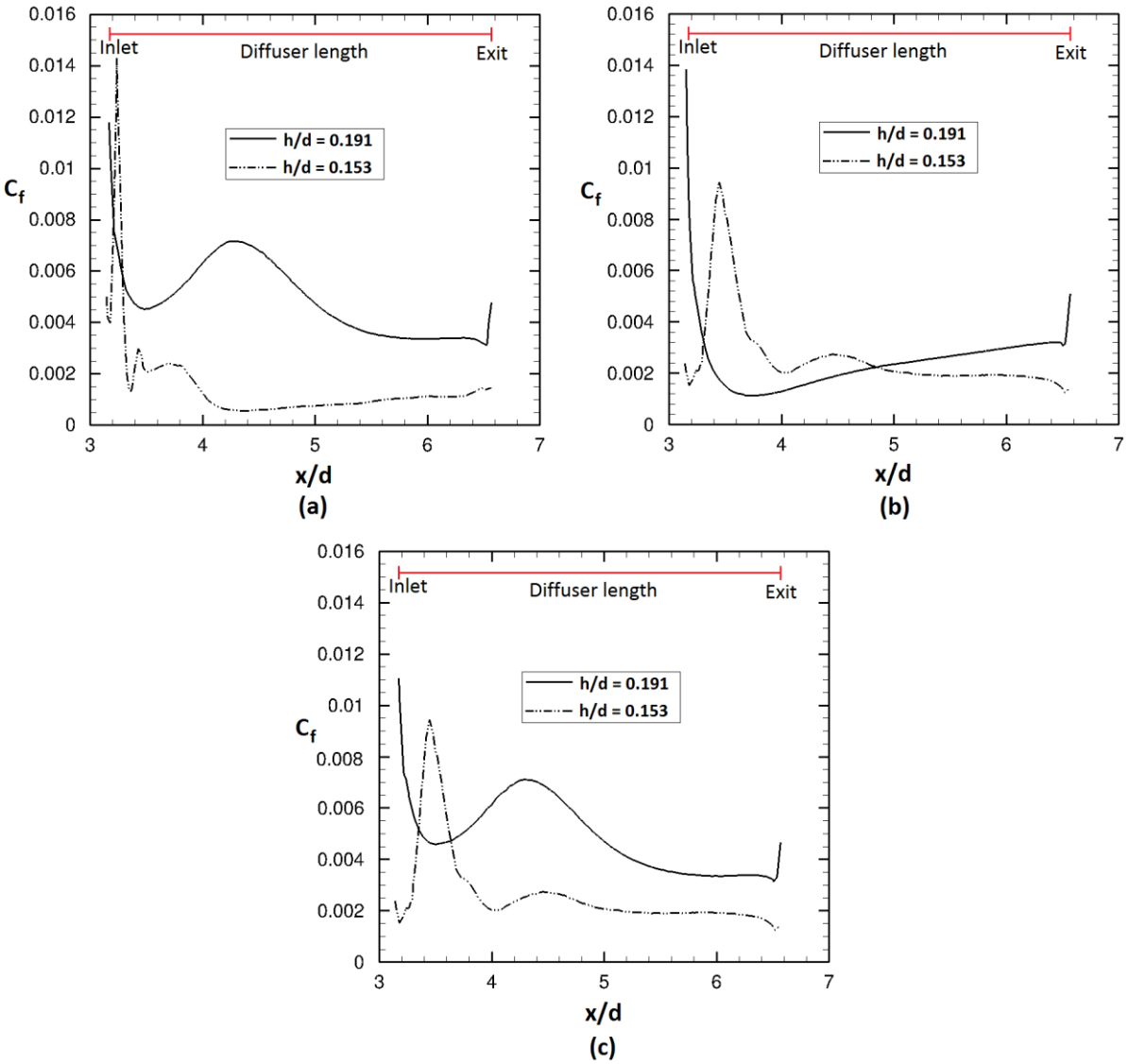

Figure 6-30: CFD predictions of skin friction coefficient (C_f) for the plane diffuser (baseline) at maximum downforce ride height $(h/d = 0.191)$ and force reduction ride height $(h/d = 0.153)$ on: **(a)** $z/d = 0.490$, **(b)** $z/d = 0$, and **(c)** $z/d = -0.490$

At $h/d = 0.191$ (Figure 6–30), there is a substantial drop in C_f around the start of the diffuser $(x/d = 3.14 \text{ to } 3.5)$ as a result of the peak velocity at the diffuser inlet gradually decelerating thus inducing localized boundary layer growth. Downstream of the diffuser inlet $(x/d = 3.5 \text{ to } 5.6)$ along $z/d = 0.490$ and -0.490 (Figures 6–30a and 6–30c), C_f increases and decreases due to the vortex strength being strong at the early part of the diffuser and gradually weakening as it travels downstream towards the diffuser exit. At the exit $(x/d = 6.54 \text{ to } 6.57)$, the sudden short rise in C_f is as a result of the turbulent wake at the near-wake region of diffuser bluff body.

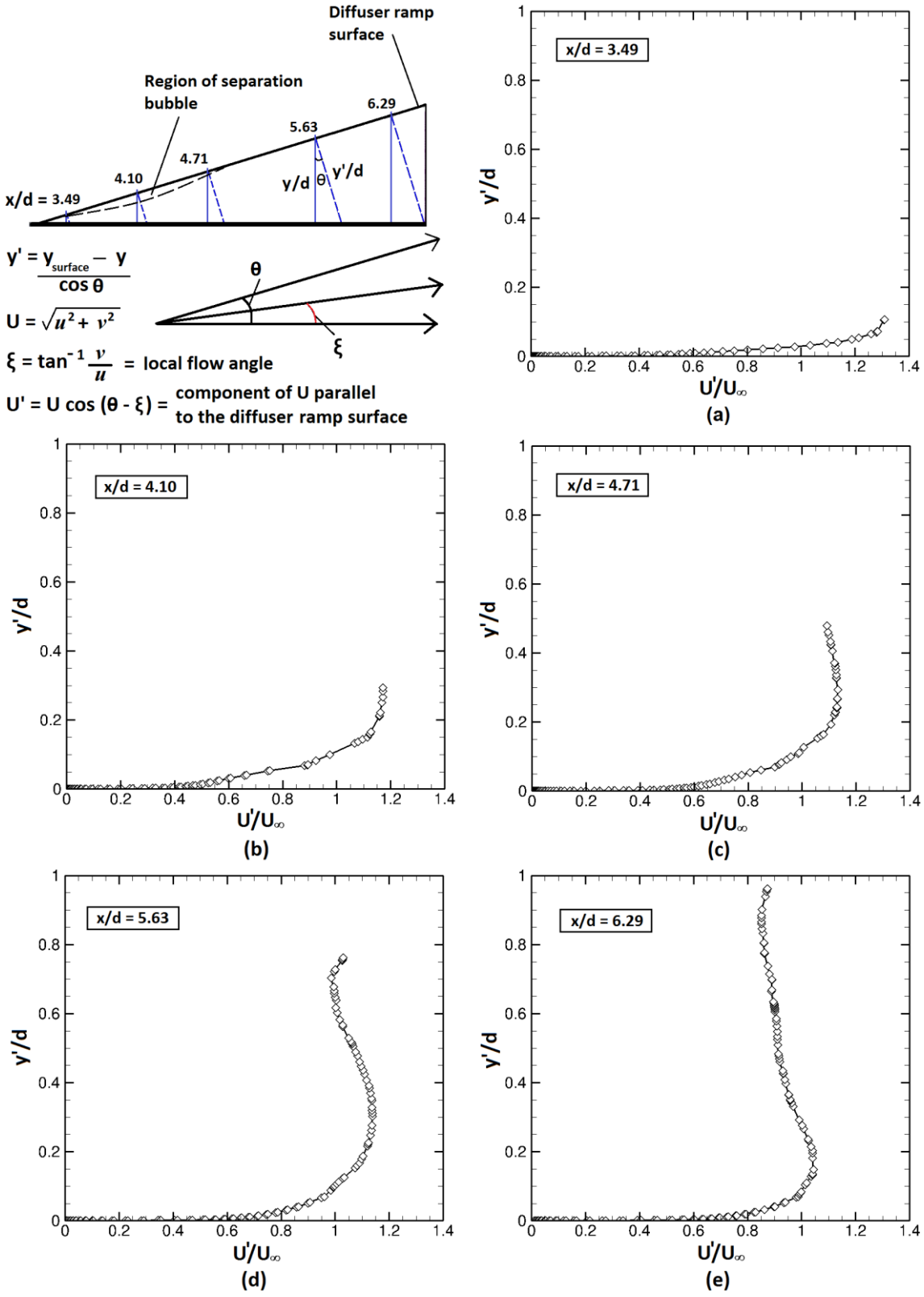

Figure 6-31: CFD-predicted boundary layer profiles normal to the diffuser ramp surface for maximum downforce ride height $(h/d = 0.191)$ (with $y'/d = 0$ at the diffuser surface and positive downwards; U'/U_∞ is relative to the diffuser surface) taken at: **(a)** $x/d = 3.49$ **(b)** $x/d = 4.10$ **(c)** $x/d = 4.71$ **(d)** $x/d = 5.63$ **(e)** $x/d = 6.29$

In the case of the centreline C_f distribution at $h/d = 0.191$ (Figure 6—30b), there is a gradual rise in C_f between the significant drop in C_f around the diffuser inlet region and a small sharp rise in C_f at the diffuser exit. This is because there is no presence of the longitudinal vortices along the diffuser centreline and at the diffuser exit there is a turbulent near-wake. However along the centreline, the separation bubble at the early part of the diffuser captured by wind tunnel flow visualisation (Figure 6—16) is not adequately captured by the CFD (URANS) predicted flow pathlines (Figure 6—27). Nonetheless, CFD-predicted boundary layer profiles (Figure 6—31) normal to the baseline plane diffuser ramp indicate that at the early part of the diffuser, the higher velocities are away from the ramp surface (turbulent boundary layer is less full) but towards the diffuser exit the higher velocities are closer to the ramp surface (turbulent boundary layer is fuller). This explains the gradual increase towards the diffuser exit of C_f on the diffuser ramp centreline because the growth of a turbulent boundary layer induces an increase in skin friction.

In the case of $h/d = 0.153$ (Figure 6—30a), the C_f distribution on the side of the diffuser ($z/d = 0.490$) where vortex breakdown occurs, rises and reduces sharply at the diffuser inlet region ($x/d = 3.14$ to 3.48). This is due to an intermittent turbulent flow accompanied by an increase in flow velocity at the diffuser inlet. Between $x/d = 3.48$ to 4.20, there is smaller level of intermittent turbulent flow and an increase in flow velocity hence the increase and decrease of skin friction. Further downstream of this region, the flow is dominated by flow recirculation which gives rise to the gradual increase in wall shear stress towards the diffuser exit. However, the C_f distribution for $z/d = 0$ and -0.490 (Figures 6—30b and 6—30c) appear to be similar in shape. This is because away from the region of vortex breakdown, the regions ($x/d = 3.14$ to 4.0 and 4.0 to 5.0) of intermittent flow turbulence and increase in flow velocity are longer and towards the diffuser exit there is no significant change in skin friction.

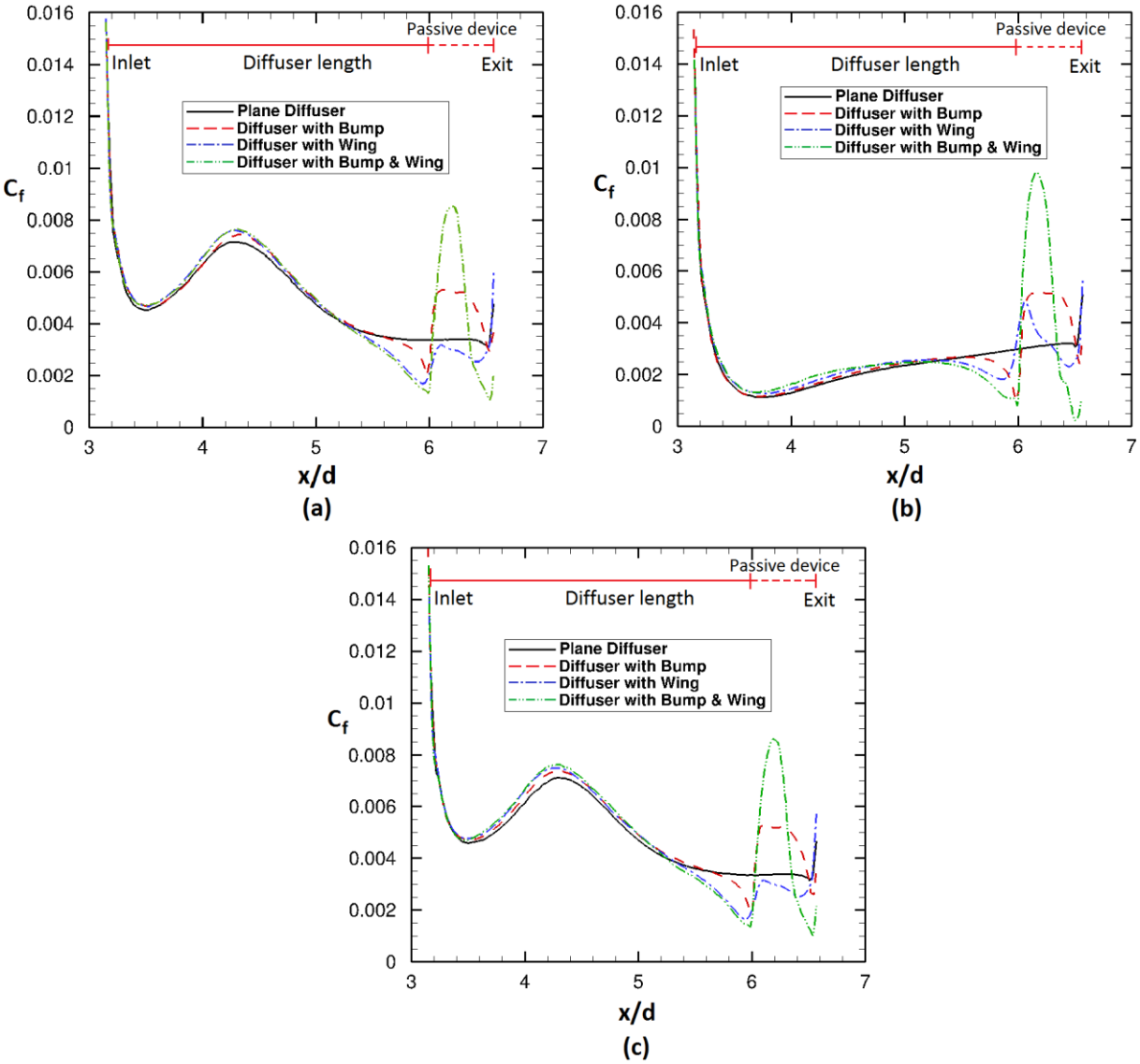

Figure 6-32: CFD predictions of skin friction coefficient (C_f) at maximum downforce ride height $(h/d = 0.191)$ for the plane diffuser (baseline) and diffuser with the passive flow control methods on: **(a)** $z/d = 0.490$, **(b)** $z/d = 0$, and **(c)** $z/d = -0.490$

The addition of the passive devices induces a change in the distribution of C_f on the diffuser ramp surface from $x/d = 5.3$ to 6.54 at the maximum-downforce regime ride height of $h/d = 0.191$ (Figure 6–32). Between $x/d = 5.3$ to 6.0, there is a drop in the local skin friction C_{f_x} as a result of the localized flow deceleration induced by leading surface of the bump and wing. Within the region $x/d = 6.0$ to 6.54 which encompasses the length of the bump and wing, there is a rise and drop in skin friction. The rise in C_f is as a result of the

viscous forces acting on the flow as it negotiates and accelerates over the early part of the protruding bump and wing surface. However, downstream of the early part of the passive flow control surfaces, there is a drop in C_f as the flow decelerates towards the diffuser exit. Also, as in the baseline case the sudden spike in C_f at the exit ($x/d = 6.54$ to 6.57) is due to the turbulent flow at the near-wake of the diffuser body.

As presented in Table 6—4, the streamwise-length-averaged skin friction coefficient $\bar{\bar{C}}_f$ as calculated using Equation 6.3 for $z/d = 0.490,\ 0$, and -0.490 at $h/d = 0.153$ is 0.0014, 0.0025, and 0.0030 for the plane diffuser.

Where,

$$\bar{\bar{C}}_f = \frac{1}{l_d}\int_{x/d=3.14}^{x/d=6.57} C_f\ dx \tag{6.3}$$

Where, l_d is the diffuser ramp length $= 0.563\ m$

This not only indicates that the diffuser flow is asymmetric between both lengthwise sides of the diffuser, but also away (in the spanwise direction) from the side where vortex breakdown occurs, skin friction drag increases towards the location of the surviving vortex. At $h/d = 0.191$, the plane diffuser flow is reasonably symmetric because the value of $\bar{\bar{C}}_f$ for both $z/d = 0.490$ and -0.490 is 0.0046 and at the diffuser spanwise centreline ($z/d = 0$), $\bar{\bar{C}}_f$ is lesser ($\bar{\bar{C}}_f = 0.0023$) because of the non-existence of a longitudinal vortex. Comparatively at $h/d = 0.191$ for $z/d = 0.490,\ 0$, and -0.490, the diffuser with the bump and the diffuser with both the bump and wing generated a higher skin friction than the diffuser with the wing as presented in Table 6—4. This is due to the higher increase in local skin friction C_{f_x} partly between $x/d =$ 6.0 to 6.56.

Table 6-4: Streamwise-length-averaged skin friction coefficient along $z/d = 0.490$, 0, and -0.490 for the plane diffuser and the diffusers with passive flow control at $h/d = 0.191$ and 0.153

h/d	$\overline{\overline{C}}_f$ at $(z/d = 0.490)$	$\overline{\overline{C}}_f$ at $(z/d = 0)$	$\overline{\overline{C}}_f$ at $(z/d = -0.490)$
0.153 (Plane Diffuser)	0.0014	0.0025	0.0030
0.191 (Plane Diffuser)	0.0046	0.0023	0.0046
0.191 (Diffuser with bump)	0.0050	0.0026	0.0050
0.191 (Diffuser with wing)	0.0046	0.0023	0.0046
0.191 (Diffuser with bump & wing)	0.0049	0.0026	0.0049

6.4 Velocity Profile Measurements

As a means to further understand the aerodynamic behaviour induced in the near-wake of the bluff body when the passive methods were employed, the near wake flow physics are examined. The experimental investigations involved analysing flow velocity and turbulence intensity measurements from LDV. In addition, the upper and lower near-wake vortical structures were assessed and the near-wake circulation was quantified for the various diffuser types.

6.4.1 Flow structures of diffuser near-wake region

The centreline $(z/d = 0)$ wake flow structures for the baseline plane diffuser and the diffusers with the various passive methods are compared in Figure 6−33, revealing that at the maximum-force flow regime ride height of $h/d = 0.191$, the wake flow structure of the baseline diffuser is similar to that of diffusers with passive flow controls. The upper and lower counter-rotating vortices remain present, with the lower vortex dominant. However, the lower vortex at the centreline plane for all four diffusers (Figure 6−33) is smaller than the lower vortex at the planes on $z/d = 0.490$ and $z/d = -0.490$ for the same ride height (Figure 5−35). This implies that the exit flow of the longitudinal streamwise vortices along both lengthwise sides of the diffuser is responsible for the increase in size of the lower vortex in the near-wake region.

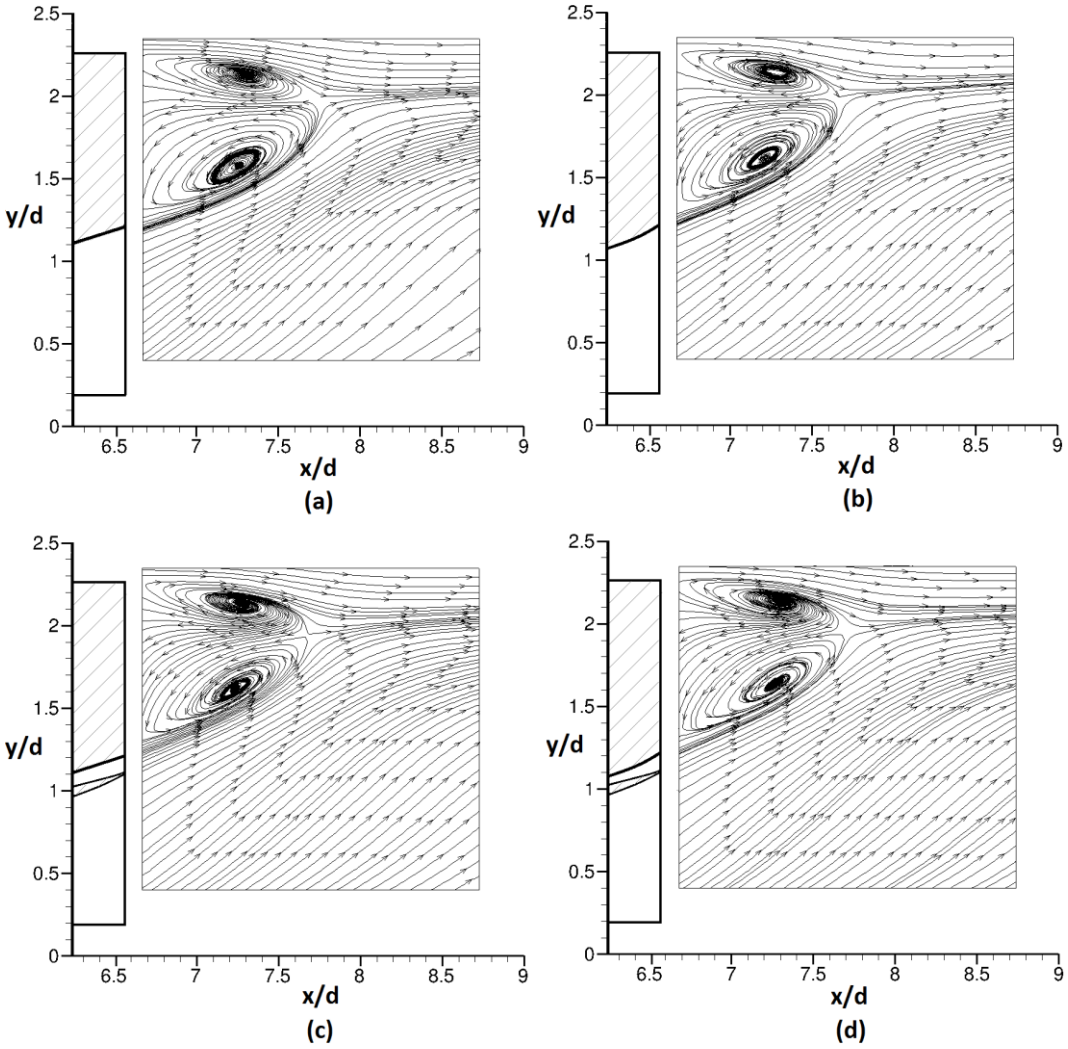

Figure 6-33: Centreline plane near-wake ***U*** flow structures measured with LDV at $h/d = 0.191$ for **(a)** plane diffuser **(b)** diffuser with bump **(c)** diffuser with wing **(d)** diffuser with both bump and wing

6.4.2 Velocity profiles of diffuser near-wake region

As stated in Section 1.2, the diffuser produces downforce through a velocity-pressure relationship governed by Bernoulli's principle, such that fast-moving flow through the diffuser generates low static pressure within the diffuser. Accordingly, increasing the mass-flow in the diffuser at a given time will generate more downforce. Hence, flow control applications whether passive or active are beneficial only if they enhance the diffuser flow velocity and supress flow separation.

The near-wake streamwise velocity (u) and the change in velocity magnitude (ΔU) are presented to indicate the increase in downforce. The diffuser system as employed does not have endplates sealed to the ground plane and also has a mass-flow inlet and exit. Therefore, the diffuser does not exist with closed boundaries because the diffuser takes in outside high-energy flow through its inlet and along its spanwise sides before reintroducing the flow to freestream through its exit. The geometric alterations caused a static pressure drop by increasing flow velocity, reducing separation and boundary layer thickness close to the diffuser exit. As a result, the passive methods increased the outflow from the diffuser. This reflects the interaction between the diffuser with passive flow-control and the circulation around the body, such that a greater net counter-clockwise[3] circulation around the entire body implies an increase in downforce.

As shown in Figure 6—34, the boundaries (dashed lines) of the higher streamwise velocities in the near-wake of the modified diffuser bluff bodies (particularly at the contour regions indicated by 'a', 'b' and 'c') extend further downstream in comparison to the corresponding boundaries of the plane diffuser, indicating that circulation around the body had increased. Also, as indicated in Figure 6—34, the diffuser with both the bump and inverted wing appeared to enhance the streamwise velocity the most. The deficit velocity magnitude contour region (labelled 'S') of the difference between U of the plane diffuser and U for each of the flow control methods as shown in Figure 6—28 also indicated that the passive flow control methods enhanced the diffuser flow velocity and, thus, net counter-clockwise circulation around the bluff body.

Figures 6—35 and 6—36 also highlight the differences in flow physics at planes on $z/d = 0.490$ and $z/d = 0$ between the plane diffuser and passive flow control diffusers in terms of velocity magnitude and turbulence intensity. The negative contours in Figure 6—35 indicate the plane diffuser's deficit in

[3] This refers to an upwash behind the diffuser body and is related to downforce generation (with clockwise or counter-clockwise directions defined by the freestream flow traveling from left to right).

velocity magnitude compared to the diffusers with passive methods. However, contour size differences in areas of positive velocity magnitude differences show higher velocity regions above and distinctly below the base plate at plane on $z/d = 0.490$ relative to centreline plane on $z/d = 0$. This explains the larger size of the lower vortex compared to the upper vortex in plane $z/d = 0.490$ when comparing Figures 5—35 and 6—33. In addition, the contour regions of relative increase in turbulence intensity levels in Figure 6—36 indicate an increase in flow turbulence on planes at $z/d = 0.490$ and $z/d = 0$ in the modified diffusers compared to the plane diffuser. Contour regions of relative decrease in turbulence indicate a turbulence deficit in the plane diffuser compared to the diffusers with the passive flow control methods. Notably, increased areas of turbulence deficit appear in the lower regions of the plane on $z/d = 0.490$ relative to the centreline plane on $z/d = 0$. This further confirms the presence of the turbulence generated by the diffused part of the longitudinal vortices at the diffuser exit.

Furthermore, the addition of the passive control devices was accompanied by an increase in drag. At the maximum downforce and drag ride height of $h/d = 0.191$, the coefficient of drag increased from that of the plane diffuser by 1.8% (with the convex bump), 1.8% (with the wing) and 2.8% (with both the bump and wing). For a 2—D incompressible flow (with density ρ) traveling around a body, the profile drag D (expressed in Equation 6.4) can be quantified by the difference in upstream velocity U_∞ and downstream flow velocity U_w at the near-wake area plane dA (Barlow et al., 1999).

$$D = \iint \rho\, U_w\, (U_\infty - U_w)\; dA \tag{6.4}$$

This means that at the wake of the diffuser bluff body, there is a loss in flow momentum relative to upstream flow and an increase in drag corresponds to an increase in loss of flow momentum. Therefore, the relative velocity magnitude differences (ΔU) and the corresponding turbulence differences ($\Delta u'$) across the near-wake planes (Figures 6—28 and 6—29) are in general terms

related to the additional profile drag induced by the convex bump and the inverted wing.

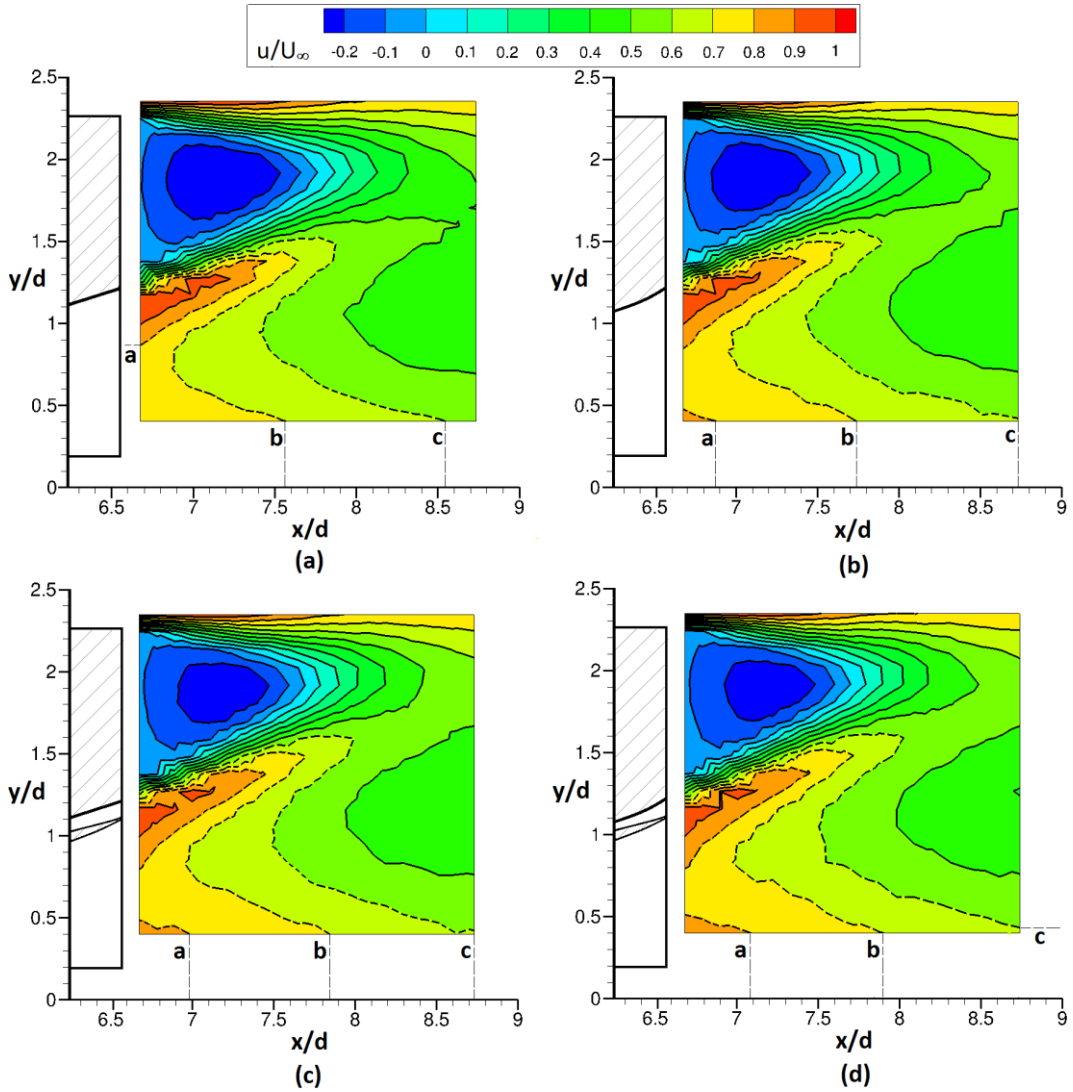

Figure 6-34: Centreline $(z/d = 0)$ plane near-wake non-dimensionalised $\boldsymbol{u}$-component contours measured with LDV at $h/d = 0.191$ for **(a)** plane diffuser (baseline), **(b)** diffuser with bump, **(c)** diffuser with wing, and **(d)** diffuser with both bump and wing

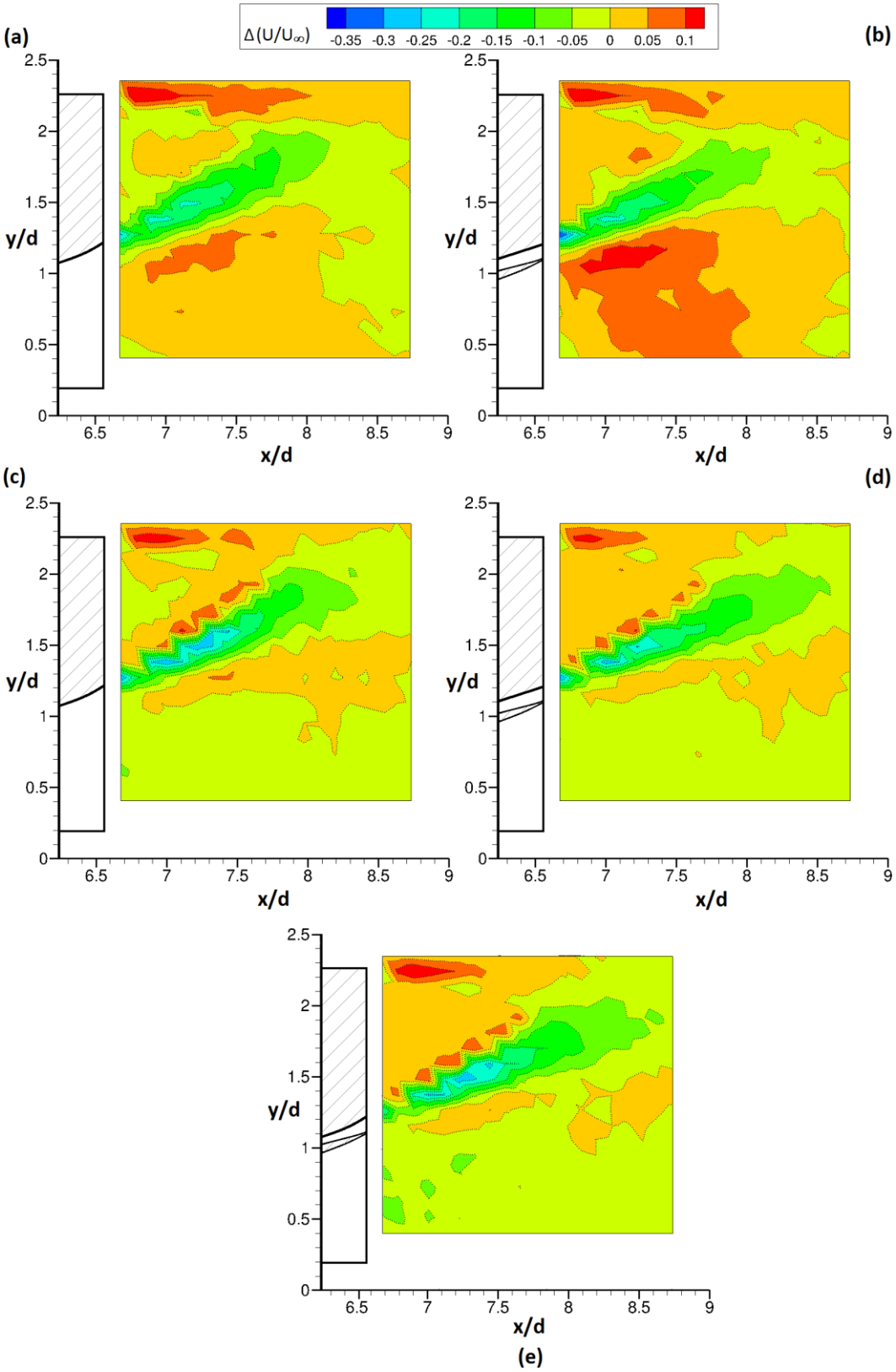

Figure 6-35: Near-wake non-dimensionalised $\boldsymbol{\Delta U}$ contours measured with LDV at $h/d = 0.191$ between plane diffuser and **(a)** diffuser with bump: plane at $z/d = 0.490$, **(b)** diffuser with wing: plane at $z/d = 0.490$, **(c)** diffuser with bump: plane at $z/d = 0$, **(d)** diffuser with wing: plane at $z/d = 0$, and **(e)** diffuser with both bump and wing: plane at $z/d = 0$

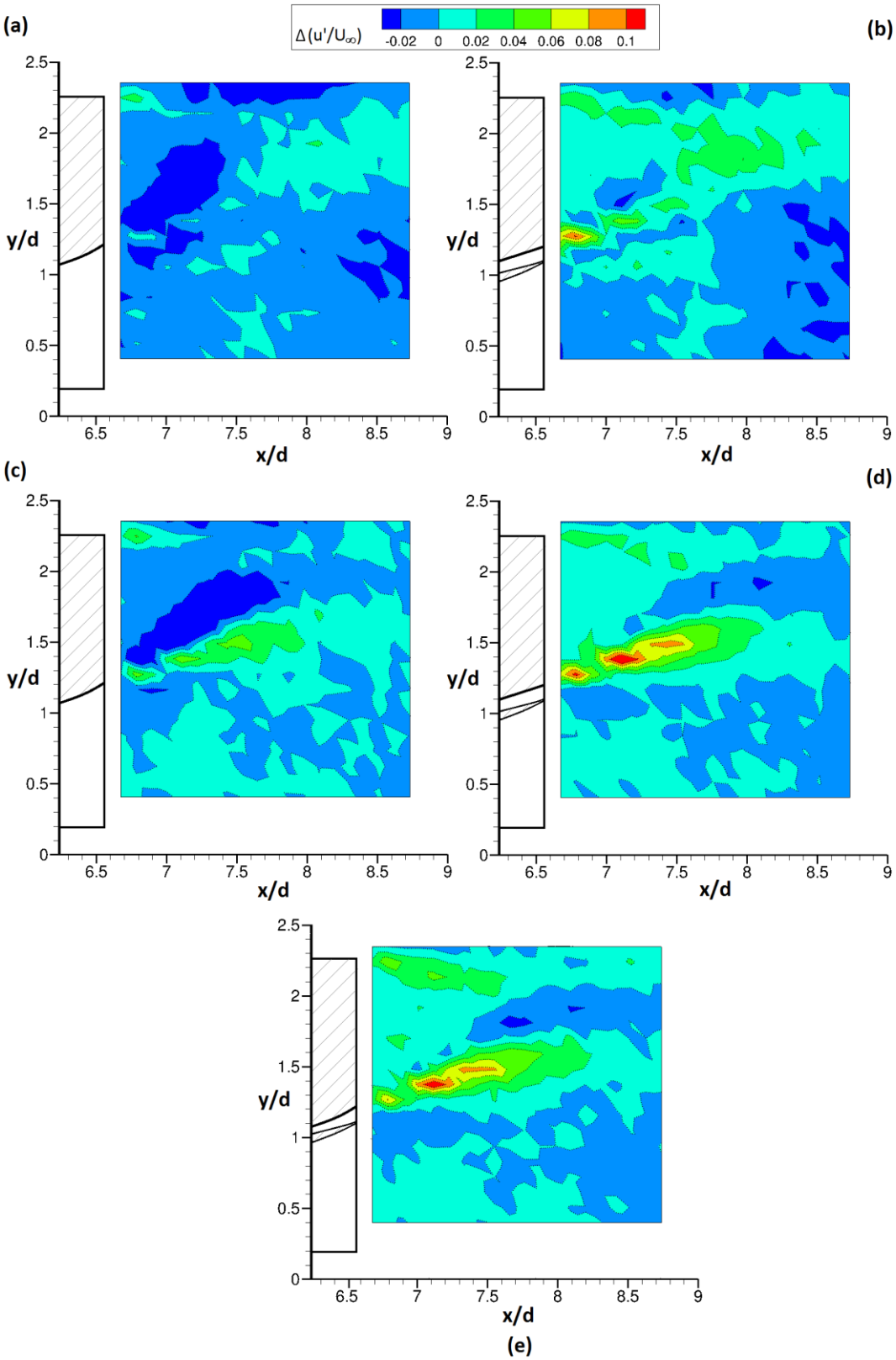

Figure 6-36: Near-wake non-dimensionalised $\boldsymbol{\Delta u'}$ contours measured with LDV at $h/d = 0.191$ between plane diffuser and **(a)** diffuser with bump: plane at $z/d = 0.490$, **(b)** diffuser with wing: plane at $z/d = 0.490$, **(c)** diffuser with bump: plane at $z/d = 0$, **(d)** diffuser with wing: plane at $z/d = 0$, and **(e)** diffuser with both bump and wing: plane at $z/d = 0$

6.4.3 Circulation in diffuser near-wake region

The flow physics of the circulation Γ on the near-wake planes can provide additional information on the lift generated by a bluff body. The Kutta-Joukowski lift theorem relates the circulation around a 2—D body to the lift acting on the body. It also states that the circulation around a lift-generating body is finite and is related to the body's boundary layer vorticity. As a result a positive lift force on the body, is accompanied by a net circulation increase (clockwise circulation) associated with a counter-clockwise boundary layer vorticity at the trailing edge. The lift force, L, generated, or in this case the body downforce, is expressed as a product of the fluid density, freestream velocity and the circulation ($L = \rho U_\infty \Gamma$). The circulation can be defined (Equation 6.5) as a line integral of the flow velocity vector $\vec{U}$ with respect to distance dl around a closed curve S, or by applying Stokes' theorem (Equation 6.6) where circulation is defined as the integral over an enclosed surface A of the curl of the velocity field (vorticity) $\vec{\omega}$ for an area element $\overrightarrow{dA}$ in the normal direction $\hat{n}$ of the vector field across the surface.

$$\oint_S \vec{U} \cdot \mathrm{d}l \tag{6.5}$$

If $\vec{\omega} = \nabla \; x \; \vec{U}$, then;

$$\Gamma = \oint_{\partial A} \vec{U} \cdot \mathrm{d}l = \iint_A \vec{\omega} \cdot \mathrm{d}A \tag{6.6}$$

If we assume flow symmetry about the body centreline plane, examination of the relative changes in the wake circulation in this plane, if independent of other vortical flow structures such as in the $y—z$ plane, changes in the circulation in the $x—y$ plane should correspond to relative changes of lift and drag generated by the body. Therefore net wake circulation levels were calculated in the centreline plane on $z/d = 0$ by expressing ω as the curl of the $u—v$ LDV velocity vector field and applying Stokes' theorem across the surface of the centreline plane (Figure 6—37).

Hence this result would infer, based on the centreline plane, a counter-clockwise circulation exists over the body, consistent with the generation of a net downforce. The result in part also corresponds to observed streamwise velocity differences between the plane diffuser and the modified diffusers illustrated in Figure 6–34 and discussed in Section 6.4.2 of this thesis. Table 6–5 outlines the relative changes in circulation with respect to the baseline diffuser and compares these changes to lift and drag data for $h/d = 0.191$.

It can be seen in Table 6–5 that the circulation integration predicts a reduction in lift in the centreline $x-y$ plane with respect to the baseline case of up to 23.5% for the diffuser with the bump. If this is compared to the change in overall body lift and drag coefficients, there is no correlation with either the magnitude or sense of the change, with respect to the diffuser baseline case. Therefore although the diffuser geometry modifications, including the bump and the wing influence changes in velocity, turbulence, and circulation in the $x-y$ plane of the bluff body near-wake region, the dominant flow features (longitudinal and spanwise vortices) that determine the lift and drag characteristics on the body, reside in the $y-z$ plane. The dominant effect of these $y-z$ flow structures also is evidenced by minimal changes in overall lift and drag when the diffuser geometry is changed in both cases.

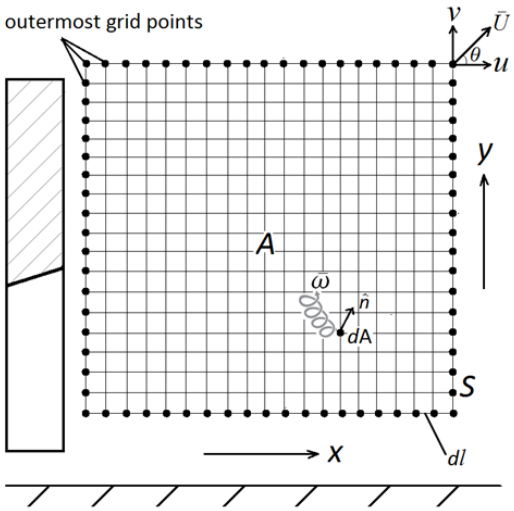

Figure 6-37: A vector field schematic across the near-wake streamwise centreline plane ($z/d = 0$)

Table 6-5: Comparisons of relative changes in the near-wake streamwise centreline plane ($z/d = 0$) circulation to changes in measured body lift and drag

Diffuser Type	C_D	C_L	Circulation Γ
Plane Diffuser (Baseline) % from Baseline	0.4637 —	-1.915 —	-1.092 —
Diffuser with Bump % from Baseline	0.4721 +1.8	-1.954 +2.0	-0.836 -23.5
Diffuser with wing % from Baseline	0.4722 +1.8	-1.973 +3.0	-0.926 -15.3
Diffuser with bump & wing % from Baseline	0.4766 +2.8	-1.983 +3.6	-0.940 -13.9

6.5 Further Discussion

The aerodynamic performance of the diffuser is dictated by its pressure recovery from the peak suction at the diffuser inlet to the near-freestream pressure at its exit. Therefore, enhancing the downforce generated by the diffuser lies in delaying its pressure recovery to freestream pressure at the diffuser exit by inducing a drop in local static pressure near the exit. Extending the area ratio of the diffuser increases the diffuser flow channel thus increasing downforce. However, as indicated by Jowsey & Passmore (2010), and Jowsey (2013), increasing the diffuser angle, which in turn increases downforce, is not indefinitely beneficial because the gain in downforce reaches a maximum after which further increases lead to downforce losses as a result of significant flow separation. As a result, altering the pressure recovery behaviour of the diffuser involves the inclusion of flow control devices within the diffuser to interact with the velocity-pressure relationship of the diffuser flow.

In this study, novel passive flow control techniques have been investigated and analysed. Passive methods have been chosen over active methods due to their cost-efficiency. However, active systems that involve blowing or suction actions on the diffuser flow boundary layer or employing the diffuser ramp surface as a moving surface as a means of mitigating boundary layer growth, can also prove effective. An established passive application on the diffuser flow

channel is the subdivision of the channel into multiple flow channels using strakes. Jowsey (2013) discovered that subdivision mitigated flow separation and enhanced the diffuser pump-down effect and pressure recovery by inducing secondary longitudinal vortices along the inner strakes. However, the novel concept as investigated and presented in this study involves altering the diffuser pressure recovery by inducing a second pressure drop and recovery region downstream of the peak drop at the diffuser inlet and close to the diffuser exit. Notably the inclusion of the inner strakes (by Jowsey, 2013) enhanced suction closer to the diffuser inlet and thus enhanced the diffuser pump-down effect. In the case of the second-stage pressure drop and recovery implemented in this present research work, the centreline surface pressures for the five ride heights that represent the different flow regimes indicate that the suction peak measurement at the diffuser inlet for the baseline diffuser case is similar to those of the diffuser with the various passive methods. In addition, the pressure distribution upstream from the location of the passive devices did not significantly change from between the various diffusers. This is because the passive methods have no control on the diffuser flow upstream of their location near the diffuser exit.

The downforce increments measured across the five ride heights (h/d = 0.764, 0.318, 0.191, 0.153, and 0.064) decreased respectively with reducing ride height: +4.9%, +0.7%, +2.0%, +0.8%, and +0.56% with the convex bump; +12.0%, +3.1%, +3.0%, +2.4%, and +1.9% with the wing; and +11.6%, +2.9%, +3.6%, +3.7%, and +0.9% with both the bump and wing. As indicated earlier in this chapter, the reducing trend is due to the increasing size of the longitudinal vortical structures which induce flow recirculation on the suction surfaces of the passive devices. Hence, in the case of the diffuser with the inverted wing or the diffuser with both the bump and wing, the use of a double element in place of the single element wing as employed in this study, can reduce the flow recirculation. The addition of a second element allows for the higher pressure from the pressure surface (top surface) of the main element to

escape to the suction surface (lower surface) through the slot gap between the main and flap elements. Therefore, the flow recirculation can be reduced because the flow velocity on the suction surfaces of both elements increases and boundary layer separation reduces. Consequently (as described by Smith, 1975 and studied as 3—D flow by Zhang and Zerihan, 2003 as the circulation effect of a double element wing), the circulation of the flap element increases the circulation of the main element thus enhancing the aerodynamic performance of the double element wing as a passive device. However, in terms of the additional drag induced by the passive devices across the five ride heights ($h/d = 0.764,\ 0.318,\ 0.191,\ 0.153$ and 0.064), the additional drag measured are respectively: +3.5%, +1.4%, +1.8%, +1.3%, and +0.5% with the convex bump; +11.0%, +4.3%, +1.9%, +2.6%, and +0.3% with the wing; and +11.3%, +4.9%, +2.8%, +4.1%, and −0.2% with both the bump and wing. The additional drag is due to the profile drag of the bump and wing. Nonetheless, the marginal increase in drag may have been kept low due to the drop in the skin friction (component of the profile drag) at the latter part of the suction surfaces of the bump and wing as the flow gradually decelerates and pressure recovers towards the diffuser exit.

6.6 Summary

In this chapter, the use of passive flow control devices (convex bump and an inverted wing separately and in combination) to enhance the downforce generated by the ground effect diffuser has been investigated. The aerodynamic principle governing the operation of the passive devices involves the inducement of a second pressure drop and recovery downstream of the suction peak of the diffuser inlet. The convex bump surface and suction surface of the inverted wing induce the second-stage pressure drop and recovery through their surface curvature, which in turn induces curvature to the flow.

In comparison with the plane diffuser (baseline), the diffuser with the passive devices generally produced more downforce across the four distinct

flow regimes established for the diffuser flow. It was observed that in the maximum downforce diffuser flow regime, the diffuser with both the convex bump and inverted wing produced the most downforce as a result of the combined suction generated by the suction surfaces of the bump and wing. However, it was also observed that with decreasing ride height the downforce increments reduce with the various passive devices. This was attributed in flow regimes A and B to the increasing flow recirculation on both sides of the suction surfaces of the passive devices as a result of the increasing size of the longitudinal vortices. In flow regimes C and D, the decrease in downforce increments was as a result of the flow recirculation and reversed flow induced by the breakdown of one of the longitudinal vortex pair.

In the near-wake of the diffuser bluff body at the maximum-force flow regime, higher flow velocities appear further downstream with the use of the passive devices relative to the plane diffuser. Therefore there is a net deficit in near-wake flow velocity and turbulence between the plane diffuser and the diffuser with passive devices and as a result the passive devices increase net-circulation around the bluff body. However, flow structures in the diffuser bluff body near-wake appear similar for all diffusers and the lower near-wake vortex is larger at either side of the diffusers as a result of the strong upwash of the diffuser longitudinal vortex pair. Finally, the drag increments with the use of the passive devices across the diffuser flow regimes were discovered to be as a result of the profile drag induced by the passive device. The skin friction component of the drag was found to increase at the early part of the diffuser where the longitudinal vortex is strong. At the location of the passive devices in the diffuser, skin friction drag increased at the early part of the location due to flow acceleration and decreased at the latter part due flow deceleration as static pressure recovery occurs.

Chapter 7

Conclusions and Future Work Recommendations

In this final chapter, the various findings that cover the objectives of this research study are summarised. The chapter then ends by proffering ideas and recommendations on future research avenues that could further provide clarity on the flow physics and enhance the aerodynamic performance of the ground-effect diffuser.

7.1 Conclusions

Experimental and parallel numerical investigations have been conducted on a bluff body diffuser, firstly to confirm findings on the diffuser flow from previous studies, secondly to provide further understanding on the diffuser flow physics, and thirdly to study potential means of augmenting the diffuser aerodynamic performance. This research confirmed the following from previous studies.

- The downforce generated by a ground-effect diffuser is dictated by the peak suction at the diffuser inlet and the pressure-recovery downstream towards the diffuser exit.
- The downforce and drag curves of the diffuser comprises of four distinct 3−D flow regimes A to D.
- The type A (force-enhancement) diffuser flow regime, which occurs at higher ride heights, is a reasonably symmetrical flow made up of two strong counter-rotating longitudinal vortices, which induce lower static

pressures along the sides of the diffuser. The vortices increase in size with reducing ride height and the velocity at the vortex core is above freestream but gradually reduces towards the diffuser exit.

- The type B (maximum-force) flow is as a result of further decrease in ride height, which induces a change in the gradient of the force curves and ends at a maximum downforce and drag. The diffuser flow remains reasonably symmetrical with enhanced low-pressure vortex cores inducing lower static pressures relative to the type A regime. The diffuser flow is under a severe adverse pressure gradient, which induces a separation bubble near the diffuser inlet and along the lengthwise centre of the diffuser ramp surface. However, the vorticity and core velocity of the vortices are strong at the early part of the diffuser but gradually become weak and unsteady as the cores of the vortices grow in size and become diffused at the later part of the diffuser thus inducing flow turbulence towards the diffuser exit. The behaviour is as a result of vortex breakdown occurring at the latter part of the diffuser.

- The type C (force-reduction) flow regime occurs below the ride heights of the type B regime and is marked by a significant gradient drop on the force curves. This is due to the complete breakdown of one of the longitudinal vortices within the diffuser thus the diffuser flow becomes asymmetric. The surviving vortex on one side of the diffuser is weak, unsteady and close to the diffuser inlet, while on the other side the flow is dominated by flow separation and reversal. The merging of boundary layers at the diffuser inlet and on the moving ground does not occur, however the flow entering the diffuser appeared to be boundary-layer dominant (blockage) thus inducing the complete vortex breakdown on one of the vortices.

- The type D (low-force) flow regime occurs at ride heights lower than those of type C regime. Similarly, the flow remains asymmetric with a

weak surviving vortex on one side of the diffuser. However, on the other side dominated by flow reversal, there is flow recirculation with a core that stretches diagonally across the diffuser ramp.

This research also revealed the following new findings.

- The onset of the complete breakdown of one of the vortices in the type C flow regime begins in the type B regime and the choice of vortex upon which the breakdown phenomenon occurs does not appear to happen at random as indicated in previous studies. Boundary layer velocity and surface pressure measurements at maximum-force ride height indicated that the vortex along the side of the diffuser with lower boundary layer velocities and lower suction is the particular vortex that undergoes the vortex breakdown in the type C regime.

- Previous studies have indicated the presence of transverse upper and lower vortices in the diffuser near-wake induced by the flow off the top of the bluff body and the upwash from the diffuser exit respectively. However, on the side of vortex breakdown in the type C regime, the diffuser near-wake is dominated by a single low-velocity vortex flow travelling *into* the diffuser exit. In the symmetrical type B regime, the near-wake flow on both sides of the diffuser comprises of a low-velocity flow of the upper and lower vortices above the diffuser exit, a high-velocity flow at the upper part of the diffuser exit, and a low-velocity flow at the lower half of the diffuser exit. Also in the type B regime, the diffusion of the longitudinal vortices at the diffuser exit generates high turbulence intensity in the bluff body near-wake.

- The inducement of a second-stage pressure drop and recovery near the diffuser exit using the pressure gradient generated by the curved surfaces of a convex bump or the suction side of an inverted wing inside the diffuser flow channel leads to an increase in downforce across the

diffuser flow regimes. However, the application of the bump and/or wing did not delay the emergence of the type C flow regime (force-reduction) as ride height was reduced because it had no control over the vortex breakdown at the diffuser inlet associated with the type C flow regime.

- The aerodynamic performance of the bump is dictated by its length and thickness. Aerodynamically efficient (lift-to-drag ratio) for length and thickness were respectively found to be within 25% to 30% of diffuser ramp length and ~ 20% of the diffuser ramp boundary layer thickness.

- The aerodynamic performance of the inverted wing is dictated by its angle of attack, chord length and the gap between the pressure surface of the wing and the flat diffuser ramp surface or the convex bump surface. Optimal aerodynamic performance (lift-to-drag ratio) was found at an angle of attack of the wing that is equal to the diffuser angle and with a chord length within ~ 25% of the diffuser ramp length. Significant aerodynamic efficiency (lift-to-drag ratio) was also found with a gap between diffuser ramp and wing that is about ~ 30% and ~ 50% of diffuser ramp boundary layer thickness for the diffuser with the wing and bump, and the diffuser with the wing respectively.

- With decreasing ride height, the additional downforce generated by the bump and wing reduces. This was found to be due to the rotating vortical structures of the vortex pair (in type A and B regimes) growing in size and in turn inducing flow recirculation regions on both sides of the bump and wing. However, in the type C and D regimes this was due to the flow recirculation on about half of the diffuser area as a result of the vortex breakdown on one side of the diffuser.

- The skin friction drag distribution on the diffuser ramp surface was found to be at its peak at the diffuser inlet due to the inlet peak velocity and at the early part of either side of the diffuser where the longitudinal vortices are strong; skin friction drag is also high as a result of the

thinning of boundary layer by the vortices. The convex bump and inverted wing as passive flow-control devices also induced additional drag (profile drag and lift-induced drag). The skin friction drag component distribution along the diffuser ramp surface where the devices are located indicated that frictional drag gradually increased at the early part of the location of the devices as flow accelerates but gradually reduced at the later part as the flow decelerates towards the diffuser exit.

- Streamwise velocity measurements indicate that the passive flow control methods (relative to the plane diffuser as the baseline case) enhanced the near-wake diffuser exit flow velocity and also the net counter-clockwise circulation around the bluff body.

- Circulation levels on the $x-y$ centreline plane indicated that the diffuser with the convex bump has the most significant effect on the $x-y$ wake circulation. However, the relative changes in this circulation plane with respect to the baseline case, were an order of magnitude greater than the overall changes in body lift and drag. Therefore it must be concluded that the $y-z$ spanwise plane circulation dominates the bluff body lift and drag characteristics.

- Computational investigations using the combined approach of steady RANS turbulence models with time-averaged transient URANS and advanced IDDES methodologies generally agreed with experimental data, however, there were degrees of deviation with respect to under- and overpredictions of forces and surface pressures. With reducing ride height, the percentage deviation in force measurements (particularly drag) significantly increased as a result of the inadequacies in modeling the complex flow physics in the diffuser body near-wake. In terms of the percentage deviations for surface pressures, this is largely due to the resolution of the computational grid in efficiently modelling the

displacement thickness of the boundary layer. However, the use of the transitional turbulence models in transient state (URANS or IDDES) adequately modelled the laminar separation bubble where the nose section merges with the flat underbody section of the body. This was paramount in capturing the downstream flow features on the diffuser ramp surface.

7.2 Recommendations for Future Work

The research study presented, although extensive still leaves room for further exploration in extending the knowledge of diffuser flow physics and the investigation of other efficient means of enhancing the aerodynamic performance of the diffuser. The following research ideas are recommended.

- The significant reduction in downforce associated with the type C regime is as a result of the complete bursting of one of the longitudinal vortex pair within the diffuser. Hence, to significantly enhance the diffuser performance flow control measures can be implemented close to the diffuser inlet on the side of the diffuser where the vortex breakdown phenomenon occurs. Active flow control systems that involve blowing or suction actions that respectively energise or extract the slow-moving boundary layer should be investigated.

- In the passive methods investigated in this study that involved the use of the single-element inverted wing, recirculation region(s) were found to be induced on one or both sides of the wing suction surface by the diffusing longitudinal vortices or the breakdown of one of the vortices. As a means of mitigating this flow disturbance which in turn adversely affects the additional downforce generated, the use of a double-element wing to induce slat and dumping effects and enhance circulation can be explored. Another concept worth investigating is the use of strakes (or vortex generators) on the suction surfaces of the wing and bump to

generate strong secondary longitudinal vortices that can further energise the flow and consequently suction, which can lead to further increases in downforce. Other methods that could also be explored is the trapping of a spanwise vortex close to the diffuser inlet using a cavity or groove across the diffuser span, or employing a convex bump along the span of the diffuser inlet to further increase flow velocity at the inlet. The trapped vortex rotating in the opposite direction to the streamwise diffuser flow, can enhance downforce by accelerating the flow through the diffuser inlet although an active suction system may be needed to maintain vortex stability and to keep the vortex within the cavity

- It was deduced that the dominant flow features that significantly dictate downforce and drag levels reside in the spanwise ($y-z$) plane. Therefore an integration of circulation in the spanwise ($y-z$) plane should be done to examine if the flow features reported in this present study or in previous studies induce significant levels of circulation that dictate the aerodynamic performance of the diffuser. If such an investigation supports this inference then any geometric changes to the diffuser (passive flow control) or active flow control systems must be setup to influence the spanwise ($y-z$) plane features if substantial increases in downforce are desired.

- This study generally focused on a diffuser in isolation. However on a racing car, flow disturbances due to the presence of external geometries such as near wake and squirt from the dynamic deformation of the rear tyres (under loading) interfere with the diffuser flow. Future studies can focus on understanding these flow interactions and their impact on the diffuser aerodynamic performance.

- The use of a high-resolution unstructured hybrid grid (tetrahedral and prismatic cells) with transient URANS and IDDES modeling approaches although generally capturing the diffuser flow physics, showed

deviations in force and surface pressure quantities between computational and experimental data. Thus, a higher resolution structured grid with the use of advanced LES methodologies should be explored to further reduce the deviations and improve correlation with experimental data.

References

Abernethy, R. B., Benedict, R. P. and Dowdell, R. B. (1985). ASME Measurement Uncertainty. ASME Journal of Fluids Engineering. Vol. 107, No. 2, pp. 161–164.

Agathangelou, B. and Gascoyne, M. (1998). Aerodynamic Considerations of a Formula 1 Racing Car, SAE Technical Report Paper 980399.

Ahmed, S., Ramm, G. and Faltin, G. (1984). Some Salient Features of the Time-Averaged Ground Vehicle Wake. SAE Technical Paper 840300, Detroit, Michigan, pp. 1–34.

Anderson, J. D. (2000). A History of Aerodynamics. Cambridge University Press, UK, Chap. 7, pp. 316–317.

ANSYS ICEM CFD (2016). Version 17.2 User Guide, www.ansys.com.

ANSYS FLUENT (2016). Version 17.2 User Guide, www.ansys.com.

Asselin, M. (1997). An Introduction to Aircraft Performance. AIAA Educational Series, American Institute of Aeronautics and Astronautics, Reston, VA, USA, Chap. 6, pp. 141–149.

Barlow, J. B., Rae, W. H. and Pope, A. (1999). Low-Speed Wind Tunnel Testing, 3rd ed., Wiley, New York, pp. 176,

Barnard, R. H. (2001). Road Vehicle Aerodynamic Design: An Introduction. MechAero Publishing, St Albans, UK, Chap. 6, pp. 140.

Beauvais, R. (1994). Laser-Doppler Velocimetry (LDV). in Mayinger, F. (ed.) Optical Measurements: Techniques and Applications. 1st Edition, Springer Berlin Heidelberg, pp 179–193.

Benedict, L. and Gould, R. (1996). Towards Better Uncertainty Estimates for Turbulence Statistics. Experimental Thermal and Fluid Science, Vol. 22, No. 2, pp. 129–136.

Bradshaw, P. (1973). Effects of Streamline Curvature on Turbulent Flow. AGARDograph AG–169.

Breslouer, O. and George, A. (2008). Exploratory Experimental Studies of Forces and Flow Structure on a Bluff Body with Variable Diffuser and Wheel Configurations. SAE Technical Paper 2008–01–0326.

Bruun, H. H. (1995) Hot-Wire Anemometry: Principles and Signal Analysis. Oxford University Press, Oxford, Chap 12, pp. 405–445.

Buchave, P., George Jr, W. K. and Lumley, J. L. (1979). The Measurement of Turbulence with the Laser Doppler Anemometer. Annual Review in Fluid Mechanics, Vol. 11, pp. 443–503.

Chometon, F. and Gilliéron, P. A Survey of Improved Techniques for Analysis of 3D Separated Flows in Automotive Aerodynamics. SAE Technical Report Paper 96–0680.

Cooper, K. R., Bertenyi, T., Dutil, G., Syms, J. and Sovran, G. (1998). The Aerodynamic Performance of Automotive Underbody Diffusers. SAE Technical Report Paper 98–0030.

Cooper, K. R., Sovran, G. and Syms, J. (2000). Selecting Automotive Diffusers to Maximise Underbody Downforce. SAE Technical Report Paper 2000–01–0354.

Correia, J. (2015). The Influence of External Disturbances on the Aerodynamic Performance of a Wing in Ground Effect. Ph.D. thesis, Cranfield University, UK.

Crowther, W. J., Jabbal, M. and Liddle, S. C. (2010). Flow Control Fallacies: a Review of Common Pitfalls in Flow Control Research. IMechE Part G: Journal of Aerospace Engineering, Vol. 225, No. 1, pp. 1–11.

Dexter, P. C. (1982). An Experimental Investigation of the Aerodynamics of Slender Axisymmetric Bodies at High Angles of Incidence. Ph.D. thesis, University of Bristol.

Dixon, S. L. (1998). Fluid Mechanics and Thermodynamics of Turbomachinery. 5th ed., Buterworth-Heinemann Publishers, Oxford, UK, Chap. 2, pp. 44–54.

Dominy, R. G. (1992). Aerodynamics of Grand Prix Cars. Proceedings of the Institute of Mechanical Engineers, Part D: Journal of Automobile Engineering, Vol. 206, No. 4, pp. 267–274.

Donelli, R. S., De Gregorio, F. and Iannelli, P. (2010). Flow Separation Control by Trapped Vortex. AIAA 2010–1409, 48th AIAA Aerospace Sciences Meeting, AIAA, Reston, VA, USA.

Dring, R. P. (1982). Sizing Criteria for Laser Anemometry Particles. ASME Journal of Fluids Engineering, Vol. 104 pp.15–17.

Duncan, W. J., Thom, A. and Young, A. (1970). Mechanics of Fluids. 2nd ed., Edward Arnold Publishers, London, UK, Chap. 7, pp. 413–414

Durrani, T. S. and Greated, C. A. (1977). Laser Systems in Flow Measurement. 1st ed., Springer, Plenum Press, New York.

Eder, A., Durst, B. and Jordan, M. (2001). Laser-Doppler Velocimetry — Principle and Application to Turbulence Measurements. In Mayinger, F., Feldmann, O. (ed.) Optical Measurements: Techniques and Applications, 1st ed., Springer Berlin Heidelberg, pp. 179–193.

Edstrand, A. M., Davis, T. B., Schmid, P. J., Taira, K. and Cattafesta, L. N. (2016). On the Mechanism of Trailing Vortex Wandering. Journal of Fluid Mechanics, Vol. 801.

ESDU. (2007). 76027 – Introduction to Design and Performance Data for Diffusers. ESDU International Ltd, Engineering Sciences Data Unit, London, UK.

Freund, J. B. and Mungalt, M. G. (1994). Drag and Wake Modification of Axisymmetric Bluff Bodies Using Coandă Blowing. Journal of Aircraft, Vo. 31, No. 3. pp. 572–578.

Gad-el-Hak, M. (2000). Flow Control: Passive, Active, and Reactive Flow Management. Cambridge University Press, Cambridge, UK, pp. 112, 151–152, 163, 176.

Gad-el-Hak, M. and Bushnell, D. M. (1991a). Status and Outlook of Flow Separation Control. AIAA 29th Aerospace Sciences Meeting, Reno, NV, U.S.A.

Gad-el-Hak, M. and Bushnell, D. M. (1991b). Separation Control: Review. ASME Journal of Fluids Engineering, Vol. 113 No. 1, pp. 5–30.

Gad-el-Hak, M., Pollard, A. and Bonnet, J-P. (eds.), (1998). Flow Control Fundamentals and Practices. Lecture Notes in Physics Monographs, Springer-Verlag Berlin Heidelberg, Chap. 1–7.

Garcia, D. L. and Katz, J. (2003). Trapped Vortex in Ground Effect. AIAA Journal, Vol. 41, No. 4, pp. 674–678.

George, A. R. (1981). Aerodynamic Effects of Shape, Camber, Pitch on Ground-vehicle Bodies. ASME Journal of Fluids Engineering, Vol. 103, No. 4, pp. 631–637.

George, A. R. and Donis, J. (1983). Flow Patterns, Pressures and Forces in the Underside of Idealised Ground Effect Vehicles. Proceedings of the ASME Fluids Engineering Division Symposium on Aerodynamics of Transportation II, Vol. 7, pp. 69–79.

Genua, E. (2009). A CFD Investigation into Ground Effect Aerodynamics. Master's thesis, Delft University of Technology.

Gibson, M. M., Verriopoulos, C. A. and Vlachos, N. S. (1984). Turbulent Boundary Layer on a Mildly Curved Convex Surface Part 1: Mean flow and Turbulence Measurements, Experiments in Fluids, Vol. 2, No. 1, pp. 17–24.

Gursul, I. and Xie, W. (2000). Origin of Vortex Wandering over Delta Wings, Journal of Aircraft, Vol. 37, No. 2, pp. 348–350.

Green, S. I. (1995). Fluid Vortices. Kluwer Academic Publishers, Dordrecht, Netherlands, Chap. 1, pp. 1–34.

Hall, M. G. (1972). Vortex Breakdown. Annual Review of Fluid Mechanics, Vol. 4, pp. 195–218.

Haller, G. (2005). An Objective Definition of a Vortex. Journal of Fluid Mechanics, Vol. 525, pp. 1–26.

Houghton, E. L. and Carpenter, P. W. (2003). Aerodynamics for Engineering Students. 5th ed., Buterworth-Heinemann Publishers, Oxford, UK, Chap. 8, pp. 507–512.

Howard, F. G. and Goodman, L. W. (1985). Axisymmetric Bluff-Body Drag Reduction Through Geometrical Modification. AIAA Journal of Aircraft, Vol. 22, No. 6, pp. 516–522.

Howell, J. P. (1994). The Influence of Ground Simulation on the Aerodynamics of Simple Car Shapes with an Underfloor Diffuser. In Proceedings of the Road Vehicle Aerodynamics Conference, Loughborough, UK.

Hucho, W-H. (1998). Aerodynamics of Road Vehicles. 4th Rev. ed., SAE International, Society of Automotive Engineers, Washington, DC, USA, Chap. 8, pp. 392–395.

Jasinski, W. J. and Selig, M. S. (1999). Experimental Study of Open-Wheel Race-Car Front Wings," SAE Technical Paper 983042.

Jeong, J. and Hussain, F. (1995). On the Identification of a Vortex. Journal of Fluid Mechanics, Vol. 285, pp. 69–94.

Johari, H. and Rixon, G. S. (2003). Effects of Pulsing on a Vortex Generator Jet. AIAA Journal, Vol. 41, No. 12, pp. 2309–2315.

Johnston, J. and Nishi, M. (1989). Vortex Generator Jets–A Means for Passive and Active Control of Boundary Layer Separation. AIAA 27th Aerospace Sciences Meeting, Reno, NV, USA.

Jowsey, L. and Passmore, M. (2010). Experimental Study of Multiple-channel Automotive Underbody Diffusers. Proceedings of the Institute of Mechanical Engineers, Part D: Journal of Automobile Engineering, Vol. 224, No. 7, pp. 865–879.

Jowsey, L. (2013). An Experimental Study of Automotive Underbody Diffusers. Ph.D. thesis, Loughborough University, UK.

Katz, J. (2006a). Aerodynamics of Race Cars. Annual Review of Fluid Mechanics, Vol. 38, 27– 63.

Katz, J. (2006b). New Directions in Race Car Aerodynamics. 2nd Rev. ed., Bentley Publishers, Cambridge, Massachusetts, Chap. 6. pp. 221–222.

Katz, J. and Morey, F. (2008). Aerodynamics of Large-Scale Vortex Generator in Ground Effect. ASME Journal of Fluids Engineering, Vol. 130, No. 7, 071101.

Klebanoff, P. S. (1971). Effects of Freestream Turbulence on a Laminar Boundary Layer. Bull. American Physical Society, Vol. 10, No. 11, p. 1323.

Kline, S. J., Abbott, D. E. and Fox, R. W. (1959). Optimum Design of Straight-walled Diffusers. ASME Journal of Basic Engineering, Vol. 81, pp. 321–331.

Knowles, K., Donogue, D. T. and Finnis, M. V. (1994). A Study of Wings in Ground Effect. RAeS Vehicle Aerodynamics Conference, Loughborough, UK.

Knowles, K. and Finnis, M. V. (1998). Development of a New Open-Jet Wind Tunnel and Rolling Road Facility. In: 2nd MIRA International Conference on Vehicle Aerodynamics, Coventry, UK.

Knowles, R. (2005). Monoposto Racecar Wheel Aerodynamics: Investigation of Near-wake Structure and Support-sting Interference. PhD thesis, Cranfield University

Krajnovic, S. and Davidson, L. (2001). Large-eddy Simulation of the Flow Around a Ground Vehicle Body. SAE World Congress Paper 2001-01-0702, Detroit, Michigan, USA.

Kuya, Y., Takeda, K., Zhang, X., Beeton, S. and Pandaleon, T. (2009). Flow Separation Control on a Race Car Wing with Vortex Generators in Ground Effect. ASME Journal of Fluids Engineering Vol. 131, No. 12, 121102.

Lambourne, N. C. and Bryer, D. W. (1962). The Bursting of Leading-Edge Vortices– Some Observations and Discussions of the Phenomenon. Ministry of Aviation, Aeronautical Research Council Reports and Memoranda, 3282.

Langtry, R. B. and Menter, F. R. (2009). Correlation-Based Transition Modeling for Unstructured Parallelized Computational Fluid Dynamics Codes. AIAA Journal, Vol 47, No. 12, pp. 2894–2906.

Launder, B. E. and Spalding, D. B. (1974). The Numerical Computation of Turbulent Flows. Computer Methods in Applied Mechanics and Engineering, Vol. 3, pp. 269–289.

Layton, W. J. (2016). Energy Dissipation in the Smagorinsky Model of Turbulence. Applied Mathematics Letters, Vol 59, pp. 56–59.

Lévêque, E., Toschi, F. and Bertoglio, J. P. (2007). Shear-improved Smagorinsky model for Large-eddy Simulation of Wall-bounded Turbulent Flows. Journal of Fluid Mechanics, Vol. 570, pp. 491–502.

Leibovich, S. (1978). The Structure of Vortex Breakdown. Annual Review of Fluid Mechanics, Vol. 10, pp. 221–246.

Lugt, H. J. (1979). The Dilemma of Defining a Vortex. In Recent Developments in Theoretical and Experimental Fluid Mechanics. (eds. Muller, U., Riesner, K. G., and Schmidt, B.), pp. 309–321.

Lupi, F., Borri, C., Facchini, L., Niemann, H.-J. and Peil, U. (2013). A New Type of Bistable Flow around Circular Cylinders with Spanwise Stiffening Rings. Vol. 123, pp. 281–290.

Marklund, J. and Lofdahl, L. (2009). Drag Reduction of a Simple Bluff Body by Changing the Rear End and Use of the Ground Effect. FEDSM2009-78502, Proceedings of ASME Fluids Engineering Division Summer Meeting, Colorado, USA, Vol. 2, pp. 291–296.

Marklund, J. (2013). Under-body and Diffuser Flows of Passenger Vehicles. Ph.D. thesis, Chalmers University of Technology, Sweden.

Massey, B. and Ward-Smith, J. (2012). Mechanics of Fluids. 9th Rev. ed., Taylor & Francis Publishers, Oxford, UK, Chap. 7, pp. 264–265.

Maskell, E. C. (1963). A Theory of the Blockage Effects on Bluff Bodies and Stalled Wings in a Closed Wind Tunnel. Aeronautical Research Council Reports and Memoranda, (ARC R&M No. 3400), London.

McKeon, B. et al. (2007). Velocity, Vorticity and Mach Number. In: Tropea C., Yarin A., Foss J. F. (eds.) Springer Handbook of Experimental Fluid Mechanics, Springer-Verlag Berlin Heidelberg, Chap. 5, pp. 296–309.

Menter, F. R. (1994). Two-Equation Eddy-Viscosity Turbulence Models for Engineering Applications. AIAA Journal, Vol. 32, No. 8, pp. 1598–1605.

Menter, F. R., Langtry, R. and Völker, S. (2006). Transition Modelling for General Purpose CFD Codes. Flow, Turbulence and Combustion, Vol. 77, pp. 277–303.

Mittal, S. and Saxena, P. (2002). Prediction of Hysteresis Associated with Static Stall of an Airfoil. AIAA Journal, Vol. 38, No. 5, pp. 933–935.

Moffat, R. J. (1988). Describing the Uncertainties in Experimental Results. Experimental Thermal and Fluid Science. Vol. 1, No. 1, pp 3–17.

Modi V. J., Mokhtarian, F., Fernando, M. and Yokomizo T. (1988). Fluid Dynamics of Airfoils with Moving Surface Boundary Layer Control. AIAA Journal of Aircraft, Vol. 25, No. 2, pp. 163–169.

Modi V. J., Mokhtarian F., Fernando M. and Yokomizo T. (1990). Drag Reduction of Bluff Bodies Through Moving Surface Boundary Layer Control. AIAA 28th Aerospace Sciences Meeting, Reno, NV, U.S.A.

Muck, K. C., Hoffmann, P. H. and Bradshaw, P. (1985). The Effect of Convex Surface Curvature on Turbulent Boundary Layers. Journal of Fluid Mechanics, Vol. 161, pp. 347–369.

Newman, B. G. (1961). The Deflexion of Plane Jets by Adjacent Boundaries-Coandă Effect. Boundary Layer and Flow Control, edited by Lachmann, G. V., vol. 1, Pergamon Press, Oxford, pp. 232–264.

Nobach, H. (2000). A Global Concept of Autocorrelation and Power Spectral Density Estimation from LDA Data sets. In: 10th International Symposium on Applications of Laser Techniques to Fluid Mechanics, Instituto Superior Técnico, Lisbon, Portugal.

Palin, R., Johnston, V., Johnson, S., D'Hooge, A., Duncan, B. and Gargoloff, J. I. (2012). The Aerodynamic Development of the Tesla Model S – Part 1 Overview. SAE International, 2012-01-0177.

Pegrum, J. M. (2006). Experimental Study of the Vortex System Generated by a Formula 1 Front Wing. Ph.D. thesis, Imperial College London, UK.

Piomelli, U. (1999). Large-eddy Simulation: Achievements and Challenges. Progress in Aerospace Sciences, Vol. 35, No. 4, pp. 335–362.

Prince, S. A., Khodagolian, V., Singh, C. and Kokkalis, T. (2009). Aerodynamic Stall Suppression on Airfoil Sections using Passive Air-Jet Vortex Generators. AIAA Journal, Vol. 47, No. 9, pp. 2232–2242.

Puglisevich, L. S. and Page, G. (2011). Large Eddy Simulation of the Flow Around a Diffuser-Equipped Bluff Body in Ground Effect. IMECE2011–62673, Proceedings of ASME International Mechanical Engineering Congress & Exposition, pp. 313–322.

Puglisevich, L. S. (2013). Large Eddy Simulation for Automotive Vortical Flows in Ground Effect. Ph.D. thesis, Loughborough University, UK.

Ranzenbach, R. and Barlow, J. B. (1994). Two-Dimensional Airfoil in Ground Effect, An Experimental and Computational Study. SAE Technical Paper 94–2509.

Ranzenbach, R. and Barlow, J. B. (1995). Cambered Airfoil in Ground Effect – Wind Tunnel and Road Conditions. AIAA Paper 95-1909.

Ranzenbach, R. and Barlow, J. B. (1996). Cambered Airfoil in Ground Effect: An Experimental and Computational Study. SAE Technical Paper 96–0909.

Ranzenbach, R. and Barlow, J. B. (1997). Multi-element Airfoil in Ground Effect - an Experimental and Computational Study. AIAA Paper 97–2238.

Rendle, S. (2011). Redbull Racing F1 Car 2010 (RB6) – Owner's Workshop Manual. Haynes Publishing, Somerset, UK, pp. 33, 47–49.

Ringleb, F. O. (1961). Separation Control by Trapped Vortices. Boundary Layer and Flow Control, Lachmann, G. V. (ed.), Pergamon, Oxford, England, UK, Vol. 1, pp. 265–294.

Ruhrmann, A. and Zhang, X. (2003). Influence of Diffuser Angle on a Bluff Body in Ground Effect", ASME, Journal of Fluids Engineering, Vol. 125, No. 2, pp. 332–338

Romano, G. et al. (2007). Measurements of Turbulent Flows. In: Tropea, C., Yarin, A., Foss, J. F. (eds.) Springer Handbook of Experimental Fluid Mechanics, Springer-Verlag Berlin Heidelberg, Chap. 10, pp. 787.

Rossow, V. J. (1992). Two-fence Concept for Efficient Trapping of Vortices on Airfoils. AIAA Journal of Aircraft, Vol. 29, No. 5, pp. 516–522.

Rossow, V. J. (1994). Aerodynamics of Airfoils with Vortex Trapped by Two Spanwise Fences. AIAA Journal of Aircraft, Vol. 31, No. 1, pp. 847–855.

Saddington, A. J., Knowles, R. D. and Knowles, K. (2007). Laser Doppler Anemometry Measurements in the Near-wake of an Isolated Formula One Wheel. Experiments in Fluids, Vol. 42, pp. 671–681.

Schewe, G. (1983). On the Forces Acting on a Circular Cylinder in Cross-flow from Subcritical up to Transcritical Reynolds Numbers. Journal Fluid Mechanics, 133, pp. 265–285.

Schlichting, H. (1999). Boundary-Layer Theory. 8th ed., Springer-Verlag.

Scholz, P., Casper, M., Ortmanns, J., Kähler, C. J. and Radespiel, R. (2008). Leading-Edge Separation Control by Means of Pulsed Vortex Generator Jets. AIAA Journal, Vol.46, No. 4, pp. 837–846.

Senior, A. E. and Zhang, X. (2000a). An Experimental Study of a Diffuser in Ground Effect. AIAA Paper 2000–0118, 38th Aerospace Sciences Meeting and Exhibit, Reno, NV, USA.

Senior, A. E. and Zhang, X. (2000b). The Force and Pressure of a Diffuser-Equipped Bluff Body in Ground Effect. ASME Journal of Fluids Engineering, Vol. 123, No. 1, pp. 105–111.

Senior, A. (2002). The Aerodynamics of a Diffuser Equipped Bluff Body in Ground Effect. Ph.D. thesis, University of Southampton, UK.

Shih, T. H., Liou, W. W., Shabbir, A., Yang, Z. and Zhu, J. (1994). New $k-\varepsilon$ Eddy Viscosity Model for High Reynolds Number Turbulent Flows-model Development and Validation. NASA Technical Memorandum 106721.

Shur, M. L., Spalart, P. R., Strelets, M. Kh. and Travin, A. (2008). A Hybrid RANS-LES Model with Delayed DES and Wall-modelled LES Capabilities. International Journal of Heat and Fluid Flow, Vol. 29, pp. 1638–1649.

Smagorinsky, J. (1963). General Circulation Experiments with the Primitive Equations. Part I: The Basic Experiment. Monthly Weather Review, Vol. 91, No. 3, pp. 99–164.

Smith, A. M. O. (1975). High-Lift Aerodynamics. Journal of Aircraft, Vol. 12, No. 6, pp. 501–530.

So, R. M. C. and Mellor, G. L. (1973). Experiment on Convex Curvature Effects in Turbulent Boundary Layers. Journal of Fluid Mechanics, Vol. 60, No. 1, pp. 43–62.

Soso, M. D. and Wilson, P. A. (2008). The Influence of an Upstream Diffuser on a Downstream Wing in Ground Effect. Proceedings of the Institute of Mechanical Engineers, Part D: Journal of Automobile Engineering, Vol. 222, No. 4, pp. 551–563.

Sovran, G. (1994). The Kinematic and Fluid-Mechanic Boundary Conditions in Underbody Flow Simulation. Proceedings of the CNR-Pininfarina Workshop on Wind Tunnel Simulation of Ground Effect, Turin, Italy.

Sovran, G. and Klomp, E. D., (1967). Experimentally Determined Optimum Geometries for Rectilinear Diffusers with Rectangular, Conical or Annular Cross-section. Fluid Mechanics of Internal Flow, Sovran, G. (ed), Elsevier, Amsterdam, pp. 270–319.

Spalart, P. R., Jou, W-H., Strelets, M., and Allmaras, S. R. (1997). Comments on the Feasibility of LES for Wings and on a Hybrid RANS/LES Approach. Proceedings of 1st AFOSR International Conference on DNS/LES. Louisiana Tech University. pp.137–147.

Spalart, P. R. (2000). Strategies for Turbulence Modelling and Simulations, International Journal of Heat and Fluid Flow, Vol. 21, pp 252–263.

Spalart, P. R., Deck, S., Shur, M. L., Squires, K. D., Strelets, M. K. and Travin, A. (2006). A New Version of Detached-eddy Simulation, Resistant to Ambiguous Grid Densities. Theoretical and Computational Fluid Dynamics, Vol. 20, No. 3, pp. 181–195.

Spalart, P. R. (2009). Detached-eddy Simulation. Annual Review of Fluid Mechanics, Vol. 41, pp. 181–202.

Spalart, P. R. (2001). Young-Person's Guide to Detached-Eddy Simulation Grids. NASA Langley Technical Report, NASA/CR–2001–211032.

Thompson, J. F., Soni, B. K. and Weatherill, N. P. (eds.) (1999). Handbook of Grid Generation, Boca Raton, Florida: CRC Press, pp 25–2; 32–5.

Tipler, J. (2009). Lotus 78 and 79: The Ground-Effect Cars. The Crowood Press Ltd., Wiltshire, UK.

Toet, W. (2013). Aerodynamics and Aerodynamic Research in Formula 1. The Aeronautical Journal, Vol. No. 117, No. 1187, pp. 1–25.

Tortosa, N. and Karbon, K. (2011). Aerodynamic Development of the 2011 Chevrolet Volt. SAE International Journal of. Passenger Cars – Mech. Syst., Vol. 4, No. 1, pp. 166–171.

Trancossi, M. (2011). An Overview of Scientific and Technical Literature on Coandă Effect Applied to Nozzles. SAE Technical Paper 2011–01–2591.

Van Dyke, M. (1982). An Album of Fluid Motion. The Parabolic Press, Stanford, California, USA, Chap. 5, pp. 74.

Walters, D. K. and Cokljat, D. (2008). A Three-Equation Eddy-Viscosity Model for Reynolds-Averaged Navier–Stokes Simulations of Transitional Flow. ASME Journal of Fluids Engineering Vol. 130, No. 12, 121401.

Welch, P. D. (1967). The Use of Fast Fourier Transform for the Estimation of Power Spectra: A Method Based on Time Averaging Over Short, Modified Periodograms. IEEE Trans. Audio Electroacoustics, Vol. AU-15, pp. 70–73.

White, F. (2011). Fluid Mechanics. 7th ed., McGraw-Hill Companies, New York, USA, Chap. 6, pp. 403–408.

Wilcox, D. C. (1988). Reassessment of the Scale-Determining Equation for Advanced Turbulence Models. AIAA Journal, Vol. 26, No. 11, pp. 1299–1310.

Winternitz, F. A. L. and Ramsay, W. J. (1957). Effects of Inlet Boundary Layer on Pressure Recovery Conversion and Losses in Conical Diffusers. Journal of the Royal Aeronautical Society, Vol 61, pp. 116–124.

Wright, P. G. (1983). The Influence of Aerodynamics on the Design of Formula One Racing Cars. International Journal of Vehicle Design, Vol. 3, No. 4, pp. 383–397.

Yang, Z., Igarashi, H., Martin, M. and Hu, H. (2008). An Experimental Investigation on Aerodynamic Hysteresis of a Low-Reynolds Number Airfoil, 46th AIAA Aerospace Sciences Meeting and Exhibit, Aerospace Sciences Meetings

Zerihan, J. and Zhang, X. (2000). Aerodynamics of a Single-Element Wing in Ground Effect. Journal of Aircraft, Vol. 37, No. 6, pp. 1058–1064.

Zhang, X. and Zerihan, J. (2003a). Aerodynamics of a Double Element Wing in Ground Effect. AIAA Journal, Vol. 41, No. 6, pp. 1007–1016.

Zhang, X. and Zerihan, J. (2003b). Edge Vortices of a Double-Element Wing in Ground Effect. Journal of Aircraft, Vol. 41, No. 5, pp. 1127–1137.

Zhang, X., Senior, A. and Ruhrmann, A. (2004). Vortices Behind a Bluff Body with an Upswept Aft Section in Ground Effect. International Journal of Heat Fluid Flow, Vol. 25, pp. 1–9.

Zhang, X., Zerihan, J., Ruhrmann, A. and Deviese, M. (2002). Tip Vortices Generated by a Wing in Ground Effect. 11th International Symposium on Applications of Laser Techniques to Fluid Mechanics, Instituto SuperiorTecnico, Lisbon, Portugal.

Zhang, X., Toet, W. and Zerihan, J. (2006). Ground Effect Aerodynamics of Race Cars. ASME Journal of Fluids Engineering, Vol. 59, No. 1, pp. 33–49.

Appendices

Appendix A — Measurements Uncertainty and Repeatability Analysis

Measurements Repeatability Analysis

The repeatability of the wind tunnel measurements were assessed in short, medium and long terms. The short-term repeatability involved repeating two consecutive test runs in a single test session. Non-consecutive test runs were done for the medium and long-term repeatability which involved resetting the ride height and yaw of the diffuser body before repeating the test runs the following day and week respectively. Measurements accessed in the repeatability analysis include: force, on-surface pressure and off-surface velocity measurements in the diffuser body near-wake using LDV. The agreement in the data from the measurements appears to be reasonably good as calculated at the reference ride height of $h/d = 0.191$ (maximum-force type B regime) for the baseline plane diffuser.

For the force measurements, the downforce C_L and drag C_D data were compared between both test runs of the short, medium and long terms. The repeatability errors for the short, medium and long terms are given as: short-term: ± 0.00013 for C_L and ± 0.00027 for C_D; mid-term: ± 0.00011 for C_L and ± 0.00022 for C_D; long-term: ± 0.00010 for C_L and ± 0.00024 for C_D. Measurements at the asymmetrical flow regimes also generally appear to fall within the repeatability errors. In terms of the measurement repeatability for the on-surface pressure measurement, the repeatability was assessed using the peak suction measured close to the diffuser inlet at $x/d = 3.19$. Respective repeatability errors for the short term, medium, and long term repeatability of surface pressures are given as: ± 0.0025, ± 0.0034, ± 0.003, and measurements along the diffuser body centreline and across the diffuser are reasonably

within the repeatability measurements. Setting up and running the LDV experiments is a time-consuming process. Therefore velocity measurement repeatability was accessed at a location on the centreline plane underneath the region of low velocity and above the region of high velocity ($y/d = 1.6$ and $x/d = 7.84$) for the symmetrical type B flow regime at $h/d = 0.191$ and the asymmetrical type C flow regime at $h/d = 0.153$. Two test runs of 2000 data sets each for the u and v components of the data point were done for both ride heights and grouped into batches of 200 data sets. Mean velocity at the data point was measured from an ensemble average of the two thousand samples and for each of the two hundred samples using a moving-average scheme. The mean velocity for each data set is within 5.3% of the mean velocity of the total data set for each ride height.

Force and Pressure Measurements Uncertainty Analysis

Error analysis was conducted to determine the total error, comprising the repeatability errors, measurement errors and stochastic errors. The model ride height was maintained to within ± 0.02 mm and yaw angle set to within $\pm 0.05°$. The freestream velocity and rolling belt speed was regulated by the wind tunnel control system to within $\pm 0.06\, m/s$ and $\pm 0.02\, m/s$ respectively. Uncertainties were evaluated based on variables that influence the force and surface pressure measurements as shown in Table A–1. The total uncertainties were calculated using the root-mean-square procedure described by Abernathy et al. (1985) and Moffat (1988) and were determined, using a 95% confidence level. The total uncertainties for the coefficients of lift and drag at the maximum downforce ride height of $h/d = 0.191$ are ± 0.0025 and ± 0.0032 respectively. The total uncertainty of the diffuser inlet pressure coefficient is ± 0.057.

Table A-1: Uncertainties evaluated based on influencing experimental variables

Variable	Error	C_L	C_D	C_p	Source
Force Balance	±0.016% $(Lift)$ ±0.078% $(Drag)$	± 0.00013	± 0.000624	—	Calibration Report for the AEROTECH Force Balance
Ride Height	±0.02 mm	± 0.0022	± 0.00076	± 0.0148	Accuracy of Drop Height Gauge
Dynamic Pressure	±0.2%	± 0.00081	± 0.00093	± 0.0097	Sensor Datasheet
Pressure Transducer	±0.25%	—	—	± 0.0011	Sensor Accuracy (% of full scale)
Pitch	±0.04°	± 0.00048	± 0.00034	± 0.053	Calculated
Yaw	±0.05°	± 0.00043	± 0.0028	± 0.0080	Calculated
	Total	$\mathbf{\pm 0.0025}$	$\mathbf{\pm 0.0032}$	$\mathbf{\pm 0.057}$	

LDV Measurements Uncertainty Analysis

The seeding response error due to the inability of the seeding particles to follow the flow was calculated with the principle presented by Dring (1982). The methodology associates the acceleration of a particle in a surrounding fluid to its Stokes number S_t and if the Stokes number is < 0.01 then the maximum velocity error is the same as its Stokes number. The estimated Stokes number S_t was calculated to be $2.8\,x\,10^{-4}$ using Equation A.1 which implied that the seeding response error was insignificant.

$$S_t = \frac{\rho_p d_p^2}{18\mu T_c} = 0.00028 \qquad (A.1)$$

Where,

ρ_p is the particle fluid density $= 912\ kg\ m^{-3}$

d_p is the particle diameter $= 0.9\,x\,10^{-6}\ m$

μ is the air dynamic viscosity $= 1.75\,x\,10^{-5}\ kg\ m^{-1}\ s^{-1}$

T_c is the characteristic acceleration time that represents time for the particle to cross the shear layer in the near − wake region $= 8.5\,x\,10^{-3}\ s$

In evaluating the mean velocity, the velocity bias was eliminated by applying the particle transit time t (Buchave et al., 1979) as the sample weighting factor which is inversely proportional to the sample velocity. This was done because at a particular point in a uniformly-seeded flow, a velocity fluctuation above the mean value can capture more samples than a

comparable velocity fluctuation below the mean velocity. As a result, the calculated mean velocity will tend to be biased towards the velocities above the mean. Thus, velocity bias was eliminated from the mean measured signals M, by using Equation A. 2 below:

$$M = \frac{\sum_{x}^{N_*} s_x t_x}{\sum_{x}^{N_*} t_x} \qquad (A.2)$$

Where,

s represents the velocity component

x as a subcript, refers to the index of the current sample from the population N_*

The sampling error was also evaluated because the interval at which the samples were obtained influenced the calculation of statistics such as population mean and variance. Furthermore, it is difficult to acquire statistically-independent samples with LDV because samples are obtained when a seeding particle crosses a set measurement threshold. As stated in Section 3.2.4, the maximum number of samples and sampling time was set at 2000 and 20 s respectively at each measurement point. When one of the set measurement thresholds was achieved, the probe moved to the next measurement position and this created a variation in sampling time and uncertainty for each measurement point. As a result, the uncertainty was evaluated with Equation A. 3 by applying the methodology provided by Benedict and Gould (1996) where at a 95% confidence level for the mean value $\overline{U}$ is:

$$1.96\sqrt{\frac{\overline{u_*{}^2}}{N_*}} \qquad (A.3)$$

Where it applies to a population distribution with $N_* > 50$ and with statistically independent samples u_*

However, the other threshold involves the estimation of the potential number of statistically independent samples, N_{eff}, from the sampling time T_m, and the integral timescale τ_1

$$N_{eff} = \frac{T_m}{2\tau_1} \tag{A.4}$$

N_{eff} is substituted into Equation A.3 only if $N_* > N_{eff}$, and thus a posteriori estimation of τ_1 is needed for the calculation of N_{eff}

The integral time scale is estimated by employing the methodology of Nobach (2000) and is defined by the correlation of two samples from the same population as deduced from the autocorrelation function. However, the autocorrelation function can be estimated from the inverse power spectral density of the data with equidistant samples. In the present case, the data is randomly-sampled so a Fourier analysis cannot be done because it could generate aliasing error. Nobach (2000) employed a method that does not involve re-sampling but includes the use of the weighting transit time to eliminate the aliasing error. Software developed by Knowles (2005) was then used to quantify N_{eff} and confidence levels of mean values with the estimation of the integral time scale τ_1 on each data point in the measurement volume. At a 95% confidence limit, it was estimated that 50% of the measurements points had an error smaller than 1% and the remainder had an error below 8%.

The LDV probe can measure velocities at any point within the measurement volume. This implied a systematic error in the measurement location within the dimensions of the LDV measurement volume. The maximum location error where the particle velocity is measured was assumed to be 50% of the $x-y-z$ dimensions of the measurement volume. This equates to systematic errors of ± 0.28, ± 0.28, and $\pm 2.5\, mm$ in the x, y, and z reference axes, respectively.

Appendix B — Wind Tunnel Model Geometry

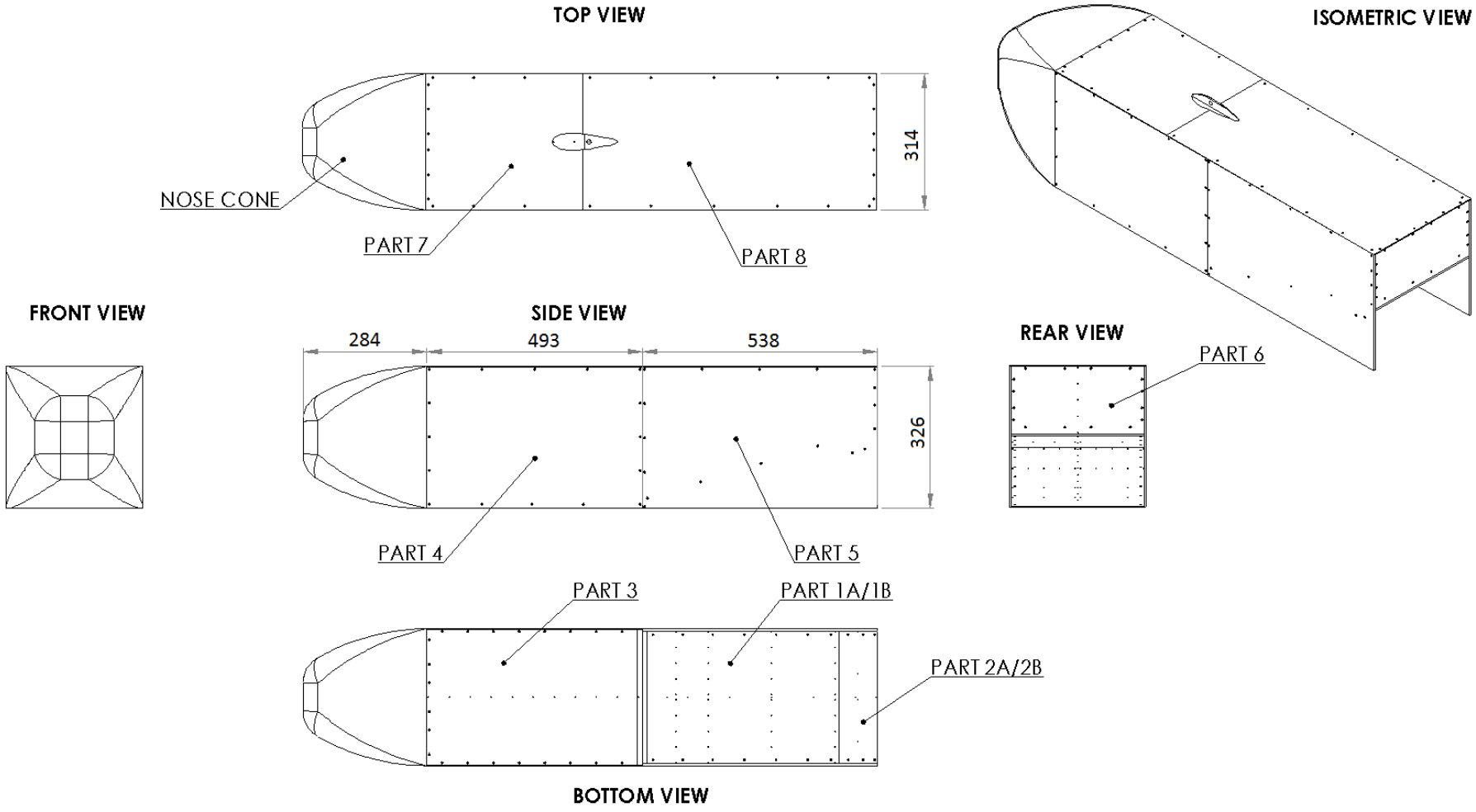

Appendix B-1: Design layout of diffuser bluff body (dimensions in mm)

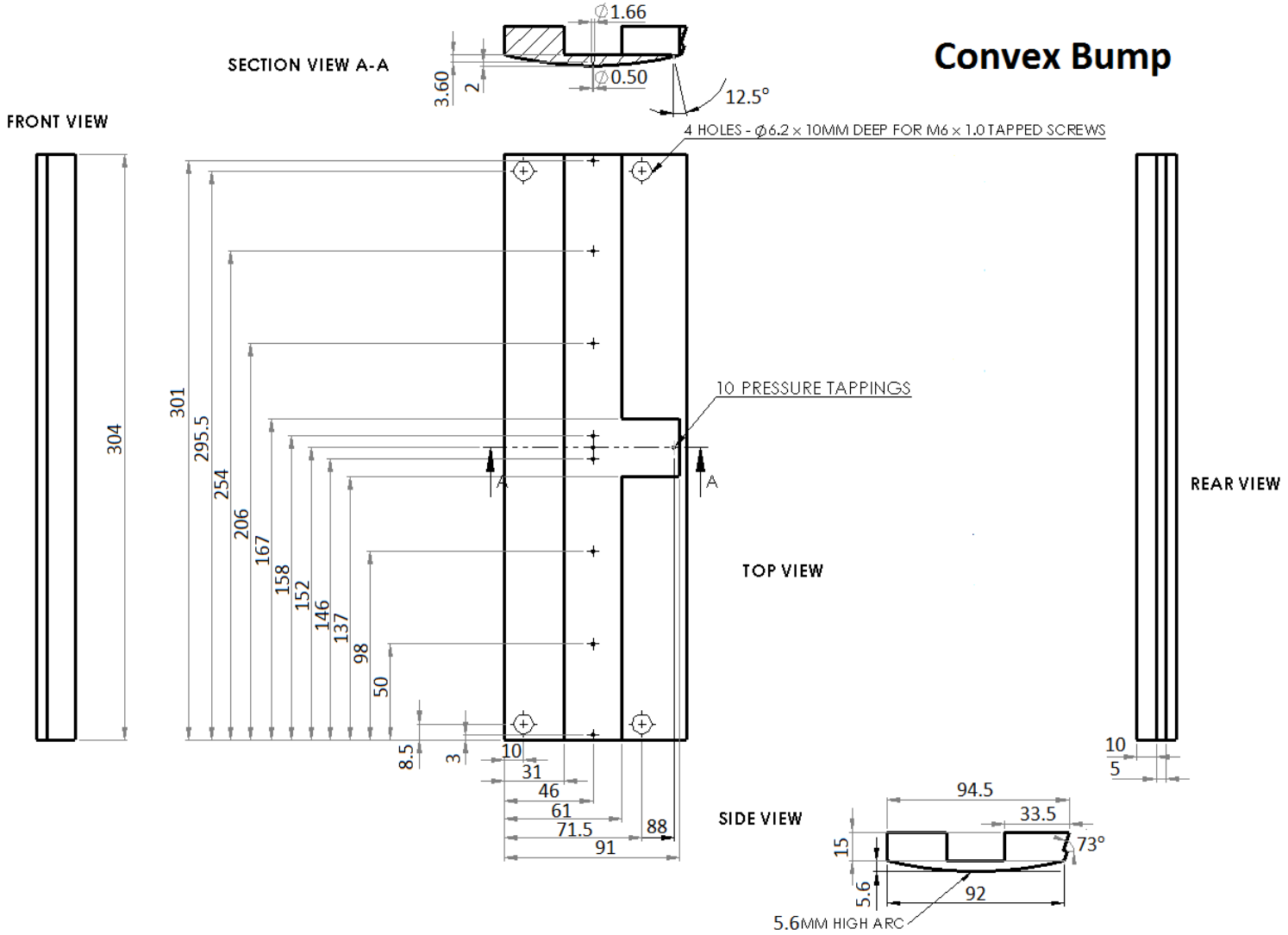

Appendix B-2: Detailed dimensions of convex bump (dimensions in mm)

Wing coordinates (in mm)

Suction side		Pressure side	
x	y	x	y
83.71093	4.212742	0	0
83.71093	3.212742	0.09171	0.724509
82.52983	2.888865	0.18342	0.999639
77.93516	1.678293	0.467721	1.586583
73.34966	0.55026	0.926271	2.127672
68.76416	-0.51358	1.384821	2.47617
64.16949	-1.49487	1.843371	2.742129
59.58399	-2.39363	2.301921	2.861352
54.99849	-3.21902	2.760471	2.943891
50.41299	-3.98021	3.219021	3.017259
45.81832	-4.65887	3.677571	3.081456
41.23282	-5.26415	4.136121	3.154824
36.64732	-5.7869	4.594671	3.228192
32.06182	-6.22711	5.053221	3.292389
27.47632	-6.61229	5.511771	3.365757
22.89082	-6.90576	6.428871	3.475809
18.30532	-7.07084	7.345971	3.595032
16.47112	-6.99747	8.272242	3.705084
14.63692	-6.82322	9.189342	3.787623
12.80272	-6.53892	11.02354	3.961872
10.97769	-6.16291	12.85774	4.090266
9.143487	-5.67685	14.69194	4.191147
8.226387	-5.39255	16.52614	4.264515
7.309287	-5.08073	18.36034	4.337883
6.401358	-4.75058	22.93667	4.484619
5.484258	-4.39291	27.52217	4.622184
5.025708	-4.20032	32.10767	4.713894
4.567158	-3.99856	36.69317	4.759749
4.108608	-3.79679	41.27867	4.778091
3.650058	-3.59503	45.86417	4.741407
3.191508	-3.37493	50.44967	4.668039
2.732958	-3.15482	55.03517	4.548816
2.283579	-2.92555	59.6115	4.392909
1.825029	-2.6971	64.197	4.181976
1.366479	-2.43949	68.7825	3.934359
0.907929	-2.09099	73.368	3.750939
0.449379	-1.54073	77.9535	3.778452
0.18342	-0.9813	82.539	4.090266
0.09171	-0.6970	83.71093	4.212742

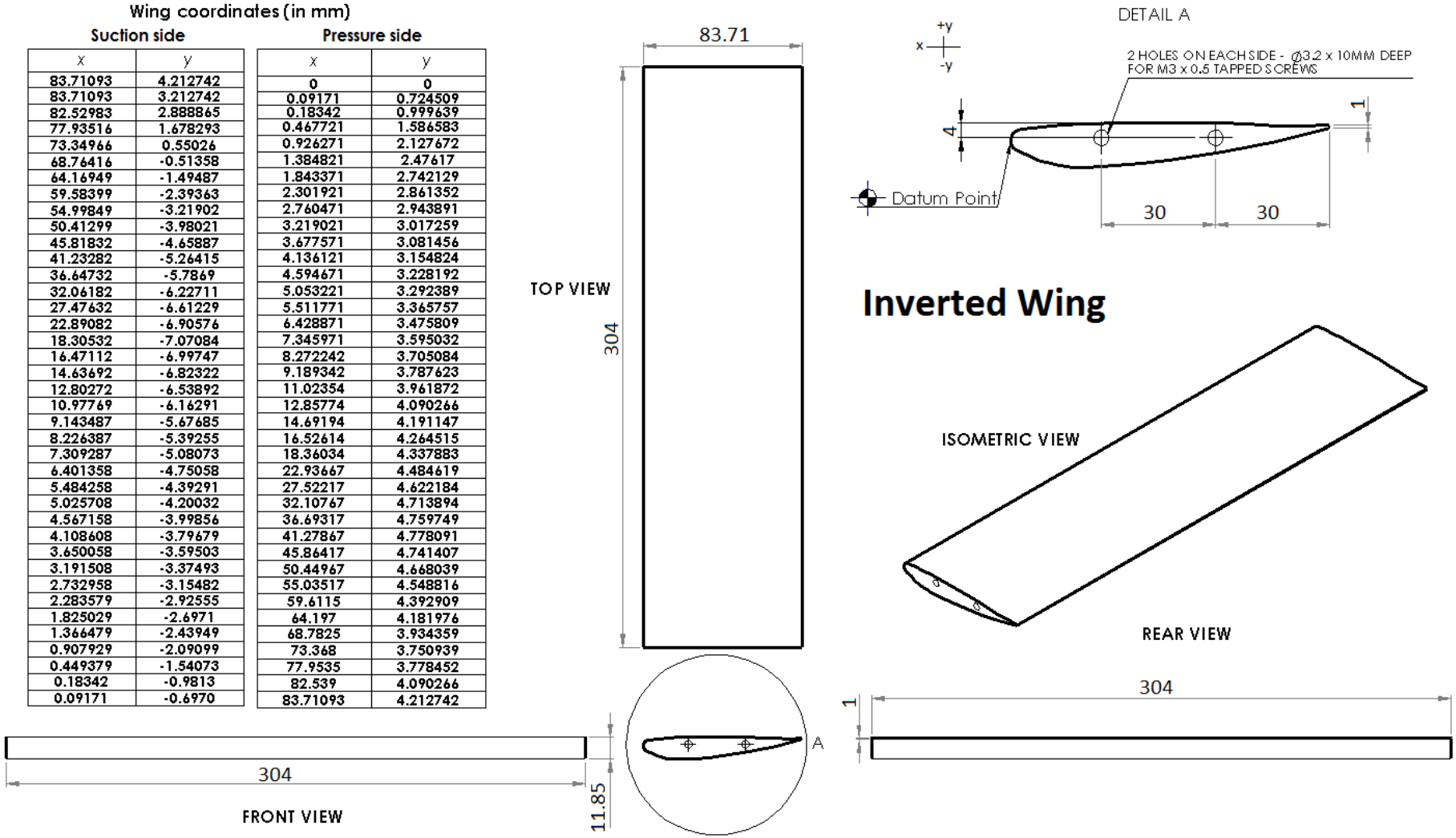

Appendix B-3: Detailed dimensions of inverted wing (dimensions in mm)

Appendix C — Experimental and Numerical Test Conditions

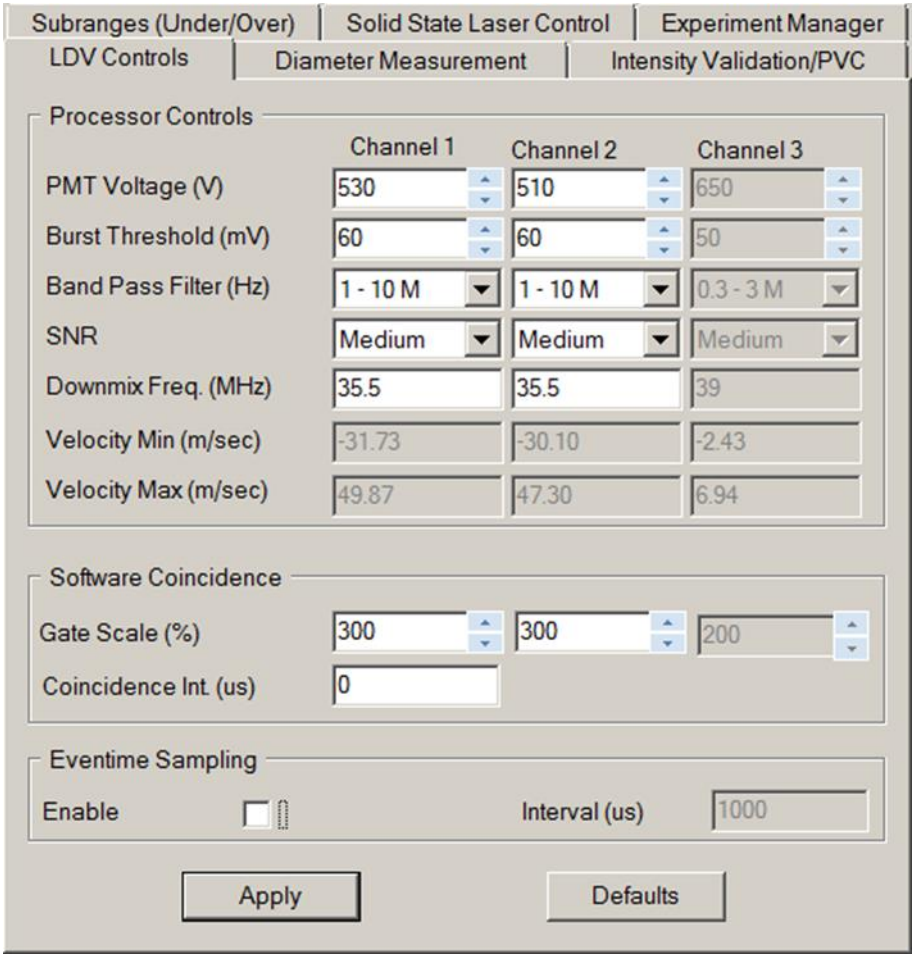

Appendix C-1: LDV controls configuration

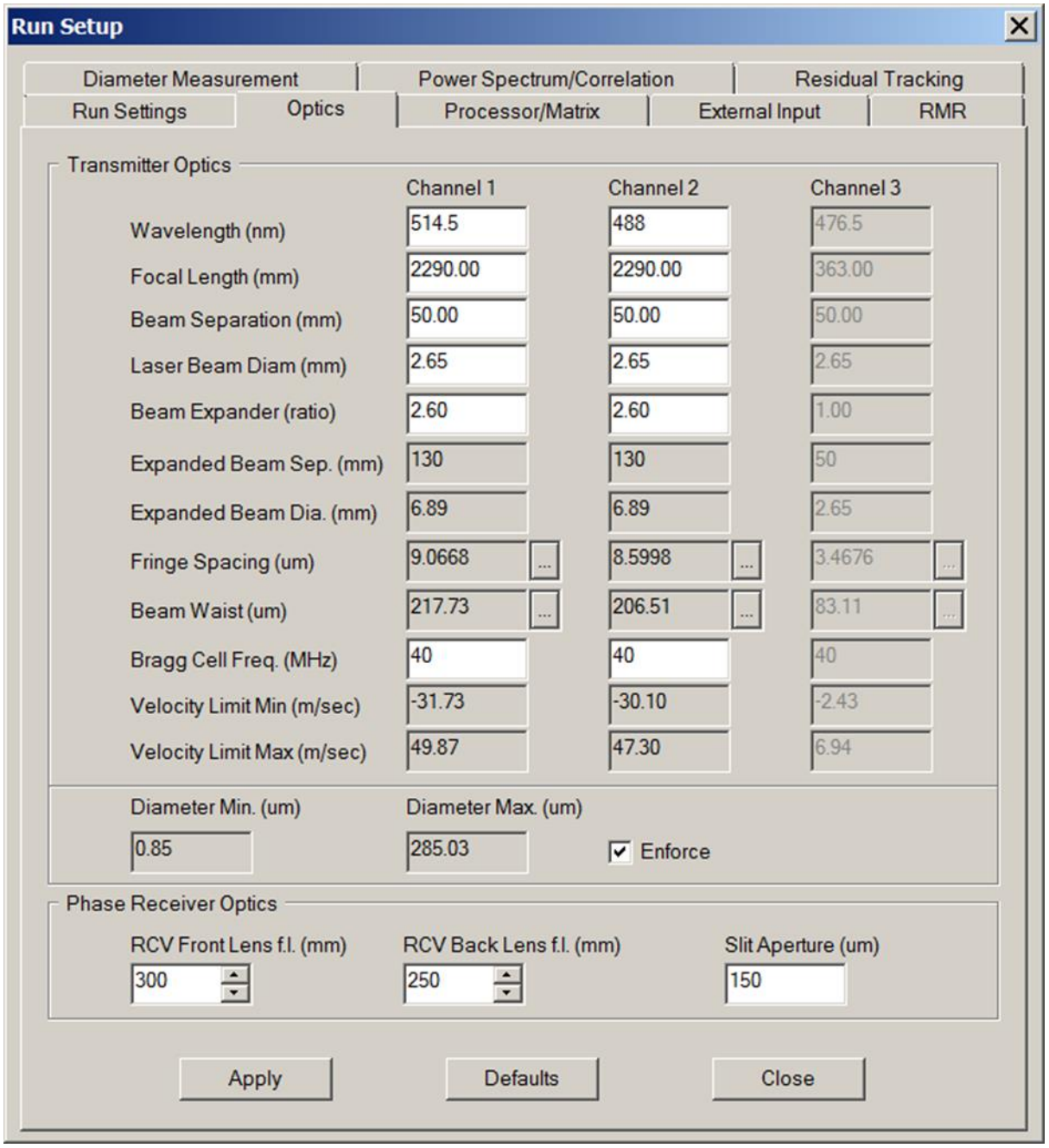

Appendix C-2: LDV optics configuration

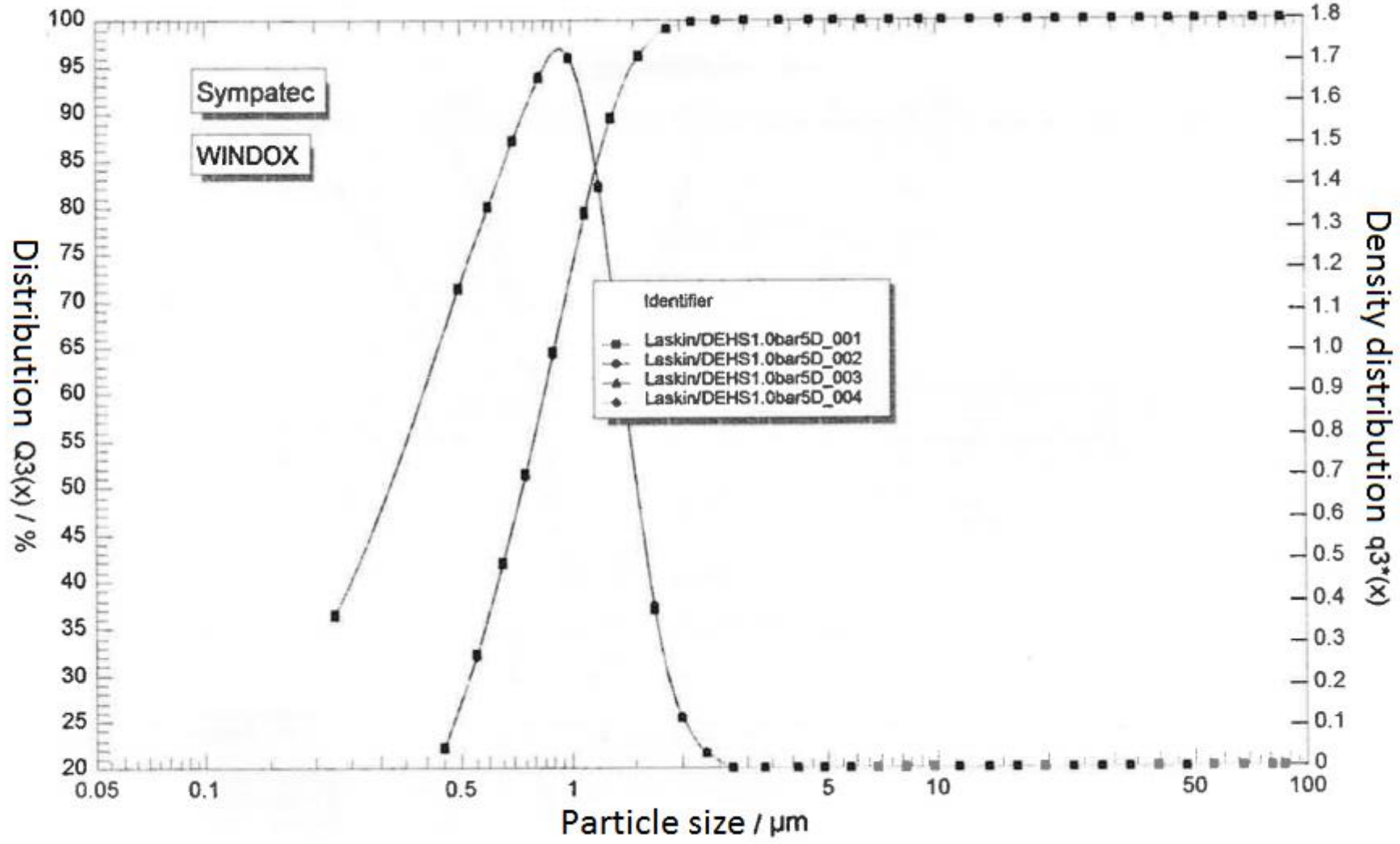

Appendix C-3: Particle size distribution for Di-Ethyl-Hexyl-Sebacat (DEHS) atomized at 1 bar

SETUP CRITERIA	RANS	URANS	IDDES
Turbulence model	$\kappa-\omega$ SST (h/d =0.764 and 0.382) transition $k-kl-\omega$ (h/d =0.191 and 0.064) transition SST $y-Re_\theta$ (h/d =0.153)	transition $k-kl-\omega$ (h/d =0.191 and 0.064)	LES and $\kappa-\omega$ SST (h/d =0.764 and 0.382) LES and transition SST $y-Re_\theta$ (h/d =0.153)
Time state	Steady	Transient (Time-averaged)	Transient (Time-averaged)
Solver type	3-D Pressure-based	3-D Pressure-based	3-D Pressure-based
Material	Air at ρ = $1.225\ kg\ m^{-3}$ μ = $1.7894\ x\ 10^5 kg\ m^{-1}\ s^{-1}$	Air at ρ = $1.225\ kg\ m^{-3}$ μ = $1.7894\ x\ 10^5 kg\ m^{-1}\ s^{-1}$	Air at ρ = $1.225\ kg\ m^{-3}$ μ = $1.7894\ x\ 10^5 kg\ m^{-1}\ s^{-1}$
Near-wall treatment	Standard	Standard	Standard
y^+	Baseline, Convex bump ($y^+ \leq 1$) Diffuser with wing, Diffuser with bump & wing ($y^+ \leq 0.1$)	Baseline, Convex bump ($y^+ \leq 1$) Diffuser with wing, Diffuser with bump & wing ($y^+ \leq 0.1$)	Baseline, Convex bump ($y^+ \leq 1$) Diffuser with wing, Diffuser with bump & wing ($y^+ \leq 0.1$)
Boundary Condition			
Inlet Type	Velocity inlet $U_\infty = 20\ m\ s^{-1}$ Turbulence intensity = 0.3% Turbulent length scale = 0.01m	Velocity inlet $U_\infty = 20\ m\ s^{-1}$ Turbulence intensity = 0.3% Turbulent length scale = 0.01m	Velocity inlet $U_\infty = 20\ m\ s^{-1}$ Turbulence intensity = 0.3% Turbulent length scale = 0.01m
Outlet Type	Pressure outlet Gauge Pressure $= 0$ Pa Turbulence intensity = 0.3% Turbulent Length scale = 0.01m	Pressure outlet Gauge Pressure $= 0$ Pa Turbulence intensity = 0.3% Turbulent Length scale = 0.01m	Pressure outlet Gauge Pressure $= 0$ Pa Turbulence intensity = 0.3% Turbulent Length scale = 0.01m
Ground	Moving ground Velocity = $20\ m\ s^{-1}$	Moving ground Velocity = $20\ m\ s^{-1}$	Moving ground Velocity = $20\ m\ s^{-1}$
Walls	Symmetry condition	Symmetry condition	Symmetry condition
Solution Methods			
Pressure-Velocity Coupling Scheme	SIMPLE	PISO with Skewness and Neighbour correction factors of 1	PISO with Skewness and Neighbour correction factors of 1
Discretization			
Cell Gradient	Green-Gauss node based	Green-Gauss node based	Green-Gauss node based
Pressure	Standard	Standard	Standard
Momentum	Second order	Second order	Bounded central differencing
Turbulent Kinetic Energy	Second order	Second order	Second order
Laminar Kinetic Energy	Second order	Second order	Second order
Intermittency	Second order (Intermittency factor of 0.46)	—	Second order (Intermittency factor of 0.46)
Momentum thickness Re	Second order	Second order	Second order
Transient Formulation	—	Bounded second order implicit	Bounded second order implicit

Appendix C-4: Computational test configurations using the ANSYS version 17.2 FLUENT solver

Appendix D — Experimental Downforce and Drag Measurements

	Baseline Plane Diffuser		Diffuser with Bump		Diffuser with Wing		Diffuser with Bump & Wing	
h/d	C_L	C_D	C_L	C_D	C_L	C_D	C_L	C_D
0.764	-0.876	0.282	-0.919	0.292	-0.981	0.313	-0.978	0.314
0.701	-0.93	0.29	-0.972	0.3	-1.034	0.322	-1.031	0.323
0.637	-0.997	0.302	-1.037	0.31	-1.101	0.333	-1.097	0.332
0.573	-1.083	0.313	-1.12	0.323	-1.186	0.347	-1.181	0.346
0.510	-1.197	0.333	-1.228	0.341	-1.298	0.366	-1.289	0.365
0.446	-1.359	0.361	-1.38	0.366	-1.442	0.391	-1.435	0.391
0.414	-1.466	0.379	-1.479	0.383	-1.537	0.407	-1.53	0.406
0.382	-1.596	0.401	-1.599	0.404	-1.659	0.428	-1.656	0.427
0.366	-1.67	0.414	-1.672	0.417	-1.737	0.44	-1.739	0.442
0.350	-1.734	0.424	-1.734	0.426	-1.816	0.45	-1.819	0.452
0.334	-1.752	0.424	-1.762	0.431	-1.827	0.449	-1.825	0.4506
0.318	-1.769	0.4298	-1.782	0.434	-1.824	0.447	-1.82	0.4501
0.303	-1.779	0.4290	-1.783	0.434	-1.813	0.443	-1.812	0.447
0.287	-1.786	0.432	-1.804	0.439	-1.831	0.445	-1.832	0.45
0.271	-1.811	0.438	-1.828	0.445	-1.853	0.45	-1.857	0.454
0.255	-1.827	0.443	-1.865	0.454	-1.872	0.454	-1.882	0.46
0.242	-1.851	0.449	-1.887	0.459	-1.887	0.458	-1.9	0.464
0.229	-1.866	0.453	-1.911	0.464	-1.911	0.463	-1.92	0.467
0.217	-1.892	0.459	-1.938	0.47	-1.939	0.468	-1.951	0.473
0.210	-1.903	0.461	-1.947	0.471	-1.953	0.47	-1.966	0.475
0.204	-1.908	0.462	-1.957	0.473	-1.964	0.472	-1.977	0.476
0.197	-1.914	0.463	-1.956	0.473	-1.97	0.471	-1.9831	0.477
0.191	-1.915	0.463	-1.954	0.472	-1.973	0.472	-1.9833	0.476
0.185	-1.91	0.462	-1.949	0.471	-1.967	0.471	-1.978	0.474
0.178	-1.89	0.459	-1.494	0.424	-1.7	0.444	-1.962	0.471
0.172	-1.396	0.399	-1.407	0.407	-1.434	0.412	-1.468	0.422
0.166	-1.339	0.388	-1.35	0.396	-1.388	0.403	-1.4	0.409
0.153	-1.305	0.38	-1.316	0.385	-1.336	0.39	-1.353	0.396
0.140	-1.291	0.374	-1.289	0.377	-1.31	0.381	-1.323	0.385
0.127	-1.276	0.37	-1.284	0.371	-1.295	0.373	-1.307	0.375
0.115	-1.248	0.367	-1.236	0.365	-1.244	0.366	-1.255	0.365
0.102	-1.237	0.363	-1.227	0.362	-1.235	0.361	-1.236	0.361
0.089	-1.2	0.349	-1.187	0.347	-1.191	0.346	-1.187	0.346
0.076	-1.174	0.329	-1.173	0.329	-1.202	0.332	-1.201	0.331
0.064	-1.058	0.3009	-1.064	0.3023	-1.078	0.3018	-1.068	0.3003

Appendix D-1: C_L and C_D wind tunnel measurements at Re = $1.8\ x\ 10^6$ ($U_\infty = 20 m/s$) for the various diffusers

Appendix E — Publications Prepared from this Thesis

Ehirim, O. H., Knowles, K. and Saddington, A. J., (2018). Ground-effect Aerodynamics: an Analytical Review on Ground-effect Diffusers. ASME Journal of Fluids Engineering. **Accepted**

Ehirim, O. H., Knowles, K. Saddington, A. J. and Finnis, M. V., (2018). Aerodynamics of a Convex Bump on a Ground-effect Diffuser. ASME Journal of Fluids Engineering. **Accepted**

Ehirim, O. H., Knowles, K. Saddington, A. J., Finnis, M. V. and Lawson, N. J., (2018). On the Near-wake of a Ground-effect Diffuser with Passive Flow Control. International Journal of Automotive Technology. **Submitted**

Ehirim, O. H., Knowles, K. Saddington, A. J. and Finnis, M. V., (2018). Passive Flow Control on the Ground-effect Diffuser using an Inverted Wing. SAE Journal of Passenger Cars – Mechanical Systems. **Submitted**